

Studying Magnetism with X-Ray Standing Waves

Dissertation
zur Erlangung des Doktorgrades
an der Fakultät für Mathematik, Informatik und Naturwissenschaften
Fachbereich Physik
der Universität Hamburg

vorgelegt von

Michał Kamiński
aus Gleiwitz (Polen)

Hamburg
2022

Gutachter/innen der Dissertation:

Prof. Dr. Andreas Stierle
Prof. Dr. Edgar Weckert

Zusammensetzung der Prüfungskommission:

Prof. Dr. Nina Rohringer
Prof. Dr. Andreas Stierle
Prof. Dr. Edgar Weckert
Dr. Martin Tolkieln

Vorsitzende/r der Prüfungskommission:

Prof. Dr. Caren Hagner

Datum der Disputation:

09.09.2022

Vorsitzender Fach-Promotionsausschusses PHYSIK:

Prof. Dr. Wolfgang J. Parak

Leiter des Fachbereichs PHYSIK:

Prof. Dr. Günter H. W. Sigl

Dekan der Fakultät MIN:

Prof. Dr. Heinrich Graener

Eidesstattliche Versicherung / Declaration on oath

Hiermit versichere ich an Eides statt, die vorliegende Dissertationsschrift selbst verfasst und keine anderen als die angegebenen Hilfsmittel und Quellen benutzt zu haben.

Hamburg, den 28.06.2022

MKaminiski.

Unterschrift des Doktoranden

Abstract

A new method for studying the magnetic structures at the atomic level was developed within the scope of this thesis. A combination of the site-selectivity of the diffraction-based x-ray standing waves (XSW) technique and sensitivity to magnetic properties of the x-ray magnetic circular dichroism (XMCD) spectroscopy leads to a completely new perspective. The XSW method makes use of the standing wave appearing as a result of an interference between the incoming and the Bragg reflected electromagnetic waves. In the magnetic x-ray standing waves (MXSW) technique, a circular polarisation of the incoming beam is used to additionally gain magnetic information via the dichroism in the absorption of the standing wave. Due to the utilisation of the x-ray interference field, the phase information is preserved, so the magnetic structure can be studied directly. The shape of the modulation in the MXSW signal is characteristic of a given distribution of the magnetic moments and yields directly structural information. The development of the new method within the scope of this thesis consisted firstly of constructing the theoretical foundations. The dynamical theory of x-ray diffraction is used to treat theoretically the scattering phenomena. The absorption of the resulting wavefield is described within the framework of the time-dependent perturbation theory. Secondly, the simulations for several systems with different magnetic ordering were conducted. The simulation results were later used to explain the observed experimental data. Finally, two MXSW experiments were performed on a platinum-cobalt alloy and an yttrium-iron-garnet single crystals. The resulting angle-dependent XMCD signals exhibit a clear variation caused by the x-ray standing wave. The comparison between the simulation results and experimental data confirmed the validity of the novel MXSW theory.

Kurzfassung

Untersuchung des Magnetismus mit stehenden Röntgenwellen

Im Rahmen dieser Arbeit wurde eine neue Methode zur Untersuchung der magnetischen Strukturen auf atomarer Ebene entwickelt. Eine Kombination aus der Ortsselektivität der auf Beugung basierenden Methode der stehenden Röntgenwellen (Eng. *x-ray standing waves*, XSW) und der Empfindlichkeit gegenüber magnetischen Eigenschaften der zirkulärer magnetischer Röntgendichroismus-Spektroskopie (Eng. *x-ray magnetic circular dichroism*, XMCD) führt zu einer völlig neuen Perspektive. Die XSW-Methode macht sich die stehende Welle zunutze, die als Ergebnis einer Interferenz zwischen den einfallenden und den Bragg-reflektierten elektromagnetischen Wellen entsteht. Bei der Methode zur Untersuchung des Magnetismus mit stehenden Röntgenwellen (Eng. *magnetic x-ray standing waves*, MXSW) wird eine zirkulare Polarisierung des einfallenden Strahls genutzt, um zusätzlich magnetische Informationen durch den Dichroismus in der Absorption der stehenden Welle zu gewinnen. Durch die Nutzung des Röntgeninterferenzfeldes bleibt die Phaseninformation erhalten, sodass die magnetische Struktur direkt untersucht werden kann. Die Form der Modulation im MXSW-Signal ist charakteristisch für eine bestimmte Verteilung der magnetischen Momente und liefert direkt eine Strukturinformation. Die Entwicklung der neuen Methode im Rahmen dieser Arbeit bestand zunächst in der Erarbeitung der theoretischen Grundlagen. Die dynamische Theorie der Röntgenbeugung wird verwendet, um die Streuphänomene zu berechnen. Die Absorption des resultierenden Wellenfeldes wird im Rahmen der zeitabhängigen Störungstheorie beschrieben. Zweitens wurden Simulationen für mehrere Systeme mit unterschiedlicher magnetischer Ordnung durchgeführt. Die Simulationsergebnisse wurden später verwendet, um die beobachteten experimentellen Daten zu erklären. Schließlich wurden zwei MXSW-Experimente an einer Platin-Kobalt-Legierung und einem Yttrium-Eisen-Granat Einkristall durchgeführt. Die resultierenden winkelabhängigen XMCD-Signale zeigen eine deutliche Variation, die durch die stehende Röntgenwelle verursacht wird. Der Vergleich zwischen den Simulationsergebnissen und den experimentellen Daten bestätigte die Gültigkeit der neuen MXSW-Theorie.

Streszczenie

Badania magnetyzmu przy użyciu rentgenowskich fal stojących

W ramach tej pracy doktorskiej, opracowana została nowa metoda badania struktury magnetycznej materiałów krystalicznych na poziomie atomowym. Nowa perspektywa uzyskana została poprzez połączenie metody rentgenowskich fal stojących (ang. *x-ray standing waves*, XSW), która dostarcza informacji strukturalnych, oraz czulej na właściwości magnetyczne spektroskopii rentgenowskiego magnetycznego dichroizmu kołowego (ang. *x-ray magnetic circular dichroism*, XMCD). W metodzie XSW wykorzystuje się falę stojącą powstającą w wyniku interferencji fal elektromagnetycznych — padającej i rozproszonej. W przypadku metody magnetycznych rentgenowskich fal stojących (ang. *magnetic x-ray standing waves*, MXSW) fala padająca jest kołowo spolaryzowana, co pozwala dodatkowo uzyskać informacje o strukturze magnetycznej, dzięki dichroizmowi w absorpcji fali stojącej. Wykorzystanie zjawiska interferencji pozwala zachować informację o fazie fali i badać strukturę magnetyczną w sposób bezpośredni. Informacja o strukturze dostarczana jest przez kształt sygnału MXSW, który jest charakterystyczny dla danego rozkładu momentów magnetycznych. W ramach tej pracy, stworzenie fundamentów nowej metody polegało w pierwszej kolejności na opracowaniu podstaw teoretycznych. Do opisu zjawiska rozpraszania wykorzystano dynamiczną teorię dyfrakcji promieniowania rentgenowskiego. Absorpcja uzyskanej w ten sposób fali opisana została z kolei w ramach zależnej od czasu teorii zaburzeń. Po drugie, wykonano symulacje komputerowe dla szeregu kryształów z różnym uporządkowaniem magnetycznym. Wyniki symulacji zostały wykorzystane później do analizy danych doświadczalnych. Na koniec, dwa doświadczenia MXSW zostały wykonane z użyciem monokryształów stopu platyny i kobaltu oraz granatu itrowo-żelazowego. Uzyskany kątowno-zależny sygnał XMCD wykazuje wyraźną zmianę powodowaną przez falę stojącą. Porównanie wyników symulacji i danych doświadczalnych pozwoliło potwierdzić słuszność opracowanej teorii MXSW.

Contents

Introduction	1
I Theoretical section	7
1 Dynamical theory of diffraction	9
1.1 Propagation equation	10
1.2 Wavefields, fundamental equations	11
1.3 Dispersion surface	13
1.4 General solution	14
1.5 Reflection geometry	15
1.6 X-ray standing wave	17
1.7 XSW structural analysis	20
1.8 The absorption correction for the wavevector	21
1.9 Scattering of the arbitrarily polarised wave	23
1.9.1 Parametrisation of the incoming wave	23
1.9.2 Boundary conditions and reflectivity	24
1.9.3 Total electric field	25
1.9.4 Correction for the complex wavevector	26
2 Absorption cross-section	29
2.1 Time-dependent perturbation theory	29
2.1.1 General formulation	29
2.1.2 Solution to the first order	31
2.1.3 The case of harmonic perturbation	32
2.1.4 Golden rule	32
2.2 Absorption of electromagnetic wave	33
2.2.1 Interaction Hamilton operator	33
2.2.2 Electric dipole approximation	34
2.2.3 Electric dipole selection rules	35
2.2.4 Cross-section	36
2.3 Absorption of the standing wave	37
3 X-ray magnetic circular dichroism	39
3.1 XMCD at the $L_{2,3}$ absorption edges in the 3d metals	40
3.1.1 Initial and final states	40
3.1.2 Geometry of the experiment	42

3.1.3	Transition matrix elements	43
3.1.4	XMCD signal	47
3.1.5	Degree of polarisation of the wave	51
3.2	XMCD at the $L_{2,3}$ absorption edges in the 5d metals	53
3.3	XMCD at the K absorption edge in the 3d metals	54
3.4	XMCD in other cases	55
3.5	Sum rules	55
4	Magnetic x-ray standing waves	57
4.1	The form of perturbation	58
4.2	Geometry of the experiment	59
4.3	Polarisation vector	61
4.4	Absorption of the standing wave	62
4.5	MXSW formula — XMCD for the standing wave	64
4.5.1	Specific cases	66
4.5.2	XMCD as difference between magnetic moment orientations	67
4.6	MXSW for many atoms	68
4.6.1	Magnetic standing wave structure factor	70
4.6.2	Specific cases	72
4.7	Correction for the complex wavevector for MXSW	73
4.8	Detection of XMCD via x-ray fluorescence	76
4.9	MXSW — classical approach	77
4.9.1	Degree of circular polarisation	78
4.10	Discussion about the Ξ_3 term	79
II	Simulations	81
5	MXSW for exemplary systems	83
5.1	Platinum-cobalt alloy	83
5.1.1	Magnetic dopant in the Pt_3Co structure	84
5.1.2	MXSW signal from Pt_3Co	88
5.2	Magnetite	93
5.2.1	MXSW signal from magnetite	94
5.3	Yttrium-iron-garnet	99
5.3.1	MXSW signal from YIG	100
5.4	Hematite	100
5.4.1	MXSW signal from hematite	101
6	XMCD-related absorption correction	103
6.1	Theory	104
6.2	Algorithm	105
6.3	Results of the simulations	107

III	Experimental section	109
7	General description of the MXSW experiment	111
7.1	Prerequisites for MXSW experiment	111
7.1.1	The sample	111
7.1.2	The experimental system	113
7.2	General schema of the MXSW experiment	116
7.3	Experimental system at the P09 beamline	118
7.3.1	Beamline optics	119
7.3.2	The diffractometer	119
7.3.3	Electromagnet system	120
7.3.4	Detectors	122
7.3.5	Control system	123
8	Experiment on the Pt₃Co crystal	125
8.1	Experimental details	125
8.2	Data analysis procedure and results	127
8.2.1	Reflectivity and beam stability	127
8.2.2	Fluorescence spectra	128
8.2.3	Fluorescence yield	129
8.2.4	MXSW signal	131
8.3	Discussion	134
9	Experiment on the YIG crystal	137
9.1	Experimental details	137
9.2	Results	139
9.2.1	Raw experimental data	139
9.2.2	Comparison with simulations	142
9.2.3	Artefact-free MXSW signal	142
9.2.4	Scans without the external magnetic field	144
9.2.5	Control scans away from the absorption edge	145
9.3	Discussion	146
	Summary and conclusions	149
A	Detailed derivations	155
A.1	Dynamical theory of diffraction	155
A.1.1	Tiepoint coordinates	155
A.1.2	General solution for X and ξ	156
A.2	Time-dependent perturbation theory	157
A.2.1	Matrix elements in electric dipole approximation	157
A.2.2	Incident flux	158
A.3	MXSW theory	158
A.3.1	Polarisation-related quantities \mathfrak{A} , \mathfrak{B} and \mathfrak{C}	158
A.4	Integral in the absorption correction	160

B	2p \rightarrow 3d transitions	163
B.1	Transitions fulfilling $\Delta m_\ell = 1$	163
B.2	Transitions fulfilling $\Delta m_\ell = 0$	164
C	Absorption correction related to XMCD	165
C.1	Influence on the phase of reflectivity	165
D	Permanent magnet system	167
D.1	First version	168
D.2	Second version	169
E	Experimental details	171
E.1	Pt ₃ Co hysteresis curve	171
E.2	Energy spectrum for YIG	171
E.3	Argon fluorescence yield	172
E.4	In- and out-of-field reflectivity	172
	List of Symbols	175
	List of Abbreviations	183
	References	185
	Acknowledgements	197

List of Figures

1.1	Definition of the polarisation unit vectors	12
1.2	Dispersion surface	14
1.3	Boundary conditions for the wavevectors	14
1.4	The amplitude ratio ξ for Si crystal, (111) reflection	17
1.5	The principle of the x-ray standing waves method	19
1.6	The relative intensity of the standing wave for Si crystal, (111) reflection	19
1.7	Schematic picture of x-ray diffraction in Bragg geometry for the absorption correction for the wavevector	22
1.8	Comparison between reflectivities for Si (111) reflection for different polarisations	25
1.9	Comparison between relative electric field intensity for Si (111) reflection for different polarisations	26
3.1	The coordinate systems for describing the XMCD experiment	42
3.2	Schema of the transitions from the 2p to the 3d states fulfilling the selection rule $\Delta m_\ell = -1$	46
4.1	The coordinate system \mathcal{O}' for the MXSW experiment, in which the diffraction process is described naturally	60
4.2	The \mathcal{O} and \mathcal{O}' coordinate systems for describing the MXSW experiment	60
5.1	Unit cell of Pt ₃ Co ordered alloy	84
5.2	The normalised MXSW signal for a dopant atom with a magnetic moment located in the Pt ₃ Co lattice. The magnetic moment is assumed to be parallel to the reflecting lattice planes and confined in the scattering plane	85
5.3	The analysis of the terms from the numerator of equation (5.1), describing the MXSW signal from the magnetic dopants having magnetic moments parallel to the reflecting lattice planes	86
5.4	The graph showing how the MXSW signal for one atom is constructed from the individual terms	86
5.5	The normalised MXSW signal for a dopant atom with a magnetic moment located in the Pt ₃ Co lattice. The magnetic moment is assumed to be perpendicular to the reflecting lattice planes and confined in the scattering plane.	87
5.6	The analysis of the terms from the numerator of equation (5.2), describing the MXSW signal from the magnetic dopants having magnetic moments perpendicular to the reflecting lattice planes	88
5.7	The normalised MXSW signal for a Pt ₃ Co crystal, assuming the natural magnetic structure	89
5.8	The normalised MXSW signal for a Pt ₃ Co crystal, curves for a few reflections	90

5.9	The normalised MXSW signal for a Pt ₃ Co crystal, data for several orientations of the Pt magnetic moment	90
5.10	The MXSW signal for a Pt ₃ Co crystal, showing the dependence on the incoming beam polarisation. The parameter δ is changed	91
5.11	The MXSW signal for a Pt ₃ Co crystal, showing the dependence on the incoming beam polarisation. The parameter β is changed	92
5.12	The normalised MXSW signal for a Pt ₃ Co crystal calculated with an absorption correction for the wavevector	92
5.13	Unit cell of magnetite	93
5.14	The normalised MXSW signal for a magnetite crystal, natural ferrimagnetic structure was assumed	95
5.15	The example of the MXSW signal for the (004) reflection from magnetite showing the principle of the magnetic x-ray standing waves method	96
5.16	The normalised MXSW signal for some hypothetical magnetic structures of the magnetite crystal	97
5.17	The normalised MXSW signal for a magnetite crystal, the curves for a few reflections	98
5.18	Unit cell of YIG	99
5.19	The normalised MXSW signal for a YIG crystal, the curves for a few reflections	100
5.20	Atomic structure of hematite	101
5.21	Magnetic structure of hematite	101
5.22	The normalised MXSW signal for an hematite crystal, the curves for a few reflections	102
6.1	Flow diagram of the iterative algorithm for introducing the absorption correction related to the XMCD effect into dynamical theory of diffraction	106
6.2	Comparison of the reflectivity curves for Pt ₃ Co single crystal with and without the iterative absorption correction related to XMCD effect	108
7.1	A general schema of an MXSW experiment	117
7.2	The EH-1 of the beamline P09 at the PETRA III synchrotron	120
7.3	The experimental system used for the MXSW experiments, close-up	121
8.1	Experimental reflected beam intensity for the Pt ₃ Co single crystal, symmetric (111) reflection, compared with theoretical functions	127
8.2	Single fluorescence spectrum for Pt ₃ Co crystal	128
8.3	A collection of fluorescence spectra from Pt ₃ Co for the entire Θ -scan	129
8.4	The experimental fluorescence yields for Pt ₃ Co for all configurations of helicity and magnetic field orientation	130
8.5	Simulated fluorescence yield for Pt ₃ Co for the experimental setting	131
8.6	Experimental fluorescence yields for Pt ₃ Co compared with theoretical functions obtained as convolution of the ones calculated from the MXSW theory with monochromator reflectivity and Lorentzian function describing the mosaicity	132
8.7	MXSW signals for the Pt ₃ Co crystal	133
8.8	The difference of the MXSW signals for Pt ₃ Co that is $\Upsilon_{+\mathbf{B}} - \Upsilon_{-\mathbf{B}}$ and $\Upsilon_{\mathbf{L}} - \Upsilon_{\mathbf{R}}$	133
8.9	The sum of the MXSW signals for Pt ₃ Co that is $\Upsilon_{+\mathbf{B}} + \Upsilon_{-\mathbf{B}}$ and $\Upsilon_{\mathbf{L}} + \Upsilon_{\mathbf{R}}$	134
8.10	Comparison between the experimental MXSW signal for the Pt ₃ Co crystal and the theoretical curve calculated assuming the magnetic moments being aligned in the (111) planes	135
9.1	Single fluorescence spectrum for a YIG crystal	139
9.2	A collection of experimental results for YIG crystal	141

9.3	Simulated Fe fluorescence yield for YIG for the experimental setting	142
9.4	The difference of the MXSW signals for YIG, that is $\Upsilon_{+\mathbf{B}} - \Upsilon_{-\mathbf{B}}$ and $\Upsilon_{\mathbf{L}} - \Upsilon_{\mathbf{R}}$	143
9.5	The sum of the MXSW signals for YIG, that is $\Upsilon_{+\mathbf{B}} + \Upsilon_{-\mathbf{B}}$ and $\Upsilon_{\mathbf{L}} + \Upsilon_{\mathbf{R}}$	143
9.6	The MXSW signal for a YIG crystal, (444) reflection, calculated for the scans without external magnetic field	144
9.7	The sum and difference of the MXSW signals $\Upsilon_{\mathbf{L}/\mathbf{R}}$ and $\Upsilon_{\pm\mathbf{B}}$ for a YIG crystal, energy above the K absorption edge ($\mathfrak{E} = 7.14$ keV)	145
9.8	Comparison between the experimental MXSW signal for the YIG crystal and the theoretical curve calculated assuming the magnetic moments being aligned along the magnetic field in the (444) planes	146
A.1	Angular relation between the vectors \mathbf{k}_0^a , \mathbf{h} and \mathbf{k}_h	155
B.1	Transitions from the 2p to the 3d states fulfilling the selection rule $\Delta m_\ell = 1$	163
B.2	Transitions from the 2p to the 3d states fulfilling the selection rule $\Delta m_\ell = 0$	164
C.1	The change of the phase of amplitude ratio ξ_σ for the σ -polarisation component after the introduction of the absorption correction related to the XMCD effect	165
D.1	The technical drawing in 3D of the first version of the permanent magnet system	168
D.2	The photo of the first version of the the permanent magnet system	168
D.3	The technical drawing in 3D of the second version of the permanent magnet system	170
D.4	The photo of the second version of the the permanent magnet system	170
E.1	Hysteresis curve for the single crystal sample of Pt_3Co	171
E.2	Energy spectrum for a YIG crystal measured in the vicinity of the Fe K absorption edge	172
E.3	Fluorescence yield of argon compared with the fluorescence yield of iron	173
E.4	Reflected beam intensity for a YIG crystal, (444) reflection. Comparison between the data measured with and without the external magnetic field	174

List of Tables

3.1	The states of the spin-orbit split 2p level in the basis of total angular momentum $\{ j, m_j\rangle\}$ and their decomposition in the basis of orbital angular momentum and spin $\{ \ell, m_\ell, s, m_s\rangle\}$	41
6.1	Changes of the R_ξ parameter in the subsequent iterations of the algorithm for introducing the absorption correction related to the XMCD effect into dynamical theory of diffraction	107

Introduction

The structure of matter on small scales since ancient times always fascinated philosophers and scientists. It constituted a mystery, which was a driving force for the development of more and more sophisticated methods enabling seeing that, what is not accessible by human eye. The crystals, due to their marvellous macroscopic forms, gained attention of humans very early in our history [1]. Even though significant progress in the field of crystallography was achieved earlier [2], it was x-ray diffraction, what provided a direct evidence for the translation periodic, three dimensional atomic structure of crystals [3].

Probably even more intriguing was ever since the phenomena of magnetism. The fact that a strong force emerges between some objects was noticed already in ancient times [4]. The observation of Ørsted, that a flow of current generates a magnetic field provided a first insight into the origin of magnetism [5]. Much deeper understanding was provided hundred years later by quantum mechanics and is related to the names of Ising [6] and Heisenberg [7]. The fact that magnetic moments of atoms order spontaneously in the crystal, often in very sophisticated manner [8], remains a fascinating and not yet fully understood phenomenon.

The fascination for both of these scientific subjects was an inspiration for the work on the topic of this thesis. A perspective of making a contribution to the better understanding of the magnetic structures of crystalline materials (not only bulk crystals, but also nanostructures) constituted a major motivation for the development of a new, direct method for structural investigations reported here.

As early as in 1913¹, it was recognised, that the structure of crystals cannot be directly deduced from diffraction patterns, since the phase of the scattered wave cannot be measured. Later on, a number of ways to solve this phase problem was developed [9]. They can be generally divided into the techniques where the phase is actually measured (for example using anomalous dispersion), and the ones where the phases are extracted from the amplitudes using mathematical relations between structure factors and constrains (for example direct methods [10]). Conceptually most appealing are the methods, where the use is made of the interference between the waves, as then the phase is measured directly, without imposing any changes on the investigated system, like in the multiple isomorphous replacement method [9]. This can be realised practically by exciting two Bragg reflections at once (three-beam-case diffraction) and measuring the so called triple phase,

¹During the 85th annual meeting of the German scientists in Vienna, 21-28.08.1913, where among others, Laue, Friedrich and Wagner gave talks about the x-ray crystallography. In his talk, Max von Laue stated: *Can the structure of a crystal be deduced from the interference diagrams? If this were the case, one of the crystallography's most important problems would be solved. But this is not the case because the phases cannot be measured!* [2]

which contains the phases of the structure factors of the three involved reflections [11]. It was also shown, that the x-ray standing waves (XSW) technique, which is of the main interest in this thesis, even though being most suited for investigation of the structure of foreign atoms in a known crystal lattice [12], can also be used to determine the phase of the structure factor directly² [13].

An experimental technique, which is most often used for magnetic structure determination is neutron diffraction. Extraction of structural information from the diffraction data is possible via the refinement process, where the experimental data is fitted by the theoretical neutron scattering cross-section calculated for a given arrangement of magnetic moments. This remains a challenging task, as it is very difficult to prove that the obtained solution is the global one [14]. In contrary to regular crystallography, no direct methods similar to three-beam-case diffraction or XSW were so far developed for studying the magnetic structures. This makes the work reported in this thesis a truly pioneering one.

Given the lack of the methods of this kind, the main aim of this project is a development of a new direct technique for studying the magnetic structures of crystalline materials at the atomic level. The idea is to combine a well-established diffraction-based standard XSW method, with the x-ray magnetic circular dichroism (XMCD). The resulting magnetic x-ray standing waves (MXSW) technique, by taking advantage of site and element selectivity coming from XSW method, and sensitivity to magnetic properties of the XMCD spectroscopy, allows to gather information about the arrangement of magnetic moments in a direct way, without any refinement or modelling.

From the physical perspective, the MXSW technique is a problem of scattering and absorption of the circularly or elliptically polarised electromagnetic wave by the pre-defined crystal lattice. When the diffraction condition is fulfilled, a reflected wave is generated by the crystal and the interference of this wave and the incoming (refracted) one leads to the appearance of a standing wave. This entity has two interesting properties — its periodicity is equal to the periodicity of the reflecting lattice planes, and it moves by half of its period as the scan through the angular reflection domain is performed. The existence and movement of the standing wave modulates the absorption rate of the atoms in the lattice. Determination of these modulations via measurement of the secondary emission yield provides information about spatial distribution of absorbing atoms. If the atoms are magnetic, and used light possesses angular momentum (what means, is circularly or elliptically polarised), the absorption additionally differs between opposite helicities and the magnetic information arises from analysing this difference. The circular dichroism in magnetised media arises due to the generation of spin-polarised electrons by the angular momentum of light and their detection by the spin-polarised final band (which is characteristic of atoms exhibiting magnetic moment). In the MXSW method one uses the standing wave appearing in the reflection domain to add the spatial resolution to the standard XMCD spectroscopy. The standing wave acts as a scanner, which turns on and off the contribution of non-equivalent magnetic ions to the overall XMCD signal, thus providing a signal which is site selective. In this way it is possible to study the distribution of magnetic moments in a direct way, since the usage of the interference field

²Via the combination of the standard XSW angular scans and the energy scans around the absorption edge. The latter changes the phase of the structure factor, what is reflected in the XSW patterns.

ensures that the phase information is not lost.

The theoretical description of the novel MXSW method was constructed within the scope of this thesis and is based on two pillars — dynamical theory of x-ray diffraction and time-dependent perturbation theory. The former is used to describe the scattering of a circularly polarised electromagnetic (EM) wave by the crystal lattice. It is an example of a physical theory, which very precisely predicted effects confirmed experimentally decades later. Among them are the famous top-hat-shaped crystal reflectivity curve³ and the existence of the standing wave. The latter was confirmed indirectly via the fine structure of the Kossel lines [19,20], later by Borrmann effect [21,22] and finally by showing directly its impact on the absorption of atoms in the lattice [23,24]. The recent development in the area of dynamical diffraction theory [25–28], shows that it remains a lively research field, with room for establishing further interesting results. Just to mention, two new conclusions are drawn from the dynamical-theory-based novel MXSW theory presented in this work — the possibility of observing an XMCD signal from the antiferromagnetic system due to the influence of the standing wave, and a perspective of generating a circular dichroism in absorption in magnetised crystal via usage of linearly π -polarised incoming wave, by taking advantage of the phase shift between refracted and reflected waves in the reflection domain.

Over the decades, the XSW technique has proven its usability for precise determination of the positions of atoms in the lattice or adsorbates on the surface, even with picometer precision [29]. Also very recently, the XSW method has been found useful for addressing a number of scientific questions [30–35]. The canonical form of the method, where the Bragg reflection for standing wave generation is used in conjunction with a detection of the x-ray fluorescence [36], was extended by incorporating other experimental techniques to broaden the applicability of the XSW. The combination with photoelectron spectroscopy supplemented the XSW with sensitivity to the chemical state of the atoms [12,37]. An excitation of the standing wave using the specular reflection of x-rays (total external reflection phenomenon) allows studying surfaces, interfaces and deposited nanostructures [38]. Alternatively, a long-period standing wave can be also produced by the multilayer, which acts as an artificial crystal, generating also a Bragg reflection [39]. It should be mentioned, that the standing waves were also used in conjunction with Compton and thermal diffuse scattering [29].

A perspective of using the standing wave for studying the magnetic properties of materials with spatial resolution was realised practically for the case of long-period standing waves excited in multilayers. Kim and Kortright [40] have connected for the very first time the XSW method with XMCD to gain additional depth sensitivity. Using a standing wave generated by the stack of $[\text{W}/\text{B}_4\text{C}]_{40}$ layers, they showed that cobalt in Pd/Co/Pd trilayer exhibits different spin-resolved electronic structure at the interfaces, compared to the center of the film. A similar studies for the Fe/Cr bilayer, revealing that a normally antiferromagnetic chromium becomes ferromagnetic in the interface region, were reported by Yang *et al.* [41]. The group of Sato [42] studied in the same way antiferromagnetically and ferromagnetically coupled Fe/Si/Fe trilayers, and found an increase of orbital mag-

³Predicted theoretically already by Ch. G. Darwin in 1914 [15,16]. At that time the agreement with experimental data was very poor, due to the large mosaic spread of the used crystals. The first measurements revealing the top-hat shape of the reflectivity curve came much later and were provided by Renninger in 1955 for calcite [17] and Bubáková in 1961 for germanium [18].

netic moment of iron in the interdiffused layer, utilising the depth selectivity granted by the standing wave. Andreeva and Odintsova [43] calculated an expected fluorescence yield from the periodic antiferromagnetically coupled multilayers, where the standing wave was generated by the investigated system itself. They clearly pointed out the advantage of using a standing wave for XMCD studies of systems with antiferromagnetic ordering. The simulations revealed a dichroism in the fluorescence yield, but the antinodes of the standing wave were found to be anchored in the layers with low absorption, what makes scanning of the sample depth impossible. Jonnard and his group [44] reported on the first MXSW experiment on Mg/Co multilayer, where the x-ray fluorescence was used to determine the XMCD signal. It was found, similarly like in the work of Andreeva and Odintsova, that the movement of the standing wave in the multilayer is very limited. An interesting idea for using the standing wave generated by the multilayer for supplementing the x-ray photoelectron emission microscopy (PEEM) with the depth selectivity was proposed by Gray *et al.* [45]. The authors pointed out, that the resulting technique can be in the future combined with the XMCD spectroscopy, to additionally gather magnetic information about the nanostructures with spatial resolution.

It should be emphasised, that the MXSW methods based on the Bragg reflection from the multilayer, even though being also a combination of the XSW with XMCD, are fundamentally different from the technique described in this thesis. They enable studies of the micro- and nanostructures and not the magnetic structure at the atomic level, understood as the orientations and magnitudes of the magnetic moments. Also from the theoretical perspective, the description of the scattering of x-rays from multilayer is different than the approach based on the dynamical theory of diffraction presented here.

An idea of using the standing wave for studying the arrangement of magnetic moments at the atomic level was expressed in the conference paper of Jaouen *et al.* [46]. The researchers performed an XSW angular scans on the magnetised, chemically disordered, nickel-platinum Ni₉₀Pt₁₀ alloy, using circularly polarised x-rays. They observed a clear variation in the XMCD signal in the reflection domain. The aim of the studies was a determination of the magnetic properties of platinum atoms depending on their position in the lattice. Given the lack of the MXSW theory, the full analysis of the experimental data was not possible. The authors stressed a necessity for development of a rigorous theory describing the effects involved.

Once the work on the project described in this thesis was highly advanced, the author became aware of a conference contribution of Kawata, presented during the meeting in Malente, Germany in 1992 [47]. Along with the idea of MXSW at the atomic level, he presented there the experimental results for yttrium-iron-garnet (YIG) single crystal. The group performed MXSW scans for the sample kept in the magnetic field, but assumed that the antiferromagnetic coupling between the iron sublattices is not perturbed and the magnetic moments align parallel (and antiparallel for the less populated sublattice) to the external magnetic field vector. The quality of obtained experimental data is very high, but no rigorous MXSW theory was developed by the authors.

In order to allow full understanding of the MXSW data, an exhaustive theoretical treatment of this subject was developed within the scope of this thesis and is presented hereafter. This is a first time, when such a rigorous MXSW theory is reported. Two new interesting phenomena, related purely to the properties of the wavefields emerging from the dynamical theory, are predicted. It is proven rigorously, that the MXSW method

can be used for studying the magnetic structures of crystalline materials based on the variations in the XMCD signal caused by the standing wave. The MXSW technique shows a number of advantages over existing methods for determination of magnetic structures of crystal. Other than neutron diffraction, it does provide structural information directly, and due to the large photon flux from x-ray sources compared to neutron fluxes available, can be easily applied to thin films. It has also advantages over the resonant elastic x-ray scattering (REXS), which typically provides only the information about orientations of the magnetic moments, and requires comparison with the model to extract the structural information [48].

The structure of the thesis is as follows. The theoretical part consists of four chapters and presents the development and results of the MXSW theory. The first chapter consists of a summary of the two-beam-case dynamical theory of diffraction in the formulation of Laue and the evaluation of the form of the wavefield in the crystal, excited by the incoming wave with arbitrary polarisation. Similarly, the second chapter presents a formalism (time-dependent perturbation theory) used later for calculating the absorption cross-section for the wavefield predicted by the dynamical theory of diffraction. The third chapter comprises a thorough discussion of the XMCD effect for a single arbitrarily polarised EM wave. The most crucial chapter 4 presents the MXSW theory that is the evaluation of the absorption cross-section for the standing wave excited by arbitrarily (thus also circularly) polarised wave. It constitutes the most important achievement of this work. The theoretical part is followed by the one devoted to computer simulations. Chapter 5 presents simulation results for four chosen magnetic systems. The results are used to present the results of the MXSW theory and show the principle of the MXSW method. Chapter 6 is devoted to the numerical evaluation of the absorption correction for the dynamical theory of x-ray diffraction, which as a classical theory, does not account for the dichroism in absorption caused by magnetism and angular momentum of light. The experimental part consists of three chapters and is initiated by the general discussion about the prerequisites for the MXSW experiment and applicability of the method, given in chapter 7. Two following chapters present the experimental results from the MXSW experiments on platinum-cobalt alloy (chapter 8) and YIG (chapter 9) single crystals. The last section contains main conclusions and outlook.

Part I

Theoretical section

Chapter 1

Dynamical theory of diffraction

The theoretical considerations start here with the subject of scattering of an x-ray wave by a crystal lattice. Essentially two approaches to this topic exist. In the so called kinematical (or geometrical) theory of diffraction the waves generated by the oscillating electrons are added up (geometrically) to predict the directions of propagation of scattered beams and evaluate their intensities [20,49–51]. In this approach multiple scattering of the waves is neglected [51]. This already leads to the conclusion, that the kinematical diffraction theory is valid only for imperfect or thin crystals (with the thickness significantly smaller than the so called extinction length), where the intensities of the multiple scattered beams are negligible.

In order to quantitatively predict the properties of the wavefields generated by the crystal lattice, another approach — dynamical theory of x-ray diffraction — is used. This theoretical formalism was initially proposed by Ch. G. Darwin and P. P. Ewald. The theory of Ewald was later reformulated by M. von Laue and is used today in that form [20,52–54]. Therein, the evaluation of amplitudes and phases of the emerging waves is based on the solution of Maxwell equations for a three-dimensional periodic continuous charge density distribution. Among the plethora of other fascinating effects like anomalous absorption, extinction, double refraction and Pendellösung, the dynamical theory of diffraction predicts the existence of the standing wave and the movement of its nodes in the reflection domain.

In the dynamical theory the problem of scattering of radiation by the crystal is divided in two parts. At first the set of all possible solutions is obtained by solving the propagation equation for spatially infinite three-dimensional periodic electron density. The electron density distribution is defined merely by the crystal unit cell, as its Fourier coefficients are proportional to the structure factors. Then, out of the set of all potentially existing waves, the actual solutions are chosen via the boundary conditions for amplitudes and wavevectors.

In this section the dynamical theory of diffraction in the formulation of Laue is summarised. The considerations are limited to the case of only one reflection excited in the crystal at the time (two-beam-case diffraction). After the general solution is obtained, only the boundary conditions characteristic of the reflection geometry are considered, as this case is of interest for the further discussion. Subsequently, the standard x-ray standing waves method is introduced. Finally, the formulae for the case of arbitrary polarisation of the incoming x-ray wave are presented.

1.1 Propagation equation

The beauty of the dynamical theory of diffraction arises from the fact, that it originates directly from the Maxwell equations. In the absence of free charges and free currents, the macroscopic Maxwell equations in differential form read [55]

$$\operatorname{div}\mathcal{D} = 0 \quad (1.1)$$

$$\operatorname{rot}\mathcal{E} = -\frac{\partial\mathcal{B}}{\partial t} \quad (1.2)$$

$$\operatorname{rot}\mathcal{H} = \frac{\partial\mathcal{D}}{\partial t} \quad (1.3)$$

$$\operatorname{div}\mathcal{B} = 0 \quad (1.4)$$

Here the symbols \mathcal{E} , \mathcal{D} , \mathcal{H} , \mathcal{B} denote electric field, electric induction, magnetic field and magnetic induction vectors, t is time. The relations between these quantities have the general form

$$\mathcal{D} = \varepsilon_0\mathcal{E} + \mathbf{P} \quad (1.5)$$

$$\mathcal{H} = \frac{\mathcal{B}}{\mu_0} - \mathbf{M} \quad (1.6)$$

where \mathbf{P} is an electric polarisation and \mathbf{M} magnetisation, ε_0 denotes the vacuum permittivity, whereas μ_0 — vacuum permeability. The effects of magnetic x-ray diffraction, that is the scattering of an electromagnetic wave on electron spins, are small even in crystals possessing magnetic ordering [56]. Additionally, such a scattering process cannot be introduced in the classical theory of diffraction considered here. Therefore, magnetic diffraction is neglected hereafter. This assumption is equivalent to setting $\mathbf{M} = 0$ in the material relations.

If the nonlinear effects are neglected, the electric polarisation is proportional to the electric field $\mathbf{P} = \varepsilon_0\chi\mathcal{E}$. The quantity χ , called electric susceptibility or polarisability, is in general a tensor. The dynamical theory of diffraction, where such general form was incorporated, was developed by G. Moilère [57–59]. The predictions of this formalism are in general in a good agreement with Laue formulation, and the effects related to the anisotropy of χ are predicted to be small, especially far from the absorption edges. It is known, that the anisotropic susceptibility can lead to appearance of structurally forbidden reflections [60, 61]. It can also influence the structure factors of the non-forbidden reflections in the vicinity of the absorption edge [62]. However, it is pointed out [60], that the components of the anisotropic structure factor are not easily accessible theoretically. Therefore, the power of the theory to predict the experimental results would be limited in the formulation accounting for the tensorial character of χ . In the experimental work on resonant scattering in GdB_4 it is shown, that the intensity of the regular (002) Bragg reflection is following the changes in the standard resonant scattering factor f'' (electronic absorption), and in particular is not significantly affected by the anisotropy of the electric susceptibility [63]. What is more, Thorkildsen *et al.* [64] studied the three-beam resonant x-ray diffraction in germanium using theoretical approach with an assumption of scalar susceptibility and achieved good agreement with experimental data. Based on these experimental reports, and taking into account methodological difficulties to estimate the components of the χ tensor, in this work the scalar character of the latter is adopted.

From the Maxwell equations and material relations, one obtains the propagation equation for a specific susceptibility χ , which defines the considered crystal

$$\text{rot rot } \boldsymbol{\mathcal{E}} + \mu_0 \varepsilon_0 (1 + \chi) \frac{\partial^2 \boldsymbol{\mathcal{E}}}{\partial t^2} = 0 \quad (1.7)$$

The crystal is assumed to be perfectly periodic, so the susceptibility is also a periodic function. Thus, it can be expanded in the Fourier series

$$\chi(\mathbf{r}) = \sum_{\mathbf{h}} \chi_{\mathbf{h}} e^{-i\mathbf{h}\cdot\mathbf{r}} \quad (1.8)$$

\mathbf{h} denotes here a reciprocal lattice vector, \mathbf{r} is a position vector. As it follows from the elementary Lorentz-Drude dispersion theory, susceptibility and electron density ρ are proportional to each other [52]. Therefore the Fourier coefficients of susceptibility $\chi_{\mathbf{h}}$ are related to structure factors $F_{\mathbf{h}}$, Fourier coefficients of electron density. These relations read

$$\chi_{\mathbf{h}} = -\frac{R_{\text{Th}} \lambda^2}{\pi V_{\text{cell}}} F_{\mathbf{h}} \quad (1.9)$$

where R_{Th} is a Thomson scattering length, λ is a wavelength of the incoming radiation and V_{cell} — volume of the unit cell. This relation allows to calculate the susceptibility Fourier coefficients for a given crystal, using the definition of the structure factor [51, 53]

$$F_{\mathbf{h}} = \sum_{j=1}^N (f_j^0 + f_j' + i f_j'') e^{i\mathbf{h}\cdot\mathbf{R}_j} = \int_{V_{\text{cell}}} \rho e^{i\mathbf{h}\cdot\mathbf{r}} d^3\mathbf{r} \quad (1.10)$$

Here, the summation is over the N atoms in the unit cell, located at the positions \mathbf{R}_j . f_j^0 denotes the atomic scattering factor of atom j , whereas f_j' and f_j'' are dispersion corrections. The numerical values of atomic scattering factors are tabulated [65, 66]. The integral definition follows from the fact, that the electron density of the crystal can be written as a Fourier series $\rho(\mathbf{r}) = \frac{1}{V_{\text{cell}}} \sum_{\mathbf{h}} F_{\mathbf{h}} e^{-i\mathbf{h}\cdot\mathbf{r}}$.

1.2 Wavefields, fundamental equations

The solution of equation (1.7) is a plane wave modulated by the term having the same periodicity as the interaction term χ . It is assumed, that the electric field can be expressed as the sum of plane waves of the form

$$\boldsymbol{\mathcal{E}} = e^{i\omega t - i\mathbf{k}_0 \cdot \mathbf{r}} \sum_{\mathbf{h}} \mathbf{E}_{\mathbf{h}} e^{-i\mathbf{h}\cdot\mathbf{r}} \quad (1.11)$$

where ω denotes the angular frequency and \mathbf{k}_0 is a wavevector of the refracted wave (also called forward-scattered wave). This form was obtained by Ewald in his version of dynamical theory [67], it is called a wavefield or an Ewald wave. The relation between the wavevectors of the waves constituting a wavefield reads $\mathbf{k}_{\mathbf{h}} = \mathbf{k}_0 + \mathbf{h}$, and can be regarded as a manifestation of Bragg's law.

The relations (1.8) and (1.11) are inserted into the propagation equation (1.7) then the following equation is obtained

$$\sum_{\mathbf{h}} \left[\mathbf{k}_{\mathbf{h}} \times (\mathbf{k}_{\mathbf{h}} \times \mathbf{E}_{\mathbf{h}}) + k^2 \mathbf{E}_{\mathbf{h}} + k^2 \sum_{\mathbf{h}'} \chi_{\mathbf{h}-\mathbf{h}'} \mathbf{E}_{\mathbf{h}'} \right] e^{i\omega t - i\mathbf{k}_{\mathbf{h}} \cdot \mathbf{r}} = 0 \quad (1.12)$$

k is the length of the wavevector in vacuum ($k = \omega/c$, c — speed of light). To ensure that the latter equation is fulfilled for each position and time, the coefficients by the complex exponents must be equal to zero. Therefore, equation (1.12) is equivalent to the infinite set of equations

$$\bigwedge_{\mathbf{h}} \mathbf{k}_{\mathbf{h}} \times (\mathbf{k}_{\mathbf{h}} \times \mathbf{E}_{\mathbf{h}}) + k^2 \mathbf{E}_{\mathbf{h}} + k^2 \sum_{\mathbf{h}'} \chi_{\mathbf{h}-\mathbf{h}'} \mathbf{E}_{\mathbf{h}'} = 0 \quad (1.13)$$

The double cross-product can be rewritten in equivalent form

$$\bigwedge_{\mathbf{h}} \mathbf{k}_{\mathbf{h}} \underbrace{(\mathbf{k}_{\mathbf{h}} \cdot \mathbf{E}_{\mathbf{h}})}_{\approx 0} - \mathbf{E}_{\mathbf{h}} k_{\mathbf{h}}^2 + k^2 \mathbf{E}_{\mathbf{h}} + k^2 \sum_{\mathbf{h}'} \chi_{\mathbf{h}-\mathbf{h}'} \mathbf{E}_{\mathbf{h}'} = 0 \quad (1.14)$$

here $k_{\mathbf{h}}^2 = \mathbf{k}_{\mathbf{h}} \cdot \mathbf{k}_{\mathbf{h}}$. It is assumed that the wave is transverse, since the interaction term is small. For each reciprocal lattice vector \mathbf{h} the amplitude of the wave reads

$$\mathbf{E}_{\mathbf{h}} = \frac{k^2}{k_{\mathbf{h}}^2 - k^2(1 + \chi_0)} \sum_{\mathbf{h}' \neq \mathbf{h}} \chi_{\mathbf{h}-\mathbf{h}'} \mathbf{E}_{\mathbf{h}'} \quad (1.15)$$

This relations, called fundamental equations of dynamical theory, imply that the amplitude of the given wave from the wavefield depends on the amplitudes of all the other waves — the waves forming a wavefield are tightly bound together and they constitute a physical entity. The prefactor in the fundamental equations is called a resonance factor and shows, that only those waves whose wavevector length is close to $k\sqrt{1 + \chi_0}$ have non-negligible amplitude. As it follows from the case, when only one wave has considerable amplitude (one-beam-case), what corresponds to the refraction process only, the refractive index \mathbf{n} for x-rays is equal to $\sqrt{1 + \chi_0} \simeq 1 + \chi_0/2$. Therefore, the constituents of the wavefield have to have wavevectors of the length close to the one of the refracted wave ($\mathbf{n}k$). Thus, it is justified to consider further the case, when only two waves have meaningful amplitudes (two-beam-case), where only one reciprocal lattice vector is involved in the scattering process. The infinite set of equations reduces to two equations

$$\begin{cases} [k_0^2 - k^2(1 + \chi_0)] \mathbf{E}_0 - k^2 \chi_{\mathbf{h}} \mathbf{E}_{\mathbf{h}} = 0 \\ [k_{\mathbf{h}}^2 - k^2(1 + \chi_0)] \mathbf{E}_{\mathbf{h}} - k^2 \chi_{\mathbf{h}} \mathbf{E}_0 = 0 \end{cases} \quad (1.16)$$

It is convenient to decompose the wave amplitudes into the σ - (perpendicular to the scattering plane) and π - (in the scattering plane) polarisation components. The σ -polarisation unit vector is defined via the cross-product $\hat{\mathbf{e}}_{\sigma} = (\mathbf{h} \times \mathbf{k}_0) / |\mathbf{h} \times \mathbf{k}_0| = (\mathbf{h} \times \mathbf{k}_{\mathbf{h}}) / |\mathbf{h} \times \mathbf{k}_{\mathbf{h}}|$, what ensures that it is perpendicular to the scattering plane and the wavevectors, since the wave is a transverse one. The π -polarisation unit vectors are given as the cross product of the

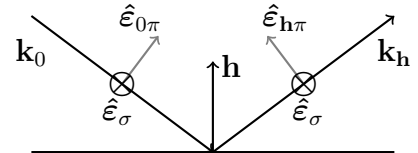


Figure 1.1: Definition of the polarisation unit vectors.

corresponding wavevector and $\hat{\mathbf{e}}_\sigma$: $\hat{\mathbf{e}}_{i\pi} = (\mathbf{k}_i \times \hat{\mathbf{e}}_\sigma) / |\mathbf{k}_i \times \hat{\mathbf{e}}_\sigma| = [\mathbf{k}_i \times (\mathbf{h} \times \mathbf{k}_i)] / (k_i |\mathbf{h} \times \mathbf{k}_i|)$, where $i \equiv 0, \mathbf{h}$. Therefore, they are perpendicular both to the wavevectors, as well as to $\hat{\mathbf{e}}_\sigma$. Polarisation unit vectors are shown also in figure 1.1. The angle between the vectors \mathbf{k}_0 and $\mathbf{k}_\mathbf{h}$ is $2\Theta_B$, where Θ_B is a Bragg angle defined by the Bragg's law $\lambda = 2d_\mathbf{h} \sin \Theta_B$, $d_\mathbf{h}$ denoting the interplanar spacing associated with reciprocal lattice vector \mathbf{h} . It follows from figure, that also the angle between the unit vectors $\hat{\mathbf{e}}_{\mathbf{h}\pi}$ and $\hat{\mathbf{e}}_{0\pi}$ is equal to $2\Theta_B$. Equations (1.16) are then multiplied by the polarisation unit vectors, what gives the following scalar equations in matrix form

$$\begin{pmatrix} k_0^2 - k^2(1 + \chi_0) & -k^2 \chi_\mathbf{h} \mathfrak{P} \\ -k^2 \chi_\mathbf{h} \mathfrak{P} & k_\mathbf{h}^2 - k^2(1 + \chi_0) \end{pmatrix} \begin{pmatrix} E_{0\mathfrak{p}} \\ E_{\mathbf{h}\mathfrak{p}} \end{pmatrix} = 0 \quad (1.17)$$

Index \mathfrak{p} denotes the σ - or π -polarisation component. \mathfrak{P} is a polarisation factor equal 1 for σ - and $\cos 2\Theta_B$ for π -polarisation.

1.3 Dispersion surface

As it follows from the Kronecker-Capelli theorem, to ensure non-zero solutions of the homogeneous systems of equations (1.17), one has to set the determinant of the matrix to zero. This gives equation of the dispersion surface

$$[k_0^2 - k^2(1 + \chi_0)] [k_\mathbf{h}^2 - k^2(1 + \chi_0)] = k^4 \chi_\mathbf{h} \chi_\mathbf{h} \mathfrak{P}^2 \quad (1.18)$$

By introducing the parameters

$$X_i := \frac{k_i^2 - k^2(1 + \chi_0)}{2k}, \quad i \equiv 0, \mathbf{h} \quad (1.19)$$

one may write equation of the dispersion surface in the form

$$X_0 X_\mathbf{h} = \frac{1}{4} k^2 \chi_\mathbf{h} \chi_\mathbf{h} \mathfrak{P}^2 \quad (1.20)$$

The dispersion surface for an exemplary Bragg reflection from silicon is shown in figure 1.2. Since $\chi_0, \chi_\mathbf{h}, \chi_\mathbf{h}$ are very small, their values were increased by a factor of $5 \cdot 10^3$ for the left picture, to make the difference between the spheres of radius $\mathbf{n}k$ centred at \mathbf{O} and \mathbf{H} and the dispersion surface visible in the vicinity of the tiepoint — the common origin of the wavevectors. Due to the fact, that $\mathbf{n}k \approx k_0 \approx k_\mathbf{h}$, one can approximate the parameter $X_i \approx k_i - \mathbf{n}k$ and interpret it as a distance from the tiepoint to the spheres of the radius $\mathbf{n}k$, which can be well approximated as lines, as seen in figure 1.2b.

A relation exists between the coordinates of the tiepoint on the dispersion surface ($X_0, X_\mathbf{h}$) and amplitude ratio $\xi := E_\mathbf{h}/E_0$. It is obtained from one of equations (1.17) and relation (1.19) and reads

$$\xi = \frac{2X_0}{k \chi_\mathbf{h} \mathfrak{P}} \quad (1.21)$$

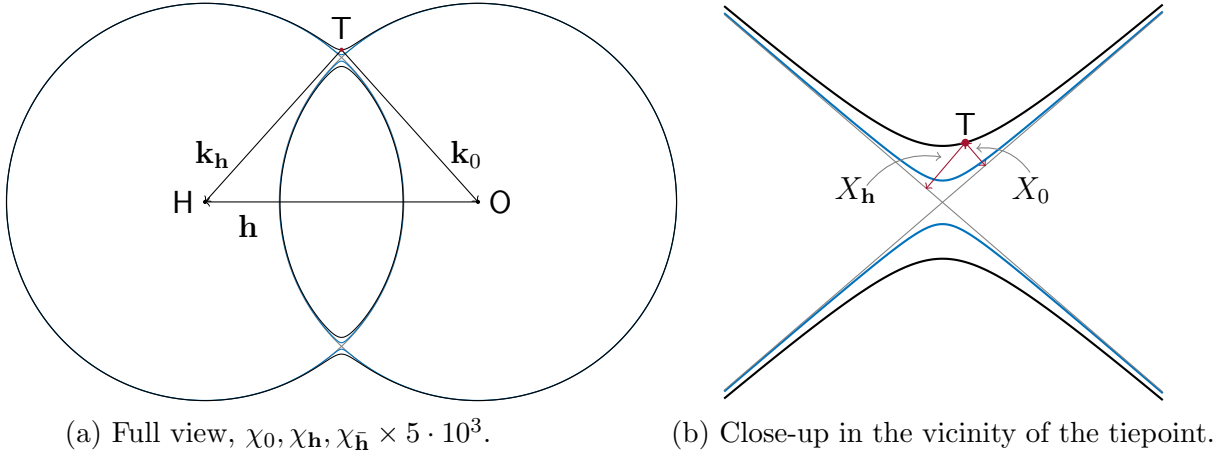


Figure 1.2: Dispersion surface — cut by the scattering plane, the case of non-absorbing crystal ($f'' = 0$). Calculated for the silicon crystal, $\mathbf{h} = (400)$ reflection, energy of the incoming x-ray wave $\mathfrak{E} = 7$ keV. The dispersion surface consists of four branches, two for σ -polarisation (black line) and two for π (blue line). The spheres of radius $n\mathbf{k}$ centred at reciprocal lattice nodes O and H are drawn in gray. Tiepoint T is the common origin of the wavevectors \mathbf{k}_0 and \mathbf{k}_h .

1.4 General solution

To proceed further, the relation between the wavevectors inside the crystal \mathbf{k}_0 , \mathbf{k}_h and the wavevector of the incoming wave \mathbf{k}_0^a is needed. The components of the wavevectors parallel to the crystal surface have to be the same to ensure continuity, the difference may appear only in the out-of-plane direction (Snell's law): $\mathbf{k}_0 = \mathbf{k}_0^a - k\kappa\mathbf{n}$, where $\kappa \in \mathbb{C}$, \mathbf{n} is a unit vector normal to the crystal surface. The considered setting is sketched in figure 1.3. The angles are defined as $\psi_0 = \angle(\mathbf{n}, \mathbf{k}_0) \approx \angle(\mathbf{n}, \mathbf{k}_0^a)$ (the latter holds, since the interaction is small), $\psi_h = \angle(\mathbf{n}, \mathbf{k}_h)$.

Using the boundary condition for \mathbf{k}_0 , and knowing that κ is very small, one can write the coordinate of the tiepoint as

$$X_0 = -k \left(\kappa\gamma_0 + \frac{1}{2}\chi_0 \right) \quad (1.22)$$

where $\gamma_0 = \cos \psi_0$. The variation of the angle of incidence of the incoming wave is taken into account via the departure angle $\Delta\Theta$, which is a difference between the incidence defined by the Bragg condition and actual one (see figure A.1 in appendix A.1.1). Using the Ewald construction and simple geometrical relations, one obtains for the second coordinate

$$X_h = -k \left(\frac{1}{2}\chi_0 + \sin 2\Theta_B \Delta\Theta + \kappa\gamma_h \right) \quad (1.23)$$

where $\gamma_h = \cos \psi_h$. Equations (1.22) and (1.23) merged together give

$$X_h = \gamma X_0 - k \left[\frac{1}{2}\chi_0(1 - \gamma) + \sin 2\Theta_B \Delta\Theta \right] \quad (1.24)$$

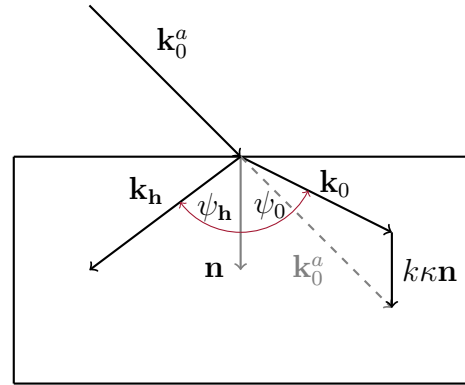


Figure 1.3: Boundary conditions for the wavevectors. The vectors \mathbf{k}_0^a and \mathbf{k}_0 may differ only in the out-of-plane component $k\kappa\mathbf{n}$. The sketch is made for the transmission geometry, symmetric reflection (see 1.5 for details).

The quantity $\gamma := \gamma_{\mathbf{h}}/\gamma_0$ is called asymmetry ratio. Detailed derivation of equations (1.22)-(1.24) is given in appendix A.1.1.

Equation (1.24) provides a relation between the tiepoint coordinates and geometrical conditions in the experiment — γ , Θ_B and $\Delta\Theta$. Further on, it is inserted into the dispersion surface equation (1.20) and solved for X_0 (for details see appendix A.1.2). One obtains

$$X_0 = \frac{k\sqrt{\chi_{\mathbf{h}}\chi_{\bar{\mathbf{h}}}}|\mathfrak{P}|}{2\sqrt{|\gamma|\text{sgn}(\gamma)}} \left[\eta \pm \sqrt{\eta^2 + \text{sgn}(\gamma)} \right] \quad (1.25)$$

$$\eta := \frac{\frac{1}{2}\chi_0(1 - \gamma) + \sin 2\Theta_B\Delta\Theta}{\sqrt{|\gamma|\sqrt{\chi_{\mathbf{h}}\chi_{\bar{\mathbf{h}}}}|\mathfrak{P}|}} \quad (1.26)$$

This is a general solution of the two-beam-case dynamical theory of diffraction. Equation (1.25) establishes a dependence of the tiepoint position on the departure angle $\Delta\Theta$ (via the parameter η). X_0 depends on the polarisation, since separate dispersion surfaces for each polarisation component exist (figure 1.2), as well as mutual orientation of reflecting lattice plane and physical surface of the crystal, parametrised via the asymmetry ratio γ . The same holds true for the amplitude ratio ξ , which is obtained from (1.25) using (1.21)

$$\xi = \frac{\text{sgn}(\mathfrak{P})\text{sgn}(\gamma)}{\sqrt{|\gamma|}} \frac{\sqrt{\chi_{\mathbf{h}}\chi_{\bar{\mathbf{h}}}}}{\chi_{\bar{\mathbf{h}}}} \left[\eta \pm \sqrt{\eta^2 + \text{sgn}(\gamma)} \right] \quad (1.27)$$

The \pm sign indicates, that for pure σ - or π -polarisation, in fact two solutions for each $\Delta\Theta$ exist. They correspond to two tiepoints, each lying on the separate branch of the dispersion surface. One concludes that two wavefields always exist in the crystal, what might be regarded as a double refraction (and reflection) phenomenon in the crystal in the x-ray regime.

1.5 Reflection geometry

The term $\sqrt{\eta^2 + \text{sgn}(\gamma)}$ in equations (1.25) and (1.27) indicates an existence of two fundamentally different geometrical cases. If the wavevectors of both the refracted (\mathbf{k}_0) and the reflected ($\mathbf{k}_{\mathbf{h}}$) waves are directed towards the inside of the crystal, γ is positive and one talks about Laue or transmission geometry. When the wavevector of reflected wave is directed towards the entrance surface, $\gamma < 0$ then the case is called Bragg or reflection geometry. The latter is of interest in this case.

Consider the boundary conditions for the amplitudes. The relations between the electric fields on two sides of the boundary between media I and II emerge directly from Maxwell equations and read

$$\mathbf{n} \cdot \mathcal{D}_I - \mathbf{n} \cdot \mathcal{D}_{II} = 0 \quad (1.28)$$

$$\mathbf{n} \times \mathcal{E}_I - \mathbf{n} \times \mathcal{E}_{II} = 0 \quad (1.29)$$

The first equation implies, that the difference in the dielectric vector component perpendicular to the boundary vanishes. Assuming that χ is very small, the same holds true for the electric field (the relation (1.5)). The second equation implies that the parallel

components of the electric field cannot differ, thus in the case of weak interaction the electric field is the same on two sides of the boundary. In mathematical form

$$\mathcal{E}_I = \mathcal{E}_{II} \quad (1.30)$$

The incoming wave is assumed to be a plane wave given by equation $\mathcal{E}_0^a = \mathbf{E}_0^a e^{i\omega t - i\mathbf{k}_0^a \cdot \mathbf{r}}$. At this point it is considered to be σ or π linearly polarised, so that $\mathbf{E}_0^a = E_0^a \hat{\mathbf{e}}_{\sigma,0\pi}$. Since in the reflection geometry the reflected wave \mathcal{E}_h^a emerges on the entrance crystal surface, one has

$$\mathcal{E}_0^a + \mathcal{E}_h^a = \mathcal{E}_0^{(\pm)} + \mathcal{E}_h^{(\pm)} \quad (1.31)$$

The symbols on the right-hand-side denote the waves inside the crystal, respectively the refracted and the reflected one. In fact, as mentioned earlier, four waves exist, since two wavefields are always excited at once. They all must be taken into account when considering a thin crystal — a thin film for example. In the case of thick bulk crystal, one of the wavefields is absorbed before reaching the exit surface, since it is directed towards the inside of the crystal. Therefore, for each $\Delta\Theta$ only one wavefield needs to be considered at once. The proper sign in equations (1.25) and (1.27) is chosen via the term $-\text{sgn}(\Re\eta)$ [52].

Equation for the full electric fields (1.31) can be transformed to the one for the amplitudes only. Let the origin of the coordinate system coincide with the boundary surface. Then the dependence of the electric fields on the position on the surface in equation (1.31) is only via the terms $e^{-i\mathbf{k}_i \cdot \mathbf{r}_s}$, where \mathbf{r}_s denotes the position on the crystal surface and $i \equiv 0, \mathbf{h}$. Due to the continuity of the tangential components of the wavevectors on the boundary

$$\mathbf{k}_0^a \cdot \mathbf{r}_s = \mathbf{k}_0^{(+)} \cdot \mathbf{r}_s = \mathbf{k}_0^{(-)} \cdot \mathbf{r}_s, \quad \mathbf{k}_h^a \cdot \mathbf{r}_s = \mathbf{k}_h^{(+)} \cdot \mathbf{r}_s = \mathbf{k}_h^{(-)} \cdot \mathbf{r}_s \quad (1.32)$$

To ensure, that the relation (1.31) is fulfilled at each point of the boundary surface, the following must hold true¹ [20]

$$\mathbf{E}_0^a = \mathbf{E}_0^{(\pm)}, \quad \mathbf{E}_h^a = \mathbf{E}_h^{(\pm)} \quad (1.33)$$

From above and equation for the amplitude ratio (1.27), one obtains directly the form of the reflected wave outside of the crystal

$$\mathbf{E}_h^a = -\frac{\text{sgn}(\Im)}{\sqrt{|\gamma|}} \frac{\sqrt{\chi_h \chi_{\bar{h}}}}{\chi_{\bar{h}}} \left[\eta - \text{sgn}(\Re\eta) \sqrt{\eta^2 - 1} \right] \mathbf{E}_0^a \quad (1.34)$$

One should note, that what is actually measured in an experiment is reflectivity. It is defined as a ratio of the energy received by the detector per unit time per unit area divided by the intensity of the incoming beam [52]. To obtain the measure of the power

¹This result can be also obtained mathematically by multiplying equation (1.31) by the term $e^{i\mathbf{k}_0^a \cdot \mathbf{r}_s}$ and integrating over the whole surface, which is assumed to be infinite. One assumes that the wavevectors are almost equal $\mathbf{k}_0^a \approx \mathbf{k}_0^{(+)} \approx \mathbf{k}_0^{(-)}$ due to small interaction term. Integration results in an always-wanishing (due to the finite value of \mathbf{h}) Dirac delta distribution appearing by \mathbf{h} -component terms. It cancels them and decouples equation (1.31) into (1.33). Similar procedure leads to the second equation from the pair (1.33) (one multiplies (1.31) by $e^{i\mathbf{k}_h^a \cdot \mathbf{r}_s}$).

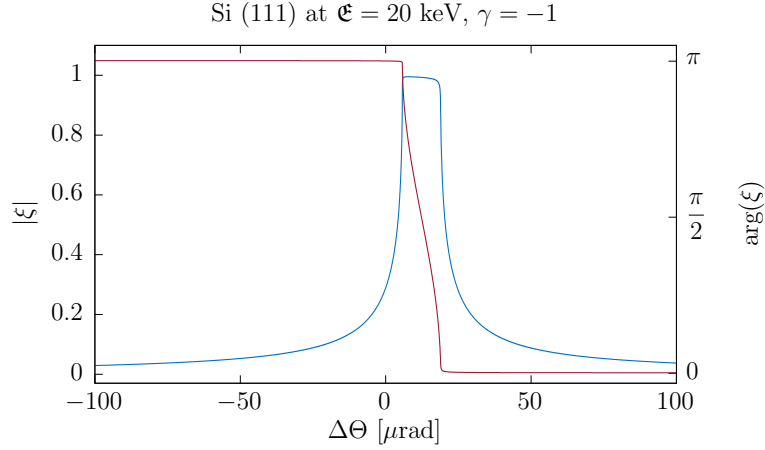


Figure 1.4: Amplitude ratio ξ for Si crystal, (111) reflection at $\mathfrak{E} = 20$ keV. The characteristic top-hat rocking curve is asymmetric due to the standing wave, which either enhances or reduces the absorption (anomalous absorption effect), depending on the position of its nodes and antinodes, which changes due to the change of the phase $\arg(\xi)$ from π to 0 in the reflection domain. For non-absorbing crystal, a total reflection domain exists, where $|\xi| = 1$.

of the beams, one needs to multiply the intensities $|E_i^a|^2$, $i \equiv 0, \mathbf{h}$, by the beam cross-sections. In terms of the projection of the beams on the crystal surface S , those are given by $S_0 = \gamma_0 S$ and $S_{\mathbf{h}} = |\gamma_{\mathbf{h}}| S$, for incoming and emerging waves respectively. With that, the reflectivity reads $I_{\mathbf{h}}^a = |\gamma| |\xi|^2$. For a symmetric reflection ($\gamma = -1$) it is then simply a modulus squared of the amplitude ratio $|\xi|^2$. In the case of the asymmetric reflection, $|\gamma|$ accounts for the change of the cross-section of the reflected beam with respect to the incoming one (due to the non-zero angle between the crystal surface and reflecting lattice planes). In the total reflection domain (the case of non-absorbing crystal), the amplitude ratio $|\xi|^2 = 1$, and the relation $|E_{\mathbf{h}}^a|^2 |\gamma_{\mathbf{h}}| = |E_0^a|^2 \gamma_0$ is a manifestation of the conservation of energy [20].

1.6 X-ray standing wave

In the scattering process, the reflected wave interferes with the refracted one. The intensity of the total electric field inside the crystal reads

$$I = \mathcal{E} \mathcal{E}^* = |\mathbf{E}_0 e^{i\omega t - i\mathbf{k}_0 \cdot \mathbf{r}} + \mathbf{E}_{\mathbf{h}} e^{i\omega t - i\mathbf{k}_{\mathbf{h}} \cdot \mathbf{r}}|^2 \quad (1.35)$$

Assume at this point, that the wavevector \mathbf{k}_0 is real and use the diffraction condition $\mathbf{k}_{\mathbf{h}} = \mathbf{k}_0 + \mathbf{h}$

$$\begin{aligned} I &= (E_0^a)^2 [1 + |\xi|^2 + 2\Re(\xi e^{-i\mathbf{h} \cdot \mathbf{r}})] = \\ &= (E_0^a)^2 \{1 + |\xi|^2 + 2|\xi| \cos[-\mathbf{h} \cdot \mathbf{r} + \arg(\xi)]\} \end{aligned} \quad (1.36)$$

Since the components of the wavevectors of the refracted and reflected waves parallel to the reciprocal lattice vector \mathbf{h} are opposite, the interference of the waves results in

a standing wave in this direction. This fact is also evident in the last equation, which describes the spatial variations in the intensity of the interference field (via the term $\mathbf{h} \cdot \mathbf{r}$). Such time independent variations are characteristic of a standing wave [29].

Let us examine the properties of the standing wave, which are what makes it an interesting entity. The argument of the cosine function may be written as $\mathbf{h} \cdot \mathbf{r} = 2\pi z/d_{\mathbf{h}} = 2\pi(\mathcal{N}d_{\mathbf{h}} + \Delta)/d_{\mathbf{h}}$, where $\mathcal{N} \in \mathbb{Z}$ and $\Delta \in \mathbb{R}$. Due to the periodicity of the cosine function, the first term in the sum can be discarded and one may define a variable $z_{\mathbf{h}} = \Delta/d_{\mathbf{h}}$, which is a fractional coordinate taking the values from the range $[0; 1]$. Of course a shift of z by another interplanar spacing $d_{\mathbf{h}}$ leads to the same value of the cosine, and therefore also of the intensity. As a conclusion, the periodicity of the standing wave is exactly the same as periodicity of the lattice in the direction of the reciprocal lattice vector \mathbf{h} .

Secondly, as it again follows from the properties of the cosine function, a shift of its argument results in a shift of the maxima and minima. As one can see in figure 1.4, the phase of reflectivity changes in the reflection domain by π . Due to the presence of the term $\arg(\xi)$ in the expression (1.36), this change of phase results in the movement of the nodes and antinodes of the standing wave. It moves in a way that after the reflection domain is crossed, the antinodes will be at the initial positions of the nodes and vice versa. The maxima are located in between the lattice planes² at the low angular side ($\Delta\Theta \rightarrow -\infty$, $\arg(\xi) = \pi$) and coincide with them for the high angular side ($\Delta\Theta \rightarrow \infty$, $\arg(\xi) = 0$).

These two properties of the standing wave make it an ideal tool for studying the positions of atoms in the lattice in the element selective manner. Within an electric dipole approximation an absorption cross-section for a given atom is proportional to the intensity of the electric field at the position of its core [12], what is discussed in more details in the next chapter (2.3). The measure of the absorption cross-section can be obtained via detecting the emitted photoelectrons or subsequent decay processes — fluorescence or Auger electrons emission. The controlled movement of the standing wave causes variations in the amount of emitted electrons or fluorescence photons, which are characteristic of the position of the absorbing atom. The changes of the standing wave intensity with the incidence angle $\Delta\Theta$ are known for a given $z_{\mathbf{h}}$. Since the absorption cross-section is proportional to the intensity, the comparison between the theoretical intensity patterns and measured yields, gives direct information about the atom positions. Because of the fact, that the energy of emitted electrons or fluorescence radiation is characteristic of the given element and related to its electronic structure, the obtained structural information is element selective. The principle of the x-ray standing waves (XSW) method is illustrated schematically in figure 1.5. The next figure (1.6) shows the patterns of the standing wave intensity for silicon crystal, (111) reflection.

Though the effects caused by the existence of the standing wave in the lattice under the diffraction conditions were observed earlier (Borrmann effect and fine structure of the Kossel lines), the first experimental demonstration of the standing waves method came from the neutron science. Knowles already in 1955 observed a variation in the

²One should note, that the definition of the origin of the unit cell is arbitrary. The change of the origin leads to the shift of the lattice planes. The considerations presented here are valid for the choice of origin such that $F_{\mathbf{h}} \in \mathbb{R}$ for $f'' = 0$ [52]. Of course the way the standing wave moves does not depend on the choice of origin. The nodes of the standing wave at the low angular side of the reflection coincide with the planes of maximum electron density [52], called diffraction planes [12].

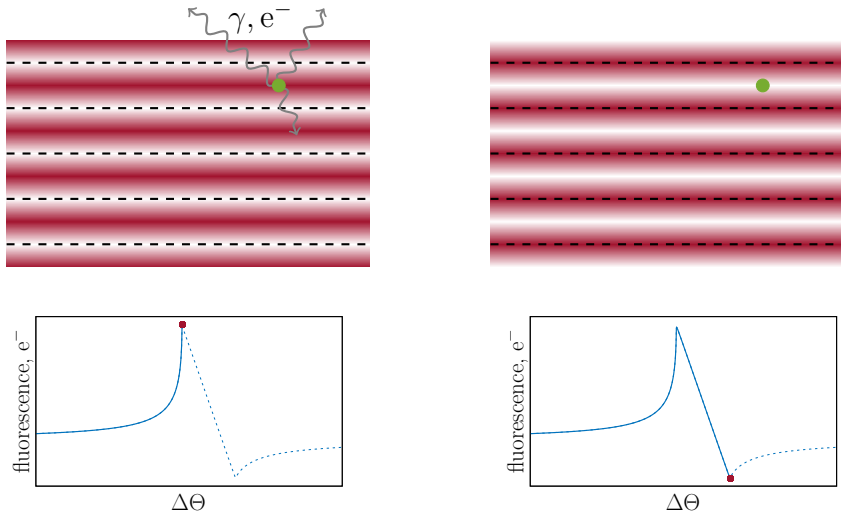


Figure 1.5: The principle of the x-ray standing waves method. The atom of interest (green dot) is located in between the lattice planes (black dashed lines). The intensity of the electromagnetic radiation (standing wave) is represented by the colour map in the top pictures. The graphs show the yield of fluorescence or electrons emitted by the green atom. On the low angular side of the reflection domain, the antinodes of the standing wave lie between the lattice planes and coincide with the atom, thus enhancing the absorption and secondary emission. In contrary, the atom emits no fluorescence/electrons when the nodes of the standing wave coincide with it, what happens on the high angular side of the reflection. The shape of the variation of the yield indicates, that the atom is located at the position $z_{\mathbf{h}} = 0.5$ with respect to the lattice planes.

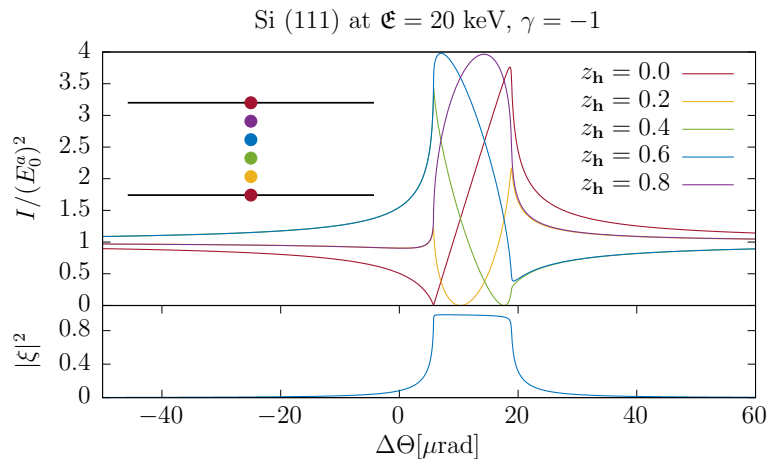


Figure 1.6: The relative intensity of the standing wave (as defined by the formula (1.36)) for Si crystal, (111) reflection, energy 20 keV, plotted against the incidence angle for a few positions in the crystal with respect to the reflecting lattice planes ($z_{\mathbf{h}}$). Due to the proportionality between the absorption cross-section and the intensity, at the same time the curves represent the variations in secondary emission yield for the atoms located at positions $z_{\mathbf{h}}$ (inset).

γ -rays emission from the calcite single crystal in the reflection domain caused by the neutrons standing wave, whose shape agreed well with the dynamical theory calculation [23]. A similar direct evidence of the existence of the x-ray standing wave was given by Batterman, who measured the variations of the K fluorescence emission from germanium single crystal [24]. A few years later, he demonstrated that the standing wave can be used to determine the positions of the foreign atoms in the known lattice (in that case arsenic dopant atoms in the silicon crystal), thus establishing the XSW method [36]. Since then it was used for numerous system and extended for various experimental conditions, keeping the basic principle described herein. More variations of the XSW method were discussed in the introduction to this work, and a good review of applications is given in the book of Zegenhagen and Kazimirov [68].

1.7 XSW structural analysis

Consider the case of a number of atoms of a given element located at various positions in the unit cell. Then the total yield is a sum of the contributions from each atom. Due to the proportionality between the absorption cross-section and standing wave intensity, the normalised yield from n atoms of the same kind reads

$$\begin{aligned} y &= \frac{1}{n} \sum_{j=1}^n [1 + |\xi|^2 + 2\Re(\xi e^{-i\mathbf{h}\cdot\mathbf{R}_j})] = \\ &= 1 + |\xi|^2 + 2\Re\left(\xi \underbrace{\frac{1}{n} \sum_{j=1}^n e^{-i\mathbf{h}\cdot\mathbf{R}_j}}_{(F_{sw}^{\mathbf{h}})^*}\right) = \\ &= 1 + |\xi|^2 + 2\Re|\xi| |F_{sw}^{\mathbf{h}}| \cos[\arg(\xi) - \arg(F_{sw}^{\mathbf{h}})] \end{aligned} \quad (1.37)$$

The quantity $F_{sw}^{\mathbf{h}}$ is the standing wave structure factor. By fitting equation (1.37) to the experimental fluorescence or electron yield, one obtains the modulus and phase of the standing wave structure factor. Traditionally two quantities are defined: coherent fraction $f_c := |F_{sw}^{\mathbf{h}}|$ and coherent position $p_c := \arg(F_{sw}^{\mathbf{h}})/2\pi$. It is the sensitivity to the phase of $F_{sw}^{\mathbf{h}}$, what gives direct structural information in the XSW method.

One may define an atomic distribution function for a given element as a normalised sum of three dimensional Dirac delta distributions

$$G(\mathbf{r}) = \frac{1}{n} \sum_{j=1}^n \delta^{(3)}(\mathbf{r} - \mathbf{R}_j) \quad (1.38)$$

If one assumes that the considered crystalline system is periodic, then also the atomic distribution function is periodic, so it can be expanded in the Fourier series

$$G(\mathbf{r}) = \frac{1}{V_{\text{cell}}} \sum_{\mathbf{h}} G_{\mathbf{h}} e^{-i\mathbf{h}\cdot\mathbf{r}} \quad (1.39)$$

with Fourier coefficients given as

$$G_{\mathbf{h}} = \int_{V_{\text{cell}}} G(\mathbf{r}) e^{i\mathbf{h}\cdot\mathbf{r}} d^3\mathbf{r} \quad (1.40)$$

Inserting the definition of G (1.38) into the previous equation yields

$$G_{\mathbf{h}} = \int_{V_{\text{cell}}} \frac{1}{n} \sum_{j=1}^n \delta^{(3)}(\mathbf{r} - \mathbf{R}_j) e^{i\mathbf{h}\cdot\mathbf{r}} d^3\mathbf{r} = \frac{1}{n} \sum_{j=1}^n e^{i\mathbf{h}\cdot\mathbf{R}_j} = F_{sw}^{\mathbf{h}} \quad (1.41)$$

The last equations shows, that what is actually measured in the XSW experiment is a Fourier coefficient of the atomic distribution function. In certain cases a determination of one coefficient already provides valuable information [36], but at least two reflections are needed to determine the atom position unambiguously in two dimensions [69]. It is also possible to obtain a picture of atomic distribution by measuring a number of Fourier coefficients $G_{\mathbf{h}}$ and performing an inverse Fourier transform [70].

1.8 The absorption correction for the wavevector

When deriving the expression (1.36) for the standing wave intensity it was assumed that the wavevector \mathbf{k}_0 is real. This assumption is justified under certain experimental conditions, but is obviously not true in general (already because $\chi \in \mathbb{C}$).

At first one needs the expression for the wavevector in the crystal. From the boundary condition $\mathbf{k}_0 = \mathbf{k}_0^a - k\kappa\mathbf{n}$ and equation (1.22) one gets

$$\mathbf{k}_0 = \mathbf{k}_0^a + \frac{1}{\gamma_0} (X_0 + \frac{1}{2}k\chi_0) \mathbf{n} \quad (1.42)$$

The imaginary part of the wavevector gives a damping factor when inserted into the complex exponent. If the absorption coefficient μ is defined via Beer-Lambert law $I = I_0 e^{-\mu d}$, where d is a crystal thickness, one has

$$\mu = -(2\Im X_0 + k\Im\chi_0) \quad (1.43)$$

or using the relation between the tiepoint position and amplitude ratio (1.21)

$$\mu = -\{k\Im[\Im(\chi_{\bar{\mathbf{h}}})\Re(\xi) + \Re(\chi_{\bar{\mathbf{h}}})\Im(\xi)] + k\Im\chi_0\} \quad (1.44)$$

The last transformation helps to understand the meaning of the terms constituting the full absorption coefficient. The first term arising from the dynamical theory considerations describes the anomalous absorption, which is related to the standing wave enhancing or suppressing the absorption. The second term, which is non-zero even in the non-absorbing crystal ($\chi \in \mathbb{R}$), is responsible for the extinction effect. The incident beam does not penetrate deep into the crystal, since it is reflected on the first few lattice planes. The last term is the standard linear absorption.

Due to the existence of the absorption term, the total electric field intensity inside the crystal becomes depth dependent

$$I(z) = (E_0^a)^2 [1 + |\xi|^2 + 2\Re\Re(\xi e^{-i\mathbf{h}\cdot\mathbf{r}})] e^{-\mu z/\gamma_0} \quad (1.45)$$

z/γ_0 is the distance along the path of the incoming wave, whereas z denotes the distance from the crystal surface.

When the experiment is performed on a thick single crystal, the secondary emission yield coming from the whole sample is an integral of the intensity over z from zero to infinity. One should additionally account for an absorption of the fluorescence or emitted electrons on the way from the emitting atom to the detector. If the angle between the sample surface and the fluorescence/electron detector is α (fig. 1.7), the attenuation factor is $\exp(-\mu_{lin}z/\sin \alpha)$. In case of fluorescence detection, the absorption coefficient is equal $\mu_{lin} = -k\Im\chi_0$ and must be calculated for the energy of fluorescence radiation.

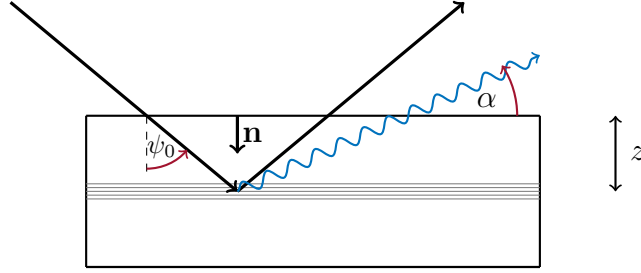


Figure 1.7: Schematic picture of x-ray diffraction in Bragg geometry. The wave-like line depicts fluorescence radiation emitted towards the detector. α is an angle between the crystal surface and the detector, ψ_0 the angle between the \mathbf{k}_0 and surface normal \mathbf{n} .

If the crystal is perfectly periodic, the coherent position is not depth dependent and the term containing standing wave structure factor can be taken out of the integral. What remains is an integral over the real exponent, so the formula for the yield from thick crystal reads

$$y = \left\{ 1 + |\xi|^2 + 2\Re \left[\xi (F_{sw}^h)^* \right] \right\} \underbrace{\left(\frac{\mu}{\gamma_0} + \frac{\mu_{lin}}{\sin \alpha} \right)^{-1}}_{z_{\text{eff}}} \quad (1.46)$$

An inverse of the expression in the round brackets is an effective thickness.

The secondary emission yield depends in fact also on the footprint of the incoming beam on the sample surface — the bigger is the footprint, the more fluorescence or electrons will be emitted. This effect is taken into account by multiplying the previous equation by the footprint S , which is equal to S_0/γ_0 , where S_0 is a cross-section of the incoming beam. This cross-section is constant, so it disappears due to normalisation. The final formula with all corrections reads

$$y = \left\{ 1 + |\xi|^2 + 2\Re \left[\xi (F_{sw}^h)^* \right] \right\} \frac{z_{\text{eff}}}{\gamma_0} \quad (1.47)$$

The directional cosine γ_0 matters only, when the incidence angle Θ is changed significantly in the experiment. Normally $\Delta\Theta$ is very small, in the order of tens of μrad , thus γ_0 is almost constant and also disappears due to normalisation.

1.9 Scattering of the arbitrarily polarised wave

1.9.1 Parametrisation of the incoming wave

Up to now the linearly (only σ or π) polarised wave was considered. In order to describe the experiment involving the circularly or elliptically polarised wave, one has to consider a more general expression for the incoming electromagnetic plane wave:

$$\mathcal{E}_0^a(\mathbf{r}, t) = E_0^a \underbrace{(\varepsilon_1 \hat{\mathbf{e}}_1 + \varepsilon_2 \hat{\mathbf{e}}_2)}_{\boldsymbol{\varepsilon}} e^{i\omega t - i\mathbf{k}_0^a \cdot \mathbf{r}} \quad (1.48)$$

the vectors fulfill the condition $\hat{\mathbf{e}}_i \cdot \hat{\mathbf{e}}_j = \delta_{ij}$ ³, $\hat{\mathbf{e}}_i \cdot \mathbf{k}_0^a = 0$ [55]. The choice of $\hat{\mathbf{e}}_i$ is arbitrary in the plane perpendicular to propagation direction, so one may choose the σ - and π -polarisation vectors $\hat{\mathbf{e}}_1 = \hat{\mathbf{e}}_\sigma$, $\hat{\mathbf{e}}_2 = \hat{\mathbf{e}}_{0\pi}$, which are defined in section 1.4 and shown in figure 1.1. With such a choice one denotes $\varepsilon_1 = \varepsilon_\sigma$, $\varepsilon_2 = \varepsilon_\pi$. The polarisation vector $\boldsymbol{\varepsilon}$, which is in general complex, can be parametrised in the following way

$$\boldsymbol{\varepsilon} = \begin{pmatrix} \varepsilon_\sigma \\ \varepsilon_\pi \end{pmatrix} = \begin{pmatrix} \cos \beta \\ \sin \beta e^{i\delta} \end{pmatrix} \quad (1.49)$$

$\beta, \delta \in [-\pi, \pi]$. Changing the values of β and δ gives any linear and elliptical polarisation, including the circular one.

With such a parametrisation, $\boldsymbol{\varepsilon}$ is a unit vector. This condition holds true, whenever a single plane wave is considered. The restriction on $|\boldsymbol{\varepsilon}|$ is however not absolutely necessary for further considerations. In particular, when considering the superposition of two waves, one can define a polarisation vector whose length will not be unity. In such a case it is defined as a remaining term left after factoring out two factors, the amplitude of the incoming wave E_0^a and oscillatory term common for both waves $e^{i\omega t - i\mathbf{k}_0 \cdot \mathbf{r}}$, with $\mathbf{k}_0 \in \mathbb{R}$. This should be regarded as the most general definition of $\boldsymbol{\varepsilon}$.

The values $\beta = \frac{\pi}{4}$ and $\delta = \pm \frac{\pi}{2}$ correspond to the circularly polarised wave. It means that both polarisation components are equal in magnitude, but are shifted in phase by $\pi/2$. As the wave propagates, the electric field vector rotates around the propagation direction. The helicity of the wave is determined by looking at the wave from the side of the observer (antiparallel to the wavevector). In this case $\delta = +\frac{\pi}{2}$ corresponds to the right-handed polarisation (RHP), and $\delta = -\frac{\pi}{2}$ to the left-handed polarisation (LHP) [55]. Since the case of circularly polarised incoming wave has a particular importance for the studies of magnetism, the mathematical form is given here explicitly:

$$\mathcal{E}_0^a(\mathbf{r}, t) = \frac{E_0^a}{\sqrt{2}} (\hat{\mathbf{e}}_\sigma \pm i\hat{\mathbf{e}}_{0\pi}) e^{i\omega t - i\mathbf{k}_0^a \cdot \mathbf{r}} \quad (1.50)$$

The reversal of helicity is performed via transformation $\varepsilon_\pi \rightarrow \varepsilon_\pi^*$. With the parametrisation (1.49) the component ε_σ is always real, so the complex conjugate $\varepsilon_\sigma \rightarrow \varepsilon_\sigma^*$ is not necessary. It should be noted, that the components ε_σ and ε_π are defined once by the considered form of the incoming wave and do not change later. In other words, the symbols

³ δ_{ij} denotes a Kronecker delta, $\delta_{ij} = \begin{cases} 1, & i = j \\ 0, & i \neq j \end{cases}$

have always the meaning $\varepsilon_\sigma = 1/\sqrt{2}$ and $\varepsilon_\pi = i/\sqrt{2}$, if the incoming circularly polarised wave is considered, even if the polarisation of the wave changes during the scattering or absorption processes. This approach ensures, that all the final results of the theory contain an explicit dependence on the polarisation of the incoming wave. It is then easy to compare the results for different polarisations.

1.9.2 Boundary conditions and reflectivity

Like in the previous chapter, also now only the reflection geometry and the case of a thick crystal are considered. Outside of the crystal the incoming (\mathcal{E}_0^a) and reflected (\mathcal{E}_h^a) waves exist, whose general form is the following, respectively

$$\mathcal{E}_0^a = E_0^a(\varepsilon_\sigma \hat{\mathbf{e}}_\sigma + \varepsilon_\pi \hat{\mathbf{e}}_{0\pi})e^{i\omega t - i\mathbf{k}_0^a \cdot \mathbf{r}} = \mathcal{E}_0^a \varepsilon_\sigma \hat{\mathbf{e}}_\sigma + \mathcal{E}_0^a \varepsilon_\pi \hat{\mathbf{e}}_{0\pi} \quad (1.51)$$

$$\mathcal{E}_h^a = (E_{h\sigma}^a \hat{\mathbf{e}}_\sigma + E_{h\pi}^a \hat{\mathbf{e}}_{h\pi})e^{i\omega t - i\mathbf{k}_h^a \cdot \mathbf{r}} = \mathcal{E}_{h\sigma}^a \hat{\mathbf{e}}_\sigma + \mathcal{E}_{h\pi}^a \hat{\mathbf{e}}_{h\pi} \quad (1.52)$$

The general convention for notations is that standard E denotes the amplitude of the electric field in a direction of the corresponding polarisation vector, whereas italic \mathcal{E} indicates the component of the full electric field (that is the amplitude with phase factor $e^{i\omega t - i\mathbf{k} \cdot \mathbf{r}}$), for example $\mathcal{E}_0^a = E_0^a e^{i\omega t - i\mathbf{k}_0^a \cdot \mathbf{r}}$. The wavevector of the outgoing wave is given by the diffraction condition $\mathbf{k}_h^a = \mathbf{k}_0^a + \mathbf{h}$. The coefficients ε_σ and ε_π define the polarisation of the incoming wave \mathcal{E}_0^a .

Given that only one wavefield is excited in the crystal at once (thick crystal approximation), two waves inside the crystal exist:

$$\mathcal{E}_0 = E_{0\sigma} \hat{\mathbf{e}}_\sigma e^{i\omega t - i\mathbf{k}_{0\sigma} \cdot \mathbf{r}} + E_{0\pi} \hat{\mathbf{e}}_{0\pi} e^{i\omega t - i\mathbf{k}_{0\pi} \cdot \mathbf{r}} = \mathcal{E}_{0\sigma} \hat{\mathbf{e}}_\sigma + \mathcal{E}_{0\pi} \hat{\mathbf{e}}_{0\pi} \quad (1.53)$$

$$\mathcal{E}_h = E_{h\sigma} \hat{\mathbf{e}}_\sigma e^{i\omega t - i\mathbf{k}_{h\sigma} \cdot \mathbf{r}} + E_{h\pi} \hat{\mathbf{e}}_{h\pi} e^{i\omega t - i\mathbf{k}_{h\pi} \cdot \mathbf{r}} = \mathcal{E}_{h\sigma} \hat{\mathbf{e}}_\sigma + \mathcal{E}_{h\pi} \hat{\mathbf{e}}_{h\pi} \quad (1.54)$$

In order to establish relations between the unknown electric field amplitudes in equations (1.52) - (1.54), one needs to consider the boundary conditions. Like before, one starts from equations (1.30) and (1.31). The latter can be written for each polarisation component separately, by multiplying the vector equations by polarisation unit vectors $\hat{\mathbf{e}}_\sigma$ and $\hat{\mathbf{e}}_{0\pi}$

$$\mathcal{E}_0^a \varepsilon_\sigma + \mathcal{E}_{h\sigma}^a = \mathcal{E}_{0\sigma} + \mathcal{E}_{h\sigma} \quad (1.55)$$

$$\mathcal{E}_0^a \varepsilon_\pi + \mathcal{E}_{h\pi}^a \cos 2\Theta_B = \mathcal{E}_{0\pi} + \mathcal{E}_{h\pi} \cos 2\Theta_B \quad (1.56)$$

Using the same arguments as in section 1.5, one can transform equations for the full electric field components to the ones for amplitudes only. The relations between the amplitudes of incoming and refracted waves read

$$E_0^a \varepsilon_{\mathbf{p}} = E_{0\mathbf{p}} \quad (1.57)$$

$$E_{h\mathbf{p}}^a = E_{h\mathbf{p}} \quad (1.58)$$

Here $\mathbf{p} \equiv \sigma, \pi$. The polarisation factor ($\cos 2\Theta_B$) disappears, as it stands only by the amplitudes of reflected waves, which are now decoupled from the "0" ones. The relation between the "0" and "h" amplitudes inside the crystal is given additionally via the amplitude ratios: $E_{h\mathbf{p}} = \xi_{\mathbf{p}} E_{0\mathbf{p}}$. They are known for each polarisation component from the

general solution of the dynamical theory. From equation (1.58) one has that $E_{\mathbf{hp}}^a = \xi_p E_{0p}$. The other one from the pair gives the relation between the amplitudes outside of the crystal $E_{\mathbf{hp}}^a = \xi_p \varepsilon_p E_0^a$.

Established relations between amplitudes allow to write the form of the emerging wave, based on equation (1.52)

$$\mathcal{E}_{\mathbf{h}}^a = E_0^a (\xi_\sigma \varepsilon_\sigma \hat{\mathbf{e}}_\sigma + \xi_\pi \varepsilon_\pi \hat{\mathbf{e}}_{\mathbf{h}\pi}) e^{i\omega t - i\mathbf{k}_{\mathbf{h}}^a \cdot \mathbf{r}} \quad (1.59)$$

The reflectivity, as defined in chapter 1.5, reads

$$I_{\mathbf{h}}^a = |\gamma| (\varepsilon_\sigma^2 |\xi_\sigma|^2 + |\varepsilon_\pi|^2 |\xi_\pi|^2) \quad (1.60)$$

For the circularly polarised wave

$$I_{\mathbf{h}}^a = \frac{1}{2} |\gamma| (|\xi_\sigma|^2 + |\xi_\pi|^2) \quad (1.61)$$

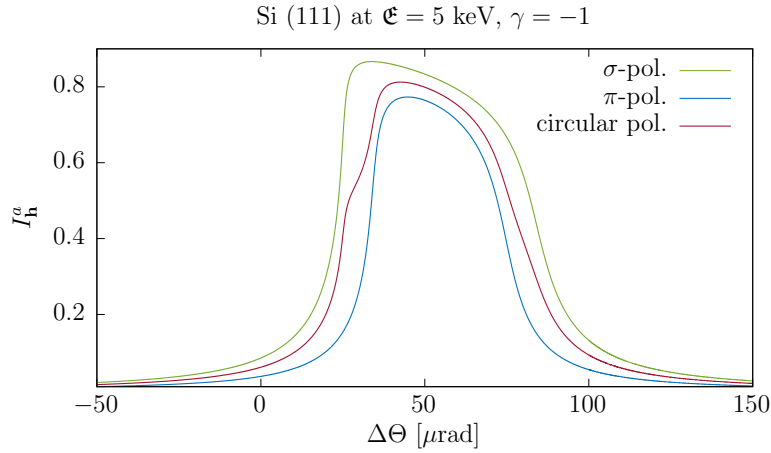


Figure 1.8: Comparison between reflectivities calculated for Si (111) reflection, energy $\mathfrak{E} = 5$ keV, symmetric reflection, for linear (σ and π) and circular polarisation of the incoming wave. At this energy a polarisation factor for π -polarisation $\cos 2\Theta_B \cong 0.69$, so the differences are particularly evident. The kink visible on the low angular side of the reflection domain for circular polarisation is related to the fact, that in this case the reflectivity is an average of the curves for σ - and π -polarisations.

1.9.3 Total electric field

From the relations between amplitudes (1.57)-(1.58) and amplitude ratios one obtains immediately the expression for the total electric field inside the crystal $\mathcal{E} = \mathcal{E}_0 + \mathcal{E}_{\mathbf{h}}$

$$\mathcal{E} = E_0^a [\varepsilon_\sigma \hat{\mathbf{e}}_\sigma (1 + \xi_\sigma e^{-i\mathbf{h} \cdot \mathbf{r}}) e^{i\omega t - i\mathbf{k}_{0\sigma} \cdot \mathbf{r}} + \varepsilon_\pi (\hat{\mathbf{e}}_{0\pi} + \xi_\pi \hat{\mathbf{e}}_{\mathbf{h}\pi} e^{-i\mathbf{h} \cdot \mathbf{r}}) e^{i\omega t - i\mathbf{k}_{0\pi} \cdot \mathbf{r}}] \quad (1.62)$$

In a similar manner as when considering the linear polarisation, one assumes that the wavevectors inside the crystal are real. This is equivalent to neglecting the phenomena of extinction and anomalous absorption introduced by the imaginary parts of the

wavevectors. One should note, that the regular absorption is still included, as it enters the formalism via the imaginary part of susceptibility Fourier coefficients. Additionally, the difference between the wavevectors for σ - and π -component is small (as already the difference from the vacuum wavevector \mathbf{k}_0^a is small), so $\mathbf{k}_{0\sigma} \simeq \mathbf{k}_{0\pi}$. Assuming these approximations, the intensity of the electric field reads

$$I = (E_0^a)^2 \left\{ \varepsilon_\sigma^2 [1 + |\xi_\sigma|^2 + 2\Re(\xi_\sigma e^{-i\mathbf{h}\cdot\mathbf{r}})] + |\varepsilon_\pi|^2 [1 + |\xi_\pi|^2 + 2\Re(\xi_\pi e^{-i\mathbf{h}\cdot\mathbf{r}}) \cos 2\Theta_B] \right\} \quad (1.63)$$

For circularly polarised incoming wave one gets

$$I = (E_0^a)^2 \left[1 + \left(\frac{1}{2}|\xi_\sigma|^2 + \frac{1}{2}|\xi_\pi|^2\right) + \Re(\xi_\sigma e^{-i\mathbf{h}\cdot\mathbf{r}}) + \Re(\xi_\pi e^{-i\mathbf{h}\cdot\mathbf{r}}) \cos 2\Theta_B \right] \quad (1.64)$$

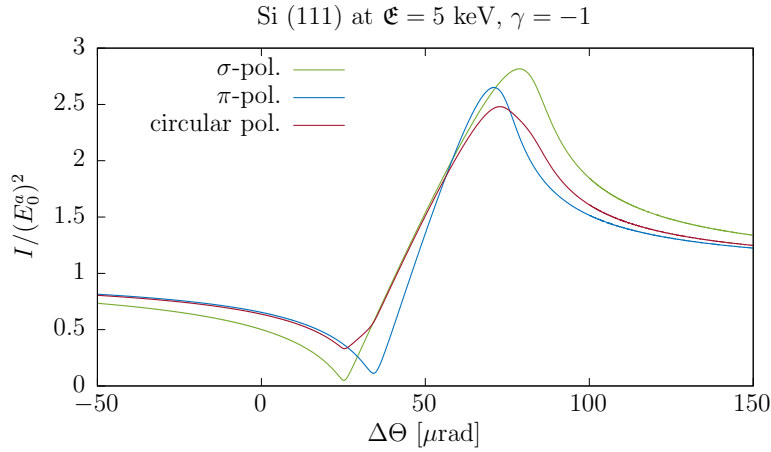


Figure 1.9: Comparison between relative electric field intensity calculated for Si (111) reflection, energy $\mathfrak{E} = 5$ keV, symmetric reflection, for linear (σ and π) and circular polarisation of the incoming wave. The functions were calculated for the position at the reflecting lattice planes ($z_{\mathbf{h}} = 0$).

1.9.4 Correction for the complex wavevector

The absorption correction for the wavevector is introduced analogously to the way described in section 1.8 for linear polarisation. The imaginary part of the wavevector remains when calculating the intensity, and gives the damping factors. The intensity of the electric field inside the crystal for arbitrary polarisation, with this correction, reads

$$I = (E_0^a)^2 \left\{ \varepsilon_\sigma^2 [1 + |\xi_\sigma|^2 + 2\Re(\xi_\sigma e^{-i\mathbf{h}\cdot\mathbf{r}})] e^{-\mu_\sigma z/\gamma_0} + |\varepsilon_\pi|^2 [1 + |\xi_\pi|^2 + 2\Re(\xi_\pi e^{-i\mathbf{h}\cdot\mathbf{r}}) \cos 2\Theta_B] e^{-\mu_\pi z/\gamma_0} \right\} \quad (1.65)$$

The effective absorption coefficient, defined via the formula (1.43) is polarisation dependent.

The considerations leading to the formula for the secondary yield excited by the standing wave in a thick crystal are the same as in the case of linear polarisation (1.8). Analogously to the formula (1.46), in the case of arbitrary polarisation

$$y = \varepsilon_\sigma^2 \left\{ 1 + |\xi_\sigma|^2 + 2\Re \left[\xi_\sigma (F_{sw}^{\mathbf{h}})^* \right] \right\} \frac{z_{\text{eff}}^\sigma}{\gamma_0} + |\varepsilon_\pi^2| \left\{ 1 + |\xi_\pi|^2 + 2\Re \left[\xi_\pi (F_{sw}^{\mathbf{h}})^* \right] \cos 2\Theta_B \right\} \frac{z_{\text{eff}}^\pi}{\gamma_0} \quad (1.66)$$

The effective thickness was already defined via the formula (1.46). In the same way as before, γ_0 in the denominator accounts for the changes of the footprint during the angular scans.

Chapter 2

Absorption cross-section

In the x-ray standing waves method one makes use of both diffraction and absorption phenomena. The first was described in the previous section, and yielded a form of the wave inside the crystal — the dependence of the electric field on the departure angle $\Delta\Theta$ (equation (1.62)). The electromagnetic wave is treated here in a classical way, what suffices to describe the absorption of EM radiation by an atom [71].

In the x-ray regime the radiation is absorbed by matter almost exclusively via the photoelectric absorption process. A photon is absorbed by the atom, what results in the electron transition to the unoccupied states or its ejection from the atom, depending on the photon energy. This process is followed by the decay of the core-hole, which is filled by another bound electron. As a result a fluorescence photon or Auger electron is emitted.

The interaction of the classical EM wave with an atom is described here using the time-dependent perturbation theory, where the interaction (time-dependent) term is a vector potential of the EM radiation. This formalism was developed by P. A. M. Dirac in 1926 [72].

After a short summary of the time-dependent perturbation theory, following [71], the case of harmonic perturbation (EM wave) is considered. The calculations are presented for a wave with arbitrary polarisation. The formula for the absorption cross-section is derived for such a general case. Subsequently, the absorption cross-section is evaluated for the electric field existing in a crystalline medium in the reflection domain that is in short for an x-ray standing wave. This result gives a firm basis for the already discussed XSW method. In this chapter only the case of linearly polarised incoming wave is considered. A general case constituting the basis of the MXSW is introduced in chapter 4.

2.1 Time-dependent perturbation theory

2.1.1 General formulation

One starts here by considering a physical system — atom in this case — which is subjected to the external perturbation. The aim is to find the probability that the atom will undergo a transition to another state.

The unperturbed physical system is described by the Hamilton operator H_0 . The

system's energy spectrum \mathfrak{E}_n is given by the Schrödinger equation

$$\mathbf{H}_0|\phi_n\rangle = \mathfrak{E}_n|\phi_n\rangle \quad (2.1)$$

where Dirac vectors $|\phi_n\rangle$ denote the stationary states of the Hamilton operator. Then one considers the situation, where the perturbation is applied starting from $t = 0$. The system will be described by the operator

$$\mathbf{H}(t) = \mathbf{H}_0 + \mathbf{W}(t) = \mathbf{H}_0 + v\mathbf{V}(t) \quad (2.2)$$

where \mathbf{W} and \mathbf{V} describe the perturbation, \mathbf{V} is large, of the order of \mathbf{H}_0 , and v is a small real parameter.

Assume, that the system is initially in the state $|\phi_i\rangle$ (eigenstate of \mathbf{H}_0). The aim is to calculate the probability $P_{fi}(t)$ of finding the system in the eigenstate $|\phi_f\rangle$ at the time t . The evolution of the system's state $|\psi(t)\rangle$ is described by the time-dependent Schrödinger equation

$$i\hbar\frac{d}{dt}|\psi(t)\rangle = \mathbf{H}(t)|\psi(t)\rangle \quad (2.3)$$

with initial condition $|\psi(0)\rangle = |\phi_i\rangle$. \hbar denotes the reduced Planck constant $\hbar = h_P/2\pi$. The sought probability $P_{fi}(t)$ is, from the postulates of quantum mechanics, given by the mean value of projection operator. In non-degenerate case $P_{fi}(t) = |\langle\phi_f|\psi(t)\rangle|^2$.

The set of eigenstates of Hamilton operator $\{|\phi_n\rangle\}$ forms a basis. $|\psi(t)\rangle$ can be expressed in this basis

$$|\psi(t)\rangle = \sum_n c_n(t)|\phi_n\rangle \quad (2.4)$$

with $c_n(t) := \langle\phi_n|\psi(t)\rangle$. Using the Schrödinger equation one can derive an expression for the time dependence of the coefficients c_n . At first one considers the case of no perturbation ($\mathbf{H} = \mathbf{H}_0$), and inserts equation (2.4) into the Schrödinger equation (2.3). This yields

$$c_n(t) = \underbrace{c_n(0)}_{:=b_n=\text{const}} e^{-i\mathfrak{E}_n t/\hbar} \quad (2.5)$$

Now, if the perturbation is no longer zero, but remains small, the solution of the Schrödinger equation is expected to be very close to the latter solution. The coefficient c_n is assumed to have the form

$$c_n(t) = b_n(t)e^{-i\mathfrak{E}_n t/\hbar} \quad (2.6)$$

Having equation for the coefficients c_n , the problem is now to determine the coefficients b_n . This is done in similar manner as before, by inserting the relation (2.4) into equation (2.3), now taking the form of the Hamilton operator containing the perturbation term. One gets

$$i\hbar\dot{c}_n(t) = \mathfrak{E}_n c_n(t) + v \sum_k \underbrace{V_{nk}(t)}_{=:\langle\phi_n|\mathbf{V}(t)|\phi_k\rangle} c_k(t) \quad (2.7)$$

The dot over c_n denotes time derivative. Insertion of the expression (2.6) gives the set of equations for the b_n coefficients

$$i\hbar\dot{b}_n(t) = v \sum_k V_{nk}(t)b_k(t)e^{i\omega_{nk}t} \quad (2.8)$$

which is equivalent to the original Schrödinger equation. The quantity $\omega_{nk} := (\mathfrak{E}_n - \mathfrak{E}_k)/\hbar$ is called Bohr angular frequency [71].

Since equation (2.8) is not exactly solvable [71], the coefficient b_n is expanded in the power series in v

$$b_n(t) = b_n^{(0)}(t) + vb_n^{(1)}(t) + v^2b_n^{(2)}(t) + \dots \quad (2.9)$$

If the parameter v is small, the series converges quickly. Putting this relation into equation (2.8) and comparing the terms staying by the same order in v , yields the recurrence relation

$$r = 0 \quad i\hbar\dot{b}_n^{(0)}(t) = 0 \quad (2.10a)$$

$$r = 1 \quad i\hbar\dot{b}_n^{(1)}(t) = \sum_k V_{nk}(t)b_k^{(0)}(t)e^{i\omega_{nk}t} \quad (2.10b)$$

⋮

$$r = p \quad i\hbar\dot{b}_n^{(p)}(t) = \sum_k V_{nk}(t)b_k^{(p-1)}(t)e^{i\omega_{nk}t} \quad (2.10c)$$

2.1.2 Solution to the first order

In order to describe the absorption of light quantum by the atom, it suffices to consider the solution in first order of v only. One starts by considering the zeroth order. Since the system is initially in the eigenstate of H_0 , one can write

$$|\psi(0)\rangle = \sum_n c_n(0)|\phi_n\rangle = \sum_n b_n(0)e^{-i\mathfrak{E}_n \cdot 0}|\phi_n\rangle = |\phi_i\rangle \quad (2.11)$$

This indicates that $b_n(0) = \delta_{ni}$. Since one considers the zeroth order in v and equation (2.10a) implies that $b_n^{(0)}$ is constant, one has

$$b_n^{(0)} = \delta_{ni} \quad (2.12)$$

and $b_n^{(p)}(0) = 0$ for $p \geq 1$. Equation (2.12) constitutes a solution in the zeroth order.

To obtain the solution in the first order, the latter is inserted into the recurrence relation (2.10b), and the resulting equation integrated. This gives

$$b_n^{(1)}(t) = \frac{1}{i\hbar} \int_0^t V_{ni}(\tilde{t})e^{i\omega_{ni}\tilde{t}}d\tilde{t} \quad (2.13)$$

Following (2.4), (2.6) and (2.9), the state vector of the system reads

$$|\psi(t)\rangle = \sum_n \left[\delta_{ni} + v \frac{1}{i\hbar} \int_0^t V_{ni}(\tilde{t})e^{i\omega_{ni}\tilde{t}}d\tilde{t} \right] e^{-i\mathfrak{E}_n t/\hbar} |\phi_n\rangle \quad (2.14)$$

Having this result, it follows from the definition of P_{fi}

$$P_{fi} = \left| \frac{v}{i\hbar} \int_0^t V_{fi}(\tilde{t})e^{i\omega_{fi}\tilde{t}}d\tilde{t} \right|^2 = \frac{1}{\hbar^2} \left| \int_0^t W_{fi}(\tilde{t})e^{i\omega_{fi}\tilde{t}}d\tilde{t} \right|^2 \quad (2.15)$$

where the fact that $vV_{fi} = W_{fi} = \langle \phi_f | \mathbf{W} | \phi_i \rangle$ was used and it was assumed that $\delta_{fi} = 0$, since one is interested here in transitions ($i \neq f$).

2.1.3 The case of harmonic perturbation

Since an absorption of the EM wave is considered here, the time dependence of the perturbation is assumed to be of the form

$$W(t) = W_0 e^{i\omega t} + W_0^\dagger e^{-i\omega t} \quad (2.16)$$

where $\omega = \mathfrak{E}/\hbar$ and a symbol X^\dagger denotes an Hermitian conjugate of the operator X . The standard form of the EM wave with time dependence given by $e^{i\omega t}$ is supplemented here by the Hermitian conjugate to fulfill the postulates of the quantum mechanics, that is to ensure, that the operator H is Hermitian.

For this form of perturbation the integral in equation (2.15) can be evaluated easily. One gets

$$P_{fi}(t) = \frac{1}{\hbar^2} \left| W_0^{fi} \frac{e^{i(\omega_{fi}+\omega)t} - 1}{\omega_{fi} + \omega} + (W_0^\dagger)^{fi} \frac{e^{i(\omega_{fi}-\omega)t} - 1}{\omega_{fi} - \omega} \right|^2 \quad (2.17)$$

One can consider two cases depending on the sign of ω_{fi} :

- $\omega_{fi} > 0$, that is the energy of the final level is higher than that of the initial one. This case corresponds to the absorption process.
- $\omega_{fi} < 0$, the final energy is lower than the initial one, so this is a stimulated emission.

Since the absorption of the photon is of interest here, one considers only the first case. Consequently, the first term in equation (2.17) is never big, as the denominator is never small, so one can discard this term and write the remaining one is the following form

$$P_{fi}(t) = \frac{|(W_0^\dagger)^{fi}|^2}{\hbar^2} \left[\frac{\sin \frac{1}{2}(\omega - \omega_{fi})t}{\frac{1}{2}(\omega - \omega_{fi})} \right]^2 \quad (2.18)$$

If one considers the probability rate $w_{fi} = P_{fi}/t$, that is the probability per unit time, the previous formula can be transformed to the form

$$w_{fi} = \frac{2\pi}{\hbar} |(W_0^\dagger)^{fi}|^2 \delta(\hbar\omega - \mathfrak{E}_{fi}) \quad (2.19)$$

in the limit of $t \rightarrow \infty$, using the properties of the Dirac delta distribution¹.

2.1.4 Golden rule

If the final states are not well separated, but instead form a continuum (for example if one considers momentum of a scattered particle), the probability which can be measured in the experiment will be given by the integral over the domain of final states. Assume that the final states are labeled by continuous set of indices Λ , and one wants to determine

¹The delta distribution is defined via the condition, that for any integrable function f $\int_{-\infty}^{\infty} f(x)\delta(x)dx = f(0)$ [73]. It can be represented by the limit of the series of functions. In the considered case, the representation which helps to transform the formula for P_{fi} is $\delta(x) = \lim_{\varepsilon \rightarrow 0^+} \frac{\varepsilon}{\pi} \frac{\sin^2(x/\varepsilon)}{x^2}$ [71].

the probability of finding the system in domain of final states $\delta\Lambda_f$ centered around Λ_f . The probability rate reads

$$\delta w_{fi} = \frac{2\pi}{\hbar} \int_{\Lambda \in \delta\Lambda_f} |(W_0^\dagger)^{fi}|^2 \delta(\hbar\omega - \mathfrak{E}_{fi}) d\Lambda \quad (2.20)$$

Now in order to evaluate this integral, one may change the variables to energy and another parameter — Ω . This transformation introduces the density of final states ϱ . The integral takes the form

$$\delta w_{fi} = \frac{2\pi}{\hbar} \int_{\substack{\Omega \in \delta\Omega_f \\ \mathfrak{E} \in \delta\mathfrak{E}_f}} |(W_0^\dagger)^{fi}|^2 \delta(\hbar\omega - \mathfrak{E} + \mathfrak{E}_i) \varrho(\Omega, \mathfrak{E}) d\Omega d\mathfrak{E} \quad (2.21)$$

In comparison to the term $\delta(\hbar\omega - \mathfrak{E} + \mathfrak{E}_i)$, function $\varrho(\Omega, \mathfrak{E}) |(W_0^\dagger)^{fi}|^2$ varies slowly with \mathfrak{E} . If the range $\delta\Omega_f$ is very small, the variation of the function with Ω can be also neglected. Additionally, one considers rather the probability per unit interval of the variable Ω . Thus, after the integration over the energy

$$w_{fi} = \frac{2\pi}{\hbar} |(W_0^\dagger)^{fi}|^2 \varrho_f \quad (2.22)$$

where the abbreviation ϱ_f denotes in fact $\varrho(\Omega_f, \mathfrak{E} = \mathfrak{E}_i + \hbar\omega)$. This result was obtained for the first time by Dirac [74], and due to its significance called a golden rule N^o2 by E. Fermi [75].

2.2 Absorption of electromagnetic wave

Now, an interaction of an atom with an arbitrarily polarised EM wave will be considered. The EM wave is at this point assumed to have a general form

$$\mathcal{E}(\mathbf{r}, t) = E_0 (\varepsilon_x \hat{\mathbf{x}} + \varepsilon_y \hat{\mathbf{y}} + \varepsilon_z \hat{\mathbf{z}}) e^{i\omega t - i\mathbf{k} \cdot \mathbf{r}} \quad (2.23)$$

where E_0 denotes an amplitude of the wave, and the expression in the brackets is a polarisation vector $\boldsymbol{\varepsilon}$.

2.2.1 Interaction Hamilton operator

For the range of energies of photons (x-ray regime) considered in this work, the non-relativistic Hamilton operator suffices to describe the interaction between the electron and the EM wave. The Hamilton operator for a single electron with mass m_e , charge e and spin described by the operator $\mathbf{S} = \frac{\hbar}{2} \boldsymbol{\sigma}$ ($\boldsymbol{\sigma}$ — Pauli matrices), interacting with an EM field described by the vector potential \mathcal{A} was derived by W. Pauli [76] and reads

$$H_{\text{Pauli}} = \underbrace{\frac{\mathbf{p}^2}{2m_e} + U(\mathbf{r})}_{H_0} + \underbrace{\frac{e^2}{2m_e} \mathcal{A}^2 - \frac{e}{2m_e} \mathbf{p} \cdot \mathcal{A} - \frac{e}{2m_e} \mathcal{A} \cdot \mathbf{p} - \frac{e}{m_e} \mathbf{S} \cdot \text{rot} \mathcal{A}}_{W(t)}. \quad (2.24)$$

\mathbf{p} denotes here the momentum operator of the electron, and U the potential energy coming from the nucleus. A Coulomb gauge is used here, what implies that in the absence of currents and charges, the scalar potential of the EM field is zero [55]. The first and last term of the perturbation part W of the operator are neglected. The first one is quadratic in vector potential, so describes two photon process (scattering). The last one acts only on the spin part of the state vector and can be neglected when considering the inter-band transitions [77]. Additionally, it remains small even for the energies from the x-ray range [78]. Therefore, the interaction term used to describe absorption is assumed to have the form

$$W(t) = -\frac{e}{2m_e} \{\mathbf{p}, \mathcal{A}\} \quad (2.25)$$

where the curly brackets denote an anticommutator, that is $\{\mathbf{p}, \mathcal{A}\} := \mathbf{p} \cdot \mathcal{A} + \mathcal{A} \cdot \mathbf{p}$.

The vector potential \mathcal{A} is related to the electric field in the chosen gauge via

$$\boldsymbol{\varepsilon} = -\frac{\partial \mathcal{A}}{\partial t} \quad (2.26)$$

Taking a vector potential in the form

$$\mathcal{A}(\mathbf{r}, t) = A_0 \boldsymbol{\varepsilon} e^{i\omega t - i\mathbf{k} \cdot \mathbf{r}} + A_0^* \boldsymbol{\varepsilon}^* e^{-i\omega t + i\mathbf{k} \cdot \mathbf{r}} \quad (2.27)$$

and setting $A_0 = iE_0/\omega$, leads to the assumed form of the electric field (2.23), supplemented by the Hermitian conjugate in order to ensure that the operator W is Hermitian.

2.2.2 Electric dipole approximation

The spatial part of the exponential term in (2.27) can be expanded in a Taylor series around the point $\mathbf{r} = 0$, assuming that $kr \ll 1$ or equivalently $\lambda \gg a_0$ (that is the wavelength of the exciting radiation λ is greater than the spatial extent of the electron wavefunction a_0)

$$e^{\pm ik_j r_j} = 1 \pm ik_j r_j - \frac{1}{2} k_j^2 r_j^2 + \dots \quad (2.28)$$

with $j \equiv x, y, z$. Taking only the first term in this expansion corresponds to the electric dipole approximation. The second term gives the magnetic dipole (via the here-neglected spin-dependent part of the Hamilton operator) and electric quadrupole transitions (via the term proportional to $\mathbf{p} \cdot \mathcal{A}$).

Even though the condition $\lambda \gg a_0$ is not obviously fulfilled in the x-ray regime, the electric dipole approximation suffices in most cases to correctly describe the absorption process occurring during the XSW experiment [12]. It remains true, that the most often considered core electron states are highly localised around the atomic nuclei, what justifies the adopted simplification. The contribution of the higher order terms becomes important for the angular-resolved detection of photoelectrons, as in such a case their angular distribution becomes asymmetric [79]. However, for the secondary radiation yield obtained via angularly integrated photoelectron signal, or also isotropic fluorescence emission, the influence of quadrupole and higher terms remains small. Therefore, in these considerations the electric dipole approximation will be used.

When the higher orders of the expansion (2.28) are neglected, the vector potential has a form $\mathcal{A}(\mathbf{r}, t) = A_0 \boldsymbol{\varepsilon} e^{i\omega t} + A_0^* \boldsymbol{\varepsilon}^* e^{-i\omega t}$ and commutes with momentum operator. Therefore,

the perturbation part of the Hamilton operator in the electric dipole approximation reads

$$W(t) = -\frac{e}{m_e} (A_0 \mathbf{p} \cdot \boldsymbol{\varepsilon} e^{i\omega t} + A_0^* \mathbf{p} \cdot \boldsymbol{\varepsilon}^* e^{-i\omega t}) \quad (2.29)$$

The matrix element $(W_0^\dagger)^{fi} = \langle f | W_0^\dagger | i \rangle$ is crucial for establishing the transition rate w_{fi} (equation (2.22)) and thus also the absorption cross-section. In this case the operator W_0^\dagger has the form $-\frac{e}{m_e} A_0^* \mathbf{p} \cdot \boldsymbol{\varepsilon}^*$ and the initial state is like earlier assumed to be an eigenstate of the H_0 , $|i\rangle = |\phi_i\rangle$. At this point the matrix elements are in fact the ones of the momentum operator, of the form $\langle f | p_j | \phi_i \rangle$, $j \equiv x, y, z$. One may consider the commutator relation

$$\begin{aligned} [r_j, H_0] &= \left[r_j, \frac{\mathbf{p}^2}{2m_e} + U(\mathbf{r}) \right] = \left[r_j, \frac{\mathbf{p}^2}{2m_e} \right] = \frac{1}{2m_e} [r_j, p_x^2 + p_y^2 + p_z^2] = \\ &= \frac{1}{2m_e} [r_j, p_j^2] = \frac{1}{2m_e} \underbrace{[r_j, p_j]}_{i\hbar} p_j + p_j [r_j, p_j] = \frac{1}{2m_e} 2i\hbar p_j = \frac{i\hbar}{m_e} p_j \end{aligned} \quad (2.30)$$

where the fact that the potential energy $U(\mathbf{r})$ commutes with \mathbf{r} , and the canonical commutation relation $[r_j, p_k] = i\hbar \delta_{jk}$ were used. Using the established relation, the matrix element can be transformed to the form

$$-\frac{e}{m_e} A_0^* \langle f | \mathbf{p} \cdot \boldsymbol{\varepsilon}^* | \phi_i \rangle = ie A_0^* \omega_{if} \langle f | \mathbf{r} \cdot \boldsymbol{\varepsilon}^* | \phi_i \rangle \quad (2.31)$$

Now the matrix elements of the position operator $\langle f | r_j | \phi_i \rangle$, $r_j = x, y, z$, are the ones determining the absorption cross-section for a given form of the EM wave parametrised here via A_0 and the polarisation vector $\boldsymbol{\varepsilon}$. The detailed derivation of equation (2.31) is given in appendix A.2.1.

2.2.3 Electric dipole selection rules

One can now consider when the matrix elements of the position operator are non-zero. The constraints for the quantum numbers of the initial and final states, which ensure non-vanishing matrix elements are called selection rules. They are obtained from the mathematical properties of the operator.

The position operators can be expressed in spherical coordinates (r, ϑ, φ) . That means, they can be written as linear combinations of the spherical harmonics $Y_\ell^{m_\ell}$

$$\begin{aligned} x &= \sqrt{\frac{2\pi}{3}} r (Y_1^{-1} - Y_1^1) \\ y &= i\sqrt{\frac{2\pi}{3}} r (Y_1^{-1} + Y_1^1) \\ z &= \sqrt{\frac{4\pi}{3}} r Y_1^0 \end{aligned} \quad (2.32)$$

Therefore, one has to consider in fact the matrix elements of the form $\langle f | r Y_1^{0,\pm 1} | \phi_i \rangle$. In the position representation, the atomic state vector can be expressed as a product of radial and angular parts $\phi_{n,\ell,m_\ell}(\mathbf{r}) = R_{n,\ell}(r) Y_\ell^{m_\ell}(\vartheta, \varphi)$ [71]. The symbols n, ℓ, m_ℓ denote the quantum numbers: principal, azimuthal and magnetic, correspondingly. This set of numbers allows to uniquely identify the electron state. The spin part of the state vector

is neglected here, as the dipole operator cannot alter the spin state. Therefore, one has an additional selection rule, $\Delta m_s = 0$, where m_s is a spin magnetic quantum number, equal $\pm 1/2$ for an electron. In fact any general state vector of an atom in a solid can be expressed as the linear combination of the atomic orbitals [80]. That is why it suffices to consider the states in the form of ϕ_{n,ℓ,m_ℓ} .

In the position representation, the matrix element is given as an integral. In the considered case one has

$$\langle f | r Y_1^{\pm 1,0} | \phi_i \rangle = \int R_{n_f, \ell_f}^* R_{n_i, \ell_i} r^3 dr \int (Y_{\ell_f}^{(m_\ell)_f})^* Y_1^{\pm 1,0} Y_{\ell_i}^{(m_\ell)_i} \sin \vartheta d\vartheta d\varphi \quad (2.33)$$

where the indices i and f denote the quantum numbers of the initial and final states, respectively. The second integral imposes the restrictions on possible transitions. It follows from the properties of spherical harmonics and orbital angular momentum operator [71], that this integral is non-zero only if

$$\begin{aligned} \Delta \ell &= \ell_f - \ell_i = \pm 1 \\ \Delta m_\ell &= (m_\ell)_f - (m_\ell)_i = \pm 1, 0 \end{aligned} \quad (2.34)$$

These are the electric dipole selection rules. Only the transitions fulfilling these conditions are allowed. It is worth to mention, that when taking into account also the higher orders in the expansion (2.28), other selection rules appear. These are for example electric quadrupole selection rules obtained for the first order term (kr), which allow the transitions fulfilling $\Delta \ell = 0, \pm 2$ and $\Delta m_\ell = 0, \pm 1, \pm 2$. All those, and higher order transitions, in fact may always appear when the photon is absorbed by the atom. It is only the probability of the higher order transitions, which is much lower than for the electric dipole ones, what follows already from the magnitude of the subsequent terms in Taylor expansion (2.28).

2.2.4 Cross-section

The absorption cross-section is obtained from the transition probability rate w_{fi} (equation (2.22)) by the summation over all possible initial and final states, and normalisation by the incident photon flux [80, 81]

$$\sigma = \frac{1}{\Phi_0} \sum_{if} w_{fi} \quad (2.35)$$

Therefore, one needs to evaluate the incoming flux Φ_0 for the considered EM wave. The energy flow is given by the length of the complex Poynting vector, defined as [55]

$$\mathbf{S} = \frac{1}{2} \mathbf{E} \times \mathcal{H}^* = \frac{1}{2} \varepsilon_0 c^2 \mathbf{E} \times \mathbf{B}^* \quad (2.36)$$

The flux is given as $|\mathbf{S}|$ divided by $\hbar\omega$ (energy of one photon) [80]. For the plane EM wave of the form (2.23)² it reads

$$\Phi_0 = \frac{\varepsilon_0 c^2}{2\hbar} |A_0|^2 k \quad (2.37)$$

²It should be noted, that for the considered definition of \mathbf{S} , one uses the complex representation of electric field, without supplementing it by complex conjugate.

Detailed calculations leading to the previous formula are given in A.2.2. Now the formula for the absorption cross-section of the plane EM wave with arbitrary polarisation can be obtained from the relations for w_{fi} (2.22), the matrix element (2.31) and the definition (2.35). Due to the presence of Dirac delta distribution under the integral (2.21), the Bohr frequency is equal to the frequency of the incoming wave $\omega_{fi} = \omega$. The absorption cross-section reads

$$\sigma = (4\pi)^2 \alpha_f \hbar \omega \sum_{if} \varrho_f |\langle f | \boldsymbol{\varepsilon}^* \cdot \mathbf{r} | \phi_i \rangle|^2 \quad (2.38)$$

α_f denotes here the fine structure constant, given by the combination of the other constants: $\alpha_f = e^2/4\pi\varepsilon_0\hbar c$, where e is the elementary charge.

2.3 Absorption of the standing wave

Having established the general formula for the absorption cross-section of the EM wave, one can return to the fact discussed in 1.6, that in the Bragg reflection regime the absorption cross-section is proportional to the standing wave intensity at the position of the atom and prove it rigorously. This is presented in this section.

At first linear polarisation of the incoming wave will be considered. All the important results are the same regardless of the specific linear polarisation, so the calculations are presented for σ -polarisation. The case of a thick crystal is considered. Following equation (1.35) and the boundary condition $\mathbf{E}_0 = \mathbf{E}_0^a$, the total electric field in the crystal reads

$$\boldsymbol{\mathcal{E}}(\mathbf{r}, t) = E_0^a \hat{\boldsymbol{\varepsilon}}_\sigma (1 + \xi e^{-i\mathbf{h}\cdot\mathbf{r}}) e^{i\omega t - i\mathbf{k}_0\cdot\mathbf{r}} \quad (2.39)$$

The vector potential associated with this electric field has the form

$$\boldsymbol{\mathcal{A}}(\mathbf{r}, t) = A_0 \hat{\boldsymbol{\varepsilon}}_\sigma (1 + \xi e^{-i\mathbf{h}\cdot\mathbf{r}}) e^{i\omega t - i\mathbf{k}_0\cdot\mathbf{r}} \quad (2.40)$$

with the condition, that $E_0^a = -i\omega A_0$. With this vector potential, the perturbation part of the Hamilton operator has a proper harmonic form proportional to $e^{i\omega t}$, so the formulae from the previous section can be used. Since now a crystalline material consisting of several atoms is considered, one has to define the position of the electrons in a new way. Let \mathbf{R} be a position of the atom in the crystal, and $\tilde{\mathbf{r}}$ the position in this atom with respect to its nucleus. Then $\mathbf{r} = \mathbf{R} + \tilde{\mathbf{r}}$. Additionally, one introduces the electric-dipole approximation by setting $\tilde{\mathbf{r}} = 0$. The coordinate system can be set arbitrarily, so let the axis $\mathcal{O}z$ coincide with the σ -polarisation unit vector $\hat{\boldsymbol{\varepsilon}}_\sigma$. The only component of the polarisation vector $\boldsymbol{\varepsilon} = \hat{\boldsymbol{\varepsilon}}_\sigma (1 + \xi e^{-i\mathbf{h}\cdot\mathbf{r}})$ is then

$$\varepsilon_z = 1 + \xi e^{-i\mathbf{h}\cdot\mathbf{R}} \quad (2.41)$$

The position vector in this expression is the one of the atom's nucleus only, so it can be taken out of the matrix element. Thus, the absorption cross-section reads

$$\sigma_{sw} = (4\pi)^2 \alpha_f \hbar \omega \left| 1 + \xi e^{-i\mathbf{h}\cdot\mathbf{R}} \right|^2 \sum_{if} \varrho_f |\langle f | \tilde{z} | \phi_i \rangle|^2 \quad (2.42)$$

The expression contains the sum over the matrix elements of position operator \tilde{z} , so it seems to be dependent on the choice of the reference system. However, it can be shown

by considering an arbitrary direction of the polarisation vector, that it leads always to the same final result for the absorption cross-section. In simple words, for the spherically symmetric system none of the physical properties may depend on the choice of the coordinate system.

Compared to the plane wave, in this case the absorption cross-section is modulated by the term $|1 + \xi e^{-i\mathbf{h}\cdot\mathbf{R}}|^2$, that is the intensity of the standing wave. In other words, the probability that a photon is absorbed (and an electron or a secondary signal emitted) is proportional to the intensity of the standing wave exactly at the position of the atom nucleus \mathbf{R} . This result validates the discussion given in chapter 1.6 and gives a rigorous basis for the XSW method.

Chapter 3

X-ray magnetic circular dichroism

The formula for the absorption cross-section contains an explicit dependence on the polarisation of the electromagnetic wave. In particular, the cross-section differs between right- and left-handed polarisations, when the circularly polarised x-ray light with energy close to the atomic resonance is absorbed by an atom with a magnetic moment. Circularly polarised light carries an angular momentum, which is parallel to the propagation direction and equal $\pm\hbar$, with the sign depending on the helicity [80]. The angular momentum of radiation couples to the magnetic moment of the atom, what causes a difference in absorption depending on the mutual orientation of those two. This effect is called x-ray magnetic circular dichroism (XMCD). The very first experimental demonstration of the dichroism in the hard x-ray regime was provided by the group of G. Schütz [82], who observed a dichroism in the absorption of the elliptically polarised x-rays emitted above and below the electron orbit plane of the DORIS storage ring. The experiment was performed on an iron foil, at the energy corresponding to the K absorption edge.

According to the Stoner's model of magnetism of metals [83], the spin magnetic moment of the atom is related to the imbalance between the number of the spin-up and spin-down valence-band electrons (where the quantisation axis is defined by the direction of the magnetic moment) [84]. Therefore, an experimental determination of the spin-dependent density of final states in the absorption experiment gives an information about the magnetic moment of the absorbing atom.

Two interactions are necessary for the XMCD effect to arise: the spin-orbit coupling and the exchange split in the final band [85]. In the simplified model based on a one-electron picture [84, 86–88], at first the quantum of the circularly polarised x-ray light is absorbed by the electron, which is consequently excited from its initial state. Due to the conservation of angular momentum, the angular momentum of the wave is transferred to the electron. If the initial level is split by the spin-orbit interaction, both the spin and the orbital part of the total angular momentum of the electron are affected in the absorption process¹. Since for one of the states from the spin-orbit split pair the spin \mathbf{S} and orbital angular momentum \mathbf{L} are parallel and in the other one antiparallel, the excited electrons are spin-polarised. The polarisation reverses with the reversal of the light helicity. In the second step of the absorption process, the spin-polarised electron transfers to the valence band, which acts as a spin detector due to the exchange split causing an imbalance in the

¹Otherwise the angular momentum of the photon is transferred purely to the orbital angular momentum of the electron, as the electric field does not act directly on the spin states.

empty spin-up and spin-down states. Summarising, the generation of the spin-polarised electrons together with their detection by the spin-split final band causes dichroism, which is measured in XMCD experiment.

This simple picture of the absorption process is not valid for all the materials and all the absorption edges (for example for the K-edge, where no spin-orbit splitting of the initial level exists), but shows how the use of the circularly polarised light gives an access to the information about the magnetism. More detailed discussion about the XMCD at several absorption edges is given in the next sections of this chapter.

In the first section of this chapter, detailed calculations of the XMCD effect at the $L_{2,3}$ absorption edges of 3d metals are presented. The formalism is presented here for the case of arbitrary mutual orientation between magnetic moment and propagation direction of the EM wave, as well as arbitrary polarisation. This general approach is crucial for further theoretical considerations about the magnetic x-ray standing waves. Secondly, a discussion about the origin of the polarisation dependence of the XMCD signal is given. This is followed by the discussion about the XMCD for the 5d metals and the case of K absorption edge of the 3d metals. Subsequently a short discussion about other, less relevant for the current work absorption edges ($L_{2,3}$ and $M_{3,4}$ in the rare-earths) is presented. Finally, the sum rules allowing a quantitative determination of the atom's spin and orbital magnetic moments from the absorption experiment are presented.

3.1 XMCD at the $L_{2,3}$ absorption edges in the 3d metals

The materials based on the 3d ferromagnetic metals (Fe, Co and Ni) are definitely one of the most important groups of the magnetic materials from the application and fundamental point of view. The magnetism of 3d metals is driven mostly by their d valence electrons. The d-electrons are probed via x-ray absorption experiments at the $L_{2,3}$ absorption edges, that is via investigating the transition from 2p core level to the 3d valence band [84, 86]. $L_{2,3}$ are preferred over the $M_{2,3}$ edges (the transition $3p \rightarrow 3d$), since those resonances are weaker and overlap energetically [86]. The transition $1s \rightarrow 3d$ (L_1 absorption edge) is dipole forbidden.

The 2p electrons have a non-zero orbital angular momentum, so they exhibit a splitting into two substates, $2p_{1/2}$ and $2p_{3/2}$, due to the spin-orbit interaction. The spin-orbit splitting is a relativistic effect describing the coupling of spin \mathbf{S} and orbital angular momentum \mathbf{L} , which form a total angular momentum $\mathbf{J} = \mathbf{L} + \mathbf{S}$ [80]. It can be understood in terms of a simple picture, as an interaction between the spin of the electron and the magnetic field created due to its orbital motion. The strength of the interaction scales with the mutual orientation of spin and orbital angular momentum [89]. The importance of the spin-orbit interaction for the magnetic dichroism was already explained in the introduction to this chapter. Now it will become clear from the rigorous calculations.

3.1.1 Initial and final states

In the case of the 2p level the orbital angular momentum is equal $\ell = 1$ and the electron spin takes the values $s = \frac{1}{2}$, $m_s = \pm\frac{1}{2}$. Therefore, two possible values of the total angular momentum are $j = \frac{1}{2}, \frac{3}{2}$. The projection of the total angular momentum on

the quantisation axis m_j takes the values $-j, \dots, j$. There are two possible initial states $|j, m_j\rangle$ for the $2p_{1/2}$ level: $|\frac{1}{2}, \pm\frac{1}{2}\rangle$ and four for the $2p_{3/2}$ one: $|\frac{3}{2}, \pm\frac{3}{2}\rangle, |\frac{3}{2}, \pm\frac{1}{2}\rangle$.

The initial states are given naturally in the basis $\{|j, m_j\rangle\}$, but in order to easily calculate the matrix elements of the dipole operator represented by spherical harmonics (2.33), a decomposition of those states in the basis $\{|\ell, m_\ell, s, m_s\rangle\}$ is needed. The transformation of the bases is based on the closure relation for the states $|\ell, m_\ell, s, m_s\rangle$ and has the form

$$|j, m_j\rangle = \sum_{m_\ell=-\ell}^{\ell} \sum_{m_s=-s}^s \langle \ell, m_\ell, s, m_s | j, m_j \rangle |\ell, m_\ell, s, m_s\rangle \quad (3.1)$$

The coefficients in this expansion are called Clebsch-Gordan coefficients [71], their values can be found in tables [90].

As an example presenting the principle, consider the decomposition of the state $|\frac{1}{2}, -\frac{1}{2}\rangle$ given in the total angular momentum representation. The terms with non-zero Clebsch-Gordan coefficients (or equivalently the only ones giving the desired $m_j = m_\ell + m_s = -\frac{1}{2}$) are

$$\begin{aligned} |\frac{1}{2}, -\frac{1}{2}\rangle &= \langle 1, 0, \frac{1}{2}, -\frac{1}{2} | \frac{1}{2}, -\frac{1}{2} \rangle |1, 0, \frac{1}{2}, -\frac{1}{2}\rangle + \langle 1, -1, \frac{1}{2}, \frac{1}{2} | \frac{1}{2}, -\frac{1}{2} \rangle |1, -1, \frac{1}{2}, \frac{1}{2}\rangle = \\ &= \frac{1}{\sqrt{3}} |1, 0, \frac{1}{2}, -\frac{1}{2}\rangle - \sqrt{\frac{2}{3}} |1, -1, \frac{1}{2}, \frac{1}{2}\rangle \end{aligned} \quad (3.2)$$

where in the second step the values of the coefficients were written explicitly. The remaining initial states with their decomposition are collected in the table 3.1.

Initial level	State vectors $ j, m_j\rangle$	State vectors $ \ell, m_\ell, s, m_s\rangle$
$2p_{1/2}$	$ \frac{1}{2}, -\frac{1}{2}\rangle$	$\frac{1}{\sqrt{3}} 1, 0, \frac{1}{2}, -\frac{1}{2}\rangle - \sqrt{\frac{2}{3}} 1, -1, \frac{1}{2}, \frac{1}{2}\rangle$
	$ \frac{1}{2}, \frac{1}{2}\rangle$	$-\frac{1}{\sqrt{3}} 1, 0, \frac{1}{2}, \frac{1}{2}\rangle + \sqrt{\frac{2}{3}} 1, 1, \frac{1}{2}, -\frac{1}{2}\rangle$
$2p_{3/2}$	$ \frac{3}{2}, -\frac{3}{2}\rangle$	$ 1, -1, \frac{1}{2}, -\frac{1}{2}\rangle$
	$ \frac{3}{2}, -\frac{1}{2}\rangle$	$\frac{1}{\sqrt{3}} 1, -1, \frac{1}{2}, \frac{1}{2}\rangle + \sqrt{\frac{2}{3}} 1, 0, \frac{1}{2}, -\frac{1}{2}\rangle$
	$ \frac{3}{2}, \frac{1}{2}\rangle$	$\sqrt{\frac{2}{3}} 1, 0, \frac{1}{2}, \frac{1}{2}\rangle + \frac{1}{\sqrt{3}} 1, 1, \frac{1}{2}, -\frac{1}{2}\rangle$
	$ \frac{3}{2}, \frac{3}{2}\rangle$	$ 1, 1, \frac{1}{2}, \frac{1}{2}\rangle$

Table 3.1: The states of the spin-orbit split 2p level in the basis of total angular momentum $\{|j, m_j\rangle\}$ and their decomposition in the basis of orbital angular momentum and spin $\{|\ell, m_\ell, s, m_s\rangle\}$ using the Clebsch-Gordan coefficients. These are the initial states for the transition $2p \rightarrow 3d$ investigated in the absorption experiment at the $L_{2,3}$ absorption edge.

The spin-orbit interaction in the final 3d level is two orders of magnitude smaller than in the 2p level [86], so is neglected hereafter. Possible final states are thus: $|2, -2, \frac{1}{2}, \pm\frac{1}{2}\rangle, |2, -1, \frac{1}{2}, \pm\frac{1}{2}\rangle, |2, 0, \frac{1}{2}, \pm\frac{1}{2}\rangle, |2, 1, \frac{1}{2}, \pm\frac{1}{2}\rangle, |2, 2, \frac{1}{2}, \pm\frac{1}{2}\rangle$.

3.1.2 Geometry of the experiment

Most often a case of parallel alignment of the wave propagation vector \mathbf{k} (and thus its angular momentum) and magnetic moment is considered, since such a situation leads to a maximum of the XMCD signal [80]. Here the general situation of an arbitrary (with respect to the magnetic moment) wave propagation direction is considered instead. The results obtained from such a treatment are more useful for understanding the case of XMCD under the Bragg reflection regime, where waves propagating in different directions exist.

The coordinate system is defined by the magnetic moment, such that it coincides with the $\mathcal{O}z$ axis (figure 3.1). The \mathbf{k} vector direction is parametrised via the spherical coordinates angles ϑ_x and φ_x , so that its coordinates read

$$\mathbf{k} = k \begin{pmatrix} \cos \varphi_x \sin \vartheta_x \\ \sin \varphi_x \sin \vartheta_x \\ \cos \vartheta_x \end{pmatrix} \quad (3.3)$$

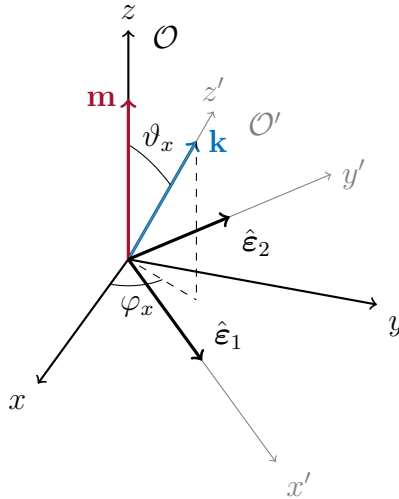


Figure 3.1: The coordinate systems for describing the XMCD experiment, assuming an arbitrary angle between \mathbf{m} and \mathbf{k} vectors. The actual system (\mathcal{O}) is set by the direction of the magnetic moment, since it defines the quantisation axis of the final band — detector of the photoelectron spin. Wavevector \mathbf{k} is defined via spherical coordinates (ϑ_x, φ_x) with respect to the coordinate system \mathcal{O} . It defines the $\mathcal{O}z'$ axis of the new, rotated coordinate system \mathcal{O}' , whose axes $\mathcal{O}x'$ and $\mathcal{O}y'$ contain the polarisation vectors. The concrete directions of the $\mathcal{O}x$ and $\mathcal{O}y$, and thus also $\mathcal{O}x'$ and $\mathcal{O}y'$, are not defined here rigorously. One should note, however, that within the used model, the actual directions of the polarisation unit vectors $\hat{\mathbf{e}}_1$ and $\hat{\mathbf{e}}_2$ are unimportant, as long as the conditions $\hat{\mathbf{e}}_1 \cdot \hat{\mathbf{e}}_2 = 0$, $\hat{\mathbf{e}}_i \cdot \mathbf{k} = 0$, $i \equiv 1, 2$, are fulfilled.

Even though it is known, that the circularly polarised light carries angular momentum, which couples to the angular momentum of the electron and leads to spin-polarised electron emission from the initial level, at this point no restriction on the polarisation vectors is imposed. The EM wave is assumed to have a general form $\mathcal{E} = E_0^a (\varepsilon_1 \hat{\mathbf{e}}_1 + \varepsilon_2 \hat{\mathbf{e}}_2) e^{i\omega t - i\mathbf{k} \cdot \mathbf{r}}$.

In the coordinate system \mathcal{O}' defined by the wave propagation direction \mathbf{k} , the polarisation unit vectors have the coordinates

$$\hat{\boldsymbol{\varepsilon}}'_1 = \begin{pmatrix} 1 \\ 0 \\ 0 \end{pmatrix} \quad \hat{\boldsymbol{\varepsilon}}'_2 = \begin{pmatrix} 0 \\ 1 \\ 0 \end{pmatrix} \quad (3.4)$$

It will become clear from the calculations, that it is the circularly polarised wave with $\varepsilon_1 = \frac{1}{\sqrt{2}}$ and $\varepsilon_2 = \frac{i}{\sqrt{2}}$ that leads to the maximum observable XMCD effect. Following the convention adopted in section 1.9.1, $\varepsilon_1 \in \mathbb{R}$ and the change of helicity is equivalent to transformation $\varepsilon_2 \rightarrow \varepsilon_2^*$.

In order to obtain the coordinates of polarisation vectors in \mathcal{O} , one needs to consider the rotation \mathbf{R} . In particular the system \mathcal{O}' is obtained via two rotations: first by ϑ_x around the axis $\mathcal{O}y$ and then by φ_x around $\mathcal{O}z$. The total rotation matrix reads

$$\begin{aligned} \mathbf{R} = \mathbf{R}_z(\varphi_x)\mathbf{R}_y(\vartheta_x) &= \begin{pmatrix} \cos \varphi_x & -\sin \varphi_x & 0 \\ \sin \varphi_x & \cos \varphi_x & 0 \\ 0 & 0 & 1 \end{pmatrix} \begin{pmatrix} \cos \vartheta_x & 0 & \sin \vartheta_x \\ 0 & 1 & 0 \\ -\sin \vartheta_x & 0 & \cos \vartheta_x \end{pmatrix} = \\ &= \begin{pmatrix} \cos \varphi_x \cos \vartheta_x & -\sin \varphi_x \cos \vartheta_x & \sin \vartheta_x \\ \sin \varphi_x \cos \vartheta_x & \cos \varphi_x \cos \vartheta_x & 0 \\ -\sin \vartheta_x & 0 & \cos \vartheta_x \end{pmatrix} \end{aligned} \quad (3.5)$$

Therefore, the polarisation vectors in \mathcal{O} read

$$\hat{\boldsymbol{\varepsilon}}_1 = \mathbf{R} \begin{pmatrix} 1 \\ 0 \\ 0 \end{pmatrix} = \begin{pmatrix} \cos \varphi_x \cos \vartheta_x \\ \sin \varphi_x \cos \vartheta_x \\ -\sin \vartheta_x \end{pmatrix} \quad (3.6a)$$

$$\hat{\boldsymbol{\varepsilon}}_2 = \mathbf{R} \begin{pmatrix} 0 \\ 1 \\ 0 \end{pmatrix} = \begin{pmatrix} -\sin \varphi_x \\ \cos \varphi_x \\ 0 \end{pmatrix} \quad (3.6b)$$

3.1.3 Transition matrix elements

The electric dipole operator, whose matrix elements determine the absorption cross-section (equation (2.38)) reads for the adopted coordinate system

$$\boldsymbol{\varepsilon}^* \cdot \mathbf{r} = (\varepsilon_1 \cos \varphi_x \cos \vartheta_x - \varepsilon_2^* \sin \varphi_x)x + (\varepsilon_1 \sin \varphi_x \cos \vartheta_x + \varepsilon_2^* \cos \varphi_x)y - \varepsilon_1 \sin \vartheta_x z \quad (3.7)$$

The expressions in brackets standing by the position operators are in fact the coordinates ε_i^* , $i \equiv x, y, z$ of the complex conjugate of the polarisation vector. Now, one expresses the position operators via spherical harmonics (equations (2.32)). This transforms the electric dipole operator to the form

$$\boldsymbol{\varepsilon}^* \cdot \mathbf{r} = \sqrt{\frac{4\pi}{3}}r \left[\frac{1}{\sqrt{2}} (\varepsilon_x^* + i\varepsilon_y^*) Y_1^{-1} + \frac{1}{\sqrt{2}} (-\varepsilon_x^* + i\varepsilon_y^*) Y_1^1 + \varepsilon_z^* Y_1^0 \right] \quad (3.8)$$

Further abbreviations are introduced: $\mathfrak{A} = \varepsilon_x^* + i\varepsilon_y^*$, $\mathfrak{B} = -\varepsilon_x^* + i\varepsilon_y^*$, $\mathfrak{C} = \varepsilon_z^*$. These symbols denote the terms related to the combinations of the polarisation vector components, which appear by the given operator $Y_1^{0,\pm 1}$.

Having the form of the operator, the cross-section can be calculated for the considered initial (2p) and final (3d) states. Since the final states exhibit a spin-split due to the exchange interaction, the excitation of the spin-up and spin-down electrons will be considered separately. The transition rates for such separate cases are denoted by $\zeta^{\uparrow\downarrow}$. Following the formula (2.38), they read

$$\zeta^{\uparrow\downarrow} = \sum_{if} |\langle f, \uparrow\downarrow | \boldsymbol{\epsilon}^* \cdot \mathbf{r} | \phi_i, \uparrow\downarrow \rangle|^2 \quad (3.9)$$

and the total cross-section is equal

$$\sigma = (4\pi)^2 \alpha_f \hbar \omega \left(\zeta^{\uparrow} \varrho_f^{\uparrow} + \zeta^{\downarrow} \varrho_f^{\downarrow} \right) \quad (3.10)$$

The symbols $\varrho_f^{\uparrow\downarrow}$ denote the density of the empty states in the spin-split final 3d band.

As discussed in section 2.2.3, if the initial and final states are written in the position representation, as atomic orbitals, the transition matrix element has the form of the integral (2.33). Using that form, the spin-dependent transition rate reads

$$\zeta^{\uparrow\downarrow} = \frac{4\pi}{3} \mathcal{R} \sum_{if} \left| \langle f, \uparrow\downarrow | \left(\frac{1}{\sqrt{2}} \mathfrak{A} Y_1^{-1} + \frac{1}{\sqrt{2}} \mathfrak{B} Y_1^1 + \mathfrak{C} Y_1^0 \right) | \phi_i, \uparrow\downarrow \rangle \right|^2 \quad (3.11)$$

where in general $\mathcal{R} := \left| \int R_{n_f, \ell_f}^*(r) R_{n_i, \ell_i}(r) r^3 dr \right|^2$. The first radial part of the wavefunction (R) is the one of the final state, whereas the second — of the initial one. In this case a transition $2p \rightarrow 3d$ is considered, what justifies why the radial part of the transition matrix element was factored out from the sum. One can also write, that here $\mathcal{R} = \left| \int R_{3d}^*(r) R_{2p}(r) r^3 dr \right|^2$.

The previous expression can be simplified further by noticing that all mixed terms of the form $\langle f | Y_1^{m_\ell} | \phi_i \rangle \langle \phi_i | Y_1^{m'_\ell} | f \rangle$, $m_\ell \neq m'_\ell$ are zero, due to the electric dipole selection rule $(m_\ell)_f - (m_\ell)_i = m_\ell, m'_\ell$, which is never fulfilled simultaneously for both matrix elements. One has

$$\begin{aligned} \zeta^{\uparrow\downarrow} &= \frac{4\pi}{3} \mathcal{R} \sum_{if} \left(\frac{1}{2} |\mathfrak{A}|^2 |\langle f, \uparrow\downarrow | Y_1^{-1} | \phi_i, \uparrow\downarrow \rangle|^2 + \frac{1}{2} |\mathfrak{B}|^2 |\langle f, \uparrow\downarrow | Y_1^1 | \phi_i, \uparrow\downarrow \rangle|^2 \right. \\ &\quad \left. + |\mathfrak{C}|^2 |\langle f, \uparrow\downarrow | Y_1^0 | \phi_i, \uparrow\downarrow \rangle|^2 \right) = \frac{4\pi}{3} \mathcal{R} \left(\frac{1}{2} |\mathfrak{A}|^2 \mathfrak{a}^{\uparrow\downarrow} + \frac{1}{2} |\mathfrak{B}|^2 \mathfrak{b}^{\uparrow\downarrow} + |\mathfrak{C}|^2 \mathfrak{c}^{\uparrow\downarrow} \right) \end{aligned} \quad (3.12)$$

where the new abbreviations read

$$\begin{aligned} \mathfrak{a}^{\uparrow\downarrow} &= \sum_{if} |\langle f, \uparrow\downarrow | Y_1^{-1} | \phi_i, \uparrow\downarrow \rangle|^2, & \mathfrak{b}^{\uparrow\downarrow} &= \sum_{if} |\langle f, \uparrow\downarrow | Y_1^1 | \phi_i, \uparrow\downarrow \rangle|^2, \\ \mathfrak{c}^{\uparrow\downarrow} &= \sum_{if} |\langle f, \uparrow\downarrow | Y_1^0 | \phi_i, \uparrow\downarrow \rangle|^2 \end{aligned} \quad (3.13)$$

Those quantities are related purely to the initial and final states. The ones marked by capital \mathfrak{A} , \mathfrak{B} and \mathfrak{C} are on the other hand related purely to the polarisation of the incoming wave and its propagation direction. The moduli squared of those, which appear

in equation for partial cross-section, read

$$|\mathfrak{A}|^2 = |\varepsilon_1 \cos \vartheta_x + i\varepsilon_2^*|^2 \quad (3.14a)$$

$$|\mathfrak{B}|^2 = |\varepsilon_1 \cos \vartheta_x - i\varepsilon_2^*|^2 \quad (3.14b)$$

$$|\mathfrak{C}|^2 = \varepsilon_1^2 \sin^2 \vartheta_x \quad (3.14c)$$

One can easily see, that the dependence on the angle φ_x vanished. Therefore, the absorption rate depends only on the mutual orientation of \mathbf{m} and \mathbf{k} vectors (fig. 3.1).

To better understand what happens with \mathfrak{A} and \mathfrak{B} under the helicity reversal (transformation $\varepsilon_2 \rightarrow \varepsilon_2^*$, remember that $\varepsilon_1 \in \mathbb{R}$), one writes the polarisation vector component ε_2 explicitly as $\Re\varepsilon_2 + i\Im\varepsilon_2$. The indices \pm will denote the values before and after the helicity reversal, correspondingly. It follows, that

$$\begin{aligned} |\mathfrak{A}_\pm|^2 &= |\varepsilon_1 \cos \vartheta_x + i(\Re\varepsilon_2 \pm i\Im\varepsilon_2)^*|^2 = |\varepsilon_1 \cos \vartheta_x + i\Re\varepsilon_2 \pm \Im\varepsilon_2|^2 = \\ &= (\varepsilon_1 \cos \vartheta_x \pm \Im\varepsilon_2)^2 + (\Re\varepsilon_2)^2 \end{aligned} \quad (3.15a)$$

$$|\mathfrak{B}_\pm|^2 = (\varepsilon_1 \cos \vartheta_x \mp \Im\varepsilon_2)^2 + (\Re\varepsilon_2)^2 \quad (3.15b)$$

One notices immediately, that the relations $|\mathfrak{A}_+|^2 = |\mathfrak{B}_-|^2$ and $|\mathfrak{A}_-|^2 = |\mathfrak{B}_+|^2$ hold. This fact can be understood by noticing, that the quantity \mathfrak{A} is related to the transition rates involving the operator Y_1^{-1} , whereas \mathfrak{B} is related to Y_1^1 . The first ones fulfil the selection rule $\Delta m_\ell = -1$, the latter $\Delta m_\ell = 1$. The reversal of helicity is equivalent to the reversal of the wave's angular momentum direction (in case of elliptical or circular polarisation), what explains the symmetry in the quantities \mathfrak{A} and \mathfrak{B} .

In order to calculate the strength of the dichroic effect, the measures of the spin-dependent transition rates $\mathfrak{a}^{\uparrow\downarrow}$, $\mathfrak{b}^{\uparrow\downarrow}$ and $\mathfrak{c}^{\uparrow\downarrow}$ need to be evaluated. The integral $\mathcal{I} = \int Y_{\ell_1}^{(m_\ell)_1} Y_{\ell_2}^{(m_\ell)_2} Y_{\ell_3}^{(m_\ell)_3} \sin \vartheta d\vartheta d\varphi$ (introduced by equation (2.33)), which dictated the electric dipole selection rules, is in fact what determines the values of the matrix elements. Its value can be calculated using the formula [71]

$$\mathcal{I} = (-1)^{(m_\ell)_3} \sqrt{\frac{(2\ell_1 + 1)(2\ell_2 + 1)}{4\pi(2\ell_3 + 1)}} \langle \ell_1, 0, \ell_2, 0 | \ell_3, 0 \rangle \langle \ell_1, (m_\ell)_1, \ell_2, (m_\ell)_2 | \ell_3, -(m_\ell)_3 \rangle \quad (3.16)$$

where two terms on the right are Clebsch-Gordan coefficients.

An exemplary matrix element is considered here in details, the remaining transition probabilities are given in figure 3.2. Consider the final state $|2, -2, \frac{1}{2}, \frac{1}{2}\rangle$ and the operator Y_1^{-1} . Keeping in mind the spin selection rule $\Delta m_s = 0$ and the one for orbital angular momentum $\Delta m_\ell = -1$ dictated by this particular operator, the only non-zero matrix element is $\langle 2, -2, \frac{1}{2}, \frac{1}{2} | Y_1^{-1} | 1, -1, \frac{1}{2}, \frac{1}{2} \rangle$. Its value is equal

$$\begin{aligned} \langle 2, -2, \frac{1}{2}, \frac{1}{2} | Y_1^{-1} | 1, -1, \frac{1}{2}, \frac{1}{2} \rangle &= \int (Y_2^{-2})^* Y_1^{-1} Y_1^{-1} \sin \vartheta d\vartheta d\varphi = \int Y_2^2 Y_1^{-1} Y_1^{-1} \sin \vartheta d\vartheta d\varphi = \\ &= -\sqrt{\frac{5}{4\pi}} \langle 2, 0, 1, 0 | 1, 0 \rangle \langle 2, 2, 1, -1 | 1, 1 \rangle = \sqrt{\frac{3}{10\pi}} \end{aligned} \quad (3.17)$$

where the property of the spherical harmonics $(Y_\ell^{m_\ell})^* = (-1)^{m_\ell} Y_\ell^{-m_\ell}$ was used.

Figure 3.2 presents all possible transitions involving the operator Y_1^{-1} , that is fulfilling the condition $\Delta m_\ell = -1$. The transition strengths are calculated by multiplying

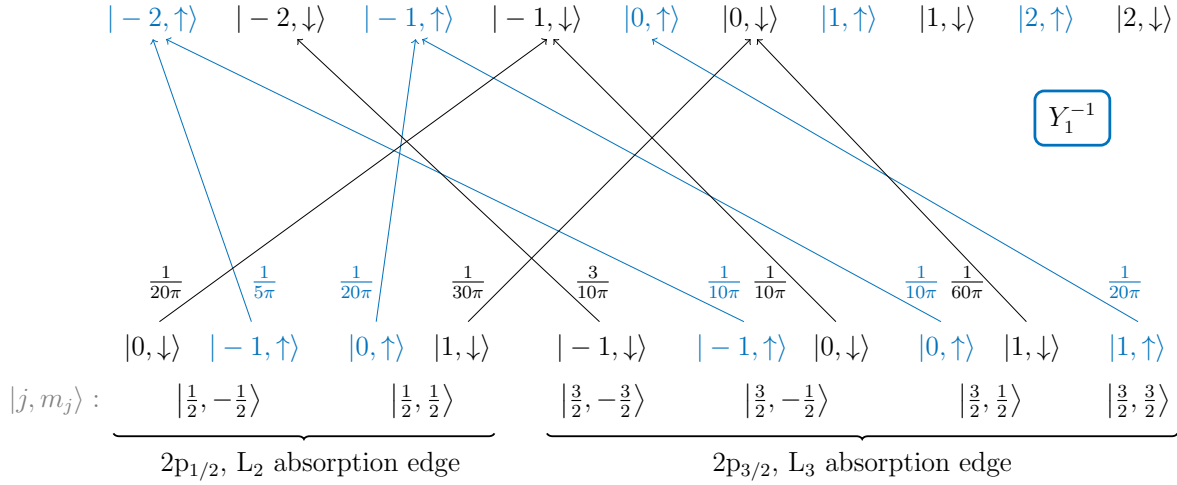


Figure 3.2: Transitions from the 2p to the 3d states fulfilling the selection rule $\Delta m_\ell = -1$. For those transitions the matrix elements of Y_1^{-1} operator are non-zero. The transitions with positive m_s are marked in blue colour for clarity. The transition strengths (written next to the arrows) are given as the modulus squared of the matrix element multiplied by the modulus squared of the coefficient in the expansion of the states $|j, m_j\rangle$ in the $\{|\ell, m_\ell, s, m_s\rangle\}$ basis (see table 3.1). The states in total angular momentum base are depicted at the bottom, for the others the abbreviation $|m_\ell, m_s = \uparrow\downarrow\rangle \equiv |\ell, m_\ell, s, m_s = \uparrow\downarrow\rangle$, where $\uparrow \equiv +\frac{1}{2}, \downarrow \equiv -\frac{1}{2}$, was used. By summing up the spin-up and spin-down contributions, one can notice that the photoelectron excitation is spin-polarised, and this polarisation is opposite for L_2 and L_3 edges.

the modulus squared of the matrix element and the corresponding coefficient from the expansion of the states $|j, m_j\rangle$ in the basis $\{|\ell, m_\ell, s, m_s\rangle\}$ (table 3.1). The summation over the transitions with spin-up and spin-down gives the values of the $\mathbf{a}^{\uparrow\downarrow}$. Depending on the absorption edge they are equal

$$\begin{aligned} \mathbf{a}_{L_2}^\uparrow &= \frac{1}{4\pi} & \mathbf{a}_{L_3}^\uparrow &= \frac{1}{4\pi} \\ \mathbf{a}_{L_2}^\downarrow &= \frac{1}{12\pi} & \mathbf{a}_{L_3}^\downarrow &= \frac{5}{12\pi} \end{aligned} \quad (3.18)$$

These values indicate, that the photoelectron excitation from the spin-orbit split 2p states is spin-polarised. For the $2p_{1/2}$ states, 3/4 of the transitions correspond to the excitation of spin-up electron, in case of $2p_{3/2}$ it is 3/8 of all transitions. Thus, the spin-polarisation of the emission is reversed for those two cases. Note, that if there was no spin-orbit splitting of the 2p states, the probabilities of the excitation of spin-up and spin-down electron would be the same ($\mathbf{a}_{L_2}^\uparrow + \mathbf{a}_{L_3}^\uparrow = \mathbf{a}_{L_2}^\downarrow + \mathbf{a}_{L_3}^\downarrow = \frac{1}{2\pi}$). It is the energy separation between the L_2 and L_3 absorption edges, what allows to generate the spin-polarised electrons.

Now consider the transitions involving the operator Y_1^1 , that is those fulfilling $\Delta m_\ell = 1$. The diagram analogous to the one in figure 3.2, showing the possible transitions, is presented in appendix B.1. Following figure, values of the coefficients $\mathbf{b}^{\uparrow\downarrow}$ are

$$\begin{aligned} \mathbf{b}_{L_2}^\uparrow &= \frac{1}{12\pi} & \mathbf{b}_{L_3}^\uparrow &= \frac{5}{12\pi} \\ \mathbf{b}_{L_2}^\downarrow &= \frac{1}{4\pi} & \mathbf{b}_{L_3}^\downarrow &= \frac{1}{4\pi} \end{aligned} \quad (3.19)$$

Similarly, like in the case of $\Delta m_\ell = -1$ transitions, also now the spin-polarisation is observed. It can be noticed, that with respect to $\mathbf{a}^{\uparrow\downarrow}$, the values of $\mathbf{b}^{\uparrow\downarrow}$ are reversed, or

$$\mathbf{a}^\uparrow = \mathbf{b}^\downarrow, \quad \mathbf{a}^\downarrow = \mathbf{b}^\uparrow \quad (3.20)$$

As it is shown at the end of this paragraph, if the perfect circular polarisation and the case of $\mathbf{k} \parallel \mathbf{m}$ (standard XMCD geometry) are considered, the transitions fulfilling $\Delta m_\ell = -1$ (described by \mathbf{a}) are the ones induced by the wave with one helicity, and the ones for which $\Delta m_\ell = 1$ (\mathbf{b}) — with the other. Thus, the result (3.20) indicates, that the reversal of the wave helicity (what is equivalent to the reversal of the direction of angular momentum) leads to the reversal of the spin-polarisation of the excited photoelectrons. This fact opens up a possibility for observing a dichroism in absorption of circularly or elliptically polarised light.

The remaining term in the expression (3.12) is the one related to Y_1^0 . The diagram showing the transitions involving this operator ($\Delta m_\ell = 0$) is also shown in appendix B.1 (figure B.2). Following the values depicted there, the coefficients $\mathbf{c}^{\uparrow\downarrow}$ read

$$\begin{aligned} \mathbf{c}_{L_2}^\uparrow &= \frac{1}{6\pi} & \mathbf{c}_{L_3}^\uparrow &= \frac{1}{3\pi} \\ \mathbf{c}_{L_2}^\downarrow &= \frac{1}{6\pi} & \mathbf{c}_{L_3}^\downarrow &= \frac{1}{3\pi} \end{aligned} \quad (3.21)$$

Concluding, the transitions in which no angular momentum of the light is transferred to the electrons, exhibit no spin-polarisation.

3.1.4 XMCD signal

Having noticed, that the spin-polarisation of the excited electrons changes upon the change of the wave's angular momentum, that is the change of helicity, the next step is to consider the difference between the cross-sections upon the helicity reversal. In order to discard the constants, one considers rather the normalised difference [89]. Even though most often the dichroic signal is defined as $\Xi = (\sigma_+ - \sigma_-)/(\sigma_+ + \sigma_-)$ [77, 86, 89], the authors use different sign convention for the phase of the wave ($-i\omega t$) than used in this work. In order to keep the quantitative results consistent with the literature, here the XMCD signal is defined as

$$\Xi = \frac{\sigma_- - \sigma_+}{\sigma_- + \sigma_+} \quad (3.22)$$

Following equations (3.10) and (3.12), as well as using the fact that $\mathbf{c}^\uparrow = \mathbf{c}^\downarrow$ and $|\mathcal{C}|^2$ does not change upon the helicity reversal, one can write

$$\begin{aligned} \Xi &= \left\{ \varrho_f^\uparrow \left[\frac{1}{2} \mathbf{a}^\uparrow (|\mathfrak{A}_-|^2 - |\mathfrak{A}_+|^2) + \frac{1}{2} \mathbf{b}^\uparrow (|\mathfrak{B}_-|^2 - |\mathfrak{B}_+|^2) \right] + \right. \\ &\quad \left. + \varrho_f^\downarrow \left[\frac{1}{2} \mathbf{a}^\downarrow (|\mathfrak{A}_-|^2 - |\mathfrak{A}_+|^2) + \frac{1}{2} \mathbf{b}^\downarrow (|\mathfrak{B}_-|^2 - |\mathfrak{B}_+|^2) \right] \right\} \cdot \\ &\quad \cdot \left\{ \varrho_f^\uparrow \left[\frac{1}{2} \mathbf{a}^\uparrow (|\mathfrak{A}_-|^2 + |\mathfrak{A}_+|^2) + \frac{1}{2} \mathbf{b}^\uparrow (|\mathfrak{B}_-|^2 + |\mathfrak{B}_+|^2) + 2\mathbf{c}|\mathcal{C}|^2 \right] + \right. \\ &\quad \left. + \varrho_f^\downarrow \left[\frac{1}{2} \mathbf{a}^\downarrow (|\mathfrak{A}_-|^2 + |\mathfrak{A}_+|^2) + \frac{1}{2} \mathbf{b}^\downarrow (|\mathfrak{B}_-|^2 + |\mathfrak{B}_+|^2) + 2\mathbf{c}|\mathcal{C}|^2 \right] \right\}^{-1} \quad (3.23) \end{aligned}$$

Now, one evaluates the expressions in the round brackets. Due to the symmetry between the quantities $|\mathfrak{A}_\pm|^2$ and $|\mathfrak{B}_\pm|^2$ (see equations (3.15)), the relations $|\mathfrak{A}_-|^2 - |\mathfrak{A}_+|^2 = |\mathfrak{B}_+|^2 - |\mathfrak{B}_-|^2$ and $|\mathfrak{A}_-|^2 + |\mathfrak{A}_+|^2 = |\mathfrak{B}_-|^2 + |\mathfrak{B}_+|^2$ hold. The combination of $|\mathfrak{A}_\pm|^2$ and $|\mathfrak{B}_\pm|^2$ from the numerator reads

$$|\mathfrak{A}_-|^2 - |\mathfrak{A}_+|^2 = -4\varepsilon_1 \Im \varepsilon_2 \cos \vartheta_x \quad (3.24)$$

whereas the one from the denominator is equal to

$$|\mathfrak{A}_-|^2 + |\mathfrak{A}_+|^2 = 2 (\varepsilon_1^2 \cos^2 \vartheta_x + |\varepsilon_2|^2) \quad (3.25)$$

From the values of the coefficients $\mathfrak{a}^{\uparrow\downarrow}$, $\mathfrak{b}^{\uparrow\downarrow}$ and \mathfrak{c} (equations (3.18), (3.19), (3.21)) one can see, that for each absorption edge

$$\mathfrak{a}^\uparrow + \mathfrak{a}^\downarrow = \mathfrak{b}^\uparrow + \mathfrak{b}^\downarrow = 2\mathfrak{c} \quad (3.26)$$

This fact can be seen as a manifestation of the results' independence from the choice of the coordinate system. If no spin-dependent detection appears in the experiment, there should be no difference in absorption strength for transitions associated with Y_1^{-1} , Y_1^1 or Y_1^0 . The form of the combination of those present in the cross-section formula depends on the choice of coordinate system.

Using the relation (3.20), the following expression appears in the denominator

$$\frac{1}{2} (|\mathfrak{A}_-|^2 + |\mathfrak{A}_+|^2) + |\mathfrak{c}|^2 = \varepsilon_1^2 + |\varepsilon_2|^2 = 1 \quad (3.27)$$

since it is assumed that the polarisation vector components of the incoming wave are normalised. With that, the XMCD signal reads

$$\Xi = 2\varepsilon_1 \Im \varepsilon_2 \underbrace{\frac{(\varrho_f^\uparrow - \varrho_f^\downarrow)}{(\varrho_f^\uparrow + \varrho_f^\downarrow)}}_{\Pi_\gamma} \underbrace{\frac{(\mathfrak{a}^\downarrow - \mathfrak{a}^\uparrow)}{(\mathfrak{a}^\downarrow + \mathfrak{a}^\uparrow)}}_{\Pi_e^s} \cos \vartheta_x \quad (3.28)$$

Four important terms influence the final value of the XMCD signal. Π_γ is the circular polarisation degree. $\Delta\varrho_f^s := \varrho_f^\uparrow - \varrho_f^\downarrow$ is the absolute imbalance between the density of unoccupied states in the final band with spin-up and spin-down. The normalised quantity $\Delta\varrho_f^s/\varrho_f$, $\varrho_f = \varrho_f^\uparrow + \varrho_f^\downarrow$ is the spin-polarisation of the final band. Π_e^s denotes the photoelectron polarisation. Finally, the term $\cos \vartheta_x$ accounts for the geometrical conditions in the experiment, $\vartheta_x = \angle(\mathbf{m}, \mathbf{k})$.

The term Π_γ is discussed in more details in the next section. Particularly, it is shown there, that indeed it denotes a degree of circular polarisation. At this point one can already notice, that for any linear polarisation $\Xi = 0$, because for such a wave there is no phase shift between polarisation unit vectors $\hat{\mathbf{e}}_1$ and $\hat{\mathbf{e}}_2$, so $\Im \varepsilon_2 = 0$ and the XMCD signal vanishes. This is obvious, since linearly polarised light carries no angular momentum, so it cannot induce a spin-polarised electron excitation, which is the key mechanism leading to the dichroism in absorption. Only circularly or elliptically polarised light gives rise to an XMCD signal.

Spin-polarisation of the final band takes the values from 0 (no polarisation, $\varrho_f^\uparrow = \varrho_f^\downarrow = \frac{1}{2}\varrho_f$) to 1 (full polarisation, $\varrho_f^\uparrow = \varrho_f$), assuming that "↑" denotes the minority

spin (thus majority of the holes have the spin-up and the magnetic moment is parallel to $\mathcal{O}z$). As mentioned already at the beginning, the spin-polarised final band serves as a detector for the spin-polarised electrons excited by the EM wave. If the final band is unpolarised, no dichroism is observed. What is more, $\Delta\varrho_f^s$ is directly related to the spin magnetic moment of the atom. The energy integral of the spin-dependent density of states gives a number of the holes with up- (N_h^\uparrow) and down-spin (N_h^\downarrow). According to the Stoner model of metals magnetism [80,83], the magnitude of the magnetic moment is given as a difference in the number of electrons or holes with a given spin state in the final band

$$m = \mu_B (N_e^\downarrow - N_e^\uparrow) = \mu_B (N_h^\uparrow - N_h^\downarrow) \quad (3.29)$$

where μ_B is a Bohr magneton and the relation between the density of states and number of holes reads

$$N_h^{\uparrow\downarrow} = \int_{\mathcal{E}_F}^{\infty} \varrho_f^{\uparrow\downarrow} d\mathcal{E} \quad (3.30)$$

where \mathcal{E}_F denotes the Fermi energy, that is the energy of the highest occupied state. The equivalence between the differences in number of electrons and holes in (3.29) exists, since the maximum number of electrons in a given shell N_{total} is fixed, and $N_h + N_e = N_{\text{total}}$. For example, for 3d band one has $N_h^\uparrow + N_e^\uparrow = 5$ and $N_h^\downarrow + N_e^\downarrow = 5$. The relation of the magnetic moment to the number of holes is useful, since it is the density of final empty states, what determines the absorption cross-section measured in spectroscopy experiments.

The photoelectron-polarisation is another prerequisite for the dichroism to appear. The value of this quantity is characteristic of a given transition. In case of the considered $2p \rightarrow 3d$ transition, for the L_2 absorption edge $\Pi_e^s = -\frac{1}{2}$ and for the L_3 $\Pi_e^s = \frac{1}{4}$. As it was already discussed, it is the spin-orbit interaction what gives non-zero values of Π_e^s . Notice, that the sign of the photoelectron polarisation is opposite for $2p_{1/2}$ and $2p_{3/2}$, and the number of $2p_{3/2}$ is twice that of $2p_{1/2}$ ones. Thus, without the energy separation between the levels, the electron polarisation would vanish, and so would also the XMCD signal.

The cosine term ($\cos\vartheta_x$) is responsible for scaling the signal with the projection of the photon angular momentum on the quantisation axis (direction of the magnetic moment). The electrons emitted from the initial level are spin-polarised in the direction of the wave propagation. The spin-polarisation of the final band (which serves as a detector for the electrons) is on the other hand given by the direction of the magnetic moment. Therefore, the strongest XMCD effect is observed if those two directions coincide. The signal vanishes if \mathbf{m} and \mathbf{k} are perpendicular to each other ($\cos\vartheta_x = 0$).

At the end one analyses the case of an ideally circularly polarised incoming wave and $\vartheta_x = 0$ ($\mathbf{k} \parallel \mathbf{m}$), as this case is often of the particular interest. Using the decomposition (1.49) one can show easily, that the function $\Pi_\gamma(\beta, \delta) = 2 \cos\beta \sin\beta \sin\delta$ has an extremum if and only if $\sin\delta = 0 \wedge \sin 2\beta = 0$ or $\cos\delta = 0 \wedge \cos 2\beta = 0$. The first case corresponds to linear polarisation, which leads to $\Xi = 0$, so is discarded. The second set of equations yields the values of β and δ for the circular polarisation. The polarisation vector components are $\varepsilon_1 = \frac{1}{\sqrt{2}}$ and $\varepsilon_2 = \frac{i}{\sqrt{2}}$. The polarisation rate is maximal and is equal to one. The polarisation-related quantities read $|\mathfrak{A}_+|^2 = |\mathfrak{B}_-|^2 = 2$ and

$|\mathfrak{A}_-|^2 = |\mathfrak{B}_+|^2 = |\mathfrak{C}|^2 = 0$. The cross-section has, therefore, a simple form

$$\sigma_{\pm} = \frac{(4\pi)^3}{3} \alpha_f \hbar \omega \mathcal{R} \sum_{\uparrow\downarrow} \sum_{if} \varrho_f^{\uparrow\downarrow} |\langle f, \uparrow\downarrow | Y_1^{\mp 1} | \phi_i, \uparrow\downarrow \rangle|^2 \quad (3.31)$$

This result shows that the transitions described by \mathfrak{a} and related to the operator Y_1^{-1} are induced by the light with one helicity (RHP), and the ones whose strength is given by \mathfrak{b} (related to Y_1^1) — with the other (LHP). This explains the symmetry in the \mathfrak{a} and \mathfrak{b} quantities (3.20), since the reversal of the light helicity is equivalent to the reversal of the angular momentum of the wave and thus the direction of the spin-polarisation of the electrons. This discussion also justifies, that the reversal of the orientation of the quantisation axis (that is the orientation of the magnetic moment), keeping the helicity fixed, leads to the same effect as a reversal of helicity. In such a case the spin-polarisation direction of the excited electrons stays the same, but the polarisation of the final band, which detects the electrons, changes.

The fact that the reversal of the magnetic moment direction is equivalent to the reversal of helicity can be shown also rigorously. Looking at figure 3.1, one can see that if the direction of the $\mathcal{O}z$ axis was reversed, the angle between the magnetic moment and the propagation direction would be equal to $\pi - \vartheta_x$. Since it was proven that the angle φ_x does not influence the final results, the reversal of magnetic moment direction can be introduced in the formalism by the transformation $\vartheta_x \rightarrow \pi - \vartheta_x$. This imposes a change on the wave-related quantities \mathfrak{A} , \mathfrak{B} and \mathfrak{C} , whose moduli enter the expression for the cross-section. $|\mathfrak{C}|^2$ does not change under the considered transformation, as it contains only $\sin^2 \vartheta_x$. Affected are the values of $|\mathfrak{A}|^2$ and $|\mathfrak{B}|^2$, in which the term $\cos \vartheta_x$ changes the sign under the reversal of the magnetic moment. As expected, this leads to the transformation $\mathfrak{A} \leftrightarrow \mathfrak{B}$ (see equations (3.15)). Instead of considering the XMCD signal as a difference between the cross-sections for different helicities, the difference between two opposite magnetic moment orientations can be considered. This can be written formally as

$$\begin{aligned} \Xi_{\mathbf{m}} = \frac{\sigma_+^{-\mathbf{m}} - \sigma_+^{+\mathbf{m}}}{\sigma_+^{-\mathbf{m}} + \sigma_+^{+\mathbf{m}}} = & \left\{ \varrho_f^{\uparrow} \left[\frac{1}{2} \mathfrak{a}^{\uparrow} (|\mathfrak{A}_+^{-\mathbf{m}}|^2 - |\mathfrak{A}_+^{+\mathbf{m}}|^2) + \frac{1}{2} \mathfrak{b}^{\uparrow} (|\mathfrak{B}_+^{-\mathbf{m}}|^2 - |\mathfrak{B}_+^{+\mathbf{m}}|^2) \right] + \right. \\ & \left. + \varrho_f^{\downarrow} \left[\frac{1}{2} \mathfrak{a}^{\downarrow} (|\mathfrak{A}_+^{-\mathbf{m}}|^2 - |\mathfrak{A}_+^{+\mathbf{m}}|^2) + \frac{1}{2} \mathfrak{b}^{\downarrow} (|\mathfrak{B}_+^{-\mathbf{m}}|^2 - |\mathfrak{B}_+^{+\mathbf{m}}|^2) \right] \right\} \cdot \\ & \cdot \left\{ \varrho_f^{\uparrow} \left[\frac{1}{2} \mathfrak{a}^{\uparrow} (|\mathfrak{A}_+^{-\mathbf{m}}|^2 + |\mathfrak{A}_+^{+\mathbf{m}}|^2) + \frac{1}{2} \mathfrak{b}^{\uparrow} (|\mathfrak{B}_+^{-\mathbf{m}}|^2 + |\mathfrak{B}_+^{+\mathbf{m}}|^2) + 2\mathfrak{c}|\mathfrak{C}|^2 \right] + \right. \\ & \left. + \varrho_f^{\downarrow} \left[\frac{1}{2} \mathfrak{a}^{\downarrow} (|\mathfrak{A}_+^{-\mathbf{m}}|^2 + |\mathfrak{A}_+^{+\mathbf{m}}|^2) + \frac{1}{2} \mathfrak{b}^{\downarrow} (|\mathfrak{B}_+^{-\mathbf{m}}|^2 + |\mathfrak{B}_+^{+\mathbf{m}}|^2) + 2\mathfrak{c}|\mathfrak{C}|^2 \right] \right\}^{-1} \quad (3.32) \end{aligned}$$

Now one can transform the “ $-\mathbf{m}$ ” quantities using $|\mathfrak{A}_+^{-\mathbf{m}}|^2 = |\mathfrak{B}_+^{+\mathbf{m}}|^2 = |\mathfrak{A}_+^{+\mathbf{m}}|^2$ and $|\mathfrak{B}_+^{-\mathbf{m}}|^2 = |\mathfrak{A}_+^{+\mathbf{m}}|^2 = |\mathfrak{B}_+^{+\mathbf{m}}|^2$. This leads immediately to the same formula for the XMCD signal, as the one obtained by considering the difference in cross-sections for opposite helicities (equation (3.23)). This is a rigorous proof, that reversal of helicity is equivalent to reversal of the magnetic moment direction, so that $\Xi = \Xi_{\mathbf{m}}$.

Even though in the energy range of hard x-rays, typically spin-polarised electrons with negligible orbital angular momentum are probed [89], at the end one should give a comment on the contribution to the magnetic dichroism of the orbital-polarisation in the final

states. By orbital-polarisation one understands an imbalance in the density of the empty final states with magnetic quantum numbers m_ℓ and $-m_\ell$ [80]. Aside of spin-polarisation, the contribution of orbital one is significant for the case of soft x-ray resonances, such as $L_{2,3}$ absorption edges of 3d metals. The two-step model of absorption considered earlier can be extended to include the orbital-polarisation. The angular momentum transferred from the photon is carried by the photoelectron partly as spin and orbital angular momentum degrees of freedom, due to the spin-orbit splitting of the initial state. For the considered $L_{2,3}$ absorption edges, one can calculate the orbital-polarisation of the excited photoelectrons in a similar manner as it is done for the spin-polarisation. The orbital polarisation can be defined analogously as a sum over the possible final state magnetic quantum numbers

$$\Pi_e^\ell = \frac{1}{2} \left(\sum_{m_\ell=-\ell}^{\ell} m_\ell \sum_{if} |\langle f_{m_\ell} | Y_1^{\pm 1,0} | \phi_i \rangle|^2 \right) \left(\sum_{if} |\langle f_{m_\ell} | Y_1^{\pm 1,0} | \phi_i \rangle|^2 \right)^{-1} \quad (3.33)$$

The sum over the initial and final states is a quantity similar to the spin-dependent quantities **a**, **b** and **c**, where the states with given spin ($\pm 1/2$) were considered, but now it comprises only the final states distinguished by the quantum number m_ℓ , denoted here by $|f_{m_\ell}\rangle$. It gives the overall transition strength for the transitions leading to the given value of m_ℓ . The orbital-polarisation is calculated separately for the operators $Y_1^{\pm 1,0}$.

One can check using figure 3.2 (and the ones in appendix — B.1 and B.2), that the orbital polarisation for the transitions involving the operators $Y_1^{\pm 1}$ is equal 3/4, regardless of the absorption edge (and reverses the sign under the reversal of the helicity, just like the electron spin-polarisation). For the transitions where no orbital angular momentum is transferred from the photon, no orbital-polarisation of the electron appears.

Similarly like in the case of photoelectron spin, the orbital angular momentum of the excited electron can be detected by the orbital-polarised final band. Skipping the detailed derivation given elsewhere [89], one can write the total XMCD signal, as a sum of the spin and orbital angular momentum contributions

$$\Xi = \left(\frac{\Delta \varrho_f^s}{\varrho_f} \Pi_e^s + \frac{6}{\ell_f(\ell_f + 1)} \frac{\Delta \varrho_f^\ell}{\varrho_f} \Pi_e^\ell \right) \Pi_\gamma \cos \vartheta_x \quad (3.34)$$

where the first term in the sum in the brackets is the original, spin-polarisation related part. The orbital-polarised density of states is defined via the sum

$$\Delta \varrho_f^\ell = \sum_{m_\ell=-\ell}^{\ell} m_\ell \varrho_{m_\ell} \quad (3.35)$$

with ϱ_{m_ℓ} being densities of m_ℓ projected substates. Again, to observe the XMCD signal coming from the electron orbital-polarisation, the final band has to exhibit non-zero polarisation $\Delta \varrho_f^\ell$.

3.1.5 Degree of polarisation of the wave

In this section it is shown, that $\Pi_\gamma = 2\varepsilon_1 \mathfrak{S} \varepsilon_2$ is a degree of circular polarisation of a single plane EM wave propagating along the $\mathcal{O}z$ axis, with polarisation given by the

polarisation vector components ε_1 and ε_2 . On the other hand, the cosine term appears, when one calculates the degree of circular polarisation *projected* on an ideal propagation direction that is parallel to the magnetic moment. It is important for further considerations to proof rigorously, that the XMCD signal is directly proportional to such a degree of circular polarisation.

As defined by Jackson [55], the circular polarisation rate reads

$$\Pi_{circ} = \frac{|\hat{\boldsymbol{\varepsilon}}_{rhp}^* \cdot \boldsymbol{\mathcal{E}}|^2 - |\hat{\boldsymbol{\varepsilon}}_{lhp}^* \cdot \boldsymbol{\mathcal{E}}|^2}{|\hat{\boldsymbol{\varepsilon}}_{rhp}^* \cdot \boldsymbol{\mathcal{E}}|^2 + |\hat{\boldsymbol{\varepsilon}}_{lhp}^* \cdot \boldsymbol{\mathcal{E}}|^2 + |\hat{\boldsymbol{\varepsilon}}_0^* \cdot \boldsymbol{\mathcal{E}}|^2} \quad (3.36)$$

The terms $|\hat{\boldsymbol{\varepsilon}}_{rhp}^* \cdot \boldsymbol{\mathcal{E}}|^2$ and $|\hat{\boldsymbol{\varepsilon}}_{lhp}^* \cdot \boldsymbol{\mathcal{E}}|^2$ denote the intensities of the right-handed circularly and left-handed circularly polarised waves propagating in the direction perpendicular to the unit vectors $\hat{\boldsymbol{\varepsilon}}_{rhp}$ and $\hat{\boldsymbol{\varepsilon}}_{lhp}$. $|\hat{\boldsymbol{\varepsilon}}_0^* \cdot \boldsymbol{\mathcal{E}}|^2$ is a remaining intensity, that is an intensity of the wave with a polarisation vector $\hat{\boldsymbol{\varepsilon}}_0$ being perpendicular to both $\hat{\boldsymbol{\varepsilon}}_{rhp}$ and $\hat{\boldsymbol{\varepsilon}}_{lhp}$ [55]. If one is interested in the degree of circular polarisation in the direction of propagation (standard situation), this last term vanishes, as the EM wave is a transverse one. In the considered situation, however, one is interested in the degree of polarisation in the direction of the magnetic moment. A wave propagates in a different direction and the component $|\hat{\boldsymbol{\varepsilon}}_0^* \cdot \boldsymbol{\mathcal{E}}|^2$ is non-zero.

Using the discussed scalar products and choosing the unit vectors appropriately, one can analyse the polarisation composition of the wave in any direction.

A general case of the wave propagating in arbitrary direction is considered. Using the components of the polarisation vectors in the \mathcal{O} coordinate system, the wave has the form

$$\boldsymbol{\mathcal{E}} = [\varepsilon_1 (\cos \vartheta_x \hat{\boldsymbol{x}} + \sin \vartheta_x \cos \vartheta_x \hat{\boldsymbol{y}} - \sin \vartheta_x \hat{\boldsymbol{z}}) + \varepsilon_2 (-\sin \vartheta_x \hat{\boldsymbol{x}} + \cos \vartheta_x \hat{\boldsymbol{y}})] e^{i\omega t - i\mathbf{k} \cdot \mathbf{r}} \quad (3.37)$$

The quantisation axis of the spin-polarised final band is fixed by the direction of the magnetic moment. It is this direction in which the angular momentum of the light should be aligned. Therefore, the degree of circular polarisation considered in this direction is governing the strength of the XMCD. One can obtain the *content* of the desired polarisation in the arbitrary incoming wave, by assuming the following forms of the circular polarisation unit vectors

$$\hat{\boldsymbol{\varepsilon}}_{rhp} = \frac{1}{\sqrt{2}} (\hat{\boldsymbol{x}} + i\hat{\boldsymbol{y}}) \quad (3.38a)$$

$$\hat{\boldsymbol{\varepsilon}}_{lhp} = \frac{1}{\sqrt{2}} (\hat{\boldsymbol{x}} - i\hat{\boldsymbol{y}}) \quad (3.38b)$$

The component of the wave propagating in the $x\mathcal{O}y$ plane is unimportant for the XMCD effect, but of course contributes to the total intensity of the wave, and thus enters the denominator of (3.36). Its intensity can be obtained via the polarisation vector $\hat{\boldsymbol{\varepsilon}}_0 = \hat{\boldsymbol{z}}$.

The intensities appearing in the formula for the polarisation degree read

$$|\hat{\boldsymbol{\varepsilon}}_{rhp}^* \cdot \boldsymbol{\mathcal{E}}|^2 = \frac{1}{2} [(\varepsilon_1 \cos \vartheta_x + \Im \varepsilon_2)^2 + (\Re \varepsilon_2)^2] \quad (3.39a)$$

$$|\hat{\boldsymbol{\varepsilon}}_{lhp}^* \cdot \boldsymbol{\mathcal{E}}|^2 = \frac{1}{2} [(\varepsilon_1 \cos \vartheta_x - \Im \varepsilon_2)^2 + (\Re \varepsilon_2)^2] \quad (3.39b)$$

$$|\hat{\boldsymbol{\varepsilon}}_0^* \cdot \boldsymbol{\mathcal{E}}|^2 = \varepsilon_1^2 \sin^2 \vartheta_x \quad (3.39c)$$

and the polarisation degree itself

$$\Pi_{circ} = 2\varepsilon_1 \Im \varepsilon_2 \cos \vartheta_x \quad (3.40)$$

The first term, that is $2\varepsilon_1 \Im \varepsilon_2$ can be regarded as a circular polarisation degree in the propagation direction. The cosine term performs a projection on a chosen direction of interest. Overall, Π_{circ} gives the information on the content of the circularly polarised wave propagating in a chosen direction.

As expected, $\Pi_{circ} = \Pi_\gamma \cos \vartheta_x$.

One can note, that the quantities $|\mathfrak{A}|^2$, $|\mathfrak{B}|^2$ and $|\mathfrak{C}|^2$ are in fact the intensities of the components of the incoming wave. One notices, that $|\mathfrak{A}_\pm|^2 = 2|\hat{\mathbf{e}}_{rhp}^* \cdot \boldsymbol{\mathcal{E}}_\pm|^2$, $|\mathfrak{B}_\pm|^2 = 2|\hat{\mathbf{e}}_{lhp}^* \cdot \boldsymbol{\mathcal{E}}_\pm|^2$ and $|\mathfrak{C}|^2 = |\hat{\mathbf{e}}_0^* \cdot \boldsymbol{\mathcal{E}}_\pm|^2$.

3.2 XMCD at the $L_{2,3}$ absorption edges in the 5d metals

The general formula for Ξ , which is important for the further considerations, was already obtained in the previous paragraph. In particular, it was shown, that the XMCD signal is driven by a few factors: $\Xi = \Pi_\gamma \Pi_e^s \cos \vartheta_x \Delta \varrho_f^s / \varrho_f$. Among them only the photoelectron polarisation Π_e^s depends on the considered transition, that is the investigated system and the absorption edge. To describe the XMCD effect at other absorption edges and for other systems, all one needs to evaluate is Π_e^s and Π_e^ℓ , the latter in case of significant contribution from orbital polarisation. In this and the following paragraphs only a short discussion about the origin of the photoelectron polarisation for other systems than 3d metals, and other absorption edges, is given.

The simple two-step model in one-electron picture considered for the transitions at the $L_{2,3}$ absorption edges of the 3d metals explains also well the absorption process at the $L_{2,3}$ edges of the 5d metals [89]. Also in this case a combination of the strong spin-orbit coupling in the initial 2p state and the exchange-split of the 5d band responsible for magnetism leads to the dichroism in absorption of circularly polarised x-rays. Since the transition here is 2p \rightarrow 5d, the calculations lead to the same values of the photoelectron polarisation $\Pi_e^s = -\frac{1}{2}, \frac{1}{4}$, for the L_2 and L_3 edges respectively (the principal quantum number enters the formalism only in the radial integral, which does not influence the final result).

Magnetic moments of the 5d metals impurities in iron matrix were studied experimentally by Schütz *et al.* [91]. The values of the magnetic moments calculated based on the simple two-step model of XMCD were reported to be in a good agreement with theoretical predictions based on relativistic multiple scattering Green function formalism [92]. This formalism was also used to validate the assumptions of the two-step model, what showed that it remains a good approximation in the case of 5d metals.

It should be noted, that the 5d ions are non-magnetic as pure metals, their magnetic moment is induced by the proximity of the magnetic ions in compounds and alloys. It was also reported, that 4d and 5d pure metals may exhibit magnetism in systems with reduced dimensions like nanoparticles [93].

3.3 XMCD at the K absorption edge in the 3d metals

The case of the XMCD at the K absorption edge of the 3d metals lies also in the region of interest for the research with hard x-rays. It is, however, much more challenging for interpretation, since the assumptions of the simple two-step model are not directly fulfilled. Orbital-polarisation, unlike the spin one at the $L_{2,3}$ absorption edges, plays a vital role in understanding the emergence of the dichroism at the K absorption edge. It should be also noted, that at the K resonance one does not probe directly the 3d bands, which are the ones responsible for magnetism in those systems.

Keeping in mind the electric-dipole selection rules, the transition taking place during the absorption process at the K absorption edge is from the 1s states to the empty 4p states. The 1s orbital has no orbital angular momentum ($\ell = 0$), so no spin-orbit splitting of this state exists. Therefore, the first assumption of the two-step model is not fulfilled, and the dichroism must arise due to different interactions. A small Zeeman splitting into otherwise degenerate states with $m_s = \pm\frac{1}{2}$ due to the external or exchange magnetic field exists in the initial 1s state. Additionally, in contrast to the $L_{2,3}$ absorption edges, one considers a spin-orbit splitting of the final state. The exchange interaction leads also to the splitting of the spin-orbit coupled $4p_{1/2}$ and $4p_{3/2}$ states [80].

One considers the same one-electron picture as earlier. The following matrix elements are non-zero in this case: $\langle 1, -1, \frac{1}{2}, \pm\frac{1}{2} | Y_1^{-1} | 0, 0, \frac{1}{2}, \pm\frac{1}{2} \rangle$, $\langle 1, 0, \frac{1}{2}, \pm\frac{1}{2} | Y_1^0 | 0, 0, \frac{1}{2}, \pm\frac{1}{2} \rangle$, $\langle 1, 1, \frac{1}{2}, \pm\frac{1}{2} | Y_1^1 | 0, 0, \frac{1}{2}, \pm\frac{1}{2} \rangle$. They can be calculated using the integral representation, and then the Clebsch-Gordan coefficients (equation (3.16)). Then, since the final state is spin-orbit split, one has to consider the decomposition given in the table 3.1. Keeping in mind, that the electric-dipole operator cannot flip the spin, one can calculate the overall transition strengths **a**, **b** and **c**. Regardless of the spin direction, they are all equal $1/4\pi$. This indicates, that there is no spin-polarised electron emission in this case. In fact a small spin-polarisation arises from the fact, that the radial integrals are not the same for the final spin-orbit split states, $\mathcal{R}_{1/2} \neq \mathcal{R}_{3/2}$, with $\mathcal{R}_j = \left| \int R_{4p_j}^*(r) R_{1s}(r) r^3 dr \right|^2$ [77].

Since the initial state is 1s and has no orbital angular momentum, excited photoelectrons exhibit full orbital-polarisation in case of the transition involving the operators $Y_1^{\pm 1}$ (that is induced by the light with angular momentum). In other words, the entire angular momentum of light is transferred to the photoelectron as an orbital angular momentum degree of freedom, since there is no spin-orbit splitting of the initial state and the electric dipole operator does not act on the spin part of the state vector. The orbital-polarisation reverses the sign under the reversal of the light helicity. If the valence shell possesses an orbital-polarisation $\Delta_{\varrho\ell}$ itself, the polarisation of the excited electron can be detected and thus a dichroism in absorption observed [80].

The K absorption edge XMCD is sensitive directly to the orbital-polarisation of the final states only [94]. The influence of the spin magnetic moment of the p-shell arises only due to the spin-orbit coupling. Since the orbital-polarisation in 3d transition metals is negligible, and the spin-orbit interaction in the 4p band weak [89], the XMCD signal is in this case only of the order 10^{-3} [77].

3.4 XMCD in other cases

Another resonances probed in order to gather information about the magnetism are the $L_{2,3}$ and $M_{3,4}$ absorption edges of 4f metals. The first of those lie in the energy region of hard x-rays, whereas the latter are like $L_{2,3}$ absorption edges of the 3d metals in the soft x-ray regime.

In the case of L-edges of 4f metals, one probes the transition from the spin-split 2p states to the empty s and d states, whereas the majority constitutes the latter ones. In the 4f metals the overlap between the wavefunction of the neighbouring atoms is small and thus the exchange interaction is mediated by the conduction band electrons (RKKY interaction). The empty states in this band are probed in the absorption experiment at the L-edges, thus one has insight into the foundations of magnetism in the 4f systems.

To describe the emergence of XMCD at the L-edges in the 4f metals, one can consider the same two-step model as for the L-edges in 3d and 5d metals. The calculation yields the same values of electron spin- and orbital-polarisations. Though, in contrast to 3d and 5d metals, it was shown by comparison of band-structure calculations with experimental results for Gd and Tb [95], that this simple model does not provide a good relation between the spin-polarised density of states and the XMCD signal [96]. This discrepancy might be assigned to the negligence of the spin-orbit interaction in the final states in the one-electron model [89]. Even the simple relation saying that the magnitude of the magnetic moment should scale with the XMCD signal, does not always hold true for the case of L-edges and 4f metals. It is only certain, that qualitative conclusions about the changes of the magnetic moment can be drawn from following the changes in the XMCD signal coming from the given system exposed to the changes of some experimental conditions [89]. The best practical way to extract information from the XMCD signal is based on band structure calculations and their comparison with experimental data [77].

In case of the soft x-ray $M_{4,5}$ resonances the $3d \rightarrow 4f$ transitions are considered, so one probes directly the localised 4f states responsible for magnetism in rare-earths. The same approach as for the $L_{2,3}$ -edges of 3d metals can be used to successfully describe the XMCD effect. By considering the transitions from the spin-orbit split initial states $3d_{5/2}$ (M_4 -edge) and $3d_{7/2}$ (M_5 -edge) to final 4f states one gets the values of spin- and orbital-polarisation of excited electrons. Application of the sum rules allows to calculate the spin and orbital magnetic moments separately. A number of comparisons with the data obtained from the neutron experiments has proven the validity of this approach [89].

3.5 Sum rules

The dependence of the general expression for the absorption cross-section (equation (2.38)) on the density of the final unoccupied states ρ_f allows to access the number of the electron-holes in the final band via determining energy-dependent absorption spectra. The integral of the density of final states (that is, due to proportionality — integral of the absorption spectrum) gives the number of holes. On the other hand, the energy integral of the spin-specific density of states $\rho_f^{\uparrow\downarrow}$ yields the number of the electron-holes with a given spin state. This quantity in turn is related to the magnetic moment (equation (3.29)).

As mentioned already in section 3.1.4, the XMCD signal is proportional to the imbal-

ance in the spin- and orbital-polarised density of states $\Delta\rho_f^s$ (equation (3.34)). The general expression for the XMCD signal (3.34) contains also the spin- and orbital-polarisations of the excited electron. For the $L_{2,3}$ absorption edges the orbital-polarisation is the same for both resonances, whereas the spin-polarisation is opposite in sign and two times bigger for the L_2 -edge. This indicates, that having the XMCD data for the transitions from the pair of spin-orbit split states (that is measured at two absorption edges: $L_{2,3}$ or $M_{3,4}$), one can by appropriate subtraction and addition of those two signals obtain the measure of the spin- and orbital-polarised densities of final states [89]. This idea lays the foundations for the sum rules, which allow to extract the spin and orbital magnetic moments from the XMCD data.

Rigorously, sum rules were derived by Thole [97] and Carra [98], in a localised model, considering a single ion in an arbitrary crystal-field symmetry and including hybridisation effects. The sum rules give the relation between the expectation value of the spin and orbital angular momentum and the integrated absorption spectra. The spin-polarisation of the photoelectron is opposite in sign, so addition of the XMCD spectra measured at two absorption edges gives the measure of the orbital magnetic moment. The difference discards the orbital contribution to the XMCD signal, so the spin magnetic moment is obtained in this way. Following the notations adopted by Stöhr and Siegmann [80], the sum rules allowing calculation of spin (m_{spin}) and orbital ($m_{orb.}$) magnetic moments read

$$-A + 2B = \frac{C}{N_h\mu_B} m_{spin} \quad (3.41a)$$

$$A + B = -\frac{3C}{2N_h\mu_B} m_{orb.} \quad (3.41b)$$

where $A = \int_{L_2} (\sigma_- - \sigma_+) d\mathcal{E}$ and $B = \int_{L_3} (\sigma_- - \sigma_+) d\mathcal{E}$ denote the integrated absolute (that is without normalisation) XMCD signal at the L_2 and L_3 (or M_4 and M_5) absorption edges, respectively. N_h is the number of electron-holes in the final band and $C = \int_{L_2+L_3} \sigma_{lin} d\mathcal{E}$ denotes the integrated absorption spectrum measured at both absorption edges with linear polarisation (or equivalently an average of the spectra for two helicities).

One should note that these sum rules are valid, if the effects of anisotropic spin and charge distribution average out. Experimentally, this can be achieved by performing measurements for three orthogonal directions and averaging. The anisotropic sum rules are discussed elsewhere [80].

The sum rules presented here can be successfully applied to the XMCD data for $L_{2,3}$ absorption edges in 3d and 5d metals, as well as $M_{4,5}$ edges of rare-earths. As mentioned earlier, other cases require more sophisticated data analysis to extract the magnetic information.

Chapter 4

Magnetic x-ray standing waves

The previous sections provided two important theoretical results. The dynamical theory of x-ray diffraction gives an answer to the question, how arbitrarily, including circularly polarised waves are scattered by the crystal lattice. The previous section about the XMCD effect treats the absorption of a single, plane, arbitrarily polarised EM wave in a magnetised material and describes the changes of absorption cross-section under the helicity reversal.

These two subjects are brought together in the current chapter to open a completely new perspective. As concluded in the first chapter, the scattering process leads to the appearance of the standing wave, which by monitoring the secondary yield can be used to determine the positions of the atoms in the lattice. Since the spectroscopic methods utilised to determine the secondary yield (fluorescence, Auger or photoelectron spectroscopy) are element specific, so is the structural information from the XSW experiment. The XMCD method on the other hand provides in general an information about magnetic moments of the absorbing atoms. These two experimental approaches can be connected in order to open an access to magnetic properties with spatial resolution, where the former emerge from the XMCD studies and the position sensitivity comes from the XSW technique.

The information about the magnetic structure can be obtained by employing a standing wave formed during the Bragg reflection of the circularly or elliptically polarised EM wave and monitoring the differential (XMCD) absorption signal while the standing wave moves through the lattice. The standing wave causes modulations in the absorption strength and, therefore, enhances or decreases the contribution to the XMCD of some lattice sites. This supplements the element and magnetic sensitive XMCD spectroscopy by the site selectivity.

The absorption cross-section is measured in the XSW technique indirectly, that is via secondary yield of electrons or fluorescence radiation. Normally the cross-section is determined by measuring the attenuation of the beam transmitted through the sample, and this is the only direct measurement of this quantity. The question which arises is, whether the XMCD signal can be also observed in the secondary yield, that is when the absorption cross-section is monitored in an indirect way. The answer is positive, a dichroism is also observed in fluorescence or electron secondary yield [99]. A more detailed discussion of this issue is given at the end of the current chapter.

Theoretically, the idea is simple. One considers at first the scattering of the circularly

or elliptically polarised EM wave by the given crystal lattice, what yields an exact form of the electric field (or equivalently vector potential) in dependence on the incident angle. This was already presented in section 1.9. Then the absorption cross-section for such a vector potential is calculated within the framework of time-dependent perturbation theory (chapter 2) and its changes under the helicity reversal studied. The resulting difference in absorption cross-sections is dependent on the incidence angle and on the spin-polarised density of states. Such an MXSW signal can be then interpreted in terms of the arrangement of the magnetic moments of the given atomic specie.

Chapter is organised as follows. At first the absorption cross-section is evaluated for the vector potential of the wavefield in the crystal under the diffraction conditions, using the same approach as in the previous one about the standard XMCD method. At first it is done for the simplest case of one atom with magnetic moment in the unit cell. The direction of the magnetic moment is arbitrary with respect to the lattice planes. In the second section a case of multiple magnetic atoms is considered, what leads to the introduction of a new quantity — a magnetic standing wave structure factor, which governs the MXSW signal and carries the magnetic structural information. Initially, no imaginary part of the wavevectors is considered. The correction taking into account extinction and anomalous absorption effects is introduced in section 4.7.

4.1 The form of perturbation

As stated already, in simple words the aim of this chapter is to evaluate a cross-section for the standing wave formed by the incoming circularly or elliptically polarised wave under the diffraction conditions. The form of the electric field existing inside the crystal during the Bragg reflection in the reflection geometry was already obtained in section 1.9, using the dynamical theory of x-ray diffraction. It is given by equation 1.62 and is repeated here for convenience

$$\mathcal{E} = E_0^a \left[\varepsilon_\sigma \hat{\boldsymbol{\varepsilon}}_\sigma (1 + \xi_\sigma e^{-i\mathbf{h}\cdot\mathbf{r}}) e^{i\omega t - i\mathbf{k}_{0\sigma}\cdot\mathbf{r}} + \varepsilon_\pi (\hat{\boldsymbol{\varepsilon}}_{0\pi} + \xi_\pi \hat{\boldsymbol{\varepsilon}}_{\mathbf{h}\pi} e^{-i\mathbf{h}\cdot\mathbf{r}}) e^{i\omega t - i\mathbf{k}_{0\pi}\cdot\mathbf{r}} \right]$$

The amplitude ratios for σ - and π -polarisation components ξ_σ and ξ_π are predicted by the dynamical theory of diffraction. The quantities ε_σ and ε_π are two parameters defining the polarisation of the incoming wave. Without the loss of generality it is assumed that $\varepsilon_\sigma \in \mathbb{R}$, so that the phase shift between the polarisation components is carried in ε_π . The full discussion about the form of the incoming wave is given in section 1.9.1.

Following the procedure adopted in section 2.3, the vector potential of the wavefield can be written simply in the form

$$\mathcal{A} = A_0 \left[\varepsilon_\sigma \hat{\boldsymbol{\varepsilon}}_\sigma (1 + \xi_\sigma e^{-i\mathbf{h}\cdot\mathbf{r}}) e^{i\omega t - i\mathbf{k}_{0\sigma}\cdot\mathbf{r}} + \varepsilon_\pi (\hat{\boldsymbol{\varepsilon}}_{0\pi} + \xi_\pi \hat{\boldsymbol{\varepsilon}}_{\mathbf{h}\pi} e^{-i\mathbf{h}\cdot\mathbf{r}}) e^{i\omega t - i\mathbf{k}_{0\pi}\cdot\mathbf{r}} \right] \quad (4.1)$$

taking $E_0^a = -i\omega A_0$, what can be easily checked using the definition $\mathcal{E} = -\partial_t \mathcal{A}$ in Coulomb gauge.

As mentioned in the introduction, at first the simpler case of real wavevectors, $\mathbf{k}_{0\sigma}, \mathbf{k}_{0\pi} \in \mathbb{R}$ is considered. This is equivalent to negligence of extinction and anomalous absorption. Also the effect of attenuation of the secondary signal on the way from the emitting atom to the detector is neglected in the first step. Such a simpler case is

introduced, as it well presents the general idea without unnecessary complication. The correction for the imaginary part of the wavevectors is provided in section 4.7. It is also assumed, that the difference between the wavevectors for each of the polarisation components is small, that is $\mathbf{k}_{0\sigma} \approx \mathbf{k}_{0\pi}$, what remains true also for high scattering angles when the polarisation factor \mathfrak{P} is significantly different from unity for π -polarisation.

Similarly like in section 2.3 comprising the absorption of the standing wave generated by the linearly polarised incoming wave, the position of the electron undergoing the transition induced by the photons from the wavefield is defined as $\mathbf{r} = \mathbf{R} + \tilde{\mathbf{r}}$, where \mathbf{R} is the position of the atom and $\tilde{\mathbf{r}}$ position of the electron with respect to the nucleus. As discussed in section 2.2.3, it is justified to consider the absorption process within the electric dipole approximation. This is equivalent to setting $\tilde{\mathbf{r}} = 0$, what means that the absorption of the photon happens approximately at the position of the nucleus, that is the spatial extent of the electron wavefunction is small. With that, the vector potential reads

$$\mathcal{A} = A_0 \left[\varepsilon_\sigma \hat{\mathbf{e}}_\sigma (1 + \xi_\sigma e^{-i\mathbf{h}\cdot\mathbf{R}}) + \varepsilon_\pi (\hat{\mathbf{e}}_{0\pi} + \xi_\pi \hat{\mathbf{e}}_{\mathbf{h}\pi} e^{-i\mathbf{h}\cdot\mathbf{R}}) \right] e^{i\omega t - i\mathbf{k}_0\cdot\mathbf{R}} \quad (4.2)$$

In such a form it commutes with the momentum and position operators, so all considerations from chapter 2 remains valid and what one needs to consider only from now on are the components of the polarisation vector. The way they are generally defined is described in section 1.9.1. Before giving their explicit form, one needs to set the coordinate system for further calculations.

4.2 Geometry of the experiment

As discussed in chapter 3, the main coordinate system is set by the direction of the magnetic moment, which defines the quantisation axis for the absorption process. In the adopted two-step model, an excited electron is detected by the polarised final band, and thus the direction of this polarisation is defined by the magnetic moment direction. One considers here an arbitrary orientation of the magnetic moment with respect to the wavevectors \mathbf{k}_0 , $\mathbf{k}_\mathbf{h}$ and the reflecting lattice planes parametrised by their reciprocal lattice vector \mathbf{h} . The relation between the latter is given strictly by the diffraction condition $\mathbf{k}_\mathbf{h} = \mathbf{k}_0 + \mathbf{h}$. These three vectors span also a plane, which is called a scattering plane.

The diffraction process is described naturally in the coordinate system \mathcal{O}' . It is defined by assuming that the reciprocal lattice vector is along the $\mathcal{O}z'$ axis, so that $\mathbf{h}' = h(0, 0, 1)$ ¹, σ -polarisation unit vector $\hat{\mathbf{e}}_\sigma$ along the $\mathcal{O}y'$ direction and the scattering plane is the $x'\mathcal{O}z'$ one. The coordinate system \mathcal{O}' is shown in figure 4.1. Following their definitions given in section 1.2, the polarisation unit vectors in \mathcal{O}' read

$$\hat{\mathbf{e}}'_\sigma = \hat{\mathbf{y}}' \quad (4.3a)$$

$$\hat{\mathbf{e}}'_{0\pi} = \hat{\mathbf{x}}' \sin \Theta_B + \hat{\mathbf{z}}' \cos \Theta_B \quad (4.3b)$$

$$\hat{\mathbf{e}}'_{\mathbf{h}\pi} = -\hat{\mathbf{x}}' \sin \Theta_B + \hat{\mathbf{z}}' \cos \Theta_B \quad (4.3c)$$

The main coordinate system \mathcal{O} is defined by the magnetic moment chosen to be along $\mathcal{O}z$, such that $\mathbf{m} = m(0, 0, 1)$. The mutual relation between the coordinate systems is

¹Before the vectors were written only as columns. Note, that there is no difference between the column and row vectors, as the metric is Euclidean, so row ones will be sometimes used in the text for convenience.

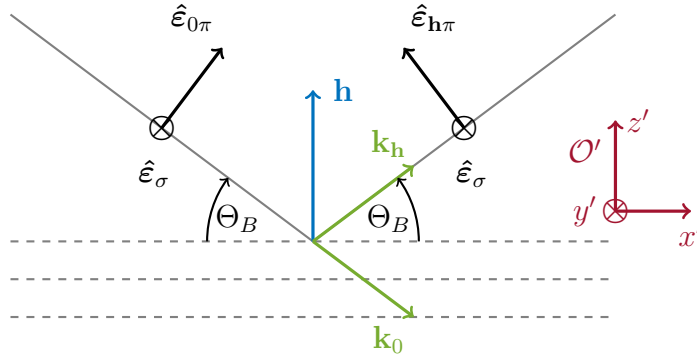


Figure 4.1: The coordinate system \mathcal{O}' , in which the diffraction process is described naturally. It is defined by the reciprocal lattice vector \mathbf{h} chosen to coincide with the axis $\mathcal{O}z'$ and the σ -polarisation unit vector $\hat{\mathbf{e}}_\sigma$ set parallel to $\mathcal{O}y'$ direction. The scattering plane spanned by the wavevectors of refracted and reflected waves \mathbf{k}_0 and \mathbf{k}_h is the $x'Oz'$ one. The polarisation unit vectors are defined in section 1.2.

given by the angles (ϑ_m, φ_m) . The coordinate system \mathcal{O} is obtained from the \mathcal{O}' one by two rotations, in the same way as in section 3.1.2, though now the roles of the coordinate systems are exchanged. The transformation is given by the matrix \mathbf{R} (equation (3.5)). The coordinate systems, as well as \mathbf{h} and \mathbf{m} vectors are depicted in figure 4.2.

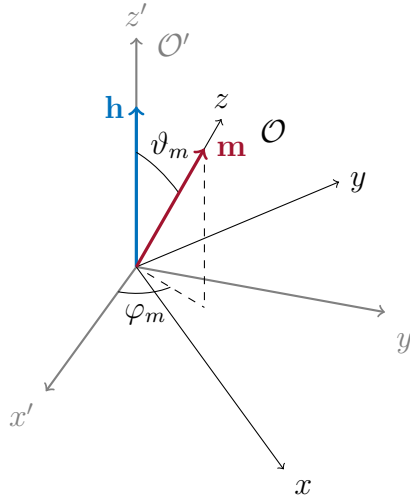


Figure 4.2: The coordinate systems for describing the MXSW experiment. The actual one (\mathcal{O}) is defined by the magnetic moment direction, since it defines the quantisation axis of the final band. \mathcal{O}' is used to describe the diffraction process and was defined in figure 4.1. The plane $x'Oz'$ is the scattering plane and it contains the vectors \mathbf{h} , \mathbf{k}_0 and \mathbf{k}_h . The relation between the coordinate systems \mathcal{O} and \mathcal{O}' is parametrised by the angles (ϑ_m, φ_m) .

Since now the coordinates in the rotated system (that is \mathcal{O}) are needed, in order to transform the coordinates of the vectors given in \mathcal{O}' one needs to consider the reverse transformation \mathbf{R}^{-1} . Equivalently, it is a composition of rotations, first around $\mathcal{O}z'$ by

$-\varphi_m$ and then around $\mathcal{O}y'$ by $-\vartheta_m$, or in short $\mathbf{R}^{-1} = \mathbf{R}_{y'}(-\vartheta_m)\mathbf{R}_{z'}(-\varphi_m)$. The matrix reads

$$\mathbf{R}^{-1} = \begin{pmatrix} \cos \varphi_m \cos \vartheta_m & \sin \varphi_m \cos \vartheta_m & -\sin \vartheta_m \\ -\sin \varphi_m & \cos \varphi_m & 0 \\ \cos \varphi_m \sin \vartheta_m & \sin \varphi_m \sin \vartheta_m & \cos \vartheta_m \end{pmatrix} \quad (4.4)$$

The coordinates of the polarisation unit vectors can be obtained by the general relation $\hat{\boldsymbol{\varepsilon}}_i = \mathbf{R}^{-1}\hat{\boldsymbol{\varepsilon}}'_i$. In the actual coordinate system \mathcal{O} they read

$$\hat{\boldsymbol{\varepsilon}}_\sigma = \mathbf{R}^{-1} \begin{pmatrix} 0 \\ 1 \\ 0 \end{pmatrix} = \begin{pmatrix} \sin \varphi_m \cos \vartheta_m \\ \cos \varphi_m \\ \sin \varphi_m \sin \vartheta_m \end{pmatrix} \quad (4.5a)$$

$$\hat{\boldsymbol{\varepsilon}}_{0\pi} = \mathbf{R}^{-1} \begin{pmatrix} \sin \Theta_B \\ 0 \\ \cos \Theta_B \end{pmatrix} = \begin{pmatrix} \cos \varphi_m \cos \vartheta_m \sin \Theta_B - \sin \vartheta_m \cos \Theta_B \\ -\sin \varphi_m \sin \Theta_B \\ \cos \varphi_m \sin \vartheta_m \sin \Theta_B + \cos \vartheta_m \cos \Theta_B \end{pmatrix} \quad (4.5b)$$

$$\hat{\boldsymbol{\varepsilon}}_{\mathbf{h}\pi} = \mathbf{R}^{-1} \begin{pmatrix} -\sin \Theta_B \\ 0 \\ \cos \Theta_B \end{pmatrix} = \begin{pmatrix} -\cos \varphi_m \cos \vartheta_m \sin \Theta_B - \sin \vartheta_m \cos \Theta_B \\ \sin \varphi_m \sin \Theta_B \\ -\cos \varphi_m \sin \vartheta_m \sin \Theta_B + \cos \vartheta_m \cos \Theta_B \end{pmatrix} \quad (4.5c)$$

4.3 Polarisation vector

As written in section 1.9.1, the polarisation vector, which appears later in the formula for the absorption cross-section, is defined in the way that the vector potential (4.2) may be written in the form

$$\mathcal{A} = A_0 \boldsymbol{\varepsilon} e^{i\omega t - i\mathbf{k}_0 \cdot \mathbf{R}} \quad (4.6)$$

and then the polarisation vector itself

$$\boldsymbol{\varepsilon} = \varepsilon_\sigma \hat{\boldsymbol{\varepsilon}}_\sigma (1 + \xi_\sigma e^{-i\mathbf{h} \cdot \mathbf{R}}) + \varepsilon_\pi (\hat{\boldsymbol{\varepsilon}}_{0\pi} + \xi_\pi \hat{\boldsymbol{\varepsilon}}_{\mathbf{h}\pi} e^{-i\mathbf{h} \cdot \mathbf{R}}) \quad (4.7)$$

Now, using the coordinates (4.5) one can write the polarisation vector in terms of unit vectors of the coordinate system \mathcal{O}

$$\boldsymbol{\varepsilon} = \varepsilon_\sigma [(\varepsilon_\sigma)_x \hat{\mathbf{x}} + (\varepsilon_\sigma)_y \hat{\mathbf{y}} + (\varepsilon_\sigma)_z \hat{\mathbf{z}}] (1 + \xi_\sigma e^{-i\mathbf{h} \cdot \mathbf{R}}) + \varepsilon_\pi \{ [(\varepsilon_{0\pi})_x \hat{\mathbf{x}} + (\varepsilon_{0\pi})_y \hat{\mathbf{y}} + (\varepsilon_{0\pi})_z \hat{\mathbf{z}}] + [(\varepsilon_{\mathbf{h}\pi})_x \hat{\mathbf{x}} + (\varepsilon_{\mathbf{h}\pi})_y \hat{\mathbf{y}} + (\varepsilon_{\mathbf{h}\pi})_z \hat{\mathbf{z}}] \xi_\pi e^{-i\mathbf{h} \cdot \mathbf{R}} \} \quad (4.8)$$

where the symbols $(\varepsilon_j)_k$, with $j \equiv \sigma, 0\pi, \mathbf{h}\pi$, $k \equiv x, y, z$, denote the components of the polarisation unit vectors. Grouping the terms staying by the basis vectors $\hat{\mathbf{x}}$, $\hat{\mathbf{y}}$, $\hat{\mathbf{z}}$ provides the expressions for the coordinates of $\boldsymbol{\varepsilon}$

$$\varepsilon_x = \varepsilon_\sigma (1 + \xi_\sigma e^{-i\mathbf{h} \cdot \mathbf{R}}) \sin \varphi_m \cos \vartheta_m + \varepsilon_\pi [(1 - \xi_\pi e^{-i\mathbf{h} \cdot \mathbf{R}}) \cos \varphi_m \cos \vartheta_m \sin \Theta_B + (1 + \xi_\pi e^{-i\mathbf{h} \cdot \mathbf{R}}) \sin \vartheta_m \cos \Theta_B] \quad (4.9a)$$

$$\varepsilon_y = \varepsilon_\sigma (1 + \xi_\sigma e^{-i\mathbf{h} \cdot \mathbf{R}}) \cos \varphi_m - \varepsilon_\pi (1 - \xi_\pi e^{-i\mathbf{h} \cdot \mathbf{R}}) \sin \varphi_m \sin \Theta_B \quad (4.9b)$$

$$\varepsilon_z = \varepsilon_\sigma (1 + \xi_\sigma e^{-i\mathbf{h} \cdot \mathbf{R}}) \sin \varphi_m \sin \vartheta_m + \varepsilon_\pi [(1 - \xi_\pi e^{-i\mathbf{h} \cdot \mathbf{R}}) \cos \varphi_m \sin \vartheta_m \sin \Theta_B + (1 + \xi_\pi e^{-i\mathbf{h} \cdot \mathbf{R}}) \cos \vartheta_m \cos \Theta_B] \quad (4.9c)$$

The polarisation vector components are everything what is needed to evaluate the absorption cross-section for the considered electric field, and thus also the XMCD signal under the standing wave regime. One can note already, that the polarisation vector contains a dependence on the position of the atom, what implies that so will do the final absorption cross-section.

4.4 Absorption of the standing wave

Having set the form of the perturbation and the coordinate system, the cross-section can be calculated in the same way as in chapter 3. Like there, also here a two-step model of absorption by the magnetised atom is considered. This means, that the approach is strictly valid for the case of $L_{2,3}$ absorption edges in 3d and 5d metals, as well as $M_{4,5}$ resonances in rare-earths, from which only the $L_{2,3}$ in 5d systems lie in the energy region of hard x-rays. Since this is the only simple analytical model of the XMCD effect, it is used to treat the absorption of the standing wave in magnetised medium, that is to describe theoretically the MXSW method. In section 4.9 an argument is given, which justifies that the results presented hereafter can be used for any other absorption edges and systems as well.

The absorption cross-section for a given helicity can be calculated using the formula (3.10), which involves the transition strengths given by (3.12). Since the quantities \mathbf{a} , \mathbf{b} and \mathbf{c} are related to the considered quantum transitions, they remain the same. One needs to calculate here only the wave-related quantities \mathfrak{A} , \mathfrak{B} and \mathfrak{C} .

The components of the polarisation vector ε_i^* , $i \equiv x, y, z$ are the only quantities, which influence the values of \mathfrak{A} , \mathfrak{B} and \mathfrak{C} . As a reminder, they are defined as the combinations $\mathfrak{A} = \varepsilon_x^* + i\varepsilon_y^*$, $\mathfrak{B} = -\varepsilon_x^* + i\varepsilon_y^*$, $\mathfrak{C} = \varepsilon_z^*$ (see (3.8)). What is needed to evaluate the absorption cross-section are in fact the moduli $|\mathfrak{A}|^2$, $|\mathfrak{B}|^2$ and $|\mathfrak{C}|^2$. In general case they read

$$|\mathfrak{A}|^2 = |\varepsilon_x|^2 + 2\Re(i\varepsilon_x\varepsilon_y^*) + |\varepsilon_y|^2 \quad (4.10a)$$

$$|\mathfrak{B}|^2 = |\varepsilon_x|^2 - 2\Re(i\varepsilon_x\varepsilon_y^*) + |\varepsilon_y|^2 \quad (4.10b)$$

$$|\mathfrak{C}|^2 = |\varepsilon_z|^2 \quad (4.10c)$$

Thus, the task is to calculate the moduli squared of the polarisation vector components and the mixed term $\Re(i\varepsilon_x\varepsilon_y^*)$. For the considered case, the moduli read

$$\begin{aligned} |\varepsilon_x|^2 &= \varepsilon_\sigma^2 |1 + \xi_\sigma e^{-i\mathbf{h}\cdot\mathbf{R}}|^2 \sin^2 \varphi_m \cos^2 \vartheta_m + |\varepsilon_\pi|^2 |1 - \xi_\pi e^{-i\mathbf{h}\cdot\mathbf{R}}|^2 \cos^2 \varphi_m \cos^2 \vartheta_m \sin^2 \Theta_B + \\ &+ |\varepsilon_\pi|^2 |1 + \xi_\pi e^{-i\mathbf{h}\cdot\mathbf{R}}|^2 \sin^2 \vartheta_m \cos^2 \Theta_B + \\ &+ 2\varepsilon_\sigma \Re[\varepsilon_\pi^* (1 + \xi_\sigma e^{-i\mathbf{h}\cdot\mathbf{R}}) (1 - \xi_\pi^* e^{i\mathbf{h}\cdot\mathbf{R}})] \sin \varphi_m \cos \varphi_m \cos^2 \vartheta_m \sin \Theta_B + \\ &- 2\varepsilon_\sigma \Re[\varepsilon_\pi^* (1 + \xi_\sigma e^{-i\mathbf{h}\cdot\mathbf{R}}) (1 + \xi_\pi^* e^{i\mathbf{h}\cdot\mathbf{R}})] \sin \varphi_m \sin \vartheta_m \cos \vartheta_m \cos \Theta_B + \\ &- 2|\varepsilon_\pi|^2 \Re[(1 - \xi_\pi e^{-i\mathbf{h}\cdot\mathbf{R}}) (1 + \xi_\pi^* e^{i\mathbf{h}\cdot\mathbf{R}})] \cos \varphi_m \sin \vartheta_m \cos \vartheta_m \sin \Theta_B \cos \Theta_B \quad (4.11a) \end{aligned}$$

$$\begin{aligned} |\varepsilon_y|^2 &= \varepsilon_\sigma^2 |1 + \xi_\sigma e^{-i\mathbf{h}\cdot\mathbf{R}}|^2 \cos^2 \varphi_m + |\varepsilon_\pi|^2 |1 - \xi_\pi e^{-i\mathbf{h}\cdot\mathbf{R}}|^2 \sin^2 \varphi_m \sin^2 \Theta_B + \\ &- 2\varepsilon_\sigma \Re[\varepsilon_\pi^* (1 + \xi_\sigma e^{-i\mathbf{h}\cdot\mathbf{R}}) (1 - \xi_\pi^* e^{i\mathbf{h}\cdot\mathbf{R}})] \sin \varphi_m \cos \varphi_m \sin \Theta_B \quad (4.11b) \end{aligned}$$

$$\begin{aligned}
|\varepsilon_z|^2 &= \varepsilon_\sigma^2 |1 + \xi_\sigma e^{-i\mathbf{h}\cdot\mathbf{R}}|^2 \sin^2 \varphi_m \sin^2 \vartheta_m + |\varepsilon_\pi|^2 |1 - \xi_\pi e^{-i\mathbf{h}\cdot\mathbf{R}}|^2 \cos^2 \varphi_m \sin^2 \vartheta_m \sin^2 \Theta_B + \\
&+ |\varepsilon_\pi|^2 |1 + \xi_\pi e^{-i\mathbf{h}\cdot\mathbf{R}}|^2 \cos^2 \vartheta_m \cos^2 \Theta_B + \\
&+ 2\varepsilon_\sigma \Re [\varepsilon_\pi^* (1 + \xi_\sigma e^{-i\mathbf{h}\cdot\mathbf{R}}) (1 - \xi_\pi^* e^{i\mathbf{h}\cdot\mathbf{R}})] \sin \varphi_m \cos \varphi_m \sin^2 \vartheta_m \sin \Theta_B + \\
&+ 2\varepsilon_\sigma \Re [\varepsilon_\pi^* (1 + \xi_\sigma e^{-i\mathbf{h}\cdot\mathbf{R}}) (1 + \xi_\pi^* e^{i\mathbf{h}\cdot\mathbf{R}})] \sin \varphi_m \sin \vartheta_m \cos \vartheta_m \cos \Theta_B + \\
&+ 2|\varepsilon_\pi|^2 \Re [(1 - \xi_\pi e^{-i\mathbf{h}\cdot\mathbf{R}}) (1 + \xi_\pi^* e^{i\mathbf{h}\cdot\mathbf{R}})] \cos \varphi_m \sin \vartheta_m \cos \vartheta_m \sin \Theta_B \cos \Theta_B \quad (4.11c)
\end{aligned}$$

and the mixed term

$$\begin{aligned}
\Re(i\varepsilon_x \varepsilon_y^*) &= \Re \left\{ i [|\varepsilon_\pi|^2 (1 + \xi_\pi e^{-i\mathbf{h}\cdot\mathbf{R}}) (1 - \xi_\pi^* e^{i\mathbf{h}\cdot\mathbf{R}}) \sin \varphi_m \sin \vartheta_m \sin \Theta_B \cos \Theta_B + \right. \\
&+ \varepsilon_\sigma \varepsilon_\pi^* (1 + \xi_\sigma e^{-i\mathbf{h}\cdot\mathbf{R}}) (1 + \xi_\pi^* e^{i\mathbf{h}\cdot\mathbf{R}}) \cos \varphi_m \sin \vartheta_m \cos \Theta_B + \\
&\left. - \varepsilon_\sigma \varepsilon_\pi^* (1 + \xi_\sigma e^{-i\mathbf{h}\cdot\mathbf{R}}) (1 - \xi_\pi^* e^{i\mathbf{h}\cdot\mathbf{R}}) \cos \vartheta_m \sin \Theta_B] \right\} \quad (4.12)
\end{aligned}$$

Having calculated these quantities, one can easily obtain the expressions for the sought moduli $|\mathfrak{A}|^2$, $|\mathfrak{B}|^2$ and $|\mathfrak{C}|^2$. The full expressions are given in appendix A.3.1, since they are straightforwardly obtained from the expressions (4.11) and (4.12). A particular interest lies here in changes under the helicity reversal, that is a transformation $\varepsilon_\pi \rightarrow \varepsilon_\pi^*$. In order to notice these differences easier, the coefficient ε_π is written explicitly as $\varepsilon_\pi = \Re\varepsilon_\pi + i\Im\varepsilon_\pi$ in the terms which change under the helicity reversal, that is contain the ε_π alone. The part, which does not change, is denoted by prime and the one proportional to $\Im\varepsilon_\pi$ by double prime, such that $|\mathfrak{A}_\pm|^2 = \mathfrak{A}' \pm \mathfrak{A}''$, $|\mathfrak{B}_\pm|^2 = \mathfrak{B}' \pm \mathfrak{B}''$, $|\mathfrak{C}_\pm|^2 = \mathfrak{C}' \pm \mathfrak{C}''$, where "+" corresponds to the initial helicity, and "-" after the reversal. The explicit formulae for this quantities are presented in appendix A.3.1.

Some similarities can be noticed in the expressions for \mathfrak{A}'' , \mathfrak{B}'' and \mathfrak{C}'' . By denoting

$$\begin{aligned}
\Xi_1 &= 2\varepsilon_\sigma (\Im\varepsilon_\pi) \Re \left\{ i [(1 + \xi_\sigma e^{-i\mathbf{h}\cdot\mathbf{R}}) (1 - \xi_\pi^* e^{i\mathbf{h}\cdot\mathbf{R}}) \sin \varphi_m \cos \varphi_m \sin^2 \vartheta_m \sin \Theta_B + \right. \\
&\left. + (1 + \xi_\sigma e^{-i\mathbf{h}\cdot\mathbf{R}}) (1 + \xi_\pi^* e^{i\mathbf{h}\cdot\mathbf{R}}) \sin \varphi_m \sin \vartheta_m \cos \vartheta_m \cos \Theta_B] \right\} \quad (4.13a)
\end{aligned}$$

$$\begin{aligned}
\Xi_2 &= 2\varepsilon_\sigma (\Im\varepsilon_\pi) \Re [(1 + \xi_\sigma e^{-i\mathbf{h}\cdot\mathbf{R}}) (1 + \xi_\pi^* e^{i\mathbf{h}\cdot\mathbf{R}}) \cos \varphi_m \sin \vartheta_m \cos \Theta_B + \\
&- (1 + \xi_\sigma e^{-i\mathbf{h}\cdot\mathbf{R}}) (1 - \xi_\pi^* e^{i\mathbf{h}\cdot\mathbf{R}}) \cos \vartheta_m \sin \Theta_B] \quad (4.13b)
\end{aligned}$$

it can be written, that

$$\mathfrak{A}'' = \Xi_1 + \Xi_2, \quad \mathfrak{B}'' = \Xi_1 - \Xi_2, \quad \mathfrak{C}'' = -\Xi_1 \quad (4.14)$$

In a similar manner, one can analyse the structure of the quantities \mathfrak{A}' , \mathfrak{B}' and \mathfrak{C}' , which do not change under the helicity reversal. The difference between \mathfrak{A}' and \mathfrak{B}' is in the last two terms. They can be denoted by Ξ_3 , which reads

$$\begin{aligned}
\Xi_3 &= 2\Re \left\{ i [|\varepsilon_\pi|^2 (1 + \xi_\pi e^{-i\mathbf{h}\cdot\mathbf{R}}) (1 - \xi_\pi^* e^{i\mathbf{h}\cdot\mathbf{R}}) \sin \varphi_m \sin \vartheta_m \sin \Theta_B \cos \Theta_B + \right. \\
&+ \varepsilon_\sigma (\Re\varepsilon_\pi) (1 + \xi_\sigma e^{-i\mathbf{h}\cdot\mathbf{R}}) (1 + \xi_\pi^* e^{i\mathbf{h}\cdot\mathbf{R}}) \cos \varphi_m \sin \vartheta_m \cos \Theta_B + \\
&\left. - \varepsilon_\sigma (\Re\varepsilon_\pi) (1 + \xi_\sigma e^{-i\mathbf{h}\cdot\mathbf{R}}) (1 - \xi_\pi^* e^{i\mathbf{h}\cdot\mathbf{R}}) \cos \vartheta_m \sin \Theta_B] \right\} \quad (4.15)
\end{aligned}$$

The remaining ones will be called Ξ_4 . Then the quantities \mathfrak{A}' and \mathfrak{B}' can be written simply as

$$\mathfrak{A}' = \Xi_4 + \Xi_3, \quad \mathfrak{B}' = \Xi_4 - \Xi_3 \quad (4.16)$$

As mentioned already, the cross-section for the atom exhibiting a spin-polarisation in the final band is given by the formula (3.10), with the transition rates $\zeta_{\pm}^{\uparrow\downarrow}$ dependent on spin direction of excited photoelectron and helicity of the radiation, given in this case by

$$\zeta_{\pm}^{\uparrow\downarrow} = \frac{4\pi}{3}\mathcal{R} \left[\frac{1}{2}(\Xi_4 + \Xi_3 \pm \Xi_1 \pm \Xi_2) \mathbf{a}^{\uparrow\downarrow} + \frac{1}{2}(\Xi_4 - \Xi_3 \pm \Xi_1 \mp \Xi_2) \mathbf{b}^{\uparrow\downarrow} + (\mathbf{c}' \mp \Xi_1) \mathbf{c} \right] \quad (4.17)$$

Since the spin-dependent measures of the transition rates \mathbf{a} , \mathbf{b} and \mathbf{c} were evaluated in the previous paragraph for the case of the $L_{2,3}$ absorption edge, the previous equation fully defines the absorption cross-section of the standing wave generated by the arbitrarily polarised incoming plane EM wave. Having this result, one can consider the XMCD signal that is the difference between the absorption cross-sections under the helicity reversal.

4.5 MXSW formula — XMCD for the standing wave

This section is the crucial one for the entire work. A formula describing the dependence of the XMCD signal on the incidence angle $\Delta\Theta$ (via the amplitude ratios ξ) under the regime of the standing wave is derived hereafter. The dependence of the signal on the position of absorbing atom indicates, that thanks to the interference field a standard XMCD spectroscopy gains in addition spatial resolution. This effect appears in the same way as the XSW method supplements standard spectroscopic techniques by position sensitivity.

The dependence of the absorption cross-section on helicity (via the alternating signs) is apparent in equation (4.17), what indicates a possibility of observing a dichroism. One uses the formula for the cross-section (3.10) and the definition of the XMCD signal (3.22). The initial formula reads

$$\begin{aligned} \Xi = & \left\{ \varrho_f^{\uparrow} \left[\frac{1}{2} \mathbf{a}^{\uparrow} (|\mathfrak{A}_-|^2 - |\mathfrak{A}_+|^2) + \frac{1}{2} \mathbf{b}^{\uparrow} (|\mathfrak{B}_-|^2 - |\mathfrak{B}_+|^2) + \mathbf{c} (|\mathfrak{C}_-|^2 - |\mathfrak{C}_+|^2) \right] + \right. \\ & \left. + \varrho_f^{\downarrow} \left[\frac{1}{2} \mathbf{a}^{\downarrow} (|\mathfrak{A}_-|^2 - |\mathfrak{A}_+|^2) + \frac{1}{2} \mathbf{b}^{\downarrow} (|\mathfrak{B}_-|^2 - |\mathfrak{B}_+|^2) + \mathbf{c} (|\mathfrak{C}_-|^2 - |\mathfrak{C}_+|^2) \right] \right\} \cdot \\ & \cdot \left\{ \varrho_f^{\uparrow} \left[\frac{1}{2} \mathbf{a}^{\uparrow} (|\mathfrak{A}_-|^2 + |\mathfrak{A}_+|^2) + \frac{1}{2} \mathbf{b}^{\uparrow} (|\mathfrak{B}_-|^2 + |\mathfrak{B}_+|^2) + \mathbf{c} (|\mathfrak{C}_-|^2 + |\mathfrak{C}_+|^2) \right] + \right. \\ & \left. + \varrho_f^{\downarrow} \left[\frac{1}{2} \mathbf{a}^{\downarrow} (|\mathfrak{A}_-|^2 + |\mathfrak{A}_+|^2) + \frac{1}{2} \mathbf{b}^{\downarrow} (|\mathfrak{B}_-|^2 + |\mathfrak{B}_+|^2) + \mathbf{c} (|\mathfrak{C}_-|^2 + |\mathfrak{C}_+|^2) \right] \right\}^{-1} \quad (4.18) \end{aligned}$$

Keeping in mind the notations $|\mathfrak{A}_{\pm}|^2 = \mathfrak{A}' \pm \mathfrak{A}''$, $|\mathfrak{B}_{\pm}|^2 = \mathfrak{B}' \pm \mathfrak{B}''$, $|\mathfrak{C}_{\pm}|^2 = \mathfrak{C}' \pm \mathfrak{C}''$, one can write

$$\begin{aligned} \Xi = & \left\{ -\varrho_f^{\uparrow} [\mathbf{a}^{\uparrow} \mathfrak{A}'' + \mathbf{b}^{\uparrow} \mathfrak{B}'' + 2\mathbf{c} \mathfrak{C}''] - \varrho_f^{\downarrow} [\mathbf{a}^{\downarrow} \mathfrak{A}'' + \mathbf{b}^{\downarrow} \mathfrak{B}'' + 2\mathbf{c} \mathfrak{C}''] \right\} \cdot \\ & \cdot \left\{ \varrho_f^{\uparrow} [\mathbf{a}^{\uparrow} \mathfrak{A}' + \mathbf{b}^{\uparrow} \mathfrak{B}' + 2\mathbf{c} \mathfrak{C}'] + \varrho_f^{\downarrow} [\mathbf{a}^{\downarrow} \mathfrak{A}' + \mathbf{b}^{\downarrow} \mathfrak{B}' + 2\mathbf{c} \mathfrak{C}'] \right\}^{-1} \quad (4.19) \end{aligned}$$

Now, the relations between the transition rates can be used, namely equation (3.20) and $\mathbf{c}^{\uparrow} = \mathbf{c}^{\downarrow}$. Additionally, the relations (4.14) and (4.16) are introduced. With that, the

XMCD signal reads

$$\begin{aligned} \Xi = & \left\{ \varrho_f^\uparrow [-\mathbf{a}^\uparrow (\Xi_1 + \Xi_2) + \mathbf{a}^\downarrow (-\Xi_1 + \Xi_2) + 2\mathbf{c}\Xi_1] + \right. \\ & \left. + \varrho_f^\downarrow [-\mathbf{a}^\downarrow (\Xi_1 + \Xi_2) + \mathbf{a}^\uparrow (-\Xi_1 + \Xi_2) + 2\mathbf{c}\Xi_1] \right\} \cdot \\ & \cdot \left\{ \varrho_f^\uparrow [\mathbf{a}^\uparrow (\Xi_4 + \Xi_3) + \mathbf{a}^\downarrow (\Xi_4 - \Xi_3) + 2\mathbf{c}\mathfrak{C}'] + \right. \\ & \left. + \varrho_f^\downarrow [\mathbf{a}^\downarrow (\Xi_4 + \Xi_3) + \mathbf{a}^\uparrow (\Xi_4 - \Xi_3) + 2\mathbf{c}\mathfrak{C}'] \right\}^{-1} \end{aligned} \quad (4.20)$$

Now, the fact that $\mathbf{a}^\uparrow + \mathbf{a}^\downarrow = 2\mathbf{c}$ (equation (3.26)) can be used. It makes the terms in the nominator proportional to Ξ_1 vanish. Only the terms proportional to Ξ_2 remain and the nominator can be written simply as $(\mathbf{a}^\downarrow - \mathbf{a}^\uparrow)\Xi_2\Delta\varrho_f^s$, with $\Delta\varrho_f^s := \varrho_f^\uparrow - \varrho_f^\downarrow$. The term Ξ_2 is the one coming from the mixed term $\Re(i\varepsilon_x\varepsilon_y^*)$, that is the one which changes the sign between the quantities \mathfrak{A} and \mathfrak{B} . It changes also the sign under the helicity reversal. After the transformation the sign initially present in \mathfrak{A} appears in \mathfrak{B} and vice versa. This is an expected behaviour, the same as observed in chapter 3. This symmetry is caused by the fact, that \mathfrak{A} is related to the transitions fulfilling the condition $\Delta m_\ell = +1$, whereas \mathfrak{B} to the ones with $\Delta m_\ell = -1$.

Remembering that $\mathbf{a}^\uparrow + \mathbf{a}^\downarrow = 2\mathbf{c}$, the denominator of (4.20) can be transformed to the form

$$(\mathbf{a}^\uparrow + \mathbf{a}^\downarrow) (\Xi_4 + \mathfrak{C}') \varrho_f - (\mathbf{a}^\downarrow - \mathbf{a}^\uparrow) \Xi_3 \Delta\varrho_f^s \quad (4.21)$$

with $\varrho_f = \varrho_f^\uparrow + \varrho_f^\downarrow$. One should now consider the term $\Xi_4 + \mathfrak{C}'$, which simplifies greatly and yields a relative intensity of the standing wave $I_{sw} := I/(E_0^a)^2$, given already by equation (1.63).

Finally, the XMCD signal under the standing wave regime, or in other words the MXSW signal, reads

$$\boxed{\Xi(\Delta\Theta) = \frac{\Pi_e^s \Xi_2 \Delta\varrho_f^s}{I_{sw} \varrho_f - \Pi_e^s \Xi_3 \Delta\varrho_f^s}} \quad (4.22)$$

where the polarisation of the photoelectron is given by $\Pi_e^s = (\mathbf{a}^\downarrow - \mathbf{a}^\uparrow)/(\mathbf{a}^\downarrow + \mathbf{a}^\uparrow)$ and the formulae for the remaining symbols, collected here for the sake of convenience, read

$$\begin{aligned} \Xi_2 = & 2\varepsilon_\sigma(\Im\varepsilon_\pi)\Re \left[(1 + \xi_\sigma e^{-i\mathbf{h}\cdot\mathbf{R}}) (1 + \xi_\pi^* e^{i\mathbf{h}\cdot\mathbf{R}}) \cos\varphi_m \sin\vartheta_m \cos\Theta_B + \right. \\ & \left. - (1 + \xi_\sigma e^{-i\mathbf{h}\cdot\mathbf{R}}) (1 - \xi_\pi^* e^{i\mathbf{h}\cdot\mathbf{R}}) \cos\vartheta_m \sin\Theta_B \right] \\ \Xi_3 = & 2\Re \left\{ i \left[|\varepsilon_\pi|^2 (1 + \xi_\pi e^{-i\mathbf{h}\cdot\mathbf{R}}) (1 - \xi_\pi^* e^{i\mathbf{h}\cdot\mathbf{R}}) \sin\varphi_m \sin\vartheta_m \sin\Theta_B \cos\Theta_B + \right. \right. \\ & \left. \left. + \varepsilon_\sigma(\Re\varepsilon_\pi) (1 + \xi_\sigma e^{-i\mathbf{h}\cdot\mathbf{R}}) (1 + \xi_\pi^* e^{i\mathbf{h}\cdot\mathbf{R}}) \cos\varphi_m \sin\vartheta_m \cos\Theta_B + \right. \right. \\ & \left. \left. - \varepsilon_\sigma(\Re\varepsilon_\pi) (1 + \xi_\sigma e^{-i\mathbf{h}\cdot\mathbf{R}}) (1 - \xi_\pi^* e^{i\mathbf{h}\cdot\mathbf{R}}) \cos\vartheta_m \sin\Theta_B \right] \right\} \\ I_{sw} = & \varepsilon_\sigma^2 \left[1 + |\xi_\sigma|^2 + 2\Re(\xi_\sigma e^{-i\mathbf{h}\cdot\mathbf{r}}) \right] + |\varepsilon_\pi|^2 \left[1 + |\xi_\pi|^2 + 2\Re(\xi_\pi e^{-i\mathbf{h}\cdot\mathbf{r}}) \cos 2\Theta_B \right] \end{aligned} \quad (4.23)$$

Since the position of the absorbing atom \mathbf{R} appears explicitly in several places, the signal carries direct structural information. The dependence on the incident angle $\Delta\Theta$ is not explicit, but is provided by the amplitude ratios $\xi_i = \xi_i(\Delta\Theta)$, $i \equiv \sigma, \pi$, given by the formula (1.27) (where the dependence on $\Delta\Theta$ is hidden in the deviation parameter η

defined by (1.26)). The photoelectron polarisation is dependent only on the considered transition, that is the absorption edge. The influence of the magnetic properties is via the imbalance in the densities of the final states $\Delta\varrho_f^s$, whose energy integral gives exactly the measure of the magnetic moment (see section about the sum rules, 3.5).

4.5.1 Specific cases

Consideration of the specific cases leads to some simplification of the rather complicated general formula for the MXSW signal from one atom (4.22). At first consider the case of circularly polarised beam. Even though the incident beam polarisation under the experimental conditions is never perfect, the deviation from the circular polarisation can be most often assumed to be small. The polarisation parameters of the incoming beam are for the circular polarisation equal $\varepsilon_\sigma = \frac{1}{\sqrt{2}}$ and $\varepsilon_\pi = \frac{i}{\sqrt{2}}$. The main formula (4.22) remains the same and the wavefield related quantities read

$$\Xi_2 = \Re \left[(1 + \xi_\sigma e^{-i\mathbf{h}\cdot\mathbf{R}}) (1 + \xi_\pi^* e^{i\mathbf{h}\cdot\mathbf{R}}) \cos \varphi_m \sin \vartheta_m \cos \Theta_B + \right. \\ \left. - (1 + \xi_\sigma e^{-i\mathbf{h}\cdot\mathbf{R}}) (1 - \xi_\pi^* e^{i\mathbf{h}\cdot\mathbf{R}}) \cos \vartheta_m \sin \Theta_B \right] \quad (4.24a)$$

$$\Xi_3 = \Re \left[i (1 + \xi_\pi e^{-i\mathbf{h}\cdot\mathbf{R}}) (1 - \xi_\sigma^* e^{i\mathbf{h}\cdot\mathbf{R}}) \right] \sin \varphi_m \sin \vartheta_m \sin \Theta_B \cos \Theta_B \quad (4.24b)$$

$$I_{sw} = 1 + \frac{1}{2} (|\xi_\sigma|^2 + |\xi_\pi|^2) + \Re (\xi_\sigma e^{-i\mathbf{h}\cdot\mathbf{r}}) + \Re (\xi_\pi e^{-i\mathbf{h}\cdot\mathbf{r}}) \cos 2\Theta_B \quad (4.24c)$$

Further simplification is a confinement of the magnetic moment direction to the scattering plane, by setting $\varphi_m = 0$. Such a case is realised in the experiment with an external magnetic field aligning the magnetic moment to this plane. Of course also if the magnetic moments lie naturally in the considered scattering plane, the MXSW signal is defined by the following formulae. The quantity Ξ_2 from the numerator of Ξ , in this case and, like before, for the circularly polarised incoming wave reads

$$\Xi_2 = \Re \left\{ (1 + \xi_\sigma e^{-i\mathbf{h}\cdot\mathbf{R}}) \left[-\sin(\Theta_B - \vartheta_m) + \xi_\pi^* e^{i\mathbf{h}\cdot\mathbf{R}} \sin(\Theta_B + \vartheta_m) \right] \right\} \quad (4.25)$$

The term Ξ_3 vanishes, and the standing wave intensity remains the same, as it obviously does not depend on the direction of the magnetic moment. The MXSW signal can be written in the simple form

$$\Xi = \Pi_e^s \frac{\Re \left\{ (1 + \xi_\sigma e^{-i\mathbf{h}\cdot\mathbf{R}}) \left[-\sin(\Theta_B - \vartheta_m) + \xi_\pi^* e^{i\mathbf{h}\cdot\mathbf{R}} \sin(\Theta_B + \vartheta_m) \right] \right\}}{1 + \frac{1}{2} (|\xi_\sigma|^2 + |\xi_\pi|^2) + \Re (\xi_\sigma e^{-i\mathbf{h}\cdot\mathbf{r}}) + \Re (\xi_\pi e^{-i\mathbf{h}\cdot\mathbf{r}}) \cos 2\Theta_B} \frac{\Delta\varrho_f^s}{\varrho_f} \quad (4.26)$$

Then of course further specific cases can be obtained by considering specific values of the angle ϑ_m , which defines the magnetic moment direction within the scattering plane. The simplest one, possible to realise experimentally by applying the magnetic field aligning the magnetic moments, is when they remain in the scattering plane and in the reflecting lattice planes, that is are perpendicular to \mathbf{h} . This case corresponds to $\vartheta_m = \frac{\pi}{2}$. The MXSW signal reads in such a case

$$\Xi = \Pi_e^s \frac{\Re \left[(1 + \xi_\sigma e^{-i\mathbf{h}\cdot\mathbf{R}}) (1 + \xi_\pi^* e^{i\mathbf{h}\cdot\mathbf{R}}) \right] \cos \Theta_B}{1 + \frac{1}{2} (|\xi_\sigma|^2 + |\xi_\pi|^2) + \Re (\xi_\sigma e^{-i\mathbf{h}\cdot\mathbf{R}}) + \Re (\xi_\pi e^{-i\mathbf{h}\cdot\mathbf{R}}) \cos 2\Theta_B} \frac{\Delta\varrho_f^s}{\varrho_f} \quad (4.27)$$

4.5.2 XMCD as difference between magnetic moment orientations

Similarly, like in chapter devoted to the standard XMCD effect (3), one can consider the case of the signal calculated not as a difference between the cross-sections for different helicities of the incoming beam, but rather as a difference between the cross-sections for opposite magnetic moment orientations. From figure 4.2 one can easily see, that the reversal of the magnetic moment orientation is equivalent to the transformation $\vartheta_m \rightarrow \vartheta_m + \pi$. The changes in the quantities defining the final signal Ξ , related to the wavefield, need to be considered.

Since under the considered transformation, both $\sin \vartheta_m$ and $\cos \vartheta_m$ change the sign, the moduli of the polarisation vector components given by equations (4.11) remain unchanged. The difference appears in the mixed term $\Re(i\varepsilon_x \varepsilon_y^*)$, in the same way as in chapter 3. The mixed term changes the sign, when the magnetic moment is flipped, thus exchanging the roles of \mathfrak{A} and \mathfrak{B} ($\mathfrak{A} \leftrightarrow \mathfrak{B}$). This is an expected behaviour, which is in this case not observed when the helicity is changed.

Using the previously introduced Ξ_2 and Ξ_3 quantities (equations (4.13b) and (4.15)), the mixed term can be written as a sum of them, $\Re(i\varepsilon_x \varepsilon_y^*) = \Xi_2 + \Xi_3$. The transformation $\vartheta_m \rightarrow \vartheta_m + \pi$ changes Ξ_2 and Ξ_3 by sign, the same as the entire mixed term. The \mathfrak{C} quantity remains unchanged. The XMCD signal calculated between two opposite orientations of the magnetic moment, following the same procedure as in section 3.1.4, can be written as

$$\begin{aligned} \Xi_{\mathbf{m}} = & \left\{ \varrho_f^\uparrow \left[\frac{1}{2} \mathfrak{a}^\uparrow (|\mathfrak{A}_+^{-\mathbf{m}}|^2 - |\mathfrak{A}_+^{+\mathbf{m}}|^2) + \frac{1}{2} \mathfrak{b}^\uparrow (|\mathfrak{B}_+^{-\mathbf{m}}|^2 - |\mathfrak{B}_+^{+\mathbf{m}}|^2) \right] + \right. \\ & \left. + \varrho_f^\downarrow \left[\frac{1}{2} \mathfrak{a}^\downarrow (|\mathfrak{A}_+^{-\mathbf{m}}|^2 - |\mathfrak{A}_+^{+\mathbf{m}}|^2) + \frac{1}{2} \mathfrak{b}^\downarrow (|\mathfrak{B}_+^{-\mathbf{m}}|^2 - |\mathfrak{B}_+^{+\mathbf{m}}|^2) \right] \right\} \cdot \\ & \cdot \left\{ \varrho_f^\uparrow \left[\frac{1}{2} \mathfrak{a}^\uparrow (|\mathfrak{A}_+^{-\mathbf{m}}|^2 + |\mathfrak{A}_+^{+\mathbf{m}}|^2) + \frac{1}{2} \mathfrak{b}^\uparrow (|\mathfrak{B}_+^{-\mathbf{m}}|^2 + |\mathfrak{B}_+^{+\mathbf{m}}|^2) + 2\mathfrak{c}|\mathfrak{C}|^2 \right] + \right. \\ & \left. + \varrho_f^\downarrow \left[\frac{1}{2} \mathfrak{a}^\downarrow (|\mathfrak{A}_+^{-\mathbf{m}}|^2 + |\mathfrak{A}_+^{+\mathbf{m}}|^2) + \frac{1}{2} \mathfrak{b}^\downarrow (|\mathfrak{B}_+^{-\mathbf{m}}|^2 + |\mathfrak{B}_+^{+\mathbf{m}}|^2) + 2\mathfrak{c}|\mathfrak{C}|^2 \right] \right\}^{-1} \quad (4.28) \end{aligned}$$

Since in the $|\mathfrak{A}|^2$ and $|\mathfrak{B}|^2$ quantities only the mixed term changes, the combinations from the numerator read $|\mathfrak{A}_+^{-\mathbf{m}}|^2 - |\mathfrak{A}_+^{+\mathbf{m}}|^2 = -2(\Xi_2 + \Xi_3)$ and $|\mathfrak{B}_+^{-\mathbf{m}}|^2 - |\mathfrak{B}_+^{+\mathbf{m}}|^2 = 2(\Xi_2 + \Xi_3)$. Using the relations between the transition rates, the numerator can be transformed to the simple form of $(\Xi_2 + \Xi_3)(\mathfrak{a}^\downarrow - \mathfrak{a}^\uparrow)\Delta\varrho_f^s$. In contrary, in the denominator the mixed terms disappear, and only the moduli of the polarisation vector components remain. Their sum $|\varepsilon_x|^2 + |\varepsilon_y|^2 + |\varepsilon_z|^2$ gives the relative standing wave intensity I_{sw} . Thus, the final XMCD signal reads

$$\Xi_{\mathbf{m}} = \Pi_e^s \frac{\Xi_2 + \Xi_3}{I_{sw}} \frac{\Delta\varrho_f^s}{\varrho_f} \quad (4.29)$$

One notices immediately, that this result differs from the one obtained by considering the difference between cross-section for opposite helicities by the term Ξ_3 (equation (4.22)). Further discussion about this term is given at the end of this chapter. This interesting feature, related to the fact that the magnetic circular dichroism is in this case induced not by a single wave, but by the interference field resulting from the existence of two waves, is one of the properties, which distinguish the new MXSW technique from the regular XMCD.

4.6 MXSW for many atoms

So far the presented formulae concern the case of one magnetic atom located at the position \mathbf{R} . In realistic cases more non-equivalent atoms of a given element can be located in the unit cell. The cases when these atoms exhibit different magnetic moments (in magnitude or direction) are of particular interest for the studies using the MXSW method, since its position sensitivity can be then fully exploited. In this section a case of n atoms of the same element (as the XMCD signal is obtained at the given absorption edge only from one atom kind) located at the positions \mathbf{R}_j is considered. In a general case those atoms are assumed to have different magnetic moments, that is exhibit different final band polarisations $(\Delta\varrho_f^s)_j$.

The formula for the signal from multiple atoms is obtained in the same way as the expression for the secondary radiation yield in section 1.7. The total absorption cross-section for all atoms is a sum of individual cross-sections. Since the XMCD signal is a normalised difference between the cross-sections for each of two helicities, the MXSW signal for many atoms may be obtained by the summation over the atoms in the nominator and denominator of (4.22). It will be denoted here by Υ and following the formula for Ξ , reads with abbreviations

$$\Upsilon = \Pi_e^s \frac{\frac{1}{n} \sum_{j=1}^n (\Xi_2)_j (\Delta\varrho_f^s)_j}{\frac{1}{n} \varrho_f \sum_{j=1}^n (I_{sw})_j - \frac{1}{n} \Pi_e^s \sum_{j=1}^n (\Xi_3)_j (\Delta\varrho_f^s)_j} \quad (4.30)$$

The quantities $(\Xi_2)_j$, $(\Xi_3)_j$ and $(I_{sw})_j$ are given by the formulae (4.23), where the substitution $\mathbf{R} \rightarrow \mathbf{R}_j$ should be made. It was assumed, that the total density of the final states ϱ_f is the same for all the atoms, since they are of the same kind, even if their magnetic moments are different.

The sums in the expression (4.30) can be transformed. The one involving the standing wave intensity gives simply the secondary fluorescence yield

$$\begin{aligned} y &= \frac{1}{n} \sum_{j=1}^n (I_{sw})_j = \\ &= \varepsilon_\sigma^2 \left\{ 1 + |\xi_\sigma|^2 + 2\Re \left[\xi_\sigma (F_{sw}^{\mathbf{h}})^* \right] \right\} + |\varepsilon_\pi|^2 \left\{ 1 + |\xi_\pi|^2 + 2\Re \left[\xi_\pi (F_{sw}^{\mathbf{h}})^* \right] \cos 2\Theta_B \right\} \end{aligned} \quad (4.31)$$

where the standing wave structure factor $F_{sw}^{\mathbf{h}} := \frac{1}{n} \sum_{j=1}^n e^{i\mathbf{h} \cdot \mathbf{R}_j}$ was already defined in the expression (1.37). This quantity carries the information about the spatial arrangement of the atoms of a given element.

For convenience, the numerator and denominator of the expression (4.30) can be multiplied by $1/\varrho_f$, so that the normalised difference in density of states $(\Delta\varrho_f^s)_j/\varrho_f$ appears. The two remaining sums involving the quantities denoted by Ξ_2 and Ξ_3 can be written in

the form

$$\begin{aligned}\Upsilon_2 &:= \frac{1}{n\varrho_f} \sum_{j=1}^n (\Xi_2)_j (\Delta\varrho_f^s)_j = \\ &= 2\varepsilon_\sigma (\Im\varepsilon_\pi) \left\{ \left[F_1^0 (1 + \Re(\xi_\sigma \xi_\pi^*)) + \Re\left((\xi_\sigma + \xi_\pi) (F_1^h)^*\right) \right] \cos \Theta_B + \right. \\ &\quad \left. - \left[F_3^0 (1 - \Re(\xi_\sigma \xi_\pi^*)) + \Re\left((\xi_\sigma - \xi_\pi) (F_3^h)^*\right) \right] \sin \Theta_B \right\}\end{aligned}\quad (4.32)$$

$$\begin{aligned}\Upsilon_3 &:= \frac{1}{n\varrho_f} \sum_{j=1}^n (\Xi_3)_j (\Delta\varrho_f^s)_j = \\ &= 4|\varepsilon_\pi|^2 \Re\left[i\xi_\pi (F_2^h)^*\right] \sin \Theta_B \cos \Theta_B + \\ &\quad + 2\varepsilon_\sigma (\Re\varepsilon_\pi) \left\{ \left[F_1^0 \Re(i\xi_\sigma \xi_\pi^*) + \Re\left(i(\xi_\sigma - \xi_\pi) (F_1^h)^*\right) \right] \cos \Theta_B + \right. \\ &\quad \left. - \left[-F_3^0 \Re(i\xi_\sigma \xi_\pi^*) + \Re\left(i(\xi_\sigma + \xi_\pi) (F_3^h)^*\right) \right] \sin \Theta_B \right\}\end{aligned}\quad (4.33)$$

With those new abbreviations, the MXSW signal from multiple atoms is expressed via the relation

$$\boxed{\Upsilon = \Pi_e^s \frac{\Upsilon_2}{y - \Pi_e^s \Upsilon_3}}\quad (4.34)$$

The symbols F have the following meaning

$$F_1^0 = \frac{1}{n\varrho_f} \sum_{j=1}^n (\Delta\varrho_f^s)_j \cos(\varphi_m)_j \sin(\vartheta_m)_j \quad (4.35a)$$

$$F_1^h = \frac{1}{n\varrho_f} \sum_{j=1}^n (\Delta\varrho_f^s)_j \cos(\varphi_m)_j \sin(\vartheta_m)_j e^{i\mathbf{h}\cdot\mathbf{R}_j} \quad (4.35b)$$

$$F_2^0 = \frac{1}{n\varrho_f} \sum_{j=1}^n (\Delta\varrho_f^s)_j \sin(\varphi_m)_j \sin(\vartheta_m)_j \quad (4.35c)$$

$$F_2^h = \frac{1}{n\varrho_f} \sum_{j=1}^n (\Delta\varrho_f^s)_j \sin(\varphi_m)_j \sin(\vartheta_m)_j e^{i\mathbf{h}\cdot\mathbf{R}_j} \quad (4.35d)$$

$$F_3^0 = \frac{1}{n\varrho_f} \sum_{j=1}^n (\Delta\varrho_f^s)_j \cos(\vartheta_m)_j \quad (4.35e)$$

$$F_3^h = \frac{1}{n\varrho_f} \sum_{j=1}^n (\Delta\varrho_f^s)_j \cos(\vartheta_m)_j e^{i\mathbf{h}\cdot\mathbf{R}_j} \quad (4.35f)$$

where F_2^0 has been added by analogy to F_1^0 and F_3^0 for completeness, even though it does not appear in the expression for the MXSW signal Υ .

Before a more detailed discussion regarding the quantities F , one should consider the meaning of the term $(\Delta\varrho_f^s)_j$. As discussed in section 3.1.4, the magnetic moment is directly

related to the energy integral over the spin-polarised density of states. This implies, that a single value of $(\Delta\rho_f^s)_j$ at the energy where the MXSW scan (angular, by changing $\Delta\Theta$) was performed, does not suffice to evaluate rigorously the magnetic moment. One would need to perform a two dimensional scan where both the energy as well as incident angle $\Delta\Theta$ would need to be changed. The energy scan over a range covering the absorption edge(s) allows calculation of the integrals needed to evaluate magnetic moment, whereas the angular scan enables the standing wave movement through the lattice and thus provides the spatial resolution. In such two dimensional scan, the fact that the Bragg angle and thus the angular position of the reflection domain change with the energy would need to be taken into account. What is challenging from the practical point of view, such a two dimensional scan would require rather increased acquisition time, in particular for the weakly magnetic systems or the case of absorption edges, where the XMCD signal is small by definition (e.g. K-edge).

Instead, use can be made out of the standard angular standing wave scan at a fixed energy by assuming that the magnetic moment is proportional to the spin-polarised density of states $(\Delta\rho_f^s)_j/\rho_f$. Such an approach, even though not allowing to compute the exact value of the magnetic moment, allows to observe the changes in this quantity between the various atoms of the same element in the system. In other words, the MXSW signal can still provide valuable information about the differences in magnetic moments of the atoms building different magnetic sublattices.

The assumption that the XMCD signal measured at the fixed energy remains proportional to the magnetic moment is also used in other magnetism-related methods. In Fourier transform holography the magnetic contrast is achieved via the XMCD effect by using the circularly polarised x-rays and tuning the energy to the fixed value at the absorption edge. The method is used to image the magnetic nanostructures under the assumption, that the contrast observed via the dichroic signal at fixed energy reproduces the changes of the magnetic moments across the sample [100, 101].

In a similar manner a magnetic contrast is added to the small angle x-ray scattering (SAXS). The absorption effects influence the diffraction via the dispersion corrections f' and f'' and thus an XMCD signal is also observed in the scattered intensity. The information about the magnetic structures on the nanometer scale is consequently obtained from the difference between the signals for each helicity. Similarly like in the case of magnetic Fourier transform holography, also magnetic SAXS is performed experimentally at one fixed energy [102]. The conclusions about the distributions of magnetic moments in the sample are drawn then under the same assumption as earlier, that is that the differences in the magnetic moments are reflected in the differences in the XMCD signal at the fixed energy.

4.6.1 Magnetic standing wave structure factor

Having justified the use of the signal recorded at the fixed energy to track the differences in magnetic moments in the lattice, one may from now on use the abbreviation $(\Delta\rho_f^s)_j/\rho_f = m_j$, with m_j denoting the magnitude of the magnetic moment of the atom j . With that, one can interpret easier the meaning of the quantities F given by equations (4.35). From figure 4.2 one can see that the components of the magnetic moment vector \mathbf{m} in the coordinate system \mathcal{O}' related to the scattering process, are simply

$$m'_x = m \cos \varphi_m \sin \vartheta_m \quad (4.36a)$$

$$m'_y = m \sin \varphi_m \sin \vartheta_m \quad (4.36b)$$

$$m'_z = m \cos \vartheta_m \quad (4.36c)$$

One can easily identify those combinations of the trigonometrical functions of the angles φ_m and ϑ_m in equations (4.35). They can be written thus in the following way

$$F_1^0 = \frac{1}{n} \sum_{j=1}^n (m'_x)_j := \overline{m'_x} \quad (4.37a)$$

$$F_1^{\mathbf{h}} = \frac{1}{n} \sum_{j=1}^n (m'_x)_j e^{i\mathbf{h} \cdot \mathbf{R}_j} \quad (4.37b)$$

$$F_2^0 = \frac{1}{n} \sum_{j=1}^n (m'_y)_j := \overline{m'_y} \quad (4.37c)$$

$$F_2^{\mathbf{h}} = \frac{1}{n} \sum_{j=1}^n (m'_y)_j e^{i\mathbf{h} \cdot \mathbf{R}_j} \quad (4.37d)$$

$$F_3^0 = \frac{1}{n} \sum_{j=1}^n (m'_z)_j := \overline{m'_z} \quad (4.37e)$$

$$F_3^{\mathbf{h}} = \frac{1}{n} \sum_{j=1}^n (m'_z)_j e^{i\mathbf{h} \cdot \mathbf{R}_j} \quad (4.37f)$$

where the symbol \overline{m} denotes the ensemble average over the atoms in the unit cell of the given kind. Now one can notice, that the quantities F are in fact the components of two vectors, which will be denoted by $\mathbf{F}_{msw}^{\mathbf{h}}$ and \mathbf{F}_{msw}^0 or $\overline{\mathbf{m}}$. Those are given by the formulae

$$\mathbf{F}_{msw}^{\mathbf{h}} = \frac{1}{n} \sum_{j=1}^n \mathbf{m}'_j e^{i\mathbf{h} \cdot \mathbf{R}_j} \quad (4.38)$$

$$\mathbf{F}_{msw}^0 = \frac{1}{n} \sum_{j=1}^n \mathbf{m}'_j \quad (4.39)$$

The relations between those vectors and the components given by equations (4.37) are

$$\mathbf{F}_{msw}^{\mathbf{h}} = F_1^{\mathbf{h}} \hat{\mathbf{x}}' + F_2^{\mathbf{h}} \hat{\mathbf{y}}' + F_3^{\mathbf{h}} \hat{\mathbf{z}}' \quad (4.40)$$

$$\mathbf{F}_{msw}^0 = F_1^0 \hat{\mathbf{x}}' + F_2^0 \hat{\mathbf{y}}' + F_3^0 \hat{\mathbf{z}}' \quad (4.41)$$

The quantity $\mathbf{F}_{msw}^{\mathbf{h}}$ will be called a magnetic standing wave structure factor. It is a magnetic counterpart to the standard standing wave structure factor $F_{sw}^{\mathbf{h}}$. The components of the $\mathbf{F}_{msw}^{\mathbf{h}}$ vector, together with the average value of the magnetic moment $\overline{\mathbf{m}}$, are what determines the value of the MXSW signal. This is an important result. The magnetic standing wave structure factor contains the information about the spatial and angular distribution of the magnetic moments in the unit cell, so the experimental determination of the MXSW signal allows to measure directly the components of the $\mathbf{F}_{msw}^{\mathbf{h}}$ vector and obtain information about the magnetic structure.

4.6.2 Specific cases

An inspection of some simplified cases can provide better understanding of the emergence of the MXSW signal. At first, consider the case of a circularly polarised incoming wave, what already greatly simplifies the formula for Υ , which becomes

$$\begin{aligned} \Upsilon = \Pi_e^s & \left\{ \left[F_1^0 (1 + \Re(\xi_\sigma \xi_\pi^*)) + \Re((\xi_\sigma + \xi_\pi) (F_1^{\mathbf{h}})^*) \right] \cos \Theta_B + \right. \\ & \left. - \left[F_3^0 (1 - \Re(\xi_\sigma \xi_\pi^*)) + \Re((\xi_\sigma - \xi_\pi) (F_3^{\mathbf{h}})^*) \right] \sin \Theta_B \right\} \cdot \\ & \cdot \left\{ 1 + \frac{1}{2} (|\xi_\sigma|^2 + |\xi_\pi|^2) + \Re[(\xi_\sigma + \xi_\pi \cos 2\Theta_B) (F_{sw}^{\mathbf{h}})^*] + \right. \\ & \left. - 2\Pi_e^s \Re[i\xi_\pi (F_2^{\mathbf{h}})^*] \sin \Theta_B \cos \Theta_B \right\}^{-1} \end{aligned} \quad (4.42)$$

In order to draw some qualitative conclusions about the strength of the MXSW signal, one can consider a very simple case of the magnetic moments aligned in the diffraction plane, perpendicular to the reciprocal lattice vector \mathbf{h} . This corresponds to the values of the angles $\varphi_m = 0$ and $\vartheta_m = \frac{\pi}{2}$ and vanishing of the m'_y and m'_z components of the magnetic moments. Consequently, also the components of the magnetic standing wave structure factor $F_2^{\mathbf{h}}$ and $F_3^{\mathbf{h}}$ (as well as F_2^0 and F_3^0) vanish, and the formula for the MXSW signal takes a very simple form

$$\Upsilon = \Pi_e^s \frac{\{ F_1^0 [1 + \Re(\xi_\sigma \xi_\pi^*)] + \Re[(\xi_\sigma + \xi_\pi) (F_1^{\mathbf{h}})^*] \} \cos \Theta_B}{1 + \frac{1}{2} (|\xi_\sigma|^2 + |\xi_\pi|^2) + \Re[(\xi_\sigma + \xi_\pi \cos 2\Theta_B) (F_{sw}^{\mathbf{h}})^*]} \quad (4.43)$$

Consider a situation, when the Bragg angle Θ_B is small, so that $\cos 2\Theta_B \simeq 1$ and there is nearly no difference in scattering between σ - and π -components, so that one can write $\xi_\pi \approx \xi_\sigma = \xi$. Then

$$\begin{aligned} \Upsilon &= \Pi_e^s \frac{F_1^0 (1 + |\xi|^2) + 2\Re[\xi (F_1^{\mathbf{h}})^*]}{1 + |\xi|^2 + 2\Re[\xi (F_{sw}^{\mathbf{h}})^*]} = \Pi_e^s F_1^0 \frac{1 + |\xi|^2 + 2\Re[\xi (F_1^{\mathbf{h}})^* / F_1^0]}{1 + |\xi|^2 + 2\Re[\xi (F_{sw}^{\mathbf{h}})^*]} = \\ &= \Pi_e^s F_1^0 \frac{1 + |\xi|^2 + 2\Re[\xi (F_{sw}^{\mathbf{h}})^*] + 2\Re\{\xi [(F_1^{\mathbf{h}})^* / F_1^0 - (F_{sw}^{\mathbf{h}})^*]\}}{1 + |\xi|^2 + 2\Re[\xi (F_{sw}^{\mathbf{h}})^*]} = \\ &= \Pi_e^s F_1^0 \left\{ 1 + \frac{2\Re[\xi ((F_1^{\mathbf{h}})^* / F_1^0 - (F_{sw}^{\mathbf{h}})^*)]}{1 + |\xi|^2 + 2\Re[\xi (F_{sw}^{\mathbf{h}})^*]} \right\} = \Pi_e^s F_1^0 \left[1 + \frac{1}{y} 2\Re(\xi \Delta F^*) \right] \end{aligned} \quad (4.44)$$

with $\Delta F := (F_1^{\mathbf{h}})^* / F_1^0 - (F_{sw}^{\mathbf{h}})^*$ being a difference between normalised magnetic standing wave structure factor and regular $(F_{sw}^{\mathbf{h}})^*$. This quantity can be then regarded as a measure of the deviation of magnetic structure from the atomic one. The presented consideration shows, that the MXSW signal is proportional to this difference. If ΔF is zero Υ is equal to $\Pi_e^s F_1^0 = \Pi_e^s \bar{m}$, that is to the XMCD signal without the standing wave, or in other words away from the reflection domain. Since the difference in scattering between the σ - and π -polarisation components was neglected here, in fact this effect leads to small variation in the XMCD signal in the reflection domain even if $\Delta F = 0$. The condition of non-vanishing of ΔF indicates, that the strongest MXSW contrast can be observed for the systems exhibiting magnetic sublattices, as then the atomic and magnetic structures are different.

Simplest examples of such magnetic systems are ferrimagnets and antiferromagnets. One should notice, however, that the periodicity of the magnetic structure has to be the same as the periodicity of the nuclear structure, or more formally, that the propagation vector \mathbf{k}_m has to be equal $(0, 0, 0)$ [8]. Consider the situation when the magnetic unit cell is bigger than the nuclear one. Since no standing wave with longer period than the dimensions of the nuclear unit cell can be excited, the MXSW signal obtained from the magnetic structure with longer period (and \mathbf{k}_m equals for example $(\frac{1}{2}, 0, 0)$) will be a measure of the projection of the average magnetic structure onto the nuclear unit cell and thus will provide no useful information about the real magnetic structure. This limits the number of the systems, where the method can be applied successfully.

4.7 Correction for the complex wavevector for MXSW

So far in this chapter it was assumed for simplicity that all the wavevectors are real. Now, similarly like in section 1.8 for the standard standing wave experiment, a correction accounting for the imaginary part of the wavevector is introduced. Since in the case of MXSW one considers a differential signal, the absorption correction should be negligible, as the correction terms in numerator and denominator remain similar.

The wavevector of the "0" wave is in fact a complex vector and is related to the vacuum wavevector via the relation (1.42). The complete expression for the vector potential within the electric dipole approximation given by (4.1) can be written in a more convenient form

$$\begin{aligned} \mathcal{A} = A_0 \left\{ \varepsilon_\sigma \hat{\boldsymbol{\varepsilon}}_\sigma [1 + \xi_\sigma e^{-i\mathbf{h}\cdot\mathbf{R}}] \exp \left[-i \left(\frac{1}{2}\chi_0 + X_0^\sigma \right) \frac{\mathbf{n}\cdot\mathbf{R}}{\gamma_0} \right] + \right. \\ \left. + \varepsilon_\pi [\hat{\boldsymbol{\varepsilon}}_{0\pi} + \xi_\pi \hat{\boldsymbol{\varepsilon}}_{\mathbf{h}\pi} e^{-i\mathbf{h}\cdot\mathbf{R}}] \exp \left[-i \left(\frac{1}{2}\chi_0 + X_0^\pi \right) \frac{\mathbf{n}\cdot\mathbf{R}}{\gamma_0} \right] \right\} e^{i\omega t - i\mathbf{k}_0^g \cdot \mathbf{R}} \quad (4.45) \end{aligned}$$

One can use the abbreviation for the scalar product $\mathbf{n}\cdot\mathbf{R} = z$, as it denotes the distance from the physical crystal surface to the absorbing atom. The expression in the curly brackets is a polarisation vector $\boldsymbol{\varepsilon}$, whose components determine all the quantities influencing the absorption cross-section. By comparison with equation (4.7) one can notice, that the considered correction can be introduced by substitution

$$\varepsilon_{\mathbf{p}} \rightarrow \varepsilon_{\mathbf{p}} \exp \left[-i \left(\frac{1}{2}\chi_0 + X_0^{\mathbf{p}} \right) \frac{z}{\gamma_0} \right] \quad (4.46)$$

with $\mathbf{p} \equiv \sigma, \pi$.

The quantities $|\mathfrak{A}|^2$, $|\mathfrak{B}|^2$ and $|\mathfrak{C}^2|$, which determine directly the absorption cross-section, involve the following combinations of polarisation parameters: ε_σ^2 , $|\varepsilon_\pi|^2$ and $\varepsilon_\sigma \varepsilon_\pi^*$. Therefore, in the expressions for moduli of the polarisation vector components (4.11) and for the mixed term $\Re(\varepsilon_x \varepsilon_y^*)$, (4.12), which define the moduli $|\mathfrak{A}|^2$, $|\mathfrak{B}|^2$ and $|\mathfrak{C}^2|$ (given explicitly by (A.22)), the following substitutions should be made to take into account the

correction for the complex wavevectors

$$\varepsilon_\sigma^2 \rightarrow \varepsilon_\sigma^2 \exp \left[(k\Im\chi_0 + 2\Im X_0^\sigma) \frac{z}{\gamma_0} \right] = \varepsilon_\sigma^2 e^{-\mu_\sigma z/\gamma_0} \quad (4.47a)$$

$$|\varepsilon_\pi|^2 \rightarrow |\varepsilon_\pi|^2 e^{-\mu_\pi z/\gamma_0} \quad (4.47b)$$

$$\varepsilon_\sigma \varepsilon_\pi^* \rightarrow \varepsilon_\sigma \varepsilon_\pi^* \exp \left\{ [k\Im\chi_0 + i((X_0^\pi)^* - X_0^\sigma)] \frac{z}{\gamma_0} \right\} \quad (4.47c)$$

where the absorption coefficient was introduced already by equation (1.43). One should note that the third substitution contains a complex number, so it should be put under the \Re symbol in the $|\mathfrak{A}|^2$, $|\mathfrak{B}|^2$ and $|\mathfrak{C}|^2$ expressions.

Apart from the imaginary parts of the wavevectors, which were neglected so far, one needs to take into account also the attenuation of the emitted secondary signal on the way from the emitting atom to the detector. This issue was already discussed in details in section 1.8. Since each of the absorption cross-sections present in the expression for the XMCD signal is affected, the correction for the absorption of the secondary radiation can be introduced via the transformation of each transition rate

$$\zeta_\pm^{\uparrow\downarrow} \rightarrow \int_0^\infty \zeta_\pm^{\uparrow\downarrow}(z) \exp \left(-\frac{\mu_{lin} z}{\sin \alpha} \right) \quad (4.48)$$

Due to the additive property of the integral, one can still perform all the transformations from the formula (4.18) to (4.22). Also in this case the order of summation and integration can be flipped, so the case of many atoms can be easily introduced. In the same way as in chapter 1.8, it is assumed that the crystal and magnetic structures are not depth dependent, so the standing wave structure factor and magnetic standing wave structure factors are assumed to be independent of z and taken out of the integral. The expressions form the numerator and denominator of the expression (4.30) with the absorption correction read

$$\begin{aligned} \Upsilon_2 = \frac{1}{n} \sum_{j=1}^n \int_0^\infty (\Xi_2)_j m_j dz = & 2\varepsilon_\sigma (\Im\varepsilon_\pi) \Re \left\{ \left\{ \left[F_1^0 (1 + \xi_\sigma \xi_\pi^*) + \xi_\sigma (F_1^h)^* + \xi_\pi^* F_1^h \right] \cos \Theta_B + \right. \right. \\ & \left. \left. - \left[F_3^0 (1 - \xi_\sigma \xi_\pi^*) + \xi_\sigma (F_3^h)^* - \xi_\pi^* F_3^h \right] \sin \Theta_B \right\} \cdot \right. \\ & \left. \underbrace{\int_0^\infty \exp \left\{ [k\Im\chi_0 + i((X_0^\pi)^* - X_0^\sigma)] \frac{z}{\gamma_0} - \frac{\mu_{lin} z}{\sin \alpha} \right\} dz}_{\mathcal{I}_2} \right\} \quad (4.49) \end{aligned}$$

$$\begin{aligned}
\Upsilon_3 &= \frac{1}{n} \sum_{j=1}^n \int_0^\infty (\Xi_3)_j m_j dz = \\
&= 4|\varepsilon_\pi|^2 \Re \left[i \xi_\pi (F_2^{\text{h}})^* \right] \sin \Theta_B \cos \Theta_B \overbrace{\int_0^\infty \exp \left\{ -\frac{\mu_\pi z}{\gamma_0} - \frac{\mu_{\text{lin}} z}{\sin \alpha} \right\} dz}^{\mathcal{I}} + \\
&\quad + 2\varepsilon_\sigma (\Re \varepsilon_\pi) \Re \left\{ i \left\{ \left[F_1^0 (1 + \xi_\sigma \xi_\pi^*) + \xi_\sigma (F_1^{\text{h}})^* + \xi_\pi^* F_1^{\text{h}} \right] \cos \Theta_B + \right. \right. \\
&\quad \quad \left. \left. - \left[F_3^0 (1 - \xi_\sigma \xi_\pi^*) + \xi_\sigma (F_3^{\text{h}})^* - \xi_\pi^* F_3^{\text{h}} \right] \sin \Theta_B \right\} \cdot \right. \\
&\quad \left. \cdot \int_0^\infty \exp \left\{ \left[k \Im \chi_0 + i ((X_0^\pi)^* - X_0^\sigma) \right] \frac{z}{\gamma_0} - \frac{\mu_{\text{lin}} z}{\sin \alpha} \right\} dz \right\} \quad (4.50)
\end{aligned}$$

The integration and summation over the $(I_{sw})_j$ provide the secondary radiation yield, calculated already in section 1.9.4 and given by equation (1.66).

The integral \mathcal{I} was already discussed in section 1.8. It gives the effective thickness z_{eff}^π , defined in equation (1.46). Thus, one needs to calculate the second integral, \mathcal{I}_2 . This is done in details in appendix A.4. The integral reads

$$\int_0^\infty \exp \left\{ \left[k \Im \chi_0 + i ((X_0^\pi)^* - X_0^\sigma) \right] \frac{z}{\gamma_0} - \frac{\mu_{\text{lin}} z}{\sin \alpha} \right\} dz = -\frac{\mu_1 + i\mu_2}{\mu_1^2 + \mu_2^2} \quad (4.51)$$

with the symbols μ_1 and μ_2 having the following meaning

$$\mu_1 = \left[\frac{k \Im \chi_0}{\gamma_0} + \frac{1}{\gamma_0} (\Im X_0^\sigma + \Im X_0^\pi) - \frac{\mu_{\text{lin}}}{\sin \alpha} \right] \quad (4.52a)$$

$$\mu_2 = \frac{1}{\gamma_0} (\Re X_0^\sigma - \Re X_0^\pi) \quad (4.52b)$$

μ_1 can be regarded as an absorption coefficient being an average one between the σ - and π -polarisations (plus the term accounting for the attenuation of emitted secondary radiation). The quantity μ_2 is related to the period of the Pendellösung oscillations. In the exponential function this quantity is the imaginary part of the argument, and thus it leads to an oscillatory modulation of the function being multiplied by the exponent.

The most general expression for the MXSW signal, with the absorption correction, has the same form as before, given by (4.34). Now the symbols Υ_2 and Υ_3 have the following meaning

$$\begin{aligned}
\Upsilon_2 &= 2\varepsilon_\sigma (\Im \varepsilon_\pi) \Re \left\{ \left\{ \left[F_1^0 (1 + \xi_\sigma \xi_\pi^*) + \xi_\sigma (F_1^{\text{h}})^* + \xi_\pi^* F_1^{\text{h}} \right] \cos \Theta_B + \right. \right. \\
&\quad \left. \left. - \left[F_3^0 (1 - \xi_\sigma \xi_\pi^*) + \xi_\sigma (F_3^{\text{h}})^* - \xi_\pi^* F_3^{\text{h}} \right] \sin \Theta_B \right\} \left(-\frac{\mu_1 + i\mu_2}{\mu_1^2 + \mu_2^2} \right) \right\} \quad (4.53)
\end{aligned}$$

$$\begin{aligned}
\Upsilon_3 = & 4|\varepsilon_\pi|^2 \Re \left[i\xi_\pi (F_2^{\text{h}})^* \right] \sin \Theta_B \cos \Theta_B z_{\text{eff}}^\pi + \\
& + 2\varepsilon_\sigma (\Re \varepsilon_\pi) \Re \left\{ i \left\{ \left[F_1^0 (1 + \xi_\sigma \xi_\pi^*) + \xi_\sigma (F_1^{\text{h}})^* + \xi_\pi^* F_1^{\text{h}} \right] \cos \Theta_B + \right. \right. \\
& \left. \left. - \left[F_3^0 (1 - \xi_\sigma \xi_\pi^*) + \xi_\sigma (F_3^{\text{h}})^* - \xi_\pi^* F_3^{\text{h}} \right] \sin \Theta_B \right\} \left(-\frac{\mu_1 + i\mu_2}{\mu_1^2 + \mu_2^2} \right) \right\} \quad (4.54)
\end{aligned}$$

and the total secondary radiation yield y is given by equation (1.66).

4.8 Detection of XMCD via x-ray fluorescence

In an x-ray standing wave experiment the determination of the absorption cross-section via measuring the attenuation of the transmitted beam is not possible. This is both due to the bulk crystals used as samples or substrates for the thin films and to the nature of the effect itself — the influence of the standing wave on the absorption cannot be seen directly in the transmitted beam². Therefore, one should discuss the possibility of detecting the XMCD signal when the absorption cross-section is determined indirectly by detecting the secondary radiation — the product of the core hole decay.

The possibility of detecting an XMCD signal via measuring the fluorescence spectra was predicted theoretically by Strange *et al.* [103] using first-principles calculation based on a fully relativistic multiple-scattering theory. Soon after it was demonstrated experimentally at the iron $L_{2,3}$ absorption edges [99] and researchers concluded that the signal is a measure of the spin-polarised density of the final states. For the case of the K-edge of the 3d metals it was shown by the group of Juhin *et al.* [104] using an yttrium-iron-garnet single crystalline sample that the fluorescence detected XMCD is proportional to the signal measured by monitoring the beam transmission. Also for the case of the cobalt K-edge in HoCo_2 a similar measurement was reported [105].

The quantitative analysis of fluorescence detected XMCD signal based on the sum rules is justified in case of dilute samples. This was shown for the $L_{2,3}$ absorption edges of the 3d metals [106, 107]. On the other hand, already in 1994 it was shown by de Groot and his group [108], that the absorption cross-section determined using the fluorescence spectroscopy can deviate from the one obtained from direct transmission measurement and that this can also affect the determination of the XMCD effect. Compared to the transmission measurement, fluorescence detected XMCD signal can show deviations related to the energy variations of fluorescence decay strengths [109, 110]. Therefore, the sum rules analysis of the XMCD signal obtained from fluorescence yield should be made with care.

Summarising, when performing a quantitative analysis of the fluorescence detected XMCD, one should remember about the possible effect related to the variations of fluorescence decay strengths. In contrary, when the absorption cross-section is detected via the electron yield, no such effects appear and the analysis is more straightforward [109]. Since in the MXSW method one is more interested in tracking the relative differences

²There is though an anomalous absorption effect, which is similar in nature to the standing wave signal seen in the secondary radiation yield. Such a signal is, however, not element sensitive, as one measures the overall effect of the sample on the transmitted beam, whereas the phototelectron, Auger or fluorescence spectroscopies offer directly an access to element-specific information.

in the magnetic moments, whose absolute value is usually assumed to be known from other studies (for example on thinner samples using the transmission mode detection), the usage of fluorescence is justified as being by far simpler in practice, especially when using the external magnetic field for sample magnetisation.

4.9 MXSW — classical approach

In the previous sections an MXSW theory was formulated using the partly classical (dynamical theory of diffraction) and partially quantum (time-dependent perturbation theory) formalism. Due to the fact that the only available simple theoretical model of the XMCD effect is the two-step model presented in chapter 3, it was used to treat the absorption of the standing wave generated by circularly or elliptically polarised light and track the changes imposed by the helicity reversal. This simple model remains strictly valid only for the cases of $L_{2,3}$ and $M_{4,5}$ absorption edges (as discussed in details in chapter about the XMCD effect).

As shown in chapter 3, the XMCD signal can be expressed in general as the product of three factors, $\Xi = \Pi_{circ} \Pi_e^s \Delta \varrho_f^s / \varrho_s$. The one related to the wave undergoing the absorption is Π_{circ} that is the degree of circular polarisation of the wave. The one related strictly to the considered absorption edge, that is the electron transition induced by the EM radiation, is the photoelectron polarisation Π_e^s . One can argue, that the presented derivation based on the quantum theory is always valid, and for the other absorption edges only Π_e^s has to be evaluated.

In the MXSW technique, what changes with respect to XMCD is only the form of the EM radiation (interference field versus single EM wave in regular XMCD). Therefore, one can try to evaluate the degree of circular polarisation for the interference field and obtain the MXSW signal based on the general formula $\Xi = \Pi_{circ} \Pi_e^s \Delta \varrho_f^s / \varrho_s$.

The procedure of calculation of such a degree of polarisation is shown in section 3.1.5. In short, one chooses appropriate polarisation unit vectors perpendicular to the propagation direction of interest (in this case always the magnetic moment direction) and calculates the scalar products. Those scalar products are a measure of the content of a given polarisation component in the arbitrary EM wave, among those also the standing wave which is of interest here.

Actually, in the formula for Π_{circ} (equation (3.36)), the difference between the moduli of scalar products with reversed helicity of the polarisation unit vectors $\hat{\boldsymbol{\epsilon}}_{rhp/thp}$ is considered, where the analysed wave $\boldsymbol{\mathcal{E}}$ remains unchanged. Thus such a situation is in fact equivalent to the reversal of the magnetic moment direction. The reversal of helicity of polarisation unit vectors means the reversal of the angular momentum direction of light. As the helicity of the wavefield $\boldsymbol{\mathcal{E}}$ is kept constant, this is equivalent to the change of the quantisation axis of the angular momentum detector, that is the magnetic moment direction. Therefore, via the presented approach, one can derive only the formula for $\bar{\Xi}_{\mathbf{m}}$, that is the XMCD signal calculated based on the absorption cross-sections for opposite magnetic moment orientations. One should note, that for the standard XMCD method, the signal calculated in such a way and the regular one, calculated based on reversal of helicity, coincide.

4.9.1 Degree of circular polarisation

As stated, a degree of circular polarisation in the direction of the magnetic moment is of interest. One considers the same coordinate systems \mathcal{O} and \mathcal{O}' (defined in figures 4.1 and 4.2). The circular polarisation unit vectors have to lie in the plane perpendicular to the magnetic moment direction, that is in the $x\mathcal{O}y$ plane. They can be assumed to have the same form as in section 3.1.5

$$\hat{\boldsymbol{\epsilon}}_{rhp} = \frac{1}{\sqrt{2}} (\hat{\mathbf{x}} + i\hat{\mathbf{y}}) \quad (4.55a)$$

$$\hat{\boldsymbol{\epsilon}}_{lhp} = \frac{1}{\sqrt{2}} (\hat{\mathbf{x}} - i\hat{\mathbf{y}}) \quad (4.55b)$$

Additionally the component parallel to the magnetic moment direction contributes to the total intensity, even though not contributing to the XMCD signal. It is taken to be equal $\hat{\boldsymbol{\epsilon}}_0 = \hat{\mathbf{z}}$.

The electric field is given naturally in the coordinate system \mathcal{O}' (equation (4.1)). One assumes that $\mathbf{k}_{0\sigma} = \mathbf{k}_{0\pi}$ and that they are real. Additionally, as before, the spatial extent of the electron wavefunction is neglected (electric dipole approximation). The electric field given in this form can be transformed to the coordinate system \mathcal{O} , as described in section 4.2. In short the electric field can be written as $\boldsymbol{\mathcal{E}} = E_0^a \boldsymbol{\epsilon} e^{i\omega t - i\mathbf{k} \cdot \mathbf{R}}$, with $\boldsymbol{\epsilon}$ being a polarisation vector. Its coordinates in the system \mathcal{O} are given by equations 4.9. The sought degree of polarisation is defined by the formula (3.36). Thus, one needs to consider the moduli squared of the scalar products $|\hat{\boldsymbol{\epsilon}}_{rhp}^* \cdot \boldsymbol{\mathcal{E}}|^2$, $|\hat{\boldsymbol{\epsilon}}_{lhp}^* \cdot \boldsymbol{\mathcal{E}}|^2$ and $|\hat{\boldsymbol{\epsilon}}_0^* \cdot \boldsymbol{\mathcal{E}}|^2$. They read

$$\begin{aligned} |\hat{\boldsymbol{\epsilon}}_{rhp}^* \cdot \boldsymbol{\mathcal{E}}|^2 &= \frac{1}{2} (E_0^a)^2 |(\hat{\mathbf{x}} - i\hat{\mathbf{y}}) \cdot (\varepsilon_x \hat{\mathbf{x}} + \varepsilon_y \hat{\mathbf{y}} + \varepsilon_z \hat{\mathbf{z}})|^2 = \frac{1}{2} (E_0^a)^2 |\varepsilon_x - i\varepsilon_y|^2 = \\ &= \frac{1}{2} (E_0^a)^2 [|\varepsilon_x|^2 + 2\Re(i\varepsilon_x \varepsilon_y^*) + |\varepsilon_y|^2] \end{aligned} \quad (4.56a)$$

$$\begin{aligned} |\hat{\boldsymbol{\epsilon}}_{lhp}^* \cdot \boldsymbol{\mathcal{E}}|^2 &= \frac{1}{2} (E_0^a)^2 |(\hat{\mathbf{x}} + i\hat{\mathbf{y}}) \cdot (\varepsilon_x \hat{\mathbf{x}} + \varepsilon_y \hat{\mathbf{y}} + \varepsilon_z \hat{\mathbf{z}})|^2 = \\ &= \frac{1}{2} (E_0^a)^2 [|\varepsilon_x|^2 - 2\Re(i\varepsilon_x \varepsilon_y^*) + |\varepsilon_y|^2] \end{aligned} \quad (4.56b)$$

$$|\hat{\boldsymbol{\epsilon}}_0^* \cdot \boldsymbol{\mathcal{E}}|^2 = (E_0^a)^2 |\hat{\mathbf{z}} \cdot (\varepsilon_x \hat{\mathbf{x}} + \varepsilon_y \hat{\mathbf{y}} + \varepsilon_z \hat{\mathbf{z}})|^2 = (E_0^a)^2 |\varepsilon_z|^2 \quad (4.56c)$$

The moduli of the polarisation vector component and the term $\Re(i\varepsilon_x \varepsilon_y^*)$ are given by equations (4.11) and (4.12). By comparison with (4.10) one notices that actually

$$|\hat{\boldsymbol{\epsilon}}_{rhp}^* \cdot \boldsymbol{\mathcal{E}}|^2 = \frac{1}{2} (E_0^a)^2 |\mathfrak{A}|^2 \quad (4.57a)$$

$$|\hat{\boldsymbol{\epsilon}}_{lhp}^* \cdot \boldsymbol{\mathcal{E}}|^2 = \frac{1}{2} (E_0^a)^2 |\mathfrak{B}|^2 \quad (4.57b)$$

$$|\hat{\boldsymbol{\epsilon}}_{in}^* \cdot \boldsymbol{\mathcal{E}}|^2 = (E_0^a)^2 |\mathfrak{C}|^2 \quad (4.57c)$$

The polarisation degree then reads

$$\begin{aligned} \Pi_{circ} &= \frac{|\hat{\boldsymbol{\epsilon}}_{rhp}^* \cdot \boldsymbol{\mathcal{E}}|^2 - |\hat{\boldsymbol{\epsilon}}_{lhp}^* \cdot \boldsymbol{\mathcal{E}}|^2}{|\hat{\boldsymbol{\epsilon}}_{rhp}^* \cdot \boldsymbol{\mathcal{E}}|^2 + |\hat{\boldsymbol{\epsilon}}_{lhp}^* \cdot \boldsymbol{\mathcal{E}}|^2 + |\hat{\boldsymbol{\epsilon}}_0^* \cdot \boldsymbol{\mathcal{E}}|^2} = \\ &= \frac{|\mathfrak{A}|^2 - |\mathfrak{B}|^2}{|\mathfrak{A}|^2 + |\mathfrak{B}|^2 + 2|\mathfrak{C}|^2} = \frac{\Re(i\varepsilon_x \varepsilon_y^*)}{|\varepsilon_x|^2 + |\varepsilon_y|^2 + |\varepsilon_z|^2} \end{aligned} \quad (4.58)$$

The expression in the denominator yields a relative standing wave intensity I_{sw} , given exactly by the last formula in (4.23). As noticed already in section 4.5.2 $\Re(i\varepsilon_x \varepsilon_y^*) = \Xi_2 + \Xi_3$. With that

$$\Pi_{circ} = \frac{\Xi_2 + \Xi_3}{I_{sw}} \quad (4.59)$$

Thus one would expect the XMCD signal to be equal

$$\Xi_{\mathbf{m}} = \Pi_e^s \frac{\Xi_2 + \Xi_3}{I_{sw}} \frac{\Delta \varrho_f^s}{\varrho_f} \quad (4.60)$$

This results coincides with the one obtained in section 4.5.2, that is when considering the XMCD signal as a difference in absorption cross-section for opposite magnetic moment orientations.

The fact that the XMCD signal is driven by the polarisation of the wavefield and a photoelectron polarisation allows to conclude, that the result obtained in this chapter for the MXSW signal is universal and in particular independent from the considered absorption edge. The polarisation of the photoelectron differs between the absorption edges, but the term related to the standing wave remains the same. Even though this classical approach works only for the case of the signal calculated based on the magnetisation reversal, it justifies the usage of the simplified two-step model for the derivation of the MXSW theory.

4.10 Discussion about the Ξ_3 term

As it was noticed in this chapter, in the case of the XMCD effect induced by the interference field, the equivalence does not exist between the signals calculated based on the helicity flipping and magnetic moment orientation reversal, or $\Xi \neq \Xi_{\mathbf{m}}$. This interesting phenomenon was not yet reported.

By examination of equations for Ξ (relation (4.22)), and $\Xi_{\mathbf{m}}$ ((4.29)), one can notice that they differ only by the term Ξ_3 , given by equation (4.15). The results for the XMCD signal obtained by the consideration of magnetic moment flipping $\Xi_{\mathbf{m}}$ and helicity reversal Ξ coincide, if one assumes that the incoming wave is circularly polarised and that the magnetic moment is lying in the scattering plane ($\varphi_m = 0$), as then the Ξ_3 term vanishes (see section 4.5.1).

Also the consideration of a single wave — either reflected or refracted one — gives a proper result. Indeed, if $\xi = 0$, the Ξ_2 quantity takes the form

$$\Xi_2 = 2\varepsilon_\sigma(\mathfrak{X}\varepsilon_\pi) (\cos \varphi_m \sin \vartheta_m \cos \Theta_B - \cos \vartheta_m \sin \Theta_B) \quad (4.61)$$

and Ξ_3 vanishes. The expression in the round brackets is nothing else than a projection of the magnetic moment \mathbf{m} on the propagation direction \mathbf{k}_0 . The first term represents the component m'_x times $\cos \Theta_B$, and the second m'_z times $\sin \Theta_B$ with minus, as the z' component of the wavevector is negative.

For the reflected wave one can set $\xi = 1$ and obtain

$$\Xi_2 = 2\varepsilon_\sigma(\mathfrak{X}\varepsilon_\pi) (\cos \varphi_m \sin \vartheta_m \cos \Theta_B + \cos \vartheta_m \sin \Theta_B) \quad (4.62)$$

with Ξ_3 again equals zero, what represents obviously a correct result, in accordance with chapter 3.

As observed, the reversal of helicity leads to a different formula for the MXSW signal than when a flip of the magnetic moment orientation is considered. Also, no expected symmetry between the \mathfrak{A} , \mathfrak{B} and \mathfrak{C} exists. The relations $|\mathfrak{A}_+|^2 = |\mathfrak{B}_-|^2$, $|\mathfrak{B}_+|^2 = |\mathfrak{A}_-|^2$

and $|\mathfrak{C}_+|^2 = |\mathfrak{C}_-|^2$, were observed in the theory of the standard XMCD effect and are related to the fact, that a reversal of helicity is equivalent to the reversal of the angular momentum of the wave. In the case of XMCD, similar symmetries were observed, when considering the reversal of the magnetic moment orientation, that is $|\mathfrak{A}_+^{+\mathbf{m}}|^2 = |\mathfrak{B}_+^{-\mathbf{m}}|^2$, $|\mathfrak{A}_-^{+\mathbf{m}}|^2 = |\mathfrak{B}_-^{-\mathbf{m}}|^2$.

In the case of MXSW only the latter appeared from the formalism, since flipping of the magnetic moment does not change the moduli of polarisation vector components $|\varepsilon_i|^2$, $i \equiv x, y, z$, but only the mixed term $\Re(i\varepsilon_x\varepsilon_y^*)$. This is what gives the symmetry between \mathfrak{A} , \mathfrak{B} and \mathfrak{C} . For the helicity reversal, the symmetry does not persist. As mentioned, $\Re(i\varepsilon_x\varepsilon_y^*) = \Xi_2 + \Xi_3$, but only the Ξ_2 term changes the sign under the helicity reversal, whereas this holds true also for Ξ_3 , when the magnetic moment is flipped.

The fact that in general the situation differs depending if the helicity is reversed, or the magnetic moment flipped, has its source in the phase changes in the wavefield in the reflection domain. The helicity change is equivalent to taking the complex conjugate of the polarisation parameter ε_π . The diffraction process breaks the symmetry, since an additional phase shift, the same for both helicities, comes from the amplitude ratios.

From a closer look at the definition of the term Ξ_3 one can notice that it consists of one term proportional to $|\varepsilon_\pi|^2$ and two proportional to $\Re\varepsilon_\pi$. This indicates, that it is possible to observe non-zero signal $\Xi_{\mathbf{m}}$ even for a linearly polarised incoming wave. The only condition is, that it must possess a π -component, since otherwise the Ξ_3 term vanishes (and the main Ξ_2 one is proportional to $\Im\varepsilon_\pi$, so vanishes for any linearly polarised incoming wave). This peculiar feature is related to the fact, that the phase difference appears between the $\hat{\varepsilon}_{0\pi}$ and $\hat{\varepsilon}_{\mathbf{h}\pi}$ polarisation components in the reflection domain. The phase difference is coming from the complex amplitude ratio ξ_π . Therefore, the MXSW theory predicts, that the difference in absorption as the magnetic moment orientation is flipped, can be observed also for the linearly polarised incoming wave, and since the vectors $\hat{\varepsilon}_{0\pi}$ and $\hat{\varepsilon}_{\mathbf{h}\pi}$ lie in the scattering plane, also for the magnetic moment component perpendicular to this plane (thus the component $F_2^{\mathbf{h}}$ in the expression for Ξ_3).

One should note, that this result was obtained within the electric dipole approximation, which is equivalent to negligence of the spatial extent of the wavefunction. Thus the spatial part of the EM field is also neglected, so the wavevector direction does not enter the quantum formalism in any place. Therefore, the appearance of the XMCD effect is in theory related only to the appearance of the complex phase between two polarisation components of the wavefield. In the quantum picture behind the effect, the propagation direction of the wave (direction of the angular momentum for the circularly or elliptically polarised wave) is what determines the spin polarisation of the excited photoelectron, and thus implies whether the XMCD effect appears or not. Since obviously no wave propagates in the direction perpendicular to the scattering plane, the observed phenomenon of XMCD effect for the linearly polarised incoming wave (with π -component) might be related to the used simplification in the form of electric dipole approximation, where propagation direction plays no role. The prediction related to the Ξ_3 coming from the presented MXSW theory should be checked experimentally, for example by performing an experiment with magnetic moments aligned perpendicular to the scattering plane and using a π -polarised incoming wave.

Part II
Simulations

Chapter 5

MXSW for exemplary systems

The first chapter of the part devoted to numerical simulations contains the results of the calculations of the MXSW signal for a few chosen crystal systems. The calculations are conducted based on the theory presented in chapter 4. The programs were written in the Matlab 9.5.0.944444 (R2018b) language [111], however, the scripts can be also used in the open-source GNU Octave.

At first, the results for the platinum-cobalt Pt₃Co alloy are shown. This system is the simplest of all presented ones, it exhibits no magnetic sublattices and contains small amount of atoms in the unit cell. Therefore, it serves as a model system to explain the meaning of the MXSW theoretical foundations.

As mentioned already, the power of the MXSW technique can be exploited fully if the system exhibits magnetic sublattices. In other words, the atoms of some element have to exhibit different magnetic moments, either in direction or in magnitude. Such a situation leads to standing-wave-like contrast in the MXSW signal. Therefore, further three systems with magnetic sublattices are considered — magnetite, yttrium-iron-garnet (YIG) and hematite. The two first ones are ferrimagnetic, whereas hematite is an antiferromagnet. By the presented simulations, it is clearly shown that using standing waves one can observe an XMCD signal from the antiferromagnet, what is impossible in the standard XMCD experiment.

5.1 Platinum-cobalt alloy

Platinum-cobalt Pt₃Co alloy crystallises in the Pm $\bar{3}$ m space group with a lattice parameter equal to 3.831 Å for the chemically ordered crystal [112]. The cobalt atom occupies the 1a Wyckoff position, what means it is located at the position (0, 0, 0), where the coordinates are written as (x, y, z) with x, y and z given as fractions of the unit cell parameters. The platinum atoms occupy the 3c positions, (0, $\frac{1}{2}$, $\frac{1}{2}$), ($\frac{1}{2}$, 0, $\frac{1}{2}$), ($\frac{1}{2}$, $\frac{1}{2}$, 0) or in short (0, $\frac{1}{2}$, $\frac{1}{2}$) \odot . The unit cell of Pt₃Co is shown in figure 5.1.

Chemical order of Pt₃Co depends on the heat treatment of the sample. The order-disorder transition temperature was reported to lie between 973 and 1073 K [112, 113]. This discrepancy was attributed to sharp dependence of this temperature on the alloy composition close to the stoichiometric value. Berg and Cohen have studied the transition kinetics in details and reported the transition temperature to be equal to 958 K, with the

two phase region present from 938 to 958 K [114]. A complete phase diagram of the platinum-cobalt alloys can be found in the article of Darling [115].

The system is ferromagnetic with the Curie temperature depending on the chemical order (generally being inverse proportional to the order parameter). For the ordered sample it was reported to be equal $T_C = 320$ K [113]. Both cobalt and platinum were found to exhibit magnetic moments, what was first detected using polarised neutron diffraction. The cobalt magnetic moment was reported to be equal to $m_{Co} = 1.64 \pm 0.04\mu_B$, whereas for Pt $m_{Pt} = 0.26 \pm 0.02\mu_B$ [113]. This means, that Pt_3Co is an interesting example of a crystal, where the otherwise non-magnetic 5d metal exhibits a magnetic moment due to the proximity of magnetic 3d metal atoms [117,118]. Based on the Fourier analysis of the diffraction data, it was found that the magnetic moments of both platinum and cobalt are aligned along the [111] crystallographic direction [113]. The crystals of Pt_3Co were also studied using XMCD spectroscopy using the photoelectron signal. A clear difference in absorption spectra for opposite magnetisation directions confirmed the magnetic nature of the platinum atoms in the investigated system [119]. The spin-polarised band structure calculations, with the exchange interaction modeled using Heisenberg Hamilton operator, were also performed for the discussed system and yielded the values of the magnetic moments in agreement with the data from neutron diffraction [120].

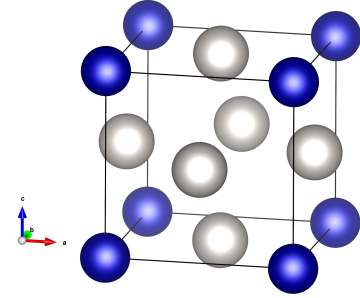


Figure 5.1: Unit cell of Pt_3Co ordered alloy. Platinum atoms are shown in white colour and cobalt in blue [116].

5.1.1 Magnetic dopant in the Pt_3Co structure

In order to give an example of the MXSW signal for one atom, at first a case of some dopant atom (for example iridium) with magnetic moment is considered. The results are presented for the energy corresponding to the Ir L_3 absorption edge, $\mathfrak{E} = 11.215$ keV (all energies of the absorption edges and fluorescence emission lines are taken from [121]). It is assumed for simplicity, that the magnetic moments are confined in the scattering plane ($\varphi_m = 0$), and in the reflecting lattice planes ($\vartheta_m = \pi/2$). The angles were defined in figure 4.2. The circular polarisation of the incoming wave is assumed and the absorption correction for the wavevector neglected. In such a case equation (4.22) simplifies to (4.27). Similarly like for the standard XSW method (section 1.6), one can identify the scalar product $\mathbf{h} \cdot \mathbf{R}$ with the fractional coordinate in the direction of the reciprocal lattice vector and call it z_h . The data is shown in figure 5.2 for a few values of z_h . One can notice, that the curves differ depending on z_h , but the observed contrast is smaller compared to the one observed in the standard XSW (see figure 1.6). This is related to the fact, that the MXSW signal is defined as a normalised difference between cross-sections, so the contrast related to the position of the dopant almost disappears. In other words, the experiment with circularly polarised standing wave does not offer here much advantage compared to the standard XSW one. The XMCD signal away from the reflection domain is actually the same as the one induced by the standing wave, neglecting the effects related purely to the wavefield — change of the polarisation due to reflection, difference in scattering

between the σ - and π -polarisation components and changes of the propagation direction in the reflection domain.

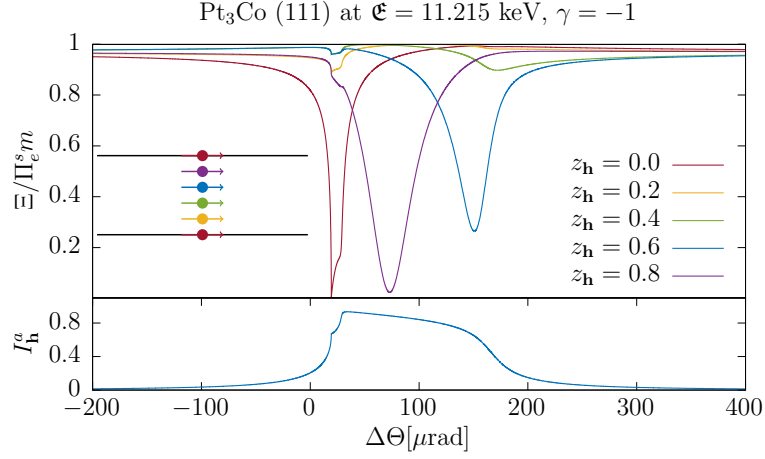


Figure 5.2: The normalised MXSW (divided by the electron polarisation and magnetic moment) signal in dependence on the Bragg departure angle $\Delta\Theta$ for a dopant atom with a magnetic moment (in this case the energy corresponds to the iridium L_3 absorption edge) located in the Pt₃Co lattice. In the part below the reflectivity curve is shown to indicate where the reflection domain is. The magnetic moment is assumed to be parallel to the reflecting lattice planes and confined in the scattering plane. The curves correspond to different locations of the magnetic dopant with respect to the reflecting lattice plane. One can notice, that the shape of the curves depends on $z_{\mathbf{h}}$, but contrast is not very high. The inset represents schematically the positions of the dopant atoms.

One can analyse the terms leading to the total MXSW signal in details. Equation (4.27) can be written in the equivalent form

$$\Xi = \left[1 + \frac{(1 - \cos 2\Theta_B) \Re(\xi_\pi e^{-i\mathbf{h}\cdot\mathbf{R}}) - \frac{1}{2} |\xi_\sigma - \xi_\pi|^2}{1 + \frac{1}{2} (|\xi_\sigma|^2 + |\xi_\pi|^2) + \Re(\xi_\sigma e^{-i\mathbf{h}\cdot\mathbf{R}}) + \Re(\xi_\pi e^{-i\mathbf{h}\cdot\mathbf{R}}) \cos 2\Theta_B} \right] \Pi_e^s m \cos \Theta_B \quad (5.1)$$

where the polarisation of the final band $\Delta\varrho_f^s/\varrho_f$ was denoted by m , given the arguments from section 4.6. The expression from the denominator comprises the standing wave intensity. One can already notice, that the MXSW signal is driven by two factors appearing in the numerator. The first one is proportional to the difference between the polarisation factors for σ - and π -polarisations, that is $(1 - \cos 2\Theta_B)$. This term is small for small Bragg angles, what is usually the case for the hard x-ray regime. The term $\Re(\xi_\pi e^{-i\mathbf{h}\cdot\mathbf{R}})$ behaves like the standing wave intensity, as it differs from it only by one and $|\xi|^2$. Compared to I_{sw} , it is greatly reduced by the $(1 - \cos 2\Theta_B)$ term (see figure 5.3, graph (a)). The second term in the sum is purely related to the difference in scattering between the σ - and π -polarisation components, as it comprises the difference between the amplitude ratios for those two cases. This term is small when far from the backscattering geometry, as presented in the graph (b) of figure 5.3. Figure 5.4 presents how the total Ξ function for the case of the atom located at the reflecting lattice planes ($z_{\mathbf{h}} = 0$) is constructed from the individual terms. The terms $(1 - \cos 2\Theta_B) \Re(\xi_\pi e^{-i\mathbf{h}\cdot\mathbf{R}})$ and $-\frac{1}{2} |\xi_\sigma - \xi_\pi|^2$ are related

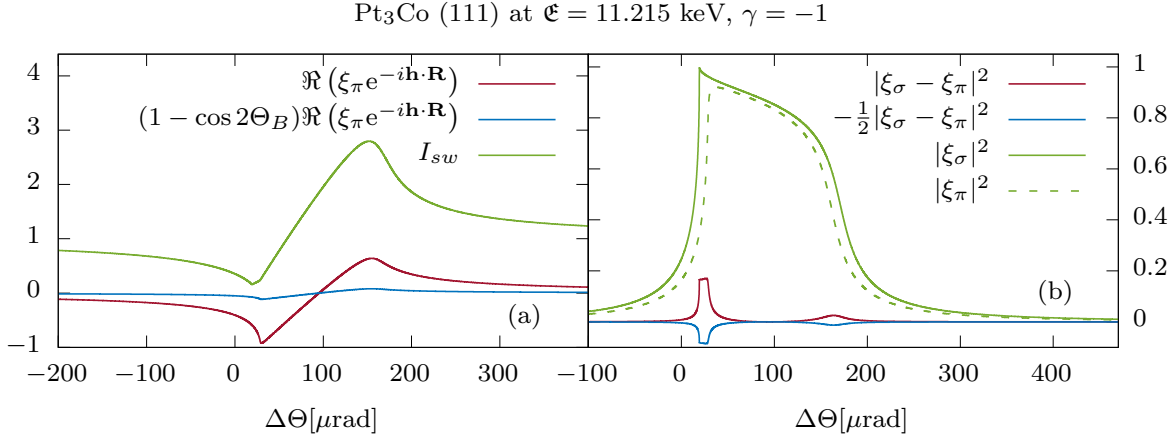


Figure 5.3: The analysis of the terms from the numerator of equation (5.1). The term $\Re(\xi_\pi e^{-i\mathbf{h}\cdot\mathbf{R}})$ (graph (a)) is similar in shape to the standing wave intensity I_{sw} , and it is greatly decreased by the term $(1 - \cos 2\Theta_B)$, which is small for Bragg angles far from $\pi/2$. The functions were calculated for the position on the lattice planes, $z_{\mathbf{h}} = 0$. The second term (graph (b)) is purely related to the difference in scattering between the σ - and π -polarisation components. This can be seen by the comparison with the moduli squared of amplitude ratios ξ_σ and ξ_π . For the considered energy the difference is small and so is the term $-\frac{1}{2}|\xi_\sigma - \xi_\pi|^2$.

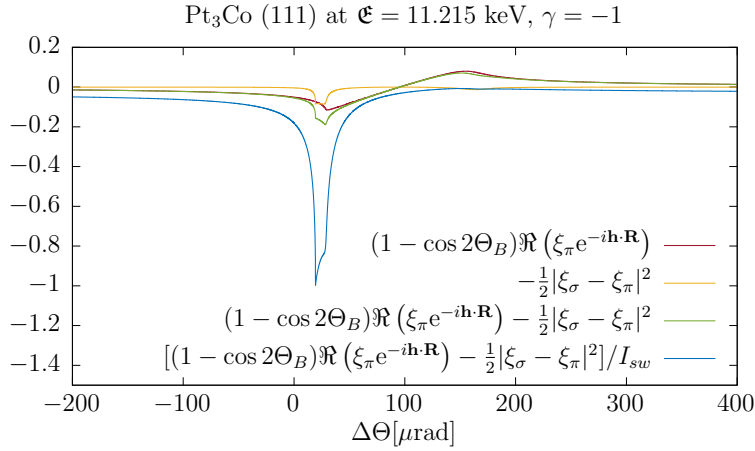


Figure 5.4: The graph showing how the MXSW signal for one atom is constructed from the terms analysed in figure 5.3. The terms $(1 - \cos 2\Theta_B)\Re(\xi_\pi e^{-i\mathbf{h}\cdot\mathbf{R}})$ and $-\frac{1}{2}|\xi_\sigma - \xi_\pi|^2$ are related to the difference in scattering between the σ - and π -polarisation components and are small. The contrast in the final signal is increased by normalisation by the I_{sw} , but remains small due to the fact, that no difference between the magnetic and atomic structure of the dopant exists. The functions were calculated for the position on the lattice planes, $z_{\mathbf{h}} = 0$.

to the change of the propagation direction caused by the reflection ($\Re(\xi_\pi e^{-i\mathbf{h}\cdot\mathbf{R}})$ term) and to the difference in scattering between the σ - and π -polarisation components. They remain small for the Bragg angles far from $\pi/2$. Therefore, also the overall variation in the XMCD signal described by the function Ξ is small, as the value of the XMCD

signal is generally determined by the cosine of the angle between the wavevector and magnetic moment, as well as circular polarisation rate. The appearance of the reflected wave propagating in the different direction than the incoming wave can cause modulation in the XMCD signal, which is high if the difference in propagation direction (related to the Bragg angle) is also high. The fact that in the discussed case the MXSW variation is small is in agreement with the argument given in section 4.6.2 that in order to observe a standing-wave-like variation in the XMCD signal, the magnetic and atomic structure of the considered element must differ. This is not the case if one considers a single magnetic dopant.

The situation is different, if the magnetic moment of the dopant is perpendicular to the reflecting lattice planes ($\vartheta_m = 0$). It follows from equation (4.26), that in such a case the MXSW signal can be written as

$$\Xi = - \left[1 - \frac{(1 + \cos 2\Theta_B) \Re(\xi_\pi e^{-i\mathbf{h}\cdot\mathbf{R}}) + \frac{1}{2} |\xi_\sigma + \xi_\pi|^2}{1 + \frac{1}{2} (|\xi_\sigma|^2 + |\xi_\pi|^2) + \Re(\xi_\sigma e^{-i\mathbf{h}\cdot\mathbf{R}}) + \Re(\xi_\pi e^{-i\mathbf{h}\cdot\mathbf{R}}) \cos 2\Theta_B} \right] \Pi_e^s m \sin \Theta_B \quad (5.2)$$

One can see, that now the signal remains strong when the Bragg angle is small, since now a plus sign is present in the terms $(1 + \cos 2\Theta_B)$ and $|\xi_\sigma + \xi_\pi|^2$. The numerator comprises then a standing-wave like signal, which multiplied by minus one and divided by original standing wave intensity remains significant. The variation in the XMCD signal is for such a magnetic moment orientation significant and its shape depends highly on the magnetic moment position. This is presented in figure 5.5. Figure 5.6 presents how the

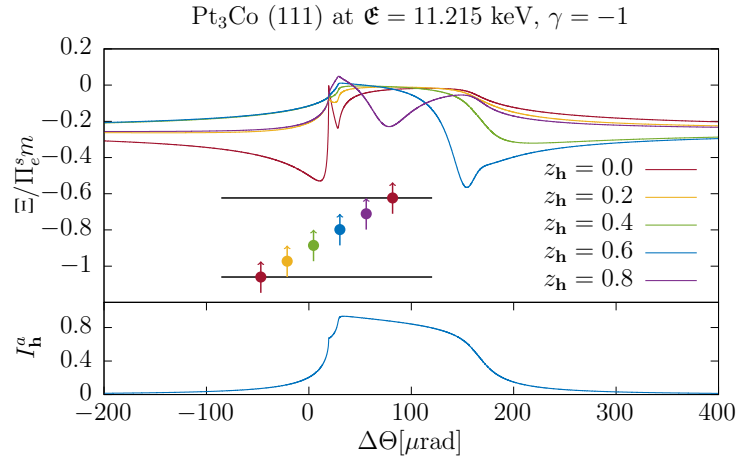


Figure 5.5: The normalised MXSW signal for a dopant atom with a magnetic moment (in this case energy corresponds to the iridium L₃ absorption edge) located in the Pt₃Co lattice, in the lower part a reflectivity curve. The magnetic moment is assumed to be perpendicular to the reflecting lattice planes and confined in the scattering plane. The curves correspond to different locations of the magnetic dopant with respect to the reflecting lattice plane. The shape of the curves resembles the shape of the standing wave intensity.

total MXSW signal is influenced by the terms from the numerator of (5.2). The shape of the curves clarifies, why the standing-wave like shape persists in Ξ in contrary to the case of magnetic moment parallel to the reflecting lattice planes. Fundamentally, this

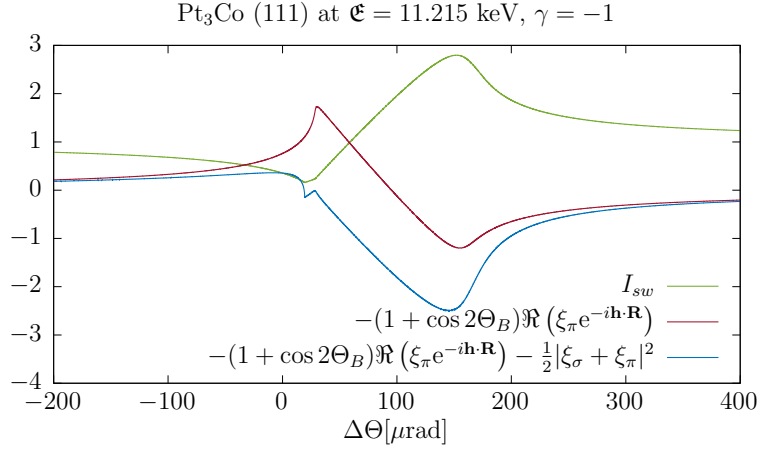


Figure 5.6: The terms from the numerator of equation (5.2). The term $-(1 + \cos 2\Theta_B)\Re(\xi_\pi e^{-i\mathbf{h}\cdot\mathbf{R}})$ is similar in shape to the standing wave intensity I_{sw} , but due to the minus sign is reversed. The shape shows, why the MXSW signal resembles the shape of the standing wave intensity. The functions were calculated for the position on the lattice planes, $z_{\mathbf{h}} = 0$.

high contrast is caused by the fact, that the propagation direction of the overall wavefield changes in the reflection domain. This effect leads to a variation in the XMCD signal, as is it proportional to the angle between wavevector and magnetic moment.

5.1.2 MXSW signal from Pt₃Co

In this section the functions for the real magnetic structure of Pt₃Co are presented. No reflections are forbidden, the standing wave structure factor for cobalt $(F_{sw}^{\mathbf{h}})^{\text{Co}} = 1$ and for platinum

$$(F_{sw}^{\mathbf{h}})^{\text{Pt}} = \begin{cases} 1, & hkl \text{ all odd or all even} \\ \frac{1}{3}, & hkl \text{ 2 odd, 1 even or 2 even, 1 odd} \end{cases} \quad (5.3)$$

Since all the magnetic moments are the same on Pt sublattice, it holds true in this case, that $\mathbf{F}_{msw}^{\mathbf{h}} = \mathbf{m}F_{sw}^{\mathbf{h}}$. Thus the MXSW method does not provide any additional information in this case, compared to regular XSW and XMCD used separately. Of course if the structure was unknown, the fact that the atomic and magnetic structure coincide could be deduced from the MXSW signal. Also the direction of the magnetic moment has a great influence on the signal, what is demonstrated in the subsequent paragraph.

The calculations were performed for energies corresponding to the platinum L₃ absorption edge and the cobalt K edge. An MXSW experiment at the L_{2,3} absorption edges of cobalt is not possible, as at such low energies the diffraction condition cannot be fulfilled for any reciprocal lattice vector. As mentioned in the introduction to this section, the magnetic moments are aligned naturally in the [111] direction, therefore, they are perpendicular to the (111) reflecting lattice planes. This corresponds to $\vartheta_m = 0$ and an arbitrary value of φ_m . At first a circular polarisation of the incoming beam is assumed, and the

absorption corrections for the wavevector neglected. The MXSW signal calculated for the spontaneous magnetic structure of Pt₃Co is shown in figure 5.7.

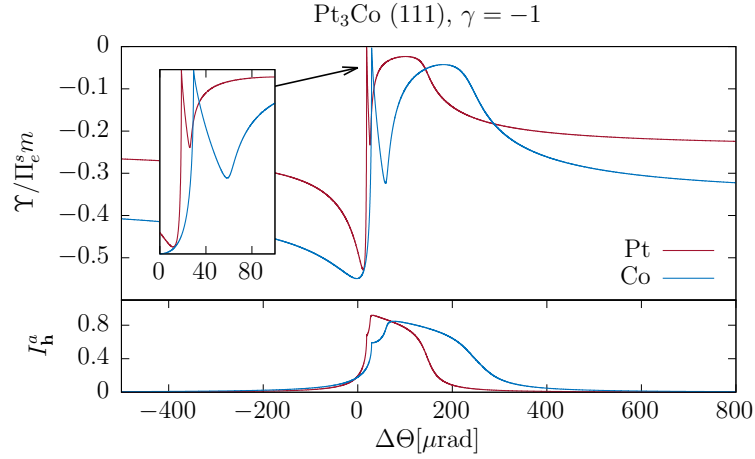


Figure 5.7: The normalised MXSW signal for a Pt₃Co crystal, in the lower part the reflectivity curves. The curves were calculated for the energies corresponding to the Pt L₃ absorption edge ($\mathcal{E} = 11.564$ keV, red curves) and Co K absorption edge ($\mathcal{E} = 7.709$ keV, blue curves). The curves for cobalt and platinum have similar shape, since the standard and magnetic standing wave structure factors are the same for the (111) reflection. The difference is related to the width of the rocking curve.

Figure 5.8 shows an MXSW signal for the platinum atom, calculated for several reflections. One can notice, that the shape changes significantly, since the angle between the magnetic moment and the reciprocal lattice vector changes. It is assumed for simplicity, that the reflections are symmetric and the magnetic moment is confined in the scattering plane. The change of the shape with the ϑ_m angle follows the general trend, that the smaller angles ensure a more standing-wave-like shape of the MXSW signal. For the high angles, the signal is dominated by the difference in scattering between the polarisation components. All presented curves are characteristic of the Pt₃Co magnetic structure and, therefore, provide direct information about the distribution of the magnetic moments.

Dependence on the ϑ_m angle

Now, consider some hypothetical magnetic structures of Pt₃Co. Namely, one can investigate the case of different orientation of magnetic moments of platinum. One assumes further that the magnetic moment is confined in the scattering plane and the angle ϑ_m is changed. Figure 5.9 shows calculated functions for the (111) symmetric reflection. The orientation of the magnetic moment was changed for all three platinum atoms, so that \mathbf{m} remains the same for all of them.

From the inspection of the graph, one can notice a smooth transition from the standing-wave-like signal for $\vartheta_m = 0$ to the one dominated by the difference in scattering between polarisation components for $\vartheta_m = \frac{\pi}{2}$. A change in background level is related to a change of the angle between the wavevector \mathbf{k}_0 and \mathbf{m} , whose cosine determines the XMCD strength away from the reflection domain. From the significant changes of the shape of

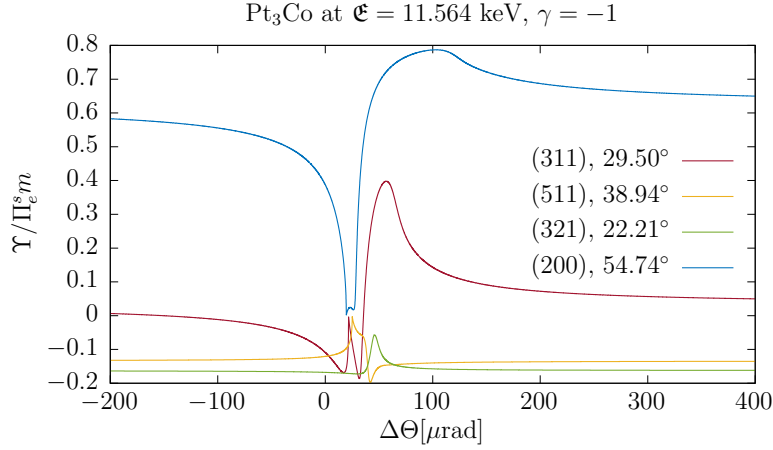


Figure 5.8: The normalised MXSW signal for a Pt_3Co crystal. The curves for a few reflections are shown. The angle between the magnetic moment and the reciprocal lattice vector of the reflection (ϑ_m) is shown in the legend. The background level changes due to the change of the Bragg angle.

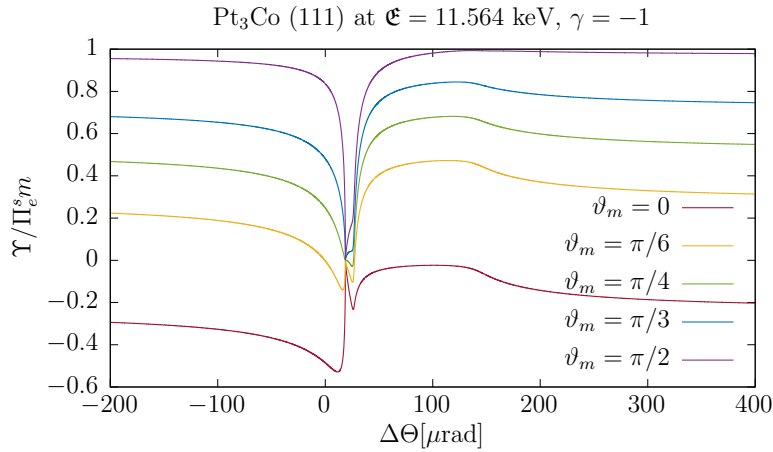


Figure 5.9: The normalised MXSW signal for a Pt_3Co crystal, (111) reflection. The data was calculated for several orientations of the Pt magnetic moment, parametrised by ϑ_m angle. The magnetic moment is assumed to lie in the scattering plane. One can notice gradual changes in signal shape.

the functions one can conclude, that the MXSW signal can provide information about the orientation of the magnetic moment.

Dependence on the incoming beam polarisation

In a real situation, the incoming beam has never perfect circular polarisation. In this paragraph the influence of the polarisation parameters ε_σ and ε_π on the MXSW signal is investigated. The calculations were performed for a real magnetic structures of the platinum-cobalt alloy. For convenience, a parametrisation proposed in section 1.9.1,

equation (1.49), is used. The influence of deviation from the values $\beta = \pi/4$ and $\delta = \pi/2$ is shown separately for both of those two angles, that is in figure 5.10 δ is varied and β kept equal to $\pi/4$, and in figure 5.11 the influence of different values of β is shown by keeping δ equal to $\pi/2$.

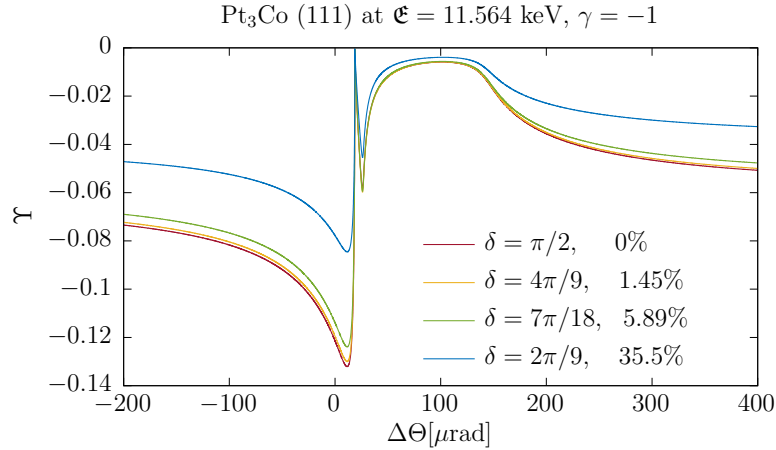


Figure 5.10: The MXSW signal for a Pt_3Co crystal, (111) reflection. It was assumed that $m = 1$ and $\Pi_e = 1/4$ (value for the L_3 edge). The functions correspond to different polarisations of the incoming beam, here a phase angle δ is varied. An angle β is kept equal to $\pi/4$. One can see, that significant changes appear only for a considerable deviation from the circular polarisation ($\delta = \pi/2$), but importantly the shape of the signal persists even in these cases. The difference between the given signal and Υ for circular polarisation is given in the legend.

Figure 5.10 presents the influence of the change of phase angle δ on the MXSW signal from platinum atoms in the Pt_3Co structure. By changing δ one changes the phase difference between the polarisation components $\hat{\epsilon}_\sigma$ and $\hat{\epsilon}_{0\pi}$. It can be seen that small deviations of the order of $\pi/18$ (that is 10°) have almost no effect on the signal (the total change is about 1.5% for the $\pi/18$ deviation). Significant changes are noticeable only for big deviation, like $2\pi/9$ shown in figure. As expected, deviation from the circular polarisation causes a decrease in the XMCD signal. Noteworthy, the shape of the signal remains very similar to the one for the circularly polarised incoming wave also for big deviations of δ from the value of $\pi/2$.

The second figure, 5.11, shows the influence of the angle β on the MXSW signal. This angle is related to the length of the polarisation components along the unit vectors $\hat{\epsilon}_\sigma$ and $\hat{\epsilon}_{0\pi}$. For $\beta = \pi/4$ those are equal. The qualitative conclusions from the data shown in this figure are the same as in the case when the influence of δ was investigated. A significant deviation from the value for circular polarisation is needed to observe changes, and the shape of the signal persists. The deviation of 5° gives the overall change in the signal of only 1.5%.

Summarising, the influence of small deviations of the incoming beam polarisation from the ideal circular polarisation is negligible. Given that no significant deviations are expected in experiments, further on, only the case of circularly polarised incoming beam is considered.

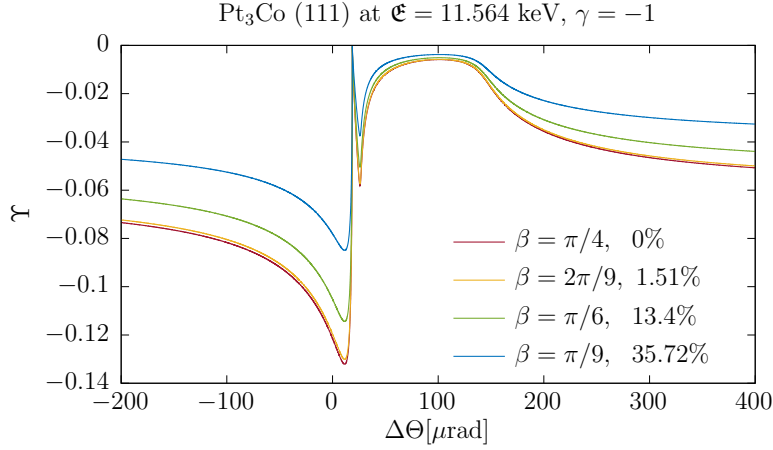


Figure 5.11: The MXSW signal for a Pt_3Co crystal, (111) reflection. It was assumed that $m = 1$ and $\Pi_e = 1/4$ (value for the L_3 edge). The functions correspond to different polarisations of the incoming beam, here an angle β , which is related to the length of polarisation vectors, is varied. An angle δ is kept equal to $\pi/2$. One can see, that significant changes appear only for a considerable deviation from the circular polarisation ($\beta = \pi/4$), but importantly the shape of the signal persists even in these cases. The difference between the given signal and Υ for circular polarisation is given in the legend.

Influence of absorption correction for wavevector

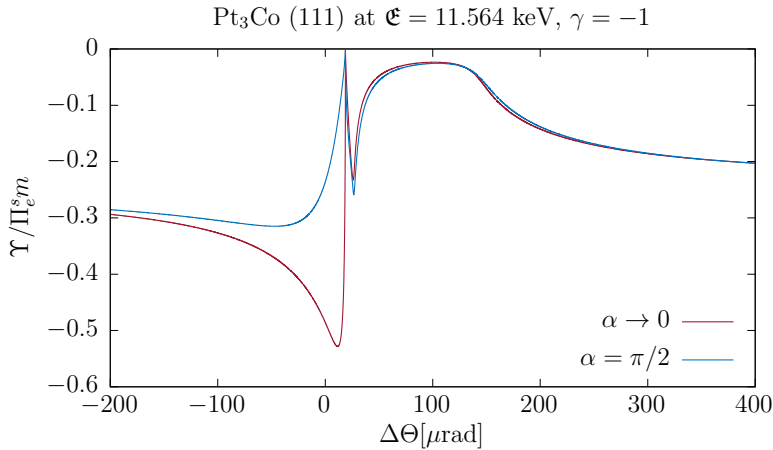


Figure 5.12: The normalised MXSW signal for a Pt_3Co crystal, (111) reflection. The signal was calculated with an absorption correction for the wavevector. α is an angle between the physical surface of the sample and the direction to the detector (see figure 1.7). The signal for grazing detection angle ($\alpha \rightarrow 0$) is the same as without the correction.

In the last subsection, the influence of the absorption correction for the wavevector (that is the effects of anomalous absorption, extinction and absorption of the secondary radiation on the way to the detector), introduced in section 4.7, is shown. The functions were calculated for the real magnetic structure of Pt_3Co . The μ_0 coefficient accounting

for the absorption of the fluorescence radiation on the way from the emitting atom to the detector was calculated for the energy corresponding to the L_α emission. The dependence on the detection angle α , defined in section 1.8, is shown in figure 5.12.

As expected from the fact, that the normalised XMCD signal is considered here, the influence of the absorption correction is rather minor. For the grazing detection angles, that is $\alpha \rightarrow 0$, the MXSW signal is the same as without the absorption correction. Since for higher values of α the influence of the extinction effect is bigger, the absorption correction introduces a noticeable change to the shape of the signal.

5.2 Magnetite

Magnetite, chemically Fe_3O_4 , is probably the first magnetic material known to humanity [122,123]. Due to its interesting magnetic structure, it is used here to demonstrate the power of the MXSW method to detect the differences in magnetic moment distributions among magnetic sublattices.

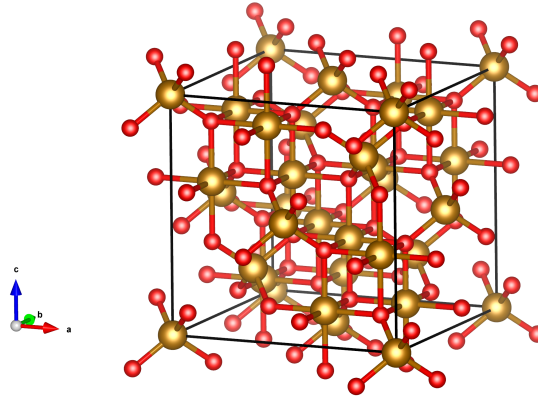


Figure 5.13: Unit cell of magnetite. Oxygen atoms are marked in red colour, iron atoms are yellow. One can notice the tetrahedrally (sites A) and octahedrally (sites B) coordinated iron atoms [116].

Under ambient conditions, magnetite crystallises in the $Fd\bar{3}m$ space group, with a lattice parameter $a = 8.3941 \text{ \AA}$. Iron atoms in magnetite exhibit two valence states — there are 16 Fe^{3+} and 8 Fe^{2+} ions. 8 Fe^{3+} ions occupy the 8a Wyckoff positions (A sites), where they are tetrahedrally coordinated by oxygen. The remaining 8 Fe^{3+} and 8 Fe^{2+} occupy randomly the octahedral 16d positions (B sites). The oxygen atoms are located at the 32e Wyckoff positions, with the parameter $x = 0.2548$ [124]. The unit cell of magnetite is presented in figure 5.13. Magnetite's chemical formula can be also written as $[\text{Fe}^{3+}]_A[\text{Fe}^{2+}\text{Fe}^{3+}]_B\text{O}_4$. An interesting feature of magnetite is, that it undergoes a so called Verwey transition [125] at 122 K, which is a sharp first-order transition characterised by a resistivity increase by two orders of magnitude and a structural distortion from cubic symmetry, as well as anomalies in other physical quantities, like specific heat or magnetic susceptibility [126, 127]. The mechanism of the phase transition is related to charge ordering on the B sites [128, 129].

Regarding the magnetic structure, the discrepancy between the expected net magnetic moment assuming ferromagnetic ordering and the lower experimental value, led to the model of ferrimagnetic ordering proposed by Louis Néel [130]. The assumption, that the magnetic moments within both A and B sublattices are parallel to each other, and antiferromagnetic order exists between those sublattices, explains the experimentally observed value of the net magnetic moment of $4.07\mu_B$ [131]. The spin magnetic moment of the Fe^{3+} ions is equal to $5\mu_B$, and the one of Fe^{2+} ions $4\mu_B$, giving an average value of $4.5\mu_B$ for the ions on the B sites. Due to the antiferromagnetic coupling, the magnetic moments of the Fe^{3+} cancel out and the observed moment is determined only by the Fe^{2+} ions [132, 133]. The Curie temperature of magnetite is equal to $T_C = 850$ K. Apart from spin magnetic moment, also the presence of orbital contribution was reported using XMCD spectroscopy at the $L_{2,3}$ absorption edges of Fe [134]. It should be noted, however, that those compensate each other at perfect stoichiometry. The ferrimagnetic structure of magnetite was confirmed using neutron diffraction [135], however, no exact reports on the orientation of the magnetic moments in the absence of the external magnetic field exists. Bulk magnetite is a soft magnet, which can be saturated in any direction in fields lower than 0.1 T [136]. The easy axis was reported to be along the crystallographic [111] direction and to change to [100] below the Verwey transition [136, 137]. When grown as a thin film, magnetite exhibits different spontaneous orientation of the magnetic moments. In the case of (111) thin film of magnetite grown on (111) platinum substrate a complete ferrimagnetic alignment of the magnetic moments in (111) plane was reported [138].

5.2.1 MXSW signal from magnetite

In this section, MXSW simulation results for magnetite are presented. The standing wave structure factor for iron atoms can be written in the form

$$(F_{sw}^{\mathbf{h}})^{\text{Fe}} = \frac{1}{24} \sum_{j=1}^{24} e^{i\mathbf{R}_j \cdot \mathbf{h}} = \frac{1}{24} \sum_{k=1}^4 \sum_{l=1}^{n_{\text{sublat.}}} e^{i(\mathbf{R}_k + \mathbf{R}_l) \cdot \mathbf{h}} = \frac{1}{24} \left[\sum_{k=1}^4 e^{i\mathbf{R}_k \cdot \mathbf{h}} \right] \left[\sum_{l=1}^{n_{\text{sublat.}}} e^{i\mathbf{R}_l \cdot \mathbf{h}} \right] \quad (5.4)$$

where the summation over all iron atoms was split into the summation over the positions related to Bravais lattice (centering, F in this case) and over the Wyckoff positions. In this case the \mathbf{R}_k positions are $(0, 0, 0)$, $(0, \frac{1}{2}, \frac{1}{2}) \odot$, so the first sum is equal to 4 for the allowed reflections (that is all hkl either odd or even). For tetrahedrally coordinated atoms (8a position, A sublattice), $n_{\text{sublat.}} = 2$ and $\mathbf{R}_l = (\frac{1}{8}, \frac{1}{8}, \frac{1}{8}), (\frac{7}{8}, \frac{3}{8}, \frac{3}{8})$. The rest of Fe atoms are located at 16d position (B sublattice) so $n_{\text{sublat.}} = 4$ and $\mathbf{R}_l = (\frac{1}{2}, \frac{1}{2}, \frac{1}{2}), (\frac{1}{4}, \frac{3}{4}, 0), (\frac{3}{4}, 0, \frac{1}{4}), (0, \frac{1}{4}, \frac{3}{4})$. Thus $F_{sw}^{\mathbf{h}}$ reads

$$(F_{sw}^{\mathbf{h}})^{\text{Fe}} = \frac{1}{6} \left(e^{\pi i(h+k+l)} + e^{i(h+3k)\pi/2} + e^{i(3h+l)\pi/2} + e^{i(k+3l)\pi/2} + e^{i(h+k+l)\pi/4} + e^{i(7h+3k+3l)\pi/4} \right) \quad (5.5)$$

Now consider the magnetic standing wave structure factor. The magnetic moments are coupled antiferromagnetically between the sublattices, so $m_A = 5\mu_B$ and $m_B = 4.5\mu_B$, the direction is the same for both sublattices (with opposite orientation). Using the normalised to one values of magnetic moment, such that $m_A = 1$ and $m_B = 9/10$, the

\mathbf{F}_{msw}^h reads

$$\begin{aligned} \mathbf{F}_{msw}^h &= \frac{1}{6} \left[\mathbf{m}_B \left(e^{\pi i(h+k+l)} + e^{i(h+3k)\pi/2} + e^{i(3h+l)\pi/2} + e^{i(k+3l)\pi/2} \right) + \right. \\ &\quad \left. + \mathbf{m}_A \left(e^{i(h+k+l)\pi/4} + e^{i(7h+3k+3l)\pi/4} \right) \right] = \\ &= \frac{1}{6} \mathbf{m}_A \left[-\frac{9}{10} \left(e^{\pi i(h+k+l)} + e^{i(h+3k)\pi/2} + e^{i(3h+l)\pi/2} + e^{i(k+3l)\pi/2} \right) + \right. \\ &\quad \left. + e^{i(h+k+l)\pi/4} + e^{i(7h+3k+3l)\pi/4} \right] \end{aligned} \quad (5.6)$$

where $\mathbf{m}_B = -\frac{9}{10}\mathbf{m}_A$ was used. Equation above shows, that in general $\mathbf{F}_{msw}^h \neq \bar{\mathbf{m}}F_{sw}^h$, with $\bar{\mathbf{m}} = -\frac{4}{15}\mathbf{m}_A$ in this case, so one can expect a significant MXSW signal carrying information about the magnetic sublattices. There are reflections, for example (008), for which the relation $\mathbf{F}_{msw}^h = \bar{\mathbf{m}}F_{sw}^h$ holds and the MXSW variation is consequently weak. The contrary is true for example for (004) reflection. This is apparent from the following simulation results.

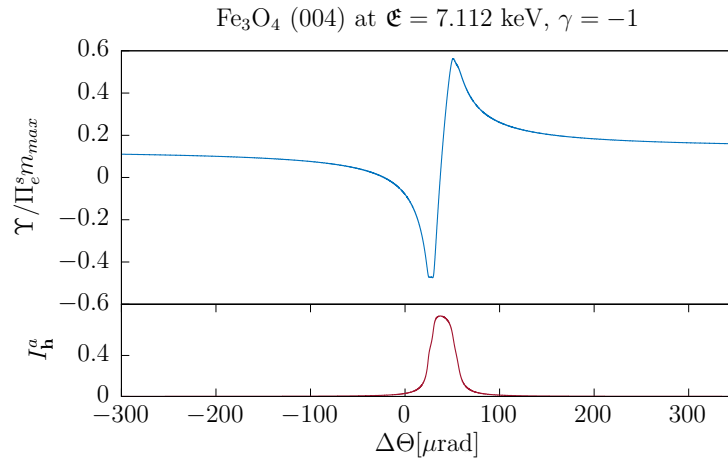


Figure 5.14: The normalised (by photoelectron polarisation and maximal magnetic moment) MXSW signal for a magnetite crystal, in the lower part the reflectivity curve. The curves were calculated for an energy corresponding to the Fe K absorption edge. It was assumed, that the magnetic moments are parallel (B sites) and antiparallel (A sites) to the $[111]$ direction, what corresponds to the ferrimagnetic natural structure of Fe_3O_4 . One can see a distinct standing-wave-like variation in the XMCD signal.

At first the (004) reflection is considered as a flagship example. The magnetic moments are assumed to be oriented parallel (B sublattice) or antiparallel (A sublattice) to the easy axis, $[111]$. For simplicity the case of $\varphi_m = 0$ is considered, thus the scattering plane is the $(1\bar{1}0)$ plane. The result of the simulations is shown in figure 5.14. One notices immediately a pronounced standing-wave-like character of the MXSW signal.

The shape of the signal can be understood easily, if one has a closer look at the proper projection of the magnetic structure. Since for the sake of simplicity it was assumed, that $\varphi_m = 0$, one needs to consider a projection on the $(1\bar{1}0)$ plane. Then the magnetic moments aligned in $[111]$ direction have no component perpendicular to the scattering plane. Figure 5.15 explains the shape of the MXSW signal shown in figure 5.14. As a consequence of the existence of the standing wave in the reflection domain the contribution

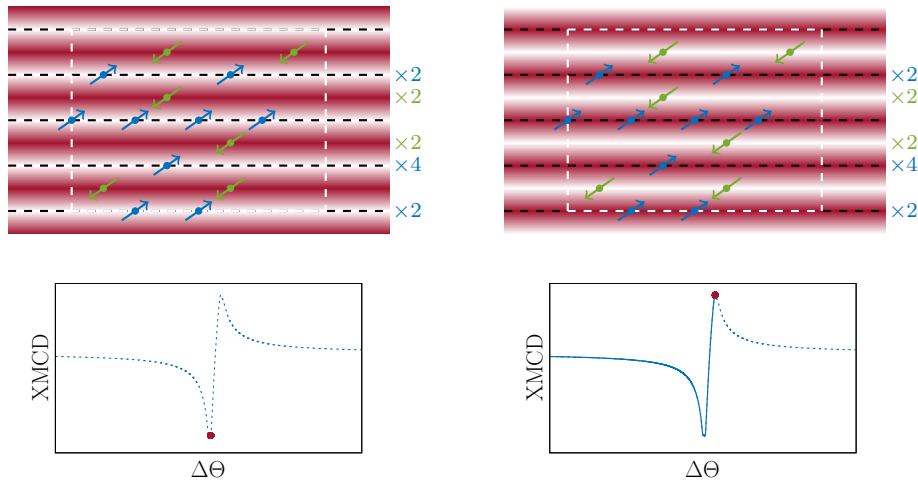


Figure 5.15: The example of the MXSW signal for the (004) reflection from magnetite showing the principle of the magnetic x-ray standing waves method. The upper images show the projection of the magnetite iron sublattice on the $(1\bar{1}0)$ plane. The ions belonging to the A sublattice are marked in green, for the B sublattice in blue. The magnetic moments are parallel or antiparallel to the $[111]$ direction. In this projection some of the magnetic atoms appear to be on top of each other, so the number on the right informs about their actual number. White dashed lines show the borders of the unit cell, the black dashed lines are the (004) planes, being also reflecting planes in this case. The intensity of the standing wave is represented by the red colour map in the top pictures. On the low angular side of the reflection domain, the antinodes of the standing wave lie between the lattice planes and coincide with the green sublattice, yielding a decreased XMCD signal, as the net magnetic moment is dictated by the Fe^{2+} ions from the blue sublattice. In contrary the XMCD signal is enhanced when the standing wave maxima coincide with the blue atoms, what happens on the high angular side of the reflection. The shape of the variation is characteristic of this distribution of the magnetic moments.

of the sublattices A (green) and B (blue) to the overall XMCD signal is either decreased or increased depending on the position of the nodes of the interference field. For the chosen (004) reflection, the tetrahedrally coordinated ions belonging to A sublattice lie between the reflection lattice planes, whereas octahedrally coordinated ones are located on those planes. Therefore, on the low angular side of the reflection domain, when the nodes are on the lattice planes, the XMCD signal is dominated by the A sublattice and thus decreased with respect to the background level, as this is dictated by the Fe^{2+} ions from the B sublattice, whose magnetic moments are oriented oppositely. Then the signal gradually increases while the standing wave moves as the reflection domain is crossed, what is caused by the change of the phase of the amplitude ratios. The standing wave maxima move onto the lattice planes, so the contribution of the B sublattice to the XMCD signal increases and the one of the A sublattice — decreases. At the point when the standing wave antinodes coincide with B sublattice, the signal is maximal, as there is no destructive contribution from the oppositely oriented ions belonging to sublattice A . After this point is reached, the XMCD signal decreases, since the standing wave disappears together with the reflected wave. The background level is dictated by the average magnetic moment and the Bragg angle, as it defines the angle between \mathbf{k}_0 and \mathbf{m} . This example shows

very clearly the power of the new MXSW method to directly gain information about the distribution of the magnetic moments in the lattice. One should note, that the shape of the MXSW signal Υ is directly related to this distribution and, therefore, can be regarded as an *image* of the magnetic structure. This is illustrated further with the use of some hypothetical arrangements of the magnetic moments in magnetite.

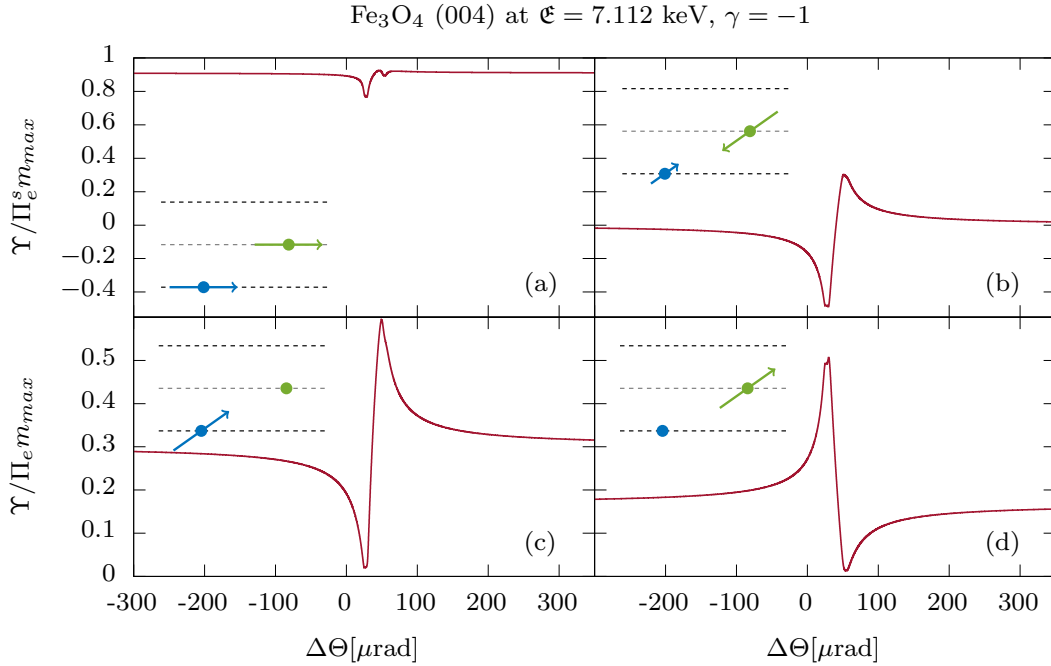


Figure 5.16: The normalised MXSW signal for some hypothetical magnetic structures of the magnetite crystal. The arrangement of the magnetic moments for each case is shown as an inset, the *A* (green) and *B* (blue) sublattices are represented schematically by one ion to avoid overcomplication of the picture. The graph (a) shows the result for the case of the same magnetic moments on both sublattices. The situation shown in the graph (b) corresponds to the antiferromagnetic structure, what leads to vanishing of the XMCD away from the reflection domain. The graphs (c) and (d) concerns the situation, when one of the sublattices is non-magnetic. One can conclude, the shape of the curves is directly related to the arrangement of the magnetic moments.

The MXSW signal for four different hypothetical magnetic structures of magnetite is shown in figure 5.16. The insets in the graphs present the considered magnetic moments arrangements. The first graph shows the result for the case of the same magnetic moments on both sublattices. For this situation it is assumed that the magnetic moments are oriented along the $[110]$ direction, what means they lie in the reflecting lattice planes. This is done to remove the influence of the components of the magnetic moments parallel to \mathbf{h} , which complicate the analysis (as the variation in XMCD effect is then highly influenced by the changes of the wavefield propagation direction). As discussed in section 5.1, in such a situation the variation in the XMCD signal in the reflection domain is weak and related to the difference in scattering between σ - and π -polarisation components. This explains the shape of the MXSW signal from the graph (a) — the standing wave does not lead to the

significant variation in the XMCD signal, as the magnetic moments are the same and the enhancement or reduction of the contribution from the given sublattice imposes no change on the overall signal. The graph (b) corresponds to the antiferromagnetic structure, as the net magnetic moment is zero in this case (keeping in mind that the iron atoms form sublattice B are twice as abundant as those form sublattice A), giving no XMCD signal away from the reflection domain (see the background level). This case presents a very interesting prospective application of the MXSW method — it allows to observe an XMCD effect in the antiferromagnetic systems. Even though when contributing at once, the magnetic moments of A and B sublattices cancel out, in the reflection domain the existence of the standing wave allows to switch off a contribution from one sublattice and observe the signal coming from the other one. With the movement of the standing wave, this leads to the variation seen in the graph (b). The last two graphs correspond to the situation of one — either A (graph (c)) or B (graph (d)) — non-magnetic sublattice. The fact that a given sublattice exhibits no magnetic moment is reflected in the MXSW curves. In the graph (c) the signal first decreases to zero, as the standing wave maxima coincide with non-magnetic A sublattice, and then increases as the magnetic B dominates the observed XMCD effect. The contrary applies to the situation from the graph (d). For the calculations concerning the situations shown in the graphs (b)-(d), the magnetic moments were assumed to be aligned along the $[111]$ axis. Summarising, four presented graphs show clearly, that the shape of the MXSW curve is directly related to the arrangement of the magnetic moments and provides easily-readable information about the magnetic structure.

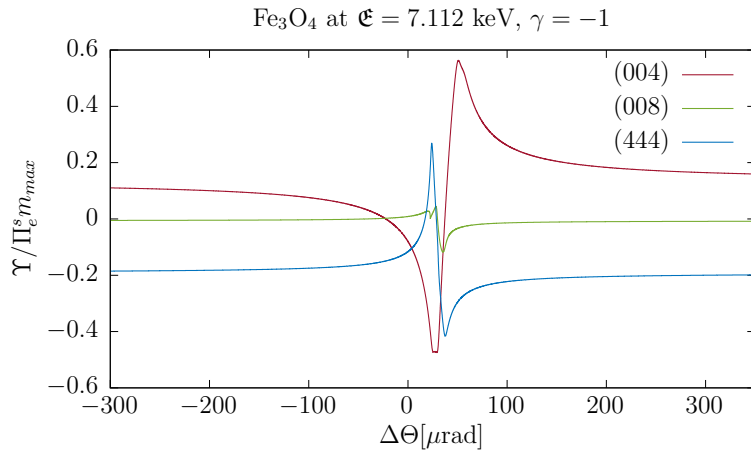


Figure 5.17: The normalised MXSW signal for a magnetite crystal, spontaneous magnetic structure. The curves for a few reflections are shown. By inspection of the projection of the magnetic structure on the $(1\bar{1}0)$ plane shown in figure 5.15 one can understand, why the (008) reflection does not lead to the significant variation in the XMCD signal.

The last figure (5.17) presented in this section shows the MXSW signal for a few chosen reflections from magnetite. A real ferrimagnetic arrangement with magnetic moments oriented in the $[111]$ direction is assumed. From the projection of the magnetic structure on the $(1\bar{1}0)$ plane shown in figure 5.15, one can see why the reflection from the (004) planes gives a standing wave with a perfect periodicity to study the magnetic structure of magnetite. In contrary, if one considers the (008) reflection (see the curve in figure 5.17),

no distinction between A and B sublattices can be made, as the maxima and minima of the standing wave coincide always at once with both sublattices. Small variation in the XMCD signal comes from the variations of the wavefield polarisation in the reflection domain, differences in scattering between the polarisation components and changes of the propagation direction in the reflection domain. As one can see, apart from the (004) also other reflections, for example (444), give an MXSW signal related to the ferrimagnetic arrangement in magnetite.

5.3 Yttrium-iron-garnet

Due to its unique physical properties, high Curie temperature equal $T_C = 560$ K and availability of very high quality single crystals, YIG ($\text{Y}_3\text{Fe}_5\text{O}_{12}$) has found applications in microwave technology and as a fascinating magnetic system for studies in experimental physics [139].

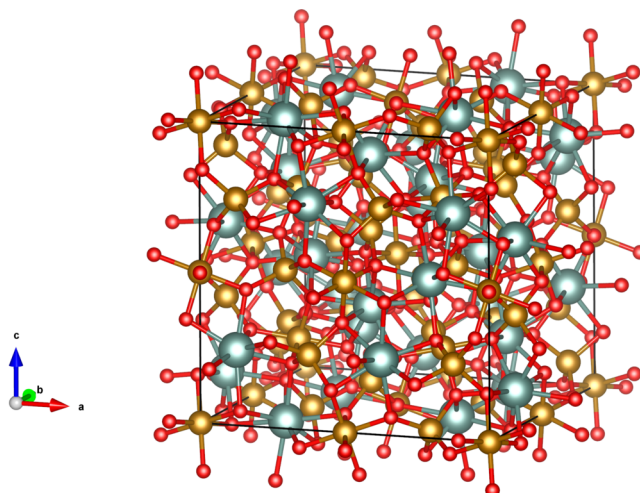


Figure 5.18: Unit cell of YIG. Oxygen atoms are marked in red colour, whereas yttrium in green, iron atoms are yellow. One can notice the tetrahedrally and octahedrally coordinated iron atoms [116].

In most of the cases [139–142] it is assumed, that YIG crystallises at ambient conditions in space group $Ia\bar{3}d$, with a lattice parameter of $a = 12.376$ Å. Yttrium occupies the 24c Wyckoff positions, oxygen is located at the 96h ones, with the parameters $x = -0.027$, $y = 0.0567$, $z = 0.15$. Iron atoms form two sublattices, 16 of them are located on the 16a Wyckoff positions and are octahedrally coordinated by oxygen atoms, whereas the remaining 24 tetrahedrally coordinated ones are on the 24d position [141]. Both sublattices are populated with Fe^{3+} ions having magnetic moment of $5\mu_B$. The magnetic structure of YIG was determined by neutron powder [140] and single crystal [143] diffraction. It exhibits ferrimagnetic ordering, as the iron magnetic moments on both sublattices were found to be aligned parallel within a sublattice and antiparallel between them [140]. In absence of the magnetic field, they are aligned along the [111] direction [143]. It was found by the group of Rodic, that better values of residual parameters are found, if the

YIG structure is refined in trigonal $R\bar{3}$ space group, especially for the data collected at low temperatures [143]. Such an assumption is also in accordance with the Landau theory of phase transitions, which requires a lowering of the symmetry during the transition at Curie temperature. On the other hand, at room temperature the trigonal distortion is small, and often the case of a cubic structure is used for simplicity [144].

5.3.1 MXSW signal from YIG

The structure of YIG is conceptually very similar to that of magnetite. The similarities appear also in the MXSW signal — one can find several reflections for which the periodicity of the standing wave is appropriate to provide information about the arrangement of the magnetic moments. For those reflections the standing wave enhances a contribution from one of the iron sublattices, what leads to the increase or decrease of the XMCD signal with respect to the background level dictated by the average magnetic moment.

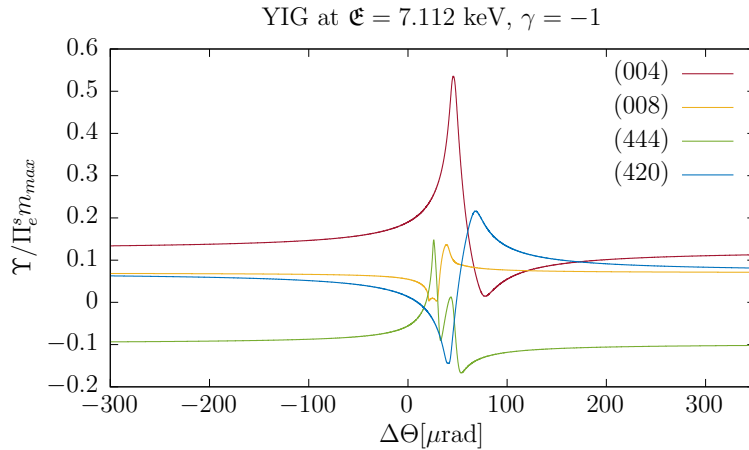


Figure 5.19: The normalised MXSW signal for a YIG crystal. The curves for a few reflections are shown. A real ferrimagnetic structure of YIG was assumed. In the same way as for magnetite, there are several reflections for which the periodicity of the standing wave is ideal for studying the magnetic moments on the sublattices of YIG.

The results of the simulations for a few YIG reflections are shown in figure 5.19. The shape of the curves is similar as for magnetite. In case of the (004), (444) and (420) reflections, their shape is related directly to the existence of magnetic sublattices and ferrimagnetic ordering in YIG. Similarly, like in the case of magnetite, the periodicity of the standing wave generated during the (008) reflection does not allow to distinguish between the sublattices, they always contribute at once to the overall XMCD signal.

5.4 Hematite

As the last example, the MXSW signal was calculated for a hematite (α - Fe_2O_3) crystal, since this system is antiferromagnetic under the ambient conditions. As it was already mentioned earlier, it is a unique property of the MXSW method, that it allows to observe

an XMCD effect in the antiferromagnets. Hematite, just like magnetite and YIG, belongs to the group of very prominent and continuously studied magnetic materials.

Under the ambient conditions, hematite crystallises in the rhombohedral space group $R\bar{3}c$, with the lattice parameters $a = 5.038 \text{ \AA}$ and $c = 13.772 \text{ \AA}$ (hexagonal setting). Iron atoms in the structure of hematite occupy the 12c Wyckoff positions ($z = 0.3553$). Oxygen atoms are located at the 18e ones ($x = 0.3059$) [145].

Regarding the magnetic structure, iron atoms exhibit two sublattices. The ions located at the positions: $\mathbf{R}_\uparrow = \{(0, 0, z), (0, 0, -z), (\frac{2}{3}, \frac{1}{3}, z + \frac{1}{3}), (\frac{2}{3}, \frac{1}{3}, -z + \frac{1}{3}), (\frac{1}{3}, \frac{2}{3}, z + \frac{2}{3}), (\frac{1}{3}, \frac{2}{3}, -z + \frac{2}{3})\}$ have one orientation of the magnetic moment. The ions located at the positions given by relation $\mathbf{R}_\downarrow = \mathbf{R}_\uparrow + (0, 0, \frac{1}{2})$ have the opposite magnetic moments. All Fe ions are trivalent and have in magnitude the same magnetic moment. Since there are 6 ions with one orientation and 6 with the opposite, in total the crystal is antiferromagnetic below the Néel temperature equal to $T_N = 955 \text{ K}$ [146]. It was found by Morin from the magnetisation studies, that hematite undergoes a phase transition at $T_M = 260 \text{ K}$ and below this temperature exhibits a very weak ferromagnetism, owing to the slight canting of the magnetic moments [147–149]. The underlying mechanisms leading to this weak ferromagnetism were explained on the basis of asymmetric exchange interaction by Dzyaloshinsky [150] and Moriya [151]. Above the Morin temperature, magnetic moments lie in the plane perpendicular to the c hexagonal axis. Below the phase transition temperature, they are aligned along the $[111]$ direction [149, 152].

5.4.1 MXSW signal from hematite

Consider first, which reflections yield a non-vanishing MXSW variation. The average magnetic moment \mathbf{F}_{msw}^0 , or $\bar{\mathbf{m}}$ (defined by equation (4.39)) is equal to zero for hematite at room temperature. Equation (4.34) shows clearly, that the MXSW signal vanishes if the magnetic standing wave structure factor is equal to zero. One can thus analyse, for which reflections the contrary holds. Using the relation $\mathbf{R}_\downarrow = \mathbf{R}_\uparrow + (0, 0, \frac{1}{2})$, \mathbf{F}_{msw}^h can be written in this case as

$$\mathbf{F}_{msw}^h = \frac{1}{12} \left[\mathbf{m}_\uparrow + \mathbf{m}_\downarrow e^{i\mathbf{h} \cdot (0,0,\frac{1}{2})} \right] \sum_{j=1}^6 e^{i\mathbf{h} \cdot (\mathbf{R}_\uparrow)_j} = \frac{1}{12} \mathbf{m}_\uparrow [1 - e^{i\pi l}] \sum_{j=1}^6 e^{i\mathbf{h} \cdot (\mathbf{R}_\uparrow)_j} \quad (5.7)$$

since the relation $\mathbf{m}_\downarrow = -\mathbf{m}_\uparrow$ holds. One can see, that l component of the \mathbf{h} vector has to be odd, so that the variation in the XMCD signal appears.

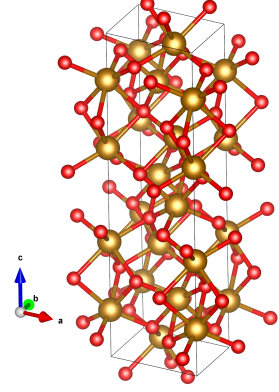


Figure 5.20: Atomic structure of hematite. Iron atoms are yellow, oxygens red [116].

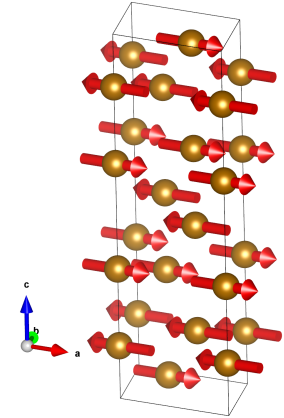


Figure 5.21: Magnetic structure of hematite. One can notice alternating orientations of the magnetic moments, resulting in antiferromagnetic ordering [116].

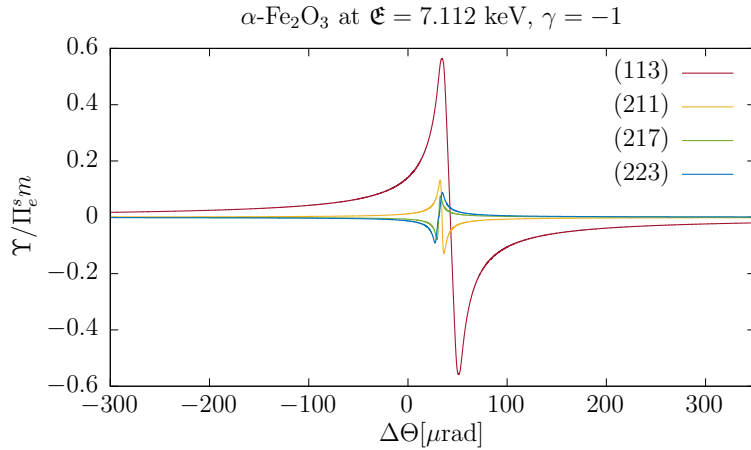


Figure 5.22: The normalised MXSW signal for an hematite crystal. The curves for a few reflections are shown. The small ferromagnetic component was neglected and the magnetic moments assumed to be oriented along [100] direction. Even though the XMCD signal away from the reflection domain vanishes, the standing wave allows to observe the effect as it can probe a single sublattice.

Figure 5.22 shows simulation results for a few reflections from hematite. A very significant signal can be observed for the (113) one. In other cases, the variation is rather weak, but this owes to the fact, that most of the useful reflections (in the light of the shown analysis of \mathbf{F}_{msw}^h) are weak. The most important conclusion here is that the XMCD signal can be observed from the real antiferromagnetic system using the standing wave. The mechanism behind this effect is the same as before — the standing wave enhances the contribution of a given sublattice to the overall XMCD signal, at the same time decreasing a destructive effect of the other one. When the antinodes of the standing wave coincide with one sublattice, the XMCD signal is the same as for a ferromagnetic arrangement. Therefore, the standing wave allows to virtually change the type of the ordering in the magnetic crystal during the rocking scan. As in all the cases discussed before, the shape of the MXSW signal is characteristic of the arrangement of the magnetic moment and for an unknown structure could be used to deduce it.

Chapter 6

XMCD-related absorption correction for the dynamical theory of diffraction

In the dynamical theory of x-ray diffraction, absorption is taken into account via the imaginary part f'' of the atomic scattering factor f (equation (1.10)) [52]. The atomic scattering factors and atoms' positions are used to calculate the structure factor, which is related to the Fourier coefficients of susceptibility. The imaginary part of the forward scattered component χ_0 is directly related to the linear absorption (see section 1.2 for details).

Within this framework, only the linear absorption is taken into account, and the absorption effects related to the distinct polarisation state of the wavefield are neglected. Even though the anomalous absorption coefficient does differ between σ - and π -polarisation components, this is related to the differences in the nature of scattering of those.

This formalism is good in the majority of cases. There are, however, situations, mostly related to the diffraction in the vicinity of the absorption edge, when the absorption effects associated with the polarisation of the wave can be significant. Among such cases lies definitely also the diffraction of the circularly or elliptically polarised incoming wave by a magnetised medium, which is considered in this work. As shown already theoretically, in such a situation the XMCD effect appears, which is basically a helicity-dependent difference in absorption. Up to now the influence of this absorption difference on χ_0 and therefore on the scattering effects in general, was neglected. This was done, since the polarisation dependent absorption cannot be easily incorporated into the framework of the dynamical theory of x-ray diffraction.

The diffraction of the circularly polarised incoming wave within the framework of the dynamical theory of diffraction was studied both for the two- and multi-beam case [153, 154]. The authors studied polarisation changes of the waves under the diffraction regime. It should be noted, that no change in absorption related to the polarisation was considered, since only non-magnetic materials were studied. Macke *et al.* have studied theoretically the impact of the dynamical effects on the resonant elastic x-ray diffraction results [48]. They have solved numerically the Maxwell equations, assuming that each atom has an atomic scattering factor given by a general tensor. This allows to account for polarisation changes related to the magnetic and charge ordering, as well as x-ray magnetic circular and linear dichroism (XMCD and XMLD). The values of the

components of the energy dependent atomic scattering factor tensors needed for such calculations are generally not known and have to be also evaluated numerically. For the example considered in the discussed paper, they were calculated using multiplet ligand field theory framework.

An indisputable advantage of the MXSW theory presented in this work, is that it is fully analytical and allows to easily simulate the theoretical functions for any system, having only generally available scalar atomic scattering factors. Therefore, instead of using a fully numerical approach presented in the paper of the group of Macke, a numerical correction is introduced to account for the absorption effects related to XMCD. Instead of using an approach based on the general tensor atomic scattering factor, a correction to the scalar one is made using the formulae for the absorption cross-section established in the magnetic x-ray standing waves theory. It is shown, that even though having sometimes a noticeable effect, the correction does not influence the predictions significantly.

6.1 Theory

The difference in absorption caused by the XMCD can be taken into account by iterative corrections of f'' . The initial value of this correction is obtained from the calculation based on the original value of f'' . The absorption cross-section for a circularly polarised wave assuming an uncorrected value of f'' was calculated in chapter 4. It is given basically by the formula (4.17), together with the general expression (3.10). Denoting $\mathcal{C} = (4\pi)^2 \alpha_f \hbar \omega$, the latter can be written also in the following way

$$\begin{aligned} \sigma_{\pm} &= \mathcal{C} \left(\varrho_f^{\uparrow} \zeta_{\pm}^{\uparrow} + \varrho_f^{\downarrow} \zeta_{\pm}^{\downarrow} + \varrho_f^{\uparrow} \zeta_{\pm}^{\downarrow} + \varrho_f^{\downarrow} \zeta_{\pm}^{\uparrow} \right) - \sigma_{\pm} = \\ &= \mathcal{C} \left[\left(\Delta \varrho_f^s + \varrho_f^{\downarrow} \right) \zeta_{\pm}^{\uparrow} - \left(\Delta \varrho_f^s - \varrho_f^{\uparrow} \right) \zeta_{\pm}^{\downarrow} + \left(\varrho_f - \varrho_f^{\downarrow} \right) \zeta_{\pm}^{\uparrow} + \left(\varrho_f - \varrho_f^{\uparrow} \right) \zeta_{\pm}^{\downarrow} \right] - \sigma_{\pm} = \\ &= \mathcal{C} \left[\Delta \varrho_f^s \left(\zeta_{\pm}^{\uparrow} - \zeta_{\pm}^{\downarrow} \right) + \varrho_f \left(\zeta_{\pm}^{\uparrow} + \zeta_{\pm}^{\downarrow} \right) \right] - \sigma_{\pm} \end{aligned} \quad (6.1)$$

what allows to transform it to the somewhat more convenient form

$$\sigma_{\pm} = \frac{1}{2} \varrho_f \mathcal{C} \left[\frac{\Delta \varrho_f^s}{\varrho_f} \left(\zeta_{\pm}^{\uparrow} - \zeta_{\pm}^{\downarrow} \right) + \left(\zeta_{\pm}^{\uparrow} + \zeta_{\pm}^{\downarrow} \right) \right] \quad (6.2)$$

The terms in round brackets read

$$\zeta_{\pm}^{\uparrow} - \zeta_{\pm}^{\downarrow} = \frac{4\pi}{3} \mathcal{R}(\mathbf{a}^{\downarrow} - \mathbf{a}^{\uparrow}) (\mp \Xi_2 - \Xi_3) \quad (6.3)$$

$$\zeta_{\pm}^{\uparrow} + \zeta_{\pm}^{\downarrow} = \frac{4\pi}{3} \mathcal{R}(\mathbf{a}^{\uparrow} + \mathbf{a}^{\downarrow}) I_{sw} \quad (6.4)$$

One has for the cross-section

$$\sigma_{\pm} = \frac{2\pi}{3} \mathcal{C} \varrho_f \mathcal{R}(\mathbf{a}^{\uparrow} + \mathbf{a}^{\downarrow}) I_{sw} \left(\mp \Pi_e^s \frac{\Delta \varrho_f^s}{\varrho_f} \frac{\Xi_2 \pm \Xi_3}{I_{sw}} + 1 \right) \quad (6.5)$$

The first term in the brackets is proportional to the spin-polarisation of the final band $\Delta \varrho_f^s$ and thus vanishes for non-magnetic material. The term Ξ_2 is proportional to the imaginary part of ε_{π} incident beam parameter and thus vanishes for linearly polarised

light. The term Ξ_3 is proportional to modulus and real part of ε_π , so persists even if the beam is linearly polarised. These terms describe the XMCD contribution to the total cross-section. If the material exhibits no spin polarisation of the final band, $\Delta\varrho_f^s = 0$, the cross-section is given by the prefactor, which can be then denoted by σ_0 , such that

$$\sigma_0 = \frac{2\pi}{3} \mathcal{C}_{\varrho_f} \mathcal{R}(\mathbf{a}^\uparrow + \mathbf{a}^\downarrow) I_{sw} \quad (6.6)$$

If several magnetic atoms contribute to the total measured signal, one sums the individual cross-sections in a similar way as described in section 4.6. The absorption cross-section per atom is obtained by

$$\sigma_\pm = \frac{2\pi}{3} \mathcal{C}_{\varrho_f} \mathcal{R}(\mathbf{a}^\uparrow + \mathbf{a}^\downarrow) \frac{1}{n} \sum_{j=1}^n \left(\mp \Pi_e^s \frac{(\Delta\varrho_f^s)_j}{\varrho_f} [(\Xi_2)_j \pm (\Xi_3)_j] + (I_{sw})_j \right) \quad (6.7)$$

or using the symbols introduced by equations (4.31), (4.32) and (4.33)

$$\sigma_\pm = \sigma_0 \left(\mp \Pi_e^s \frac{\Upsilon_2 \pm \Upsilon_3}{y} + 1 \right) \quad (6.8)$$

The term in the brackets is considered a correction to the linear absorption coefficient given by σ_0 , related to the XMCD effect. Optical theorem states that the imaginary part of the atomic scattering factor f'' is proportional to the total absorption cross-section. Therefore, one can write

$$f''_\pm = f''_0 \left(\mp \Pi_e^s \frac{\Upsilon_2 \pm \Upsilon_3}{y} + 1 \right) \quad (6.9)$$

The dispersion corrections f' and f'' are related to each other via Kramers-Kronig relations, so not only f'' , but also f' is influenced by the change in absorption caused by the XMCD effect. On the other hand, in order to obtain the correction for f' , one would need to have an energy dependence of f''_\pm , which could have been then transformed to f'_\pm using Kramers-Kronig relations. This would require similar numerical simulations as the ones used to obtain the full tensor of atomic scattering factor, what is beyond the scope of the simple correction discussed here. Therefore, the correction for f' is neglected hereafter. The XMCD experiments are performed usually for the energy lying in the pre-edge region of the absorption edge, where the change of f' with respect to the value away from the edge is small.

6.2 Algorithm

The cross-section σ_\pm , and thus also f''_\pm , depend on the quantities Υ_2 , Υ_3 and secondary radiation yield y , so also on the amplitude ratios ξ_σ and ξ_π . Those are in turn calculated assuming the knowledge of the structure factors F_0 , $F_{\mathbf{h}}$ and $F_{\mathbf{h}^*}$, which involve the resonant correction f'' . Therefore, the correction for the absorption needs to be introduced iteratively. In the first step, the cross-section is calculated assuming linear absorption only (standard dynamical theory calculation). Then this cross-section is used to correct f'' , and the amplitude ratios are calculated with such a first step correction. Those amplitude

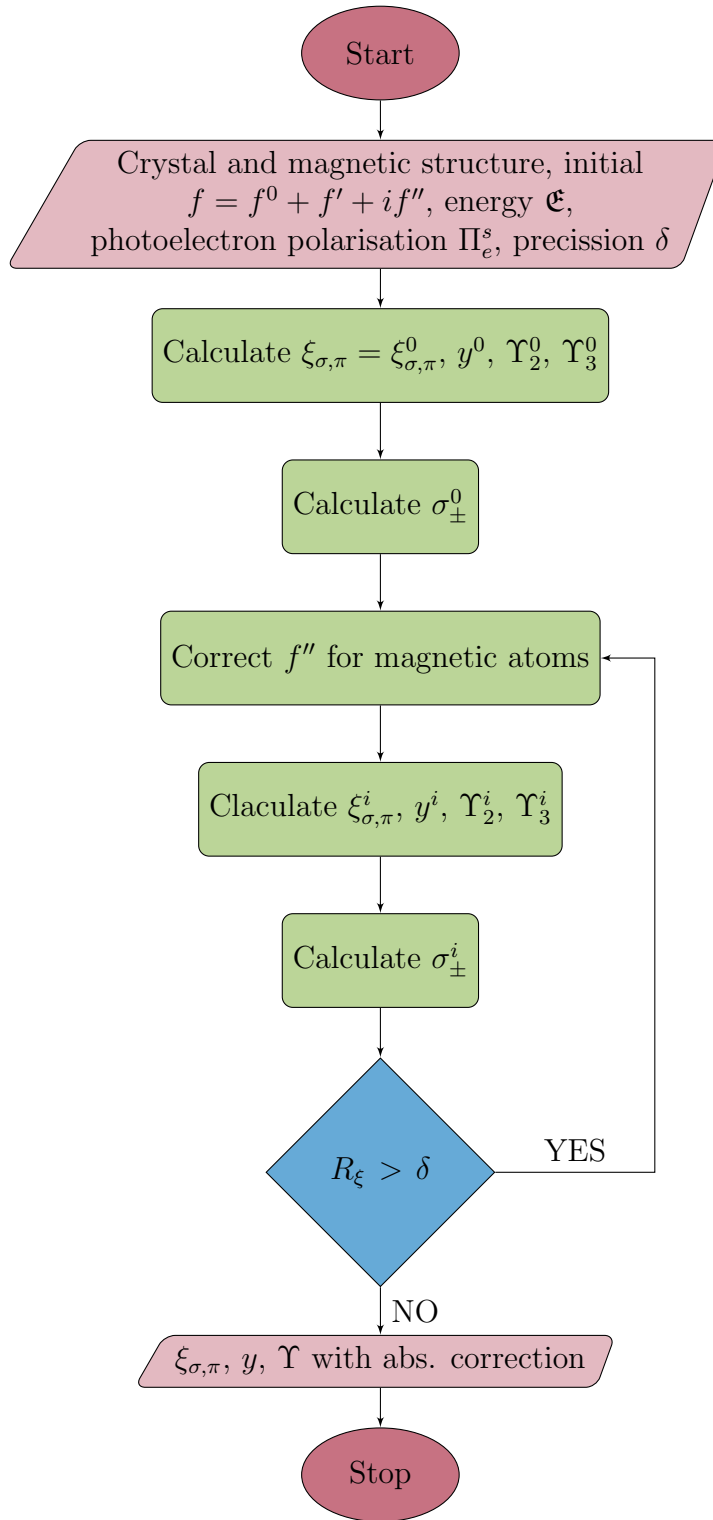


Figure 6.1: Iterative algorithm for introducing the absorption correction related to the XMCD effect into dynamical theory of diffraction. In the initial step, cross-section σ_{\pm}^0 is calculated using the tabulated value of f'' . This cross-section is then used to obtain a new value of f'' and calculate the corrected amplitude ratios $\xi_{\sigma\pi}^i$, which give again a new cross-section. This is repeated until the amplitude ratios do not change more than by a predefined δ , with R_{ξ} being defined as $R_{\xi} := \sum_{\Delta\theta} \|\xi^i - \xi^{i-1}\| / \sum_{\Delta\theta} \|\xi^{i-1}\|$.

ratios yield a new cross-section, which is taken then for the correction in the second step. This is repeated until the changes in amplitude ratios greater than a predefined value, for example 0.1%, are observed. The algorithm is summarised on the flow diagram shown in figure 6.1.

The absorption correction was implemented in the way depicted on the block diagram, that is the functions $\xi_{\sigma\pi}$, y , Υ_2 , Υ_3 and σ_{\pm} were calculated at once for the entire angular range. Alternatively, the correction can be calculated step by step, starting from the first value of $\Delta\Theta$ and then repeating the algorithm for successive angles. This means, that the proper value of the correction is obtained for an angle $(\Delta\Theta)_i$ and this value is then taken as an initial value for the next angle $(\Delta\Theta)_{i+1}$. Resulting $\xi_{\sigma\pi}(\Delta\Theta)$ functions were exactly the same as when applying the iterative algorithm at once for the entire range, so the latter is used as being more computationally effective.

6.3 Results of the simulations

One can see, that the value of the part of the cross-section, and thus also the absorption-related dispersion correction f'' is proportional to the photoelectron polarisation Π_e^s (equation (6.9)). This means, the correction can be only significant for the absorption edges, for which Π_e^s is large. Therefore, a platinum-cobalt alloy was used here as a model system for the simulations aiming at showing the influence of the discussed absorption correction. Even though there are many interesting magnetic crystals containing iron (see chapter 5), the strength of the XMCD effect is very small for the K absorption edge, so also the possible absorption correction is surely negligible.

For the simulations the real spontaneous magnetic and atomic structures of Pt₃Co, described in section 5.1, were assumed. The simulations were performed for the energy corresponding to the platinum L₃ absorption edge. As one can see in table 6.1, the calculation converges very quickly. The simulated reflectivity curves with absorption correction are compared to the original function in figure 6.2. The changes in phase of ξ_{σ} imposed by the absorption correction are presented in appendix C.

i	R_{ξ}
1	$1.201 \cdot 10^{-2}$
2	$4.002 \cdot 10^{-6}$
3	$8.390 \cdot 10^{-9}$
4	$1.365 \cdot 10^{-10}$
5	$2.953 \cdot 10^{-12}$

Table 6.1: Changes of the R_{ξ} parameter in the subsequent iterations of the algorithm. The simulations were performed for the Pt₃Co single crystal, the values of R_{ξ} are shown for the σ -polarisation component (ξ_{σ}) and for the right-handed polarisation.

By inspection of figure 6.2 one can see, that even for the case of naturally strong XMCD effect at the L₃ absorption edge ($\Pi_e^s = 1/4$), the influence of the absorption

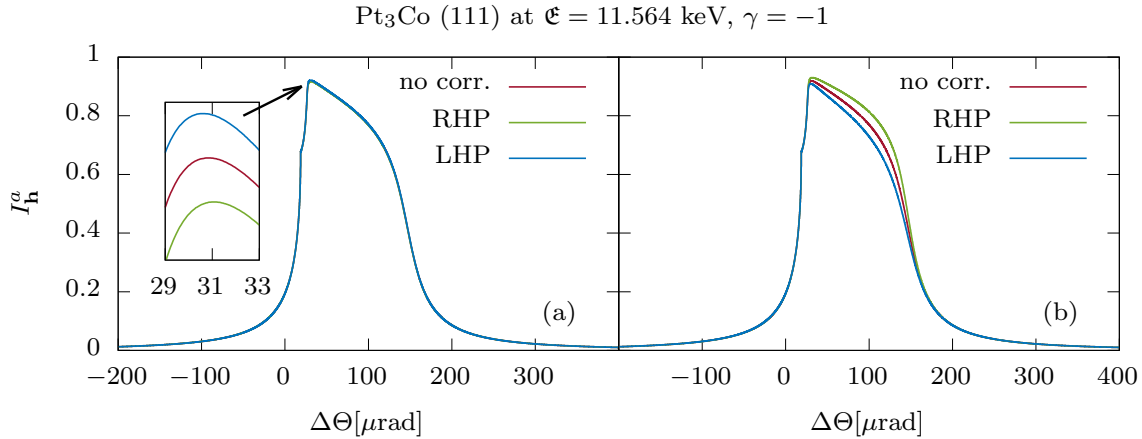


Figure 6.2: Comparison of the reflectivity curves for Pt₃Co single crystal with and without the iterative absorption correction related to XMCD effect. The graph (a) shows the result of simulations assuming the real magnetic structure of platinum-cobalt alloy, that is the orientation of the magnetic moment along [111] direction. The second graph, (b), presents the data for the simulations with magnetic moments in the reflecting lattice planes ($\vartheta = \pi/2$). One can notice, that the change after the correction is introduced, is rather small.

correction on the amplitude ratios, and thus also on all other results of the MXSW theory, is minor. In graph (a) a real magnetic structure of Pt₃Co single crystal was assumed, with magnetic moments along [111] direction. In such a setting, magnetic moments are perpendicular to the reflecting lattice planes, and given that the Bragg angle is rather small, the XMCD remains relatively weak. This weakness is reflected in the very small impact of the absorption correction. For the simulation, whose results are shown in graph (b), an orientation of the Pt magnetic moments in the reflecting lattice planes was assumed. This leads to stronger XMCD effect and increases the difference between the uncorrected and corrected functions. Even though the impact of the correction is noticeable, it remains small. As mentioned already, the absorption correction for the case of XMCD at K absorption edges is negligible, given that the strength of the XMCD effect is of the order of 10^{-3} . Summarising, the absorption correction for calculation of the scattering effects in the dynamical theory of diffraction has a small impact on the amplitude ratios, which determine the MXSW signal. This validates the approach used so far, where the scattering of the circularly polarised beam was calculated using the standard treatment of absorption with the dynamical theory of diffraction based on tabulated values of f'' . The absorption effects become important in the second step, where the XMCD signal generated by the wavefield is determined. In this step a proper description of absorption is granted by quantum mechanics.

Part III

Experimental section

Chapter 7

General description of the MXSW experiment

Given that physics is an experimental science, establishment of the theory and presentation of some computer simulations results should be followed by the experimental verification of the findings. Therefore, the last part of this work comprises a discussion about the general experimental conditions required for a successful MXSW experiment, followed by the results of two first MXSW experiments shown in the subsequent chapters.

7.1 Prerequisites for MXSW experiment

The MXSW method has indisputable advantages, among those an ability to provide information about the magnetic structures directly without refinement. On the other hand, like all experimental methods, it possesses also certain limitations. A few requirements have to be met by the sample, so that it can be studied by the MXSW technique. Those are described in details in this section. This is followed by the discussion about the experimental conditions needed for practical implementation of the MXSW method.

7.1.1 The sample

In general, the method is suitable for investigation of magnetic order in crystalline samples. The crystal lattice is needed to generate a standing wave. The quality of the crystal, understood as a small mosaic spread and small concentration of other defects (for example vacancies, dislocations, stacking faults), has to be good enough, so that the dynamical theory of diffraction can be used to describe the scattering process. Only this theory provides an accurate description of the phenomena in the reflection domain. Among those, it gives a strict phase relation between the refracted and reflected waves leading to the movement of the nodes and antinodes of the standing wave. If the mosaic spread of the crystal is big, the reflection domain is rotated between single mosaic blocks and the standing wave signal measured at once for all the mosaic blocks is blurred. For thin films, in certain cases it suffices, that the crystalline substrate is of the good quality. It can be used to generate a standing wave, which is then used to investigate the structure of the thin film. The thin film has to be in that case thinner than the coherence length of

x-rays. In this approach, the periodicity of the standing wave has to match the periodicity of the thin film lattice, or alternatively the thin film has to consist of only a few atomic layers.

Regarding the magnetic properties of the sample, it has to exhibit a spontaneous magnetic ordering, if the aim is to determine the magnetic structure. Using the MXSW method one can study ferro-, ferri- and antiferromagnetic, as well as non-collinear systems. This is in contrast to the regular XMCD method, which does not allow to observe any signal from antiferromagnetic systems, since they exhibit no net magnetisation. As discussed already at the end of section 4.6.2, the unit cells of the magnetic and atomic structures have to coincide, since in the MXSW method the standing wave generated by the periodicity of the atomic structure is used to study the magnetic structure. The periodicity of the standing wave is related to the atomic structure. The largest period of the standing wave cannot be higher than the dimensions of the atomic unit cell. If the magnetic structure has lower translational symmetry than the structural cell, the MXSW signal will be given by the projection of the average magnetic structure onto the structural unit cell, thus providing no useful information. In other words, the propagation vector of the magnetic structure has to be equal to $\mathbf{k}_m = (0, 0, 0)$.

Using XMCD spectroscopy, one can also study paramagnetic [86] and diamagnetic [155] materials, that is materials, which exhibit a net magnetisation when placed in the external magnetic field. The induced magnetic moments are parallel to the external magnetic field in case of paramagnetic atoms and antiparallel for diamagnetic ones. In general, since all the moments are the same as they are induced by the magnetic field and aligned in its direction, the spatial resolution provided by the MXSW method gives no additional information. On the other hand, it was observed by the group of Fuhrman [156] that in SmB_6 at low temperatures some samarium ions behave differently than others. The Sm^{3+} ions are diamagnetic and in the magnetic field their magnetic moments align antiparallel to the magnetic moments of Sm^{2+} , which are paramagnetic. Such an antiferromagnetic coupling between those ions could be also detected using the position sensitivity of the MXSW method. Summarising, even though the materials possessing spontaneous magnetic ordering are of the main interest for the research using the MXSW method, potentially also in the case of paramagnetic and diamagnetic substances the spatial resolution added to standard XMCD spectroscopy can be of a use.

In order to observe an XMCD effect, the energy of the incoming x-ray wave has to be tuned to the absorption edge of the atoms exhibiting a magnetic moment. Only then an excited electron has an energy allowing a transition to the unoccupied spin-polarised final states. When the energy is lower, the electron is not excited at all, and when higher, the electron leaves the atom without probing the band responsible for magnetism. At the same time, the energy has to be large enough, that some Bragg reflections can be excited. The interplanar spacing of the reflecting lattice (hkl) planes has to fulfil the condition $d_h \geq \lambda/2$ to observe a Bragg reflection. In the case of energies corresponding to the $L_{2,3}$ and $M_{4,5}$ absorption edges of respectively 3d and 4f metals, which are most often used to gather information about the magnetic moments of those elements, for many of the crystalline systems no Bragg reflection can be reached. For 3d metals the energies of $L_{2,3}$ absorption edges lie below 1 keV, so the interplanar spacing has to be larger than 6 Å. Even though there are systems with such a relatively large unit cell, the number of achievable reflections is still very limited. The same holds for the $M_{4,5}$ absorption edges of the rare

earths, whose energies are slightly higher than the ones of the $L_{2,3}$ absorption edges of the 3d metals. The energies of $M_{4,5}$ edges for the actinide series (thorium, protactinium and uranium) are well above 3 keV, so the systems containing those elements in the magnetic state are prospective candidates for MXSW experiments.

Keeping in mind the limitations related to the energy of the absorption edge, ideal systems to be investigated with the MXSW method are 5d metals. Their magnetism can be studied straightforwardly by XMCD spectroscopy performed at their $L_{2,3}$ absorption edges, whose energy lie well in the hard x-ray regime (is of the order of 10 keV). One should note, however, that none of those elements exhibit spontaneous magnetisation in their pure form. Their magnetic moment can be only induced by the proximity of other magnetic ions, and remains small. This non-trivial origin of magnetism makes the investigation of magnetic structure even more relevant.

Most of the magnetic materials exhibiting spontaneous ordering above the magnetic transition temperature (Curie or Néel) contain 3d metals. The magnetism of those systems can be studied utilising the XMCD effect appearing at the K absorption edges. The energies of those lie in the hard x-ray regime, so several Bragg reflections can be reached. As discussed in chapter 3, section 3.3, the XMCD effect for the K absorption edge of 3d metals is weak, due to the lack of spin-orbit splitting of the initial state. Therefore, to obtain a valuable MXSW signal, one needs extended data collection times, what constitutes a drawback for the measurements in this setting. With the high brilliance light sources available nowadays, such measurements become possible.

Instead of using the $M_{4,5}$ absorption edges, one can also tune the energy to the $L_{2,3}$ ones in order to perform the MXSW experiment on the system containing 4f metals. As mentioned already in section 3.4, the simple two step model does not provide a good description of the effect in this case, what makes also the analysis of the XMCD data challenging.

7.1.2 The experimental system

Since an energy of the x-ray beam has to be tuned to the absorption edge, as discussed in the previous subsection, the MXSW experiment can be performed exclusively at the synchrotron light sources or possibly also, in further perspective, at the free electron lasers (FEL). Only the former is discussed here, as the experimental part of this work was performed at a synchrotron facility. In short, x-ray photons are generated in storage rings, when the trajectory of the beam of charged particles (usually electrons or positrons) is changed either in bending magnets or insertion devices (undulators or wigglers), what is predicted by classical electrodynamics. Further details about synchrotron light sources can be found elsewhere [157, 158]. Both bending magnet, as well as insertion devices based beamlines can be used for the MXSW experiments, as in both cases tuning of the energy is possible. The flux of photons offered by the current synchrotron radiation sources is sufficient to observe an XMCD effect even in very weakly magnetic substances, like diamagnets [155].

The x-ray wave used for the XSW, and thus also the MXSW method, has to have certain properties. The x-ray radiation used for standing wave experiments has to be monochromatic, so that a single chosen Bragg reflection is excited at once. The divergence of the beam should be smaller than the width of the rocking curve, otherwise the XSW

(and MXSW) signal is smeared, since the beam covers at once a range of the incidence angles $\Delta\Theta$. The observed signal is a convolution of the theoretically expected one with the divergence profile of the incidence beam, what decreases the contrast in the standing wave signal. The same effect is related to the finite energy bandwidth of the incoming wave, which should be as small as possible.

There are no special requirements on the coherence properties of the beam, at least for the atomic scale XSW methods. Successful XSW experiments were performed also using the radiation generated by x-ray tubes [53,159]. On the other hand it should be mentioned, that the coherence properties of the radiation are more critical when the total external reflection is used to generate the standing wave, since in such a case the dimensions of the studied structures are much larger than the crystal lattice cell dimensions [160]. Though, if the structures remain smaller than typical coherence length of several micrometers, what is the case for often studied nanostructures, the XSW experiments are still feasible.

Most of the so far discussed requirements regarding the properties of the x-ray beam are common for the standard XSW method and the new MXSW one. What is certainly different in those requirements, is the need for the incoming x-ray beam to be circularly or elliptically polarised. Such a polarisation is needed to observe an XMCD effect, as the transfer of the angular momentum from the x-ray beam to the excited electron is required to make the emission of photoelectron spin-polarised. In order to obtain a desired polarisation of the beam, the unique properties of the radiation generated in the storage rings are used. This radiation is polarised linearly in the orbit of a storage ring, and elliptically above and below the orbit [157]. Already this second property was used to perform XMCD experiments [82], but the degree of circular polarisation in such cases is rather low. Alternatively, the natural linear polarisation can be changed to the desired circular one by using either special optics elements, called phase plates, or appropriate insertion devices, called helical undulators.

The phase plates generate the desired state of beam polarisation based on the difference in scattering between the σ - and π -polarisation components [161]. The waves with these polarisations are characterised by different wavevectors, while travelling through the crystal oriented in the vicinity of angular reflection domain. The difference in the wavevectors provides a desired phase between the σ - and π -components needed for the circular polarisation. More formally, the dispersion surface has two branches for each polarisation component (see figure 1.2). The wavevector is directly dependent on the position of the tiepoint on the dispersion surface (equation 1.42). This gives the following phase factor between the perpendicular polarisation components: $\exp[i(X_{0\pi} - X_{0\sigma})d]$. One can thus choose the thickness of the crystal d and the deviation angle $\Delta\Theta$ (which changes the values of $X_{0\pi}$ and $X_{0\sigma}$) such that the phase difference is equal $\pm\pi/2$. Switching of the helicity is performed by changing the departure angles $\Delta\Theta$ between the values giving appropriate phases on two sides of the reflection domain. The phase plates are operated usually in the transmission (Laue) geometry, since for the reflection geometry the phase between the polarisation components is never as large as $\pi/2$ [52].

Having given the characteristics of the x-ray beam needed for an MXSW experiment, some details should be given about the experimental equipment. XMCD experiments are usually performed with the sample placed in an external magnetic field. This allows to record the signals by switching not only the helicity, but also the magnetisation direction, what helps to remove the experimental artefacts related to imperfect polarisation

and ensures that the measured difference in cross-sections is indeed of magnetic origin. This approach was also used in the MXSW experiments reported in this work. On the other hand, ideally an MXSW experiment should be performed without magnetic field, in order to avoid perturbation of the spontaneous magnetic structure. In a sufficiently large external magnetic field, all magnetic moments align in the direction of the field, so in such conditions no observation of the ferri- or antiferromagnetic ordering is possible [143]. If one decides to perform an experiment with an external magnetic field (because for example a ferromagnetic ordering with different magnetic moments on sublattices is predicted), a source of the field is needed, either in the form of permanent magnet or electromagnet. The possibility of controlling the direction of the magnetic field (to align it for example parallel to the reflecting lattice planes) and switching its orientation along this direction, is required.

In order to orient the crystalline sample and perform the angular scans through the reflection domain, what constitutes the essence of the standing wave experiment, a diffractometer with at least three rotation degrees of freedom (circles) and a movable detector arm, is needed. The standard XSW experiments are performed also by keeping the orientation of the sample fixed and by changing the energy around the one corresponding to the diffraction condition at a given angle. This is equivalent to the performance of a rocking scan by changing the incidence angle. This approach is not applicable in the case of MXSW, since the energy has to be tuned to the absorption edge and the variation of energy changes the value of Δq_f^s , thus the observed variations in the XMCD signal would be a superposition of those changes and the changes in the contribution from different magnetic moments caused by the movement of the standing wave.

As mentioned already in section 4.8, when not detected directly in the transmission mode measurement, the XMCD effect can be determined experimentally either using emitted secondary electrons or fluorescence photons. Even though the former is more advised from the data analysis point of view, the latter is used in this work as being much more convenient from a practical point of view. The detection of emitted electrons requires a sample to be put under high vacuum conditions, otherwise they are quickly absorbed by the air. A combination of suitable vacuum system and the diffractometer is rather an uncommon equipment among the existing synchrotron beamlines. Therefore, the fluorescence detection mode is advised for MXSW experiments.

The simplest way to detect the x-ray fluorescence from a given element is to use selected filters, which absorb the radiation with other energies, leaving only the window for the fluorescence line of interest. The detection of fluorescence can be also performed using the analyser crystal, which acts as a filter passing only photons having energies within a certain narrow range. The photons, which passed through filters or analyser crystal are then detected using non-energy-dispersive detectors like photodiodes or scintillation detectors. Alternatively, and this is the preferred method for the MXSW technique, since one does not require the too high energy resolution offered by analyser crystals, the x-ray fluorescence can be detected by using energy dispersive semiconductor detectors. More details on the principle of their operation is given later in this chapter. Similarly, like in the standard XSW experiment, not only secondary radiation yield is detected, but also the intensity of the reflected wave. This data sets the angular range of the reflection domain and shows, where on the angular scale the effects of the standing wave can be expected. The reflected beam is detected using so called point detectors, which are put on

the 2Θ arm of the diffractometer. These can be scintillation detectors, avalanche photo diodes (APD) or PIN diodes.

At this point, only the experiments under ambient conditions are considered. This greatly simplifies the experimental system, but on the other hand limits the number of crystalline systems, which can be studied, as many of magnetic materials exhibit transition to magnetic state at low temperatures. In the future, the MXSW experiments could be also performed at other temperatures, so that the systems, which are non-magnetic at room temperatures, as well as the changes of the magnetic structure during the transitions, could be investigated. To control the temperature, the cryostats would need to be incorporated in the experimental system. Experiments at increased pressures could potentially give an insight into the pressure-induced changes in the magnetic structure. The use of diamond anvil cells complicates the detection of secondary radiation, but a special cell allowing detection of fluorescence exists [162].

7.2 General schema of the MXSW experiment

Regardless of the sample and the absorption edge used, all MXSW experiments consist of several common steps, which are summarised in this section. Following the discussion given in section 4.6, it is assumed that the imbalance in the density of empty states $\Delta\rho_f^s$ measured at a single energy value at the absorption edge, even though not directly proportional to the magnetic moment, in the case of the MXSW experiment gives a good measure of its changes. Therefore, it is proposed to perform the experiment at fixed energy and conduct only the angular rocking scans through the reflection domain.

The schema of a standard MXSW experiment is shown in figure 7.1. What is shown is a procedure for a single reflection. It should be repeated for several chosen reflections in order to obtain more confident structural information. The energy is tuned to the value at the absorption edge, possibly where the XMCD signal is the highest, but the choice should be made individually for each investigated system. Before choosing the energy value for the MXSW scans, an energy scan for an orientation of the sample away from any Bragg reflections should be performed for both helicities, and the fixed energy value chosen accordingly to the obtained XMCD spectrum. The best is to perform the MXSW scans for several energies in the vicinity of the absorption edge and compare the results. Provided that the assumption about the proportionality of $\Delta\rho_f^s$ to the magnetic moment is valid, the results should yield the same structural information, as long as the energy is close enough to the absorption edge that the XMCD effect can be observed.

The sample is usually mounted on a goniometer head, which is then put on the diffractometer. Depending if a magnetic field source is used additionally, the sample might have to be placed on the special holder compatible with the magnet system used.

The sample needs to be oriented, such that the diffraction (Bragg) condition is fulfilled. Usually, in the case of crystals investigated using the standing wave methods, at least the surface orientation is known. The reflection from the lattice planes parallel to the surface is then already one of two reflections needed to determine the orientation of the crystal uniquely (that is to find the orientation matrix, also called the UB matrix). The second one can be found by calculating the angle between the lattice planes of the first reflection and the ones corresponding to the other chosen ones. The lattice parameters and the

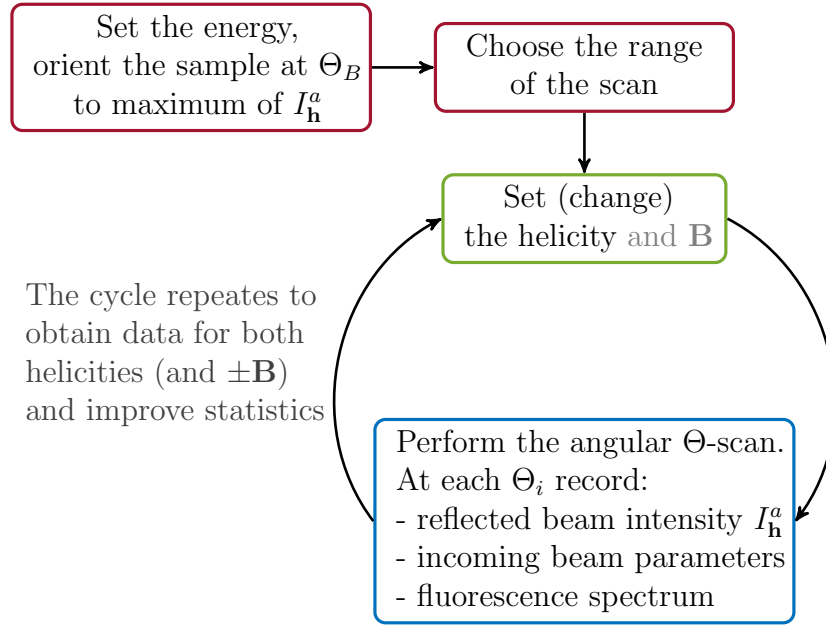


Figure 7.1: A general schema of an MXSW experiment, where the secondary radiation yield is measured by detecting the x-ray fluorescence. The red boxes refer to the preparation of the scan. The helicity (and possibly the magnetic field orientation) can be changed either as shown in the schema — after the full scan is finished — or more often using fast switching. The actual scan consists of recording the parameters of incoming beam, reflected beam intensity and the full fluorescence spectrum. The same scan is repeated for both helicities (and magnetic field orientations) multiple times in order to improve the data statistics. The energy is kept constant during the experiment. The whole procedure is repeated for several chosen reflections.

crystal system have to be known, but this is usually the case, if one is interested in determination of the magnetic structure. Also for other XSW experiments the crystal structure of the system generating the standing wave is usually known. Knowledge of the angle between the lattice planes and the Bragg angle of the second reflection allows to orient the crystal so that this second reflection is reached (more details are given in section devoted to the experiment on Pt_3Co). Based on those two reflections the orientation matrix can be calculated and any desired reflection reached. If no information about the orientation of the crystal is available beforehand, the sample can be oriented using the monochromatic x-ray beam, recording the dataset by the two-dimensional detector and finding the orientation matrix using x-ray crystallography software like XDS [163]. Alternatively, also the white beam Laue diffraction can be utilised for this purpose.

The polarisation of the beam has to be circular with a possibility to change the helicity either at the end of each angular scan or more often during the scan. The latter can be realised by fast flipping of the phase plate between the positions corresponding to the RHP and LHP (what, as discussed in section 7.1.2, is equivalent to changing the value of $\Delta\Theta$). In such a case the data corresponding to the RHP and LHP is sorted out by the electronic control system. If the MXSW experiment is performed with the sample kept in an external magnetic field in order to magnetise the sample (for example otherwise non-magnetic paramagnetic or diamagnetic systems), the field direction has to be aligned

appropriately or at least well determined (since the MXSW theory predicts the results for any arbitrary magnetic moment orientation), and the orientation has to be changed after each scan (or each second scan if the helicity is changed only once the full scan is finished). Without external magnetic field, two sets of data — for RHP and LHP — should be obtained. If the external magnetic field is used, the experiment should yield four sets, for the combinations (LHP, $+\mathbf{B}$), (RHP, $+\mathbf{B}$), (LHP, $-\mathbf{B}$), (RHP, $-\mathbf{B}$).

The actual MXSW scan is a Θ -scan (rocking scan) around the angular position, where the maximum of the reflected beam intensity is observed. This point corresponds roughly to the middle of the reflection domain (in fact the rocking curve is asymmetric and the maximum lies on the low angular side of the reflection domain, but given the contributions from mosaicity of the crystal and beam divergence, this assumption is good). The range of the scan should be big enough, to cover the whole reflection domain and such that the secondary radiation yield reaches the background level. At each step of the scan the parameters of the incoming beam, such as the intensity measured by the incident intensity monitors (for example ion chambers) and parameters determining the polarisation state (for example intensities of the σ - and π -polarisation components) are measured. The actual experimental data recorded at each angular step of the scan consists of the reflected beam intensity and the full fluorescence spectrum. The fluorescence yields, that is integrals of the chosen lines in the fluorescence spectra, recorded for both helicities, after subtraction and normalisation are used as a measure of the XMCD effect.

7.3 Experimental system at the P09 beamline

The MXSW experiments presented in this work were conducted at the P09 beamline [164] located at the PETRA III radiation source at Deutsches Elektronen-Synchrotron (DESY) in Hamburg. Therefore, a description of the experimental system at this beamline is given hereafter. Since resonant scattering beamlines are ideal experimental stations for MXSW experiments, the information given in this section remain quite general and can be useful also when the experiment is performed at another synchrotron light source.

PETRA III is a third-generation high brilliance synchrotron radiation source. The storage ring has a circumference of 2304 m, being thus the largest synchrotron light source in the world. The machine allows to produce x-ray beams characterised by very low horizontal emittance of 1.2 nm-rad. PETRA III is operated at an electron energy of 6.084 GeV. The electron beam is divided in 480 bunches in the multi bunch mode and 40 bunches in the timing mode. The ring current is 100 mA at normal operation [165].

The P09 experimental station is devoted to resonant scattering, XMCD and x-ray resonant magnetic reflectivity (XRMR). The x-ray beam is produced in a 2 m long undulator. The energy of radiation is tunable in the range of [2.7; 24] keV, the polarisation can be linear in any direction or circular. The polarisation can be changed in the reduced energy range of [2.7; 13.7] keV. In the MXSW experiments, the energies of 11.566 keV (Pt L_3 absorption edge) and 7.1135 keV (Fe K absorption edge) were used.

7.3.1 Beamline optics

A monochromatic beam is obtained at the P09 beamline using a silicon double-crystal monochromator, cooled by liquid nitrogen. Two sets of Si crystals are available, (111) or (311) oriented ones. The latter allows to achieve a better energy resolution on the cost of a smaller photon flux. The energy bandwidth using the (111) crystal is $\Delta E/E = 1.3 \times 10^{-4}$, what gives energy resolution of 1 eV at the energy of 8 keV. In the experiments reported here, the Si (111) reflection was used to monochromatise the beam.

The control over the polarisation of initially in-plane linearly polarised x-ray radiation is achieved by a double phase retarder system located in the optics hutch of the P09 experimental station. Circularly polarised x-rays are generated after passing through a properly oriented diamond crystal phase plate (quarter wave plate), as explained in section 7.1.2. Details about the design of the phase retarder are given in the paper of Francoual *et al.* [166]. In order to reduce the impact of instabilities, the polarisation of the beam can oscillate rapidly between the RHP and LHP states, and the signals corresponding to those polarisation states can be saved separately using the control electronics. This is achieved by mounting the phase plate on the piezo-driven flipper, which oscillates with a frequency of 23 Hz between the orientations corresponding to the RHP and LHP. Signal from the arbitrary wave form generator controlling the movement of the phase plate is fed also into a Raspberry Pi controlled field programmable gate array (FPGA) device, which allows to sort the measured signals into different channels directly [167], from which the histograms are made in the SIS3820 (Struck Innovative Systeme GmbH) counter board.

Rejection of higher harmonic energy components in the beam generated by the undulator, as well as focusing of the beam, is made possible by two 1 m long vertically reflecting mirrors made of SiO₂ and covered with palladium. The critical angle depends on the energy and is smaller for shorter wavelengths, what explains the principle of higher harmonic rejection using the specular reflection of the beam. The second mirror is additionally equipped with a bender allowing vertical focusing of the beam [164].

The slit system located in the first experimental hutch (EH-1) allows to define the size of the beam incident on the sample. Two passivated implanted planar silicon (PIPS) diodes placed perpendicular to each other measure the intensities of the incoming beam scattered from a glassy carbon foil and thus serve as the incident intensity and polarisation monitor. The signal from this system is used to align the phase plate, such that it generates circular polarisation (thus giving the same signal on both diodes). The next component on the incident beam path is an absorber box, which allows to insert selectively 12 foils thus attenuating the beam by known factors. The last component before the incident beam reaches the sample is the second slit system, which allows to reject the effects of the beam scattering on the first slits [164].

7.3.2 The diffractometer

The EH-1 of the P09 beamline is equipped with 6-circle Huber diffractometer (Huber Diffractionstechnik GmbH & Co. KG), where three rotation stages are for the orientation of the sample (χ , φ , Θ) and three for the detectors (2Θ , δ , γ). This allows for both horizontal and vertical scattering. A slit system located on the detector arm before the point detector allows to define the reflected beam path between the sample and the

detector. In the MXSW experiments a 4-coil electromagnet was placed additionally on the diffractometer (see figure 7.2) in order to magnetise the sample. The sample was glued on the special holder compatible with the electromagnet system. The MXSW experiments were performed in vertical scattering mode. Figure 7.2 shows the diffractometer aligned to allow rocking scans of the YIG (444) reflection.



Figure 7.2: The EH-1 of the beamline P09 at the PETRA III synchrotron. The station is equipped with 6-circle Huber diffractometer. The path of the incoming beam is marked in the photo by red arrow. The position of the detector arm is set such, that the reflected beam reaches the point detector (APD in this case). The sample is placed in the middle of 4-coil electromagnet system, in the center of rotation of the diffractometer (see the close-up in figure 7.3). The fluorescence detector (SDD) is located above the surface of the sample, such that the angle between the direction to the detector and surface of the sample is $\alpha = \pi/2$.

7.3.3 Electromagnet system

An external magnetic field was applied during the MXSW experiments using the 4-coil electromagnet constructed at the Bielefeld University [168] and modified later by the P09 beamline personnel. As can be seen in figure 7.3, the system is located on the 6-circle diffractometer and the sample is placed in a middle on a special compatible holder. A piezo-stage below the sample holder allows for adjustment of the sample's vertical position.

Constant current applied by a power supply generates a magnetic field in the coils, which is guided towards the sample by steel rods. The distance between the sample and the rods can be adjusted. By changing the value and direction of the current in each of the coils, the desired strength and direction of the magnetic field is obtained. The direction of the magnetic field is confined to the plane of the sample's surface. The device can provide a magnetic field as strong as 180 mT. The coils are water-cooled.

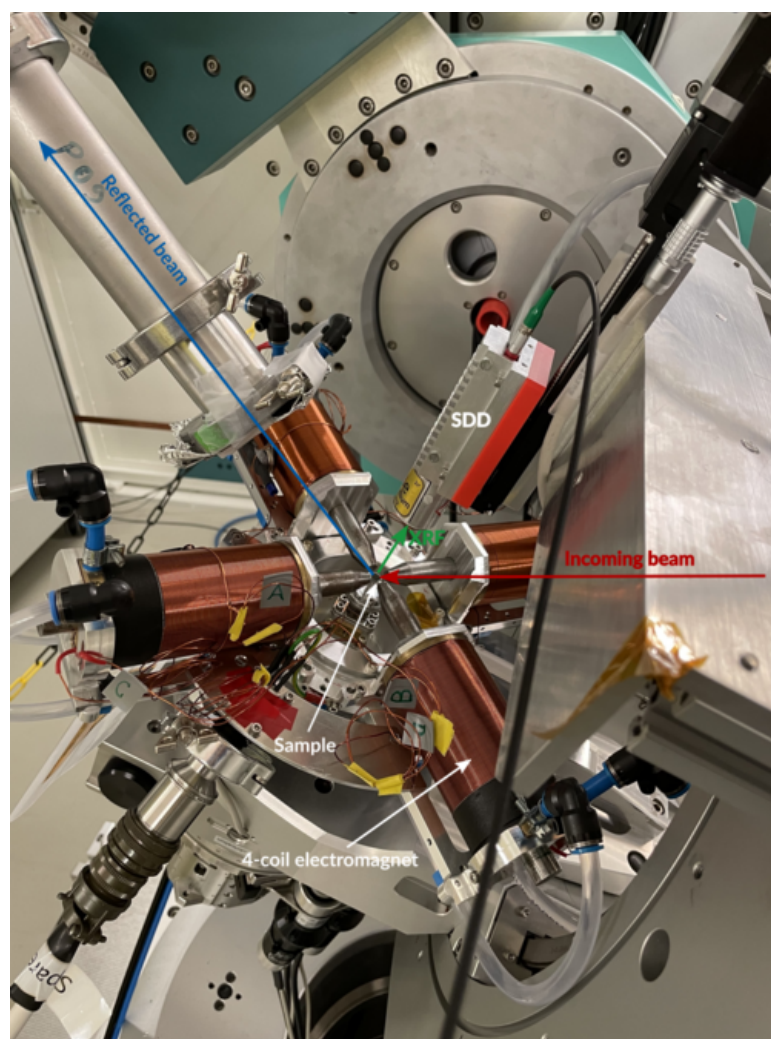


Figure 7.3: The experimental system used for the MXSW experiments, close-up. The sample is mounted in the centre of the electromagnet system on a compatible holder. The paths of the incoming (red arrow) and reflected (blue arrow) beams are shown schematically. The green arrow symbolises the fluorescence radiation emitted from the sample towards the fluorescence detector (SDD). The 4-coil electromagnet system is located on the 6-circle diffractometer.

In future experiments, the magnetic field can be also applied by the robust permanent magnet system, designed by Heiko Schulz-Ritter. Two versions of the discussed device were constructed. Both of them allow to change the magnetic field direction arbitrarily in one plane perpendicular to the sample surface (which is a scattering plane for the situation shown in figures 7.2 and 7.3). The device of the first design generates the

magnetic field of a strength of approximately 150 mT, whereas the newer one generates 250 mT. The advantage of using a permanent magnet system is that there is no need for cooling and power supply. Since these systems were not used in the reported experiments, more details are given in appendix D. They were utilised during the test experiments at the P24 beamline and were found to function properly.

7.3.4 Detectors

Reflected beam detector

The rocking curve is recorded during the MXSW scan in order to set the angular scale for the secondary radiation yield and define the angular reflection domain. The reflected beam intensity is recorded using a point detector, whose angular resolution is defined by the detector slits. Different detectors can be used as point detector for this purpose, among them there are PIN diodes, scintillation detectors and APDs. The latter was used for the MXSW experiments.

The principle of detection of an x-ray photon in an APD is the same as in all semiconductor radiation detectors — the photon is absorbed by the detector material and generates electron-hole pairs, which are collected on the electrodes. In contrary to all other semiconductor detectors, APDs are the only ones, which have an internal amplification of the signal. A high voltage applied to the depletion region of the n-p junction accelerates the photoelectrons, which by collisions excite further electrons to the conduction band (avalanche effect). This leads to the amplification of the initial photocurrent, depending on the applied reverse bias voltage [169, 170]. The internal gain improves the signal to noise ratio and allows to reach high count rates as the generated charge is collected rapidly [171].

Fluorescence detector

As mentioned earlier, the energy spectrum of x-ray fluorescence radiation can be recorded either using analyser crystals or filter foils and energy non-dispersive detector or energy dispersive detectors, for example silicon drift diode (SDD). The latter was used to record the spectra during the MXSW scans.

The detector used was a Fast SDD (Amptek, Inc.) with silicon thickness of 500 μm and 25 mm² window. The working principle of the SDD detector is based on the so called sideward depletion. A basic device consists of a pure silicon wafer with strips of diode junctions on both surfaces and an anode on the edge. Application of continuously rising potential creates a horizontal field, which guides the photoelectron towards the anode (thus the name *drift diode*). For the application in x-ray spectroscopy, this design is slightly modified, so that the drift electrodes are located only on one side of the device, leaving the other one free as the entrance window [172, 173]. An average of 3.6 eV is needed to create an electron-hole pair in silicon. An absorbed x-ray photon loses its energy by generating electron-hole pairs. The number of the charges collected on the anode is proportional to the total energy deposited by the photon. If the photon loses its entire energy inside the silicon wafer, the charge measured by the integrated preamplifier is a direct measure of the photon energy.

7.3.5 Control system

At the P09 beamline all devices are controlled via TANGO, a toolkit used for connecting hardware with software. The software used for the user control of the devices, including the diffractometer is Spock — the IPython command line application being an adopted version of spec.

The data acquisition system for the SDD detector is independent from the beamline electronics. It consist of the VME crate with a SIS3302 analog-digital converter (ADC), a counter and a controlling computer. The data is collected using the ADCgui software written by Martin Tolkiehn, which provides ready histograms of the counts per energy channel.

Scripts written in Matlab were used for the quick analysis of the experimental data. They allow a simple integration (by summing the number of counts) over the region of interest in the recorded fluorescence spectra, corresponding to the spectral lines of the magnetic elements. When plotted against the Θ angle, such integrals serve as a measure of the fluorescence yield for each helicity and magnetic field orientation. Further, an XMCD signal can be calculated as a simple difference between such yields. This quick analysis allows to control the quality of the data just after first scans are finished, and if necessary correct the errors in the experimental procedure during the measurements.

Chapter 8

Experiment on the Pt₃Co crystal

As mentioned in the previous chapter, the crystal systems containing magnetic ions of 5d metals are very good candidates for studies using the MXSW method. This is because the L_{2,3} absorption edges of those elements lie in the hard x-ray regime, what makes not only observation of the XMCD effect possible, but also enables excitation of several Bragg reflections. Being inspired by the first experimental attempt to perform MXSW experiment, where a nickel-platinum alloy was used [46], the first experiment within the framework of this project was performed on a Pt₃Co single crystal.

This chapter is organised as follows. At first some details about the sample and the experimental conditions during the measurements at the P09 station are given. Then the results are presented with the routine of data analysis being explained in parallel. The chapter is concluded with the discussion about the obtained data.

8.1 Experimental details

The single crystal of Pt₃Co alloy was bought from MaTecK Material Technologie & Kristalle GmbH. The sample is in the form of a disk with diameter of 5 mm and thickness of 1 mm. It is one side polished with roughness smaller than 0.01 μm and orientation accuracy smaller than 1°. The surface orientation is (111). The details about the structure and properties of Pt₃Co are given in section 5.1.

The MXSW experiment on Pt₃Co was performed at the P09 experimental station from 7.09.2020 to 14.09.2020. The sample was glued on the aluminium holder compatible with the electromagnet system. The crystal surface was aligned with respect to the incoming beam using the combination of height and Θ scans. The experiment was performed in the vicinity of the platinum L₃ absorption edge (nominally $\mathcal{E} = 11.564$ keV). Since the MXSW experiments are performed as angular scans at fixed energy, an energy spectrum around the nominal value was performed for both helicities of the incoming beam to choose the appropriate energy value for the actual scans. The sample was magnetised in the direction parallel to the sample surface and lying in the plane being a scattering plane for the surface (111) reflection. The electromagnet described in section 7.3.3 was used. It provided a magnetic field of 150 mT, the same for both orientations of the field (parallel and antiparallel to the incoming beam direction) measured at the surface of the sample (the measurements with a Hall probe revealed 148 mT for one orientation and 147 mT

for the other). The hysteresis curve measured for the sample at 220 K using a physical property measurement system (PPMS) revealed that this field suffices to magnetise the sample and reach saturation (see appendix E.1). For the energy spectrum measurement, the sample was aligned away from Bragg reflections. For the sake of energy alignment, a simple measure of the energy spectrum was obtained by summing the number of counts from the SDD detector for the channels corresponding to Pt L_α fluorescence line. The spectra differed between the helicities in the wide range [11.55; 11.59] keV. The changes in the region distant from the absorption edge were identified as an artefact from the phase plate. Since it was aligned for the nominal energy for the absorption edge, away from this energy it does generate waves, which differ in intensity when the helicity is changed. Due to this fact, an energy of 11.566 keV was chosen for the MXSW scans. At this energy a significant difference in spectra was observed, which was surely caused by the XMCD effect due to the proximity of the absorption edge.

Since the surface orientation of the sample, as well as the atomic structure of Pt₃Co are known, the determination of the UB matrix is straightforward. Having the angular coordinates of the (111) reflection, the ones for other ones, for example (311), can be found easily. The procedure is the following. The angle between the (111) and (311) planes for the cubic crystallographic system is equal $\tau = 29.5^\circ$. In order to find the diffractometer position for the (311) reflection, the Θ and 2Θ are aligned to the values $\Theta = \Theta_B^{(311)}$ and $2\Theta = 2\Theta_B^{(311)}$, and the position of χ is changed by τ from horizontal position. Then an angular φ scan is performed, and the position of this angle corresponding to the sought reflection found by monitoring the signal from the point detector. Those two reflections allow to define the orientation matrix and calculate (what is done by control software) the angles of the diffractometer corresponding to any other one.

For the actual MXSW scans the sample was oriented so that the (111) reflection was excited. The positions of 2Θ , Θ and χ angles were optimised by performing the scans around the nominal positions, such that the maximum of the reflected beam intensity was observed. Even though the sample was a single crystal, it became apparent by inspection with the x-ray beam, that it consists of several slightly misoriented grains. Therefore, the horizontal position of the sample, as well as φ angle were adjusted so that only one grain contributed significantly to the observed reflected intensity. Practically, this means that only one peak was observed during Θ -scan. The beam-defining slits were kept wide open.

The number of counts in the SDD detector, which was mounted above the sample surface ($\alpha = \pi/2$), was optimised by insertion of attenuation foils into the incoming beam, such that no significant number of pile-up events was seen in the fluorescence spectrum. For the MXSW scans, the helicity of the incoming beam was changed with a frequency of 23 Hz using the fast flipping schema. The sample was in the external magnetic field being in the same setting as for the energy scan. The orientation of the magnetic field was changed after each full Θ -scan. The scan having 200 steps was performed around the Θ value of 13.8978° by changing it until $\pm 0.2^\circ$ in steps of 0.02° . The data was collected for 20 s at each step of the scan. Due to relatively weak XMCD signal observed, owing to the small magnetic moment of platinum, only the scans for the (111) reflection were performed in order to obtain data with small statistical uncertainties. In total 60 scans were recorded for both orientations of the magnetic field.

8.2 Data analysis procedure and results

In this section the results obtained for the Pt₃Co crystal are presented along with the explanation of the data analysis procedure. The analysis was performed using scripts written in Matlab [111].

8.2.1 Reflectivity and beam stability

The reflectivity curve (figure 8.1) is obtained by simple summation of the data obtained from the APD detector for individual scans. A broadening of the main maximum and appearance of the side peak was observed after a certain data acquisition time, what is caused presumably by the movement of the beam position caused by machine instability. Therefore, only first 14 scans for each magnetic field orientation (28 in total) were taken for the final analysis. This number was observed to be already sufficient to obtain a decent data quality. No variation of the reflected intensity with the magnetic field orientation was observed, what means that the sample was well fixed on the holder and did not move when the magnetic field was reoriented.

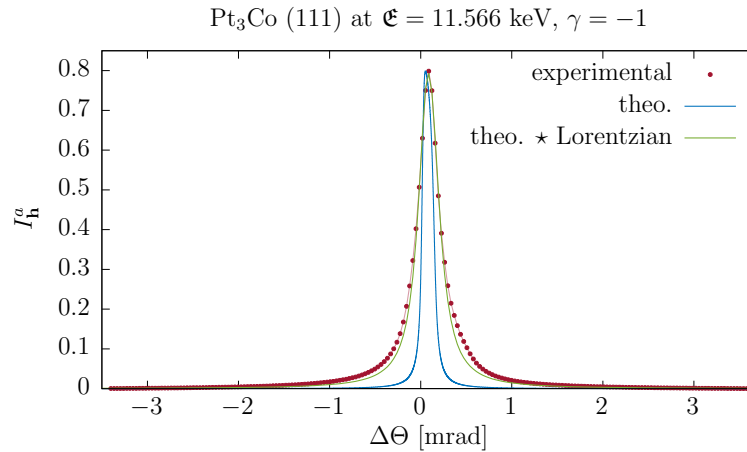


Figure 8.1: Experimental reflected beam intensity $I_{\mathbf{h}}^a$ for the Pt₃Co single crystal, symmetric (111) reflection. The data is compared with the theoretical function calculated based on dynamical theory of diffraction and convolved with a reflectivity curve of a double crystal silicon (111) monochromator (blue curve). The green curve is the blue one convolved additionally with a Lorentzian function, which accounts for the mosaicity of the crystal. From comparison between the blue theoretical curve and experimental data (red points) it can be seen, that the crystal is not an ideal one. The scale for $I_{\mathbf{h}}^a$ is set by the theoretical function. The experimental data for one orientation of the magnetic field is shown only, as it almost does not differ for the other one.

As it can be seen in figure 8.1, the position of the sample was optimised such, that the reflection from only one grain was excited. The comparison between the experimental data and the theoretical curve (the reflectivity calculated from dynamical theory for Pt₃Co convolved with the double convolution of Si (111) curves, that is the monochromator reflectivity as defined in [52]), shows that the crystal's mosaicity is significant. The contribution of this imperfection was taken into account by convolving the theoretical

curve with the Lorentzian (Cauchy) function with a scale parameter related to the width of the function, $\Gamma = 0.1817$ mrad. This value was obtained from the fitting of the theoretical function after convolution to the experimental data using the Matlab *fminsearch* function, which uses the simplex search method [174].

The examination of the signal from PIPS diodes, used to monitor the beam intensity and polarisation (via determination of the intensity of the σ - and π -polarisation components), revealed that during the scans used for analysis, the intensity of the incoming beam was very stable. The average degree of circular polarisation estimated based on the signal from PIPS diodes (assuming that ideal circular polarisation is equivalent to equal signal on both orthogonally positioned detectors) was equal 99.85%.

8.2.2 Fluorescence spectra

The raw fluorescence spectra obtained from the ADCgui software are first normalised by the average beam monitor signal (average of the signal from both PIPS diodes), summed up over the scans chosen for analysis and then fitted using the combination of quadratic background and a sum of Gaussian functions (without offset), each representing a given spectral line and given by $g(x) = C_G \exp(-(x - \mu_G)^2/2\sigma_G^2)$, where σ_G is the parameter related to the width (standard deviation), μ_G the position of the maximum and C_G the scaling parameter (height). The fitting was performed using the Matlab *nlinfit* function, which utilises the Levenberg-Marquardt nonlinear least squares algorithm [175]. An exemplary fitted spectrum, corresponding to one angular position of the Θ -scan, one helicity and one magnetic field orientation, is shown in figure 8.2.

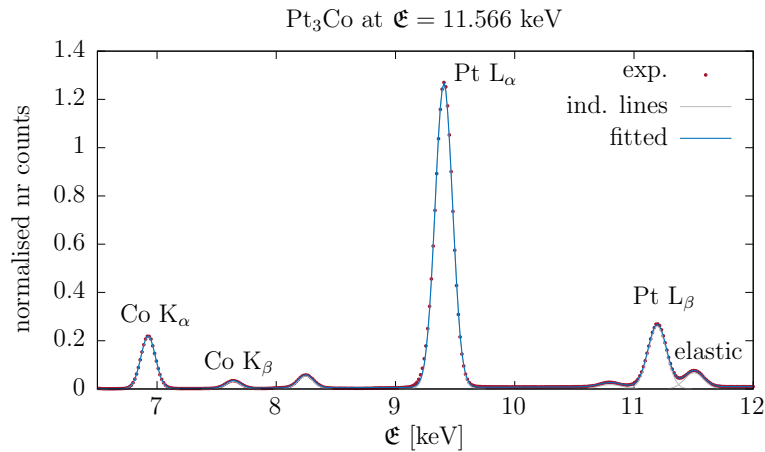


Figure 8.2: Single fluorescence spectrum for Pt₃Co crystal, recorded at 11.566 keV. It corresponds to a single angular position in the Θ -scan, one helicity and one magnetic field orientation. The experimental data was fitted using a combination of Gaussian functions for the spectral lines and a quadratic background. The Gaussian functions are plotted in gray. The energy scale was obtained by the comparison of lines' positions with nominal values for corresponding fluorescence decay channels.

The collection of spectra for the entire Θ -scan, corresponding to a single configuration of helicity and magnetic field orientation is shown in figure 8.3. The presented data is a

result of summation over all recorded scans used for analysis, corresponding to a given helicity and magnetic field orientation.

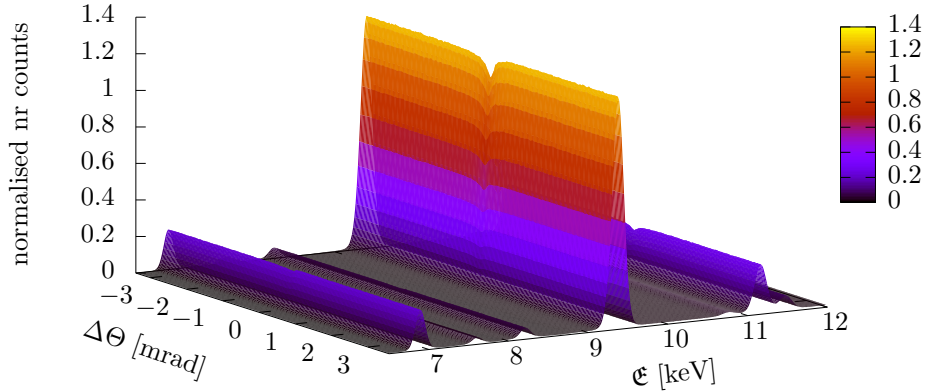


Figure 8.3: A collection of fluorescence spectra from Pt_3Co for the entire Θ -scan, recorded for one configuration of helicity and magnetic field orientation. The presented data is a sum of the data from individual scans for this setting, normalised before summation by the signal from the beam intensity monitor. The plot presents the idea of the XSW experiment, as one can easily see the variation in the intensity of the Pt L_α line, whose determination is the aim of the experiment. The shape of the variation is highly influenced by the extinction effect.

The determination of the change in the intensity of individual spectral lines is what constitutes the core of the XSW methods. The change in the Pt L_α line can be clearly seen in figure 8.3. The shape of the variation is an effect of the standing wave impact on the absorption cross-section of the atoms and additionally the extinction effect, which highly manifests itself in the case of the used SDD detector position (above the sample surface).

8.2.3 Fluorescence yield

The parameters of the Gaussian functions obtained from the fitting procedure corresponding to a given spectral line are used to calculate the fluorescence yield. This is defined as simple integral over the energy of the Gaussian function and can be calculated analytically from the parameters. For an angular position i , it reads $y_i = \sqrt{2\pi}C_G\sigma_G$. Since the used *nlinfit* Matlab function [176] returns the covariance matrix of the fitting parameters, the square root of the diagonal elements can be taken as a measure of the standard deviation of the parameters. The uncertainties of the values of the fluorescence yield are then calculated using the propagation of uncertainty [177], here taken in the form

$$\Delta y_i = \left| \frac{\partial y_i}{\partial C_G} \right| \Delta C_G + \left| \frac{\partial y_i}{\partial \sigma_G} \right| \Delta \sigma_G = \sqrt{2\pi} (\sigma_G \Delta C_G + C_G \Delta \sigma_G) \quad (8.1)$$

where Δx denotes the uncertainty of some quantity x .

Figure 8.4 shows the fluorescence yields for all four configurations of the helicity and magnetic field orientations. It was calculated based on the Pt L_α fluorescence line. An addition of the yield from the L_β line was observed not to change the shape of the data. This line is significantly weaker and additionally to some extent overlaps with the elastic scattering peak, thus increasing the experimental uncertainties for the yield. Therefore, this line was not used for the analysis.

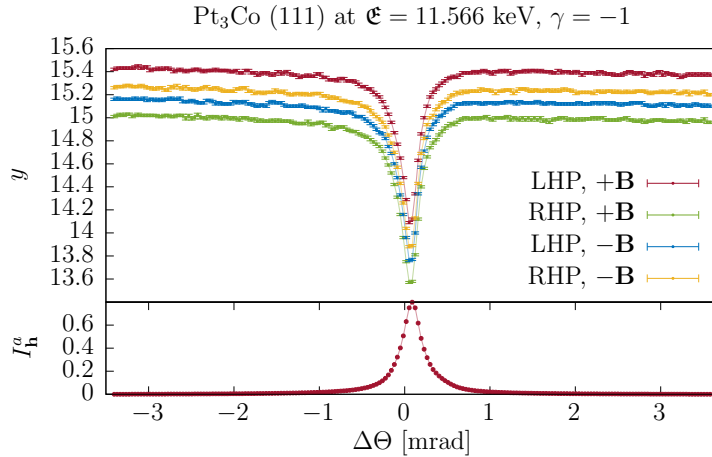


Figure 8.4: The experimental fluorescence yields for Pt₃Co calculated based on the Gaussian functions fitted to the experimental spectra for all configurations of helicity and magnetic field orientation. The shape of the variation is dominated by the extinction effect. The Pt L_α line was used for yield calculation. The differences in the yield are caused by the XMCD effect. The curves obtained for the setting after reversal of both the field orientation and the helicity of the beam should coincide (red and yellow curve, as well as blue and green). The discrepancy is related to imperfection of polarisation reversal and/or magnetisation switching.

The differences observed between the yields owe to the XMCD effect. The reversal of the magnetic moment orientation and light helicity is equivalent (at least for the considered setting that is the moments in the scattering plane and the circularly polarised incoming wave). Therefore, the yields for (RHP, + \mathbf{B}) and (LHP, - \mathbf{B}), as well as (RHP, - \mathbf{B}) and (LHP, + \mathbf{B}), should coincide. As seen in the graph, this is not exactly the case, even though the general trend is preserved. This might be caused by the fact, that the reversal of magnetisation is not complete. It can be seen from the data, that the XMCD effect is weaker for the field setting denoted as + \mathbf{B} , than for the - \mathbf{B} one. This may indicate, that the reversal of the magnetic moment orientation was not complete, what causes the differences in the yields already in the background level (away from the reflection domain) for the + \mathbf{B} and - \mathbf{B} setting, as the angles between \mathbf{k}_0 and \mathbf{m} are then different.

The expected fluorescence yields for the magnetic moments aligned in the reflecting lattice planes and scattering plane can be calculated using equation for the absorption cross-section (6.8), where the quantities Υ_2 and Υ_3 are taken in the form with absorption correction for the wavevector, given by equations (4.53) and (4.54). The result of the simulations is presented in figure 8.5. It can be noticed, that the shape of the simulated

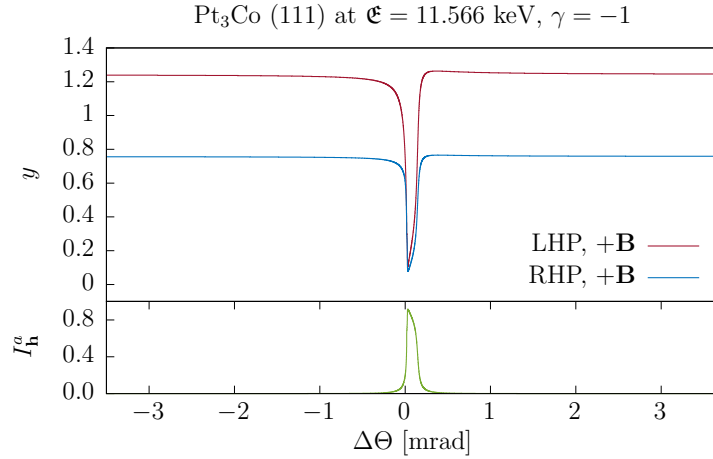


Figure 8.5: Simulated fluorescence yield for Pt_3Co for the experimental setting. The magnetic moments were aligned in the reflecting lattice planes and confined to the scattering plane using an external magnetic field. The yields were normalised by the background level (away from the reflection domain) of the yield for the linear polarisation (that is without the XMCD effect). One can notice that the experimental data shown in figure 8.4 resembles the simulation results.

fluorescence yields is similar to the experimental data. The width of the theoretical curves is smaller, and the variation more pronounced, what is related to the impact of mosaicity on the experimental result. In case of an ideal situation assumed for the simulations, no difference between the settings (RHP, + \mathbf{B}) and (LHP, $-\mathbf{B}$), as well as (LHP, + \mathbf{B}) and (RHP, $-\mathbf{B}$) is observed.

The impact of the mosaicity can be taken into account by convolution of the theoretical fluorescence yields with a Lorentzian function describing the mosaic spread of the sample, just like in the case of reflectivity. Additionally, a small impact of the monochromator is also taken into account by convolving the function with monochromator reflectivity. The parameters of the Lorentzian function are the same as obtained from the fitting of the theoretical reflectivity to the experimental data, except for the scaling parameter (height), which was adjusted by fitting to the experimental fluorescence yield. The final result of the fitting can be seen in figure 8.6, which presents the results for one magnetic field orientation. The agreement between the theoretical curves after convolution and experimental data is satisfactory. The reduction of the contrast with respect to the curves for ideal crystal is caused by mosaicity.

8.2.4 MXSW signal

The fluorescence yields obtained for four configurations of the helicity and magnetic field orientation can be used to calculate the XMCD signal also in four ways, assuming that a reversal of helicity is equivalent to the reversal of the direction of the magnetic moment. The XMCD signal can be obtained by subtracting the yields for different helicities, or for

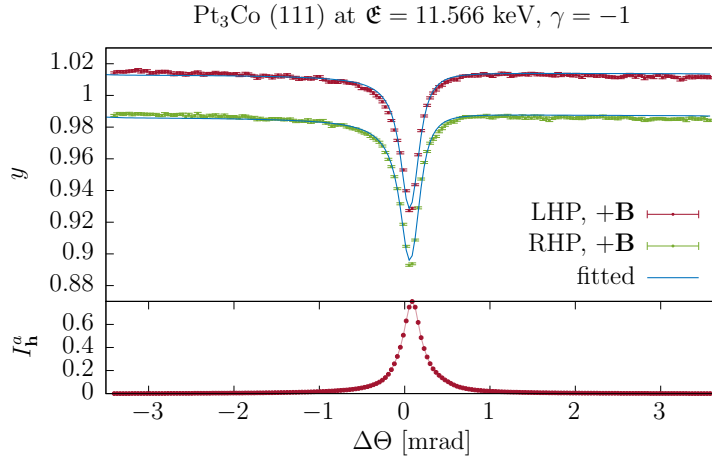


Figure 8.6: Experimental fluorescence yields for Pt₃Co compared with theoretical functions obtained as convolution of the ones calculated from the MXSW theory with monochromator reflectivity and Lorentzian function describing the mosaicity. The data was normalised by the common value such, that the curves are localised symmetrically around unity and relative difference (XMCD) remains unchanged. The data for one orientation of the magnetic field (+**B**) is shown. The parameters of the Lorentzian function are the same as the ones used for modelling the reflectivity curve, except for the scaling parameter, which was adjusted by fitting to experimental data.

opposite magnetic field orientations. Formally,

$$\Upsilon_{\pm\mathbf{B}} = \frac{y_L^{\pm\mathbf{B}} - y_R^{\pm\mathbf{B}}}{y_L^{\pm\mathbf{B}} + y_R^{\pm\mathbf{B}}}, \quad \Upsilon_{L/R} = \frac{y_{L/R}^{+\mathbf{B}} - y_{L/R}^{-\mathbf{B}}}{y_{L/R}^{+\mathbf{B}} + y_{L/R}^{-\mathbf{B}}} \quad (8.2)$$

where L and R are abbreviations for LHP and RHP. Resulting MXSW signals are presented in figure 8.7.

From the inspection of figure 8.7 it can be concluded, that the reversal of the helicity of the incoming beam in the experiment is working as expected. This conclusion can be drawn from the fact, that the MXSW signals $\Upsilon_{L/R}$ calculated based on the fluorescence yields for opposite field orientations show expected symmetry, that is $\Upsilon_L = -\Upsilon_R$. In contrary, complete symmetry does not exist between the remaining pair of signals, that is $\Upsilon_{+\mathbf{B}} \neq -\Upsilon_{-\mathbf{B}}$, though the sign of the signal is reversed. The fact, that the signal for +**B** is stronger in absolute numbers, that the one for -**B** indicates, that for the former orientation, the magnetic moments direction is closer to the propagation direction of the incoming beam, than for -**B**. An important general conclusion from the experimental MXSW signals is, that a clear and pronounced variation of the XMCD signal in the reflection domain was observed. In all the cases the absolute signal increased in the angular region (for $\Upsilon_{-\mathbf{B}}$ only slightly), where the impact of the standing wave on the observed signal is expected.

The impact of experimental artefacts can be investigated further by calculating a difference and a sum of the MXSW signals Υ presented in figure 8.7 [178]. The sum of the signals should be in ideal case equal zero, and the difference should give a measure of the XMCD signal. Using this method, one makes use of all four fluorescence yields

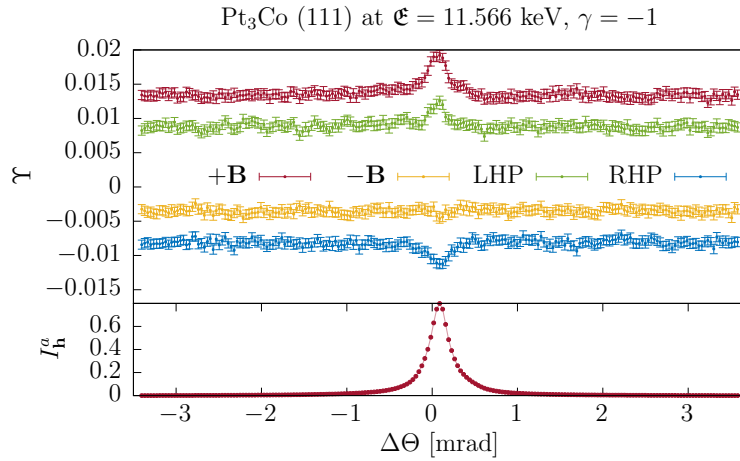


Figure 8.7: MXSW signals for the Pt₃Co crystal, calculated in all possible ways using fluorescence yields for four combinations of helicity and magnetic field orientation. The expected symmetry can be noticed for the signals calculated based on the field reversal (green and blue dots). A clear variation in the reflection domain was observed.

for calculating the XMCD signal and from the sum obtains an information about the experimental artefacts. The effect of the subtraction is shown in figure 8.8. It can be regarded as the measure of the MXSW signal obtained from the experiment on Pt₃Co, thus constituting the main experimental result of this investigation. The measure of the experimental artefacts, related to the switching of polarisation and reversal of the magnetisation that is the sum of the XMCD signals presented in figure 8.7, is shown in figure 8.9.

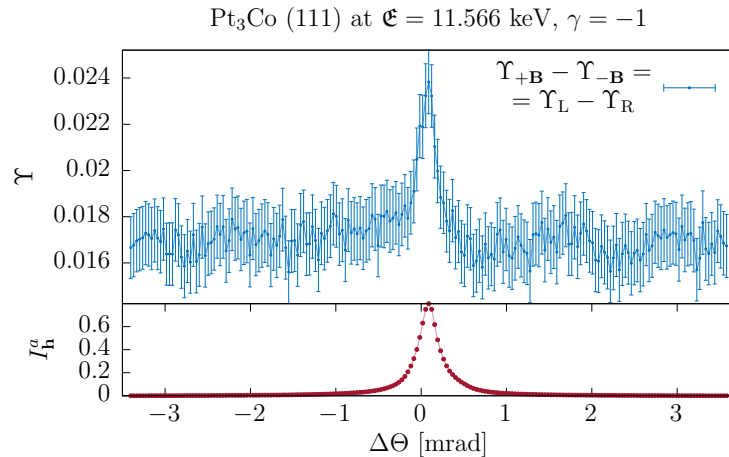


Figure 8.8: The difference of the MXSW signals for Pt₃Co presented in figure 8.7 that is $\Upsilon_{+B} - \Upsilon_{-B}$ and $\Upsilon_L - \Upsilon_R$. The signal calculated in this way can be regarded as a measure of the artefact-free XMCD, since the use of all four fluorescence yields is made for its calculation and via subtraction the influence of imperfections of the phase plate and electromagnet system is discarded.

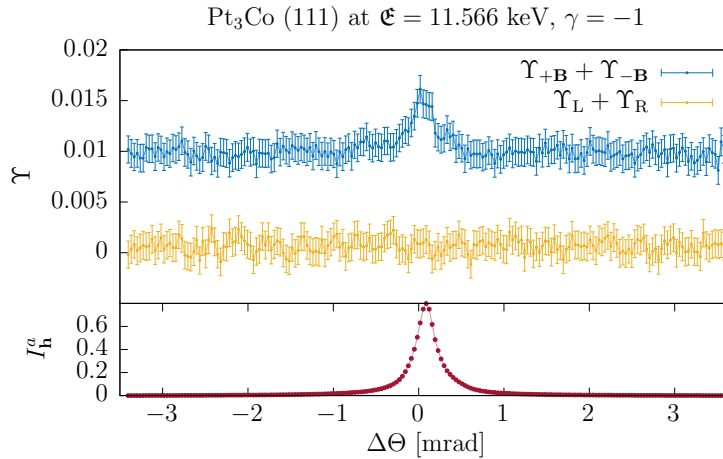


Figure 8.9: The sum of the MXSW signals for Pt₃Co presented in figure 8.7 that is $\Upsilon_{+\mathbf{B}} + \Upsilon_{-\mathbf{B}}$ and $\Upsilon_{\mathbf{L}} + \Upsilon_{\mathbf{R}}$. The signal calculated in this way can be regarded as a measure of the artefacts related to the switching of polarisation and reorientation of the magnetic field.

As it can be seen in figure 8.9, the signal being a sum of the XMCD signals calculated for fixed polarisation (that is $\Upsilon_{\mathbf{L}}$ and $\Upsilon_{\mathbf{R}}$) is almost equal to zero, what indicates, that the polarisation switching functions in the desired way. The artefact related to the magnetisation switching has a finite value and exhibits a variation in the reflection domain. Actually, this fact also supports the finding of the MXSW theory. The most probable reason for the existence of this artefact is incomplete reversal of the platinum magnetic moment directions. This means, that for the $+\mathbf{B}$ and $-\mathbf{B}$ settings, the magnetic moments are not lying on the same line having only opposite orientations, but there is an angle between the directions corresponding to $+\mathbf{B}$ and $-\mathbf{B}$. A dependence of the MXSW signal on the angle between \mathbf{h} and \mathbf{m} was observed in the simulation results (see section 5.1.2, figure 5.9). What remains here as an artefact is most likely related to the difference in MXSW signals for the magnetic moment directions occurring for the situations depicted as $+\mathbf{B}$ and $-\mathbf{B}$.

8.3 Discussion

The comparison between the experimental MXSW signal (obtained as subtraction of the initial MXSW signals shown in figure 8.7) and the prediction based on the theory for the situation of magnetic moment aligned in the reflecting lattice planes is shown in figure 8.10. A clear discrepancy between the data and theoretical prediction exists for the reflection region. Even though the theoretical curve exhibits also a slight increase on the high angular side of the reflection domain, it is smaller than the experimentally observed one. The decrease on the low angular side is not observed.

There might be several sources of the observed discrepancy between the experimental data and theoretical prediction. First of all the asymmetry observed already in the fluorescence yields background levels (figure 8.4) may indicate a lack of full control over the magnetisation of the sample. This hypothesis is also supported by the non-vanishing arte-

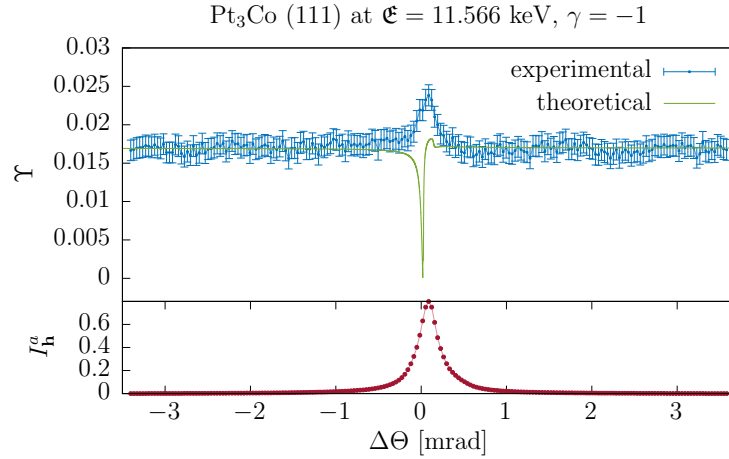


Figure 8.10: Comparison between the experimental MXSW signal for the Pt₃Co crystal and the theoretical curve calculated assuming the magnetic moments being aligned in the (111) planes. The theoretical data was normalised to the background level of the experimental MXSW signal. A discrepancy might be caused by the lack of full control over the orientations of the magnetic moments and the imperfection of the crystal.

fact shown in figure 8.9, observed only for the sum $\Upsilon_{+\mathbf{B}} + \Upsilon_{-\mathbf{B}}$. On the other hand, the hysteresis curve of the investigated sample (figure E.1) seem to indicate, that the value of the used magnetic field was sufficient to remagnetise the crystal. However, the magnetic measurement was performed at lower temperature (220 K) than the MXSW experiment (room temperature) and the magnetic properties of the crystal might differ between those conditions. It was reported for thin films of a Pt₇₂Co₂₈ alloy, that a stronger magnetic field is needed to reach saturation magnetisation at elevated temperatures [179].

Even though it was possible to perform the MXSW experiment using the reflection from one grain of the sample, what corresponds to the situation of using a single crystal, the crystal exhibits a mosaic spread, what can be seen by comparison of experimental reflectivity and the theoretical curve (figure 8.1). The fact that the mosaicity leads to smearing of the effects in the reflection domain predicted by the dynamical theory of x-ray diffraction may limit the applicability of the established MXSW theory (based solely on the dynamical theory) to such imperfect crystals. On the other hand, using the convolution with Lorentzian function accounting for the mosaic spread, a good agreement between experimental fluorescence yields and theoretical curves was achieved (figure 8.6). This would indicate, that at least qualitatively, in the sense of correct functional behaviour (reproduction of minima and maxima), the MXSW theory can give good predictions also for imperfect crystals.

As it was mentioned in the introduction to section 5.1, the chemical order in the platinum-cobalt alloy depends on the heat treatment of the sample. For the sample used in the MXSW experiment, no information about the heat treatment is known. Given an agreement between the theoretical curves calculated assuming a full chemical order and experimental reflectivity, as well as fluorescence yields, it was assumed that the crystal is in the ordered state. However, if deviations from the ideal order exist, that may influence the MXSW signal, as the Pt atoms on the Co sites would give rise to its different angular

dependence.

Summarising, the main result of the MXSW experiment on Pt₃Co crystal is an observed clear variation in the XMCD signal in the reflection domain. The signal is of a magnetic origin, as it persists when fluorescence yields for all four configurations of the helicity and magnetic field orientation are used. To investigate further the discrepancy between the experimental MXSW signal and theoretical prediction for the chemically ordered crystal with magnetic moments aligned in the reflecting lattice planes, a measurement of the hysteresis curve at room temperature and a single crystal diffraction experiment on the used sample could be made. The latter would allow to determine the occupancy parameters for the nominal Pt and Co sites, which could be used then for further theoretical simulations. The magnetic measurement would clarify, if the magnetic field during the MXSW experiment was indeed sufficient to remagnetise the sample.

At the end it should be mentioned, that a similar experiment was performed by the group of Jaouen [46]. The sample used was a nickel-platinum Ni₉₀Pt₁₀ alloy. It was reported, that the sample was in chemically disordered state. The researchers performed a standing wave experiment similar to the MXSW experiments discussed here, but no theoretical analysis of the experimental data was reported due to the lack of a theory for MXSW. The result obtained for the nickel-platinum alloy MXSW scan at the platinum L₃ absorption edge is very similar to the one reported here. Also an increase in the absolute value of the XMCD signal in the reflection domain was observed. The experiment was also performed by reversing both the magnetic field direction and the helicity of the incoming beam, though the magnetic field was aligned along the incoming beam direction. The interesting fact, that a similar result for the similar system as investigated here, but in disordered state, was reported, requires some further investigation. For example, simulations modelling the disorder using for example supercells or averaging the results for several randomly generated fillings of the basic unit cell could give insight into the dependence of the MXSW signal on the chemical order of the discussed alloys.

Chapter 9

Experiment on the YIG crystal

It was mentioned already several times in the text, and shown very clearly in chapter 5, devoted to computer simulations, that the MXSW method gives particularly useful information for systems, where the magnetic ions occupy some non-equivalent positions and an antiferromagnetic coupling exists between such magnetic sublattices. Therefore, the systems with ferrimagnetic or antiferromagnetic ordering are interesting candidates for the studies using the MXSW method.

In the part devoted to simulations three magnetic crystals exhibiting magnetic sublattices in their structure were reported: magnetite, yttrium-iron-garnet (YIG) and hematite. The crystals of magnetite and hematite are usually not of the highest quality (what was also checked for some samples using the standard XSW technique), but as mentioned already in section 5.3, very good YIG crystals are available. Therefore, the second MXSW experiment, aiming at showing the unique site selectivity of the technique, was performed using a YIG sample.

This chapter presents the experimental details and results of the MXSW experiment on YIG. It is organised in the same way as the one describing the experiment on platinum-cobalt alloy. Now the details about the experimental data analysis are omitted, since they were already explained in section 8.2.

9.1 Experimental details

The single crystal of YIG used as a sample for the MXSW experiment was bought from the MTI Corporation [180]. The sample is in the form of a disk with diameter of 5 mm and thickness of 0.5 mm. The crystal was grown using the floating zone growth method. It is one side polished and the surface orientation is (111). The details about the structure and properties of YIG are given in section 5.3.

The MXSW experiment on YIG was performed at the P09 experimental station from 1.10.2021 to 6.10.2021. Just like in the case of the experiment on Pt₃Co, the sample was glued on the holder compatible with the electromagnet system and aligned with respect to the incoming beam. Also the same experimental system was used. The sample was magnetised in the direction parallel to the sample surface and lying in the vertical scattering plane. In this experiment, the electromagnet provided the magnetic field of 175 mT measured at the surface of the sample, the same for both orientations of the

field, what was determined using a Hall probe. As reported in [181], this field should be sufficient to reach saturation magnetisation of YIG.

The experiment was performed for an energy value in the vicinity of the iron K absorption edge (nominally $\mathfrak{E} = 7.112$ keV). An energy spectrum around the nominal value was performed to choose an appropriate energy value for actual scans. For the energy spectrum measurement, the sample was aligned away from Bragg reflections. A simple measure of energy spectrum was obtained by summing the number of counts from the SDD detector for the channels corresponding to Fe K_α fluorescence line. The spectrum for linear polarisation was only recorded, since due to the weakness of the XMCD effect at the K absorption edge, the data collection time needed to observe the difference in absorption would be long. The obtained energy spectrum is presented in appendix E.2, in figure E.2. Following the report showing the XMCD spectrum from YIG [182], the maximum of the effect is expected to be observed in the vicinity of the pre-edge peak. Therefore, an energy of 7.1135 keV was chosen for the actual MXSW experiment. Some of the MXSW scans were performed also at an energy away from the absorption edge (7.14 keV), in order to ensure that the observed difference in spectra is indeed caused by the XMCD effect. The sample was oriented on the diffractometer in the same way as described in chapter 8. For the actual MXSW scans the sample was oriented so that the (444) reflection was excited. Even though the sample is of very good quality, it consists of several slightly misoriented grains. Therefore, the beam slits and φ angle were adjusted such, that only one grain contributed significantly to the observed reflected intensity. The opening of the slits for the MXSW scans was $120 \times 120 \mu\text{m}^2$.

The number of counts in the SDD detector, which was mounted above the sample surface ($\alpha = \pi/2$), was optimised by insertion of attenuation foils into the incoming beam, such that no significant number of pile-up events was seen in the fluorescence spectrum. Accidentally, this procedure was performed when the sample was at the position corresponding to the maximum of reflectivity, what also implies a significant decrease of fluorescence emission due to the extinction effect. Therefore, away from the reflection domain, the number of counts received by the detector was too high, what also led to an increase of background events. For the MXSW scans, the helicity of the incoming beam was changed with the frequency of 23 Hz using the fast flipping schema. The sample was in the external magnetic field and the orientation of the magnetic field was changed after each full Θ -scan. Some scans without the external magnetic field were performed as well, since the MXSW experiment without perturbation of the spontaneous magnetic structure is the ultimate aim.

The scans having 200 steps were performed around the Θ value of 26.0626° by changing it until $\pm 0.05^\circ$ in steps of $1.8''$. The data was collected for 10 s at each step of the scan. Due to the weakness of the XMCD signal at the K absorption edge, only the scans for one reflection were performed in order to obtain data with small statistical uncertainties. In total 82 with and 22 scans without the external magnetic field at the absorption edge were performed. Additionally 22 scans in the magnetic field at the energy well above the absorption edge were conducted.

9.2 Results

9.2.1 Raw experimental data

From the inspection of the beam monitor signal (from PIPS diodes) it became apparent, that the beam during the experiment was rather unstable. For some scans the beam intensity variations exceeded 20%. Scans where the variations were higher than 10% were rejected from further analysis. For the scans with magnetic field at the absorption edge 60 scans for both field orientations were used. For these scans an average degree of circular polarisation was estimated to be 95.7%.

A single fluorescence spectrum corresponding to one step of the angular scan and one configuration of helicity of the beam and magnetic field orientation is shown in figure 9.1. The spectra obtained from the detector were first normalised by the average (between σ - and π -polarisation components) beam monitor signal and summed for all the scans, where the beam intensity variations were lower than 10%. The procedure does not fully remove the variations in the yield caused by the fluctuations of the incoming beam intensity, what was observed by comparing the fluorescence yield for one scan before and after normalisation. This fact might be caused by the non-linear behaviour of the PIPS diodes. This was not observed in the experiment on Pt₃Co single crystal, since in that case the beam was very stable, so the overall influence of the instabilities on the fluorescence yield was minor. In the case of YIG, the normalisation procedure still allowed to reduce the influence of instabilities on the final data, so it was used.

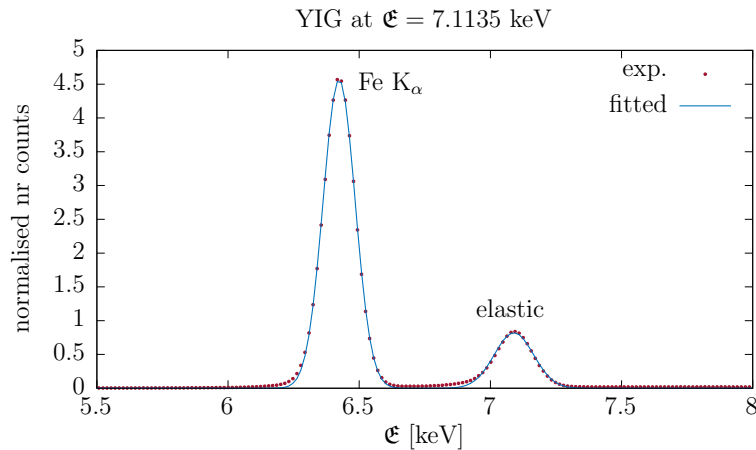


Figure 9.1: Single fluorescence spectrum for YIG crystal, recorded at 7.1135 keV. It corresponds to a single angular position in the Θ -scan, one helicity and one magnetic field orientation. The experimental data was fitted using a combination of Gaussian functions for the spectral lines. The background was not fitted due to its complicated shape. The energy scale was obtained by the comparison of lines positions with nominal values for corresponding fluorescence decay channels.

The fluorescence spectrum consists of two strong lines — the iron K_α fluorescence line and the elastic scattering peak with underlying iron K_β fluorescence line ($E = 7.058$ keV). Additionally, a weak argon K_α fluorescence line being an effect of air scattering is observed

for an energy approximately equal to 2.95 keV (not shown in the graph). In contrary to the data from the experiment on Pt₃Co, in this case the background was not fitted due to its complicated shape caused by a too high number of counts in the SDD detector. It was observed for Pt₃Co, that the inclusion of the background in the fitting procedure, changes the resulting fluorescence yields very slightly, only within the noise level. Since only the spectral lines were fitted during the fitting procedure, the agreement between the data and fitted function was worse than in the case of Pt₃Co. This directly led to high uncertainties of the Gaussian function parameters. This translated to high uncertainties of the fluorescence yield and MXSW signals, which by comparison with the variations in the experimental data were found not too reflect the actual experimental uncertainties. Therefore, the latter were estimated based on the Poisson statistics (square root of number of measured photons).

The collection of the experimental results obtained for the YIG crystal for the energy of 7.1135 keV and in a magnetic field is shown in figure 9.2. The first graph shows an experimental reflected beam intensity compared with theoretical function for the ideal YIG crystal and the one obtained after convolution with the reflectivity of the double crystal monochromator. The width of the rocking curve for the (111) Si reflection is comparable to the width of the experimental curve. The comparison between the data (red dots) and theoretical function (green) shows, that the crystal was of a very good quality. No convolution with Lorentzian or Gaussian function was needed to achieve a good agreement between the simulated reflectivity curve and the experimental data.

The second graph presents the fluorescence yields obtained for all four configurations of helicity and magnetic field orientation. Due to the instabilities of the incoming beam intensity, the noise in the signal is higher as in the case of the data for the Pt₃Co crystal (figure 8.4). In contrary to the experiment on Pt₃Co, no expected symmetry between the yields is observed. It would be expected, that the signals for configurations (LHP,+**B**), (RHP,-**B**) and (LHP,-**B**), (RHP,+**B**) coincide. Instead, the signals for one helicity (LHP) are stronger than the ones for the other one (RHP). An additional feature is a decrease in the yield observed away from the reflection domain, on the low angular side. It is particularly strong for one helicity (RHP). This feature might be an effect of another reflection excited at once with (444) one (three-beam-case). This hypothesis is supported by the fact, that an increase is observed in the argon fluorescence yield for the same angular range (see figure E.3 in appendix E.3). The fact, that the artefact on the low angular side is stronger for one helicity, might be related to the phase plate itself. Probably due to the slight change of the position of the diamond crystal when the helicity is changed, the direction of the beam is also slightly different. Then, for one helicity, the direction of the beam is closer to exact Bragg condition for this other reflection manifesting itself on the low angular side in the fluorescence yield. The source of the observed feature should be investigated further experimentally, by performing an azimuthal scan around the $\mathbf{h}_{(444)}$ vector.

The MXSW signal calculated based on equation (8.2) is shown on the bottom of figure 9.2. It is rather noisy and in the case of the points calculated as differences of the yields for different helicities ($\Upsilon_{\pm\mathbf{B}}$) does not reverse after the reversal of the magnetic field. This is the case for the other pair of MXSW signals ($\Upsilon_{L/R}$), what again may indicate a proper functioning of the phase plate. Those signals are very noisy, but a slight decrease in the signal may be observed in the reflection domain. Since the increase in the signal

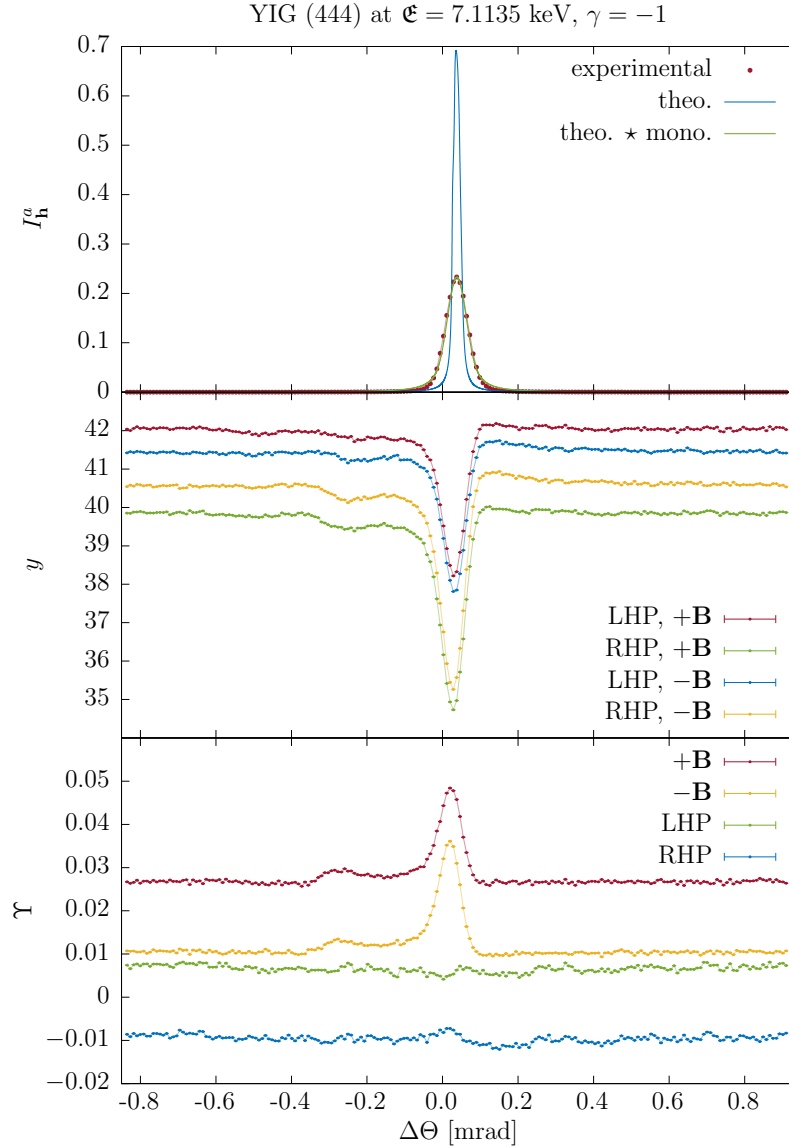


Figure 9.2: A collection of experimental results for YIG crystal. From the top: reflectivity, fluorescence yields and MXSW signal. The experimental reflected beam intensity (red dots) is compared with the theoretical function for ideal YIG crystal (blue line) and the one convolved with the reflectivity of double crystal monochromator (green line). The experimental data was normalised to the maximum of the green curve. The fluorescence yields are shown for all four configurations of the magnetic field and helicity. The last graph shows the MXSW signals calculated based on equation (8.2). For discussion see the text.

observed for $\Upsilon_{\pm B}$ (red and yellow points) is not symmetric with respect to the magnetic field reversal, it is suspected, that it is not of the magnetic origin. The shape of the $\Upsilon_{\pm B}$ might be also explained by the slight change of the direction of incoming beam during the flipping of the phase plate. A slightly different incidence angle may also for the (444) reflection lead to a higher reflectivity and thus also stronger extinction effect or standing wave intensity, what gives greater decrease in the fluorescence yield. This leads then to

the maximum observed in the $\Upsilon_{\pm\mathbf{B}}$ signals in the reflection domain.

9.2.2 Comparison with simulations

The experiment was performed in an external magnetic field, since, as apparent from figure 9.2, under the encountered experimental conditions, it is impossible to evaluate the XMCD signal based only on the difference in cross-sections for opposite helicities (see the signals $\Upsilon_{\pm\mathbf{B}}$). It was reported by Rodic *et al.* [143], that in an external magnetic field, the structure of YIG is not the same as the spontaneous one without external \mathbf{B} . In particular, the antiferromagnetic coupling between the magnetic sublattices is suppressed by the external field and all the magnetic moments align along the field lines. Such a situation was assumed for calculating the theoretical fluorescence yield and MXSW signal.

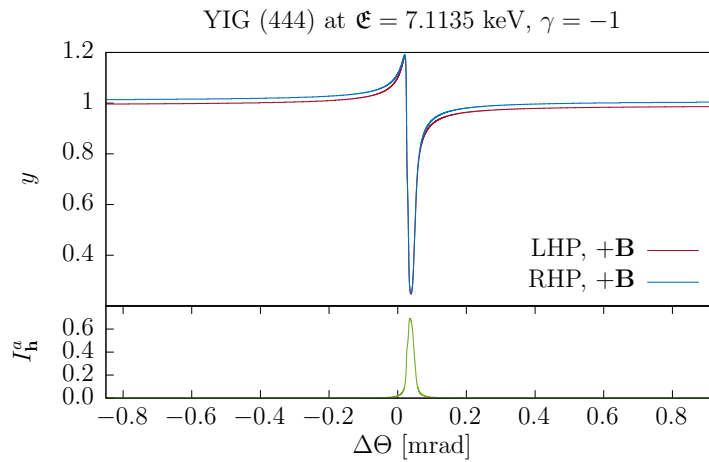


Figure 9.3: Simulated Fe fluorescence yield for YIG for the experimental setting. The magnetic moments were aligned in the reflecting lattice planes and directed along the external magnetic field. The yields were normalised by the background level (away from the reflection domain) of the yield for the linear polarisation (that is without the XMCD effect). It was assumed for the calculation, that photoelectron polarisation $\Pi_e = 0.01$.

The simulated fluorescence yield for YIG is shown in figure 9.3. For the simulations the photoelectron polarisation in the absorption process was assumed to be $\Pi_e^s = 0.01$. One can notice, that the experimental data shown in figure 9.2 (middle graph) exhibits similar behaviour as the simulated curves. A clear discrepancy on the low angular side might be caused by the second reflection, excited at the angular position very close to the investigated (444) one. This artefact makes comparison between the simulations and the experimental functions difficult.

9.2.3 Artefact-free MXSW signal

A further analysis of the MXSW signals is possible using the same approach as described in section 8.2.4, that is by calculating the difference and the sum of the signals plotted in figure 9.2 (bottom part). The difference of the signals can be regarded as an

artefact-free XMCD signal and is shown in figure 9.4. The statistical variations of the signal in the background level are relatively high, what owes to the weakness of the XMCD signal at the K absorption edge. A clear decrease of the XMCD in the reflection domain can be observed.

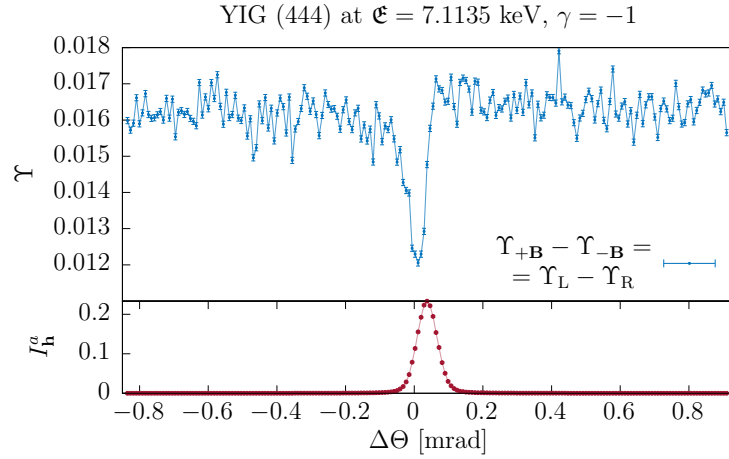


Figure 9.4: The difference of the MXSW signals for YIG presented in figure 9.2, that is $\Upsilon_{+B} - \Upsilon_{-B}$ and $\Upsilon_L - \Upsilon_R$. The signal calculated in this way can be regarded as a measure of the artefact-free XMCD, since the use of all four fluorescence yields is made for its calculation and via subtraction the influence of differences in the signal of non-magnetic origin is discarded.

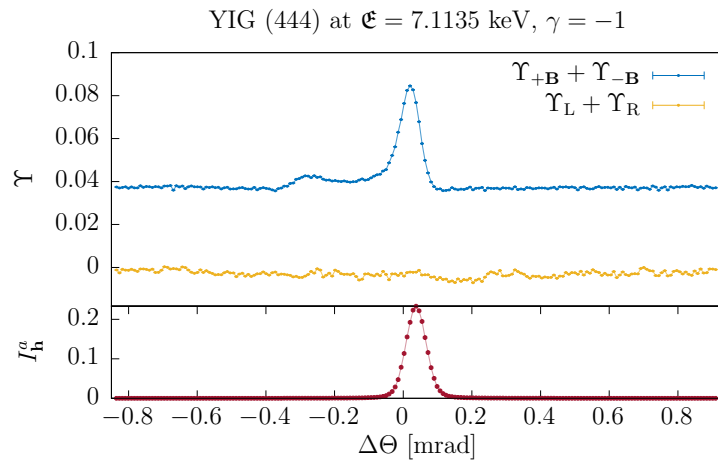


Figure 9.5: The sum of the MXSW signals for YIG presented in figure 9.2, that is $\Upsilon_{+B} + \Upsilon_{-B}$ and $\Upsilon_L + \Upsilon_R$. The signal calculated in this way can be regarded as a measure of the artefacts related to the switching of polarisation and reorientation of the magnetic field.

The sum of the individual MXSW signals Υ , in the ideal case equal to zero, is plotted in figure 9.5. The sum $\Upsilon_L + \Upsilon_R$ is as expected close to zero over the whole angular range. That is related to the symmetry between Υ_L and Υ_R observed already in figure 9.2 (bottom). A strong asymmetric (with respect to field reversal) artefact present in the $\Upsilon_{\pm B}$ signal persists, when the sum $\Upsilon_{+B} + \Upsilon_{-B}$ is calculated, and can be seen clearly in

figure 9.5. As mentioned already, it is expected, that the artefact is related to a second reflection excited on the lower angular side of the (444) reflection domain. The fact that the artefact is stronger for one helicity might be related to the slight change of the direction of the incoming beam by the phase plate. The underlying reasons for the appearance of the artefact should be investigated further experimentally.

9.2.4 Scans without the external magnetic field

Even though the feature in the fluorescence yields being stronger for one helicity indicates, that evaluation of the XMCD signal based only on helicity flipping is not feasible, the scans recorded without an external magnetic field were also analysed. 22 scans without magnetic field were recorded. They were recorded in between the scans with magnetic field, such that 11 were recorded after the $+\mathbf{B}$ setting and 11 after the $-\mathbf{B}$ one. No difference in the recorded data was observed between those two sets. An interesting first observation with respect to the scans with external magnetic field is a slight shift of the reflection domain angular position between the scans with and without magnetic field, what might be caused by magnetostriction (see figure E.4 in appendix E.4).

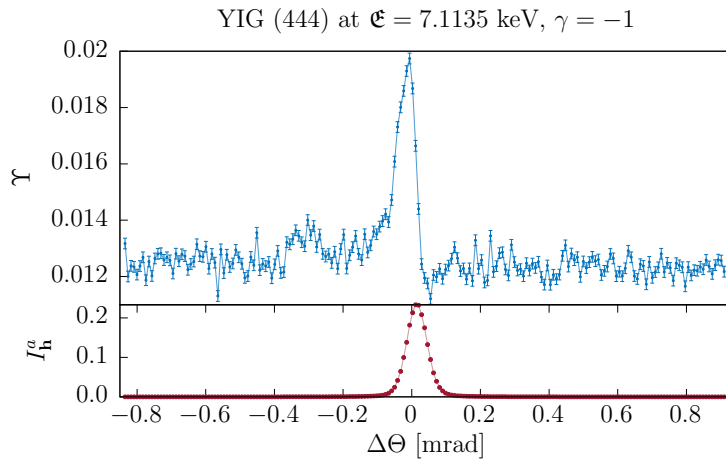


Figure 9.6: The MXSW signal for a YIG crystal, (444) reflection, calculated for the scans without external magnetic field. Of course the signal was calculated as a difference of fluorescence yields for opposite helicities. The shape is similar as the $\Upsilon_{\pm\mathbf{B}}$ shown in figure 9.2.

The MXSW signal calculated from the data for the scans without external magnetic field is shown in figure 9.6. The signal was calculated as the difference in fluorescence yields for different helicities, that is $\Upsilon_0 = (y_L - y_R)/(y_L + y_R)$. The shape of the signal is similar to the $\Upsilon_{\pm\mathbf{B}}$ one, shown in figure 9.2. Also the variation on the lower angular side of the reflection domain was observed. Since the presented analysis, based on calculating the difference and sum of the XMCD signals Υ ($\Upsilon_L \pm \Upsilon_R$, $\Upsilon_{+\mathbf{B}} \pm \Upsilon_{-\mathbf{B}}$) showed that this variation and the prominent increase in the reflection domain are of non-magnetic origin, further analysis of the out-of-field data is not possible in this case. In the future, after further investigation of the source of artefacts, the MXSW experiments without the external magnetic field could provide information about the spontaneous arrangement of the magnetic moment in crystals.

9.2.5 Control scans away from the absorption edge

In order to check that the observed difference in fluorescence yields is caused by the XMCD effect, 22 scans were recorded for the energy well above the iron K absorption edge, that is for $\mathfrak{E} = 7.14$ keV. An external magnetic field was used, as well as the helicity was reversed using the fast flipping schema. 11 scans for one orientation of the magnetic field and 11 for the other were performed. The data was analysed using the usual routine and the result is presented in figure 9.7, where the sum and difference of individual MXSW signals $\Upsilon_{L/R}$ and $\Upsilon_{\pm B}$ are presented.

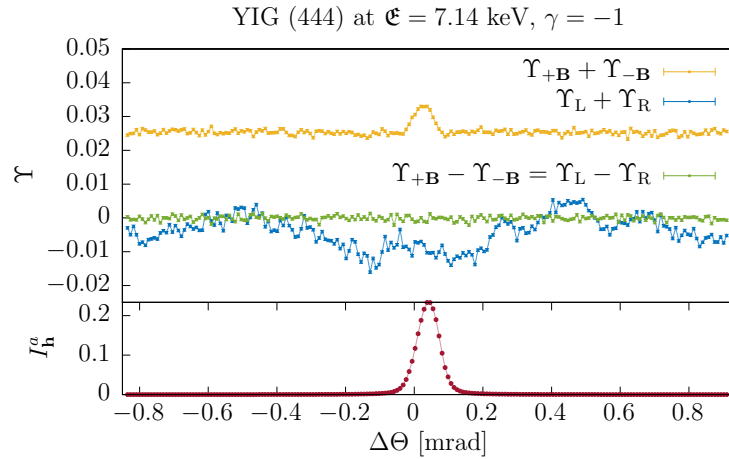


Figure 9.7: The sum and difference of the MXSW signals $\Upsilon_{L/R}$ and $\Upsilon_{\pm B}$ for a YIG crystal, energy above the K absorption edge ($\mathfrak{E} = 7.14$ keV). As expected, the difference $\Upsilon_{+B} - \Upsilon_{-B}$ and $\Upsilon_L - \Upsilon_R$ representing the XMCD signal is zero within the experimental uncertainty, since the energy is too far from the energy of the $1s \rightarrow 4p$ transition. For the discussion regarding the artefacts (sum signals) see the text.

These results are fully in agreement with expectations. The difference signals $\Upsilon_{+B} - \Upsilon_{-B}$ and $\Upsilon_L - \Upsilon_R$, being a measure of the XMCD signal, are oscillating around zero within the experimental uncertainties. This means, that for this energy away from the transition energy probed at the K absorption edge no XMCD effect appears, what was expected. In order to observe the effect, the energy has to match the energy difference between the atomic levels, what was not the case for the energy used for these scans. The data ensures that the artefact-free MXSW signal presented in figure 9.4 is indeed the XMCD signal, and the observed variation is the one caused by the impact of the standing wavefield.

What is remarkable, also in this case a sum signal $\Upsilon_{+B} + \Upsilon_{-B}$ is non-zero and exhibits an increase in the reflection domain. The feature present earlier on the low angular side (see figure 9.5) does not appear for this energy, what supports the hypothesis that it was a manifestation of another reflection. Apparently, at an energy equal to 7.14 keV the diffraction condition is not fulfilled for this reflection, so it is not excited. The increase in the reflection domain can be explained as earlier — for one helicity the direction of the incoming beam is slightly different, what leads to somewhat different standing wave and extinction angular dependence for LHP and RHP. The other sum, $\Upsilon_L + \Upsilon_R$ is related to

the polarisation switching. It oscillates around zero, as expected, and exhibits significant variations what is related to the beam instabilities. The impact of the latter on the shape of the other artefact is minor, since the helicity reversal is performed multiple times during one scan, and the magnetic field is reversed only after the full scan. That is why the beam instabilities persists in the $\Upsilon_{L/R}$ signals, what does not hold true for $\Upsilon_{\pm B}$.

9.3 Discussion

Given the arguments from section 9.2.5, the data obtained after subtraction of the signals $\Upsilon_{L/R}$ or $\Upsilon_{\pm B}$ can be regarded as a true MXSW signal, since the non-magnetic contributions are discarded when the difference is calculated the second time. The comparison of such defined experimental data with theoretical prediction is presented in figure 9.8. The theoretical curve was calculated assuming that in an external magnetic field the antiferromagnetic coupling between the sublattices in the YIG structure is destroyed and thus all the magnetic moments are aligned along the magnetic field lines. The correction for the imaginary part of the wavevector was introduced, as well as the absorption of the emitted fluorescence on the way to the detector was taken into account.

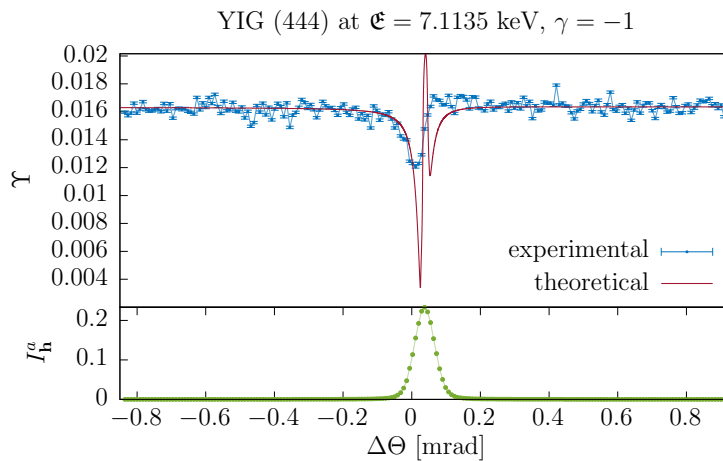


Figure 9.8: Comparison between the experimental MXSW signal for the YIG crystal and the theoretical curve calculated assuming the magnetic moments being aligned along the magnetic field in the (444) planes. The theoretical data was normalised to the background level of the experimental MXSW signal.

From the comparison between the experimental data and theoretical curve, one can see that the general trend predicted by the MXSW theory was reproduced practically. Also theoretically mainly a decrease of the XMCD signal in the reflection domain is predicted, which is related only to the variations of the wavefield polarisation and propagation direction (as the reflected wave is excited). In particular, because of utilisation of a magnetic field, no variations related to the existence of magnetic sublattices are predicted to occur. The magnetic order is changed by the external field, and in order to observe the signal coming from the spontaneous magnetic structure (what would be the most interesting), ideally only the helicity flipping should be employed to determine the XMCD signal.

The theoretical curve is slightly asymmetric when approaching the background, it is higher on the high angular side. This feature was reproduced experimentally. The increase in the middle of the reflection domain, observed in the theoretical data, is not seen in the experimental MXSW signal. This might be related to the sharpness of this feature, what causes that it was not resolved due to the broadness of the monochromator reflectivity and finite beam divergence. Another possible explanation is the fact, that for the absorption correction for the wavevector, the difference in absorption caused by the XMCD effect was neglected. The simulations aiming at estimating an impact of such an assumption on the description of the scattering process (chapter 6) were performed without the absorption correction for the wavevector. In the future, the simulations should be extended for this case in order to check, if the negligence of the impact of the XMCD effect also on this aspect of the scattering process is justified.

As made apparent over the presentation of the results, the analysis of the data revealed that there is room for the improvement of the experimental procedure in order to obtain more valuable data in the future. First of all, the impact of another reflection observed on the low angular side of the (444) reflection domain can be removed by performing an azimuthal scan and choosing another value of the φ diffractometer angle for the MXSW scans. From the shape of the artefacts calculated as $\Upsilon_{+\mathbf{B}} + \Upsilon_{-\mathbf{B}}$ it became apparent, that the phase plate may slightly change the direction of the incoming beam, what changes slightly the diffraction conditions. This feature should be investigated further in details. In order to understand it better, a separate reflected beam intensity should be recorded for LHP and RHP, the same as it is done for the fluorescence signal from SDD detector. High beam instability during the entire experiment had a major impact on the quality of the presented data.

During the redaction of the text of this dissertation, a report on the MXSW experiment on YIG of the group of Kawata, included in a conference proceedings, was found [47]. This publication constitutes the first record (and the only so clear one before this work) of the idea of using the standing wave to investigate the magnetic structure of a material at the atomic level. The authors performed similar experiment as reported in this chapter. The helicity of incoming radiation was not changed during the experiment and the XMCD signal was evaluated based on the differences in the absorption cross-section between two opposite magnetic field orientations. The researchers assumed, that the magnetic moments are aligned along the external magnetic field lines, and that the antiferromagnetic coupling between the magnetic sublattices of YIG is preserved. This assumption seem not to be in agreement with the report of Rodic *et al.* [143], where it is pointed out that the ferrimagnetic ordering does not persists in an external magnetic field of 0.2 T. On the other hand, the value of the magnetic field used by the group of Kawata is not mentioned in their report. The data obtained by the authors is of very good quality. The data-set obtained for the energy corresponding to the pre-edge feature (the same as used in this work) seem to agree with the theoretical prediction based on the theory presented here, assuming the ferrimagnetic arrangement of magnetic moments confined in the reflecting lattice planes. The possibility of aligning the magnetic moments in the reflecting lattice planes, and reversing their orientation keeping the antiferromagnetic coupling between the sublattices should be checked by recording MXSW scans for different strengths of the magnetic field and following the changes in the shape of the signal.

The theoretical considerations presented in the publication of Kawata *et al.* are dif-

ferent than the ones presented here. Kawata assumed a proportionality between the intensity of the standing wave calculated for the σ -polarised incoming wave and the absorption cross-section, allowing an unknown difference caused by the XMCD effect. This impact of the XMCD effect was then estimated from the fitting of the model function to the experimental data, using additionally the convolution with a Voigt function. Thus, in this approach the proper calculation of the cross-section for the wavefield excited by a circularly polarised incoming wave, based on the time-dependent perturbation theory is not included. As shown in the current work, the effects related to the changes of the wavefield polarisation in the reflection domain play a major role, especially if no magnetic sublattices are present in the structure. Also, only a description based on quantum mechanics can give a rigorous basis for the MXSW technique, as the phenomena of magnetic dichroism cannot be explained classically.

Summarising, the result of the MXSW experiment on YIG showed that the theoretical predictions based on the established MXSW theory are in relatively good agreement with the experimental data. The experiment provided a number of hints for the further investigation using the method. It showed, that in order to observe the signal coming from the magnetic sublattices, measurements without an external magnetic field are necessary. Alternatively, as the report of Kawata seems to indicate, a measurement in weaker magnetic field may also give the desired result.

Summary and conclusions

Within the scope of this thesis, the foundations for the new direct method for investigation of the magnetic structures of the crystalline materials at the atomic level, called magnetic x-ray standing waves, were established. In particular a firm and rigorous theoretical treatment of the subject was developed based on the dynamical theory of diffraction and time-dependent perturbation theory. The MXSW theory was used to perform simulations of the expected experimental functions for a number of magnetic systems, including ferrimagnets and antiferromagnets. Two experimental realisations of the MXSW method were reported. They provided valuable results indicating the feasibility of this technique and numerous hints laying foundations for further experimental development. It was shown, that the method can be applied also to the antiferromagnetic systems, what constitutes a complete novelty in the field of XMCD spectroscopy. The results prove, that the new technique is a valuable tool for investigation of magnetic structures of crystalline materials, providing the information directly, other than the methods used for this purpose so far.

Regarding the theoretical part, this is the first time when an exhaustive theoretical framework treating the subject of the absorption of x-ray standing wave in the magnetised medium is reported. The dynamical theory of diffraction was used, as it provides an accurate description of the scattering process in the crystal lattice, including the amplitudes and phases of the waves in the reflection domain. The result of this part provides a form of the EM wave inside the crystal in dependence on the scattering angle, for arbitrary polarisation of the incoming wave and including the effects of anomalous absorption and extinction (related to the imaginary part of the wavevector). Since an absorption of photon by the atom cannot be properly described within the classical theory, the form of the electromagnetic field obtained from the dynamical theory was used in the framework of time-dependent perturbation theory to calculate the absorption cross-section. The two-step single-electron model was presented as the theoretical picture explaining x-ray magnetic circular dichroism rigorously for the $L_{2,3}$ absorption edges. A description of the XMCD effect was obtained for an arbitrarily polarised single plane EM wave. The same model was used to treat the absorption phenomena under the XSW regime, that is the MXSW. The formalism yielded a dependence of the traditional XMCD signal on the scattering angle, that is the MXSW signal. The signal for several magnetic atoms in the unit cell with arbitrary orientations of the magnetic moments was evaluated. It was shown that such signal depends directly on the magnitudes and orientations of the magnetic moments, as well as positions of the magnetic atoms. A new quantity — magnetic standing wave structure factor — was defined in analogy to the standing wave structure factor used in standard XSW technique. The formula for the MXSW signal is fully general, it

accounts for polarisation of the incoming beam and the effects related to the complex wavevector. Even though the used quantum model is strictly valid for the $L_{2,3}$ absorption edges only, an argument based on the analysis of the changes of wavefield polarisation during the rocking scan was given to justify the applicability of the results to other cases as well.

An interesting new result was obtained when comparing the XMCD signals under the XSW regime, calculated as the difference between the absorption cross-sections for opposite magnetic moment orientations and while flipping the helicity of the incoming beam. It is a known fact, also shown here rigorously, that the signals calculated in this two ways coincide in the standard XMCD spectroscopy, that is when a single plane wave is absorbed. On the other hand, it was observed, that those two signals do not coincide when the absorption of the standing wave is considered. Additionally, the theoretical considerations yielded, that the MXSW signal calculated based on opposite magnetic moment orientation can be observed also for linearly (π -, or mixed π - and σ -) polarised wave, and a magnetic moment perpendicular to the scattering plane. The reason for these peculiarities lies in the phase changes in the reflection domain, and in particular the phase difference between the reflected and refracted π -components of the wavefield coming from the complex amplitude ratio. It should be noted, that this result was obtained within the electric dipole approximation, which neglects the propagation of the waves. An experimental verification of this finding can be performed by determining the MXSW signal for the π -polarised incoming wave and the magnetisation direction perpendicular to the scattering plane.

For the development of the MXSW theory a semi-classical approach was used, that is the scattering was considered within the classical diffraction theory based on Maxwell equations, whereas only the absorption was considered within the quantum physics. This means, that the XMCD (and thus also MXSW) signal was evaluated for the wavefield calculated neglecting the effects of magnetic dichroism on the scattering process itself. The impact of the difference in absorption depending on the helicity of the incoming beam and magnetic state of the crystal on the diffraction process was estimated using a numerical iterative algorithm and was found to be generally small. This justifies the adopted theoretical framework, where the scattering and absorption phenomena are treated separately.

The theory of the MXSW was first used to perform computer simulations, that is calculate numerically the data for a number of chosen representative magnetic systems. A simple ferromagnetic platinum-cobalt alloy Pt_3Co was used to demonstrate the sensitivity of the MXSW method to the position of magnetic ions and discuss the dependence of the signal on the orientation of the magnetic moment. In this crystal all Pt and Co ions are equivalent, so it was concluded, that even though the variation in the XMCD signal exists also in this case, it is weak and does not provide additional information compared to standard XMCD. The variation is related to the properties of the standing wave itself. Pt_3Co was also used to demonstrate the influence of the deviation of the incoming beam polarisation from the circular one. It was shown based on simulation results, that for an elliptically polarised beam the absolute value of the MXSW signal generally decreases, as expected, but the shape of the function in the angular domain persists. Small deviations from ideal circular polarisation expected in the experiment are anticipated not to have a noticeable impact on the measured data. Finally, the influence of the absorption correction accounting for the anomalous absorption, extinction and absorption of the secondary

signal on the way to the detector was shown for the considered crystal.

After the discussion regarding the simplest case of magnetic ordering, the simulation results for systems possessing magnetic sublattices were presented. Using magnetite as an example, the power of the MXSW method to provide site selective magnetic information was demonstrated. This crystal consists of two sublattices of iron ions, with antiferromagnetic coupling between them. Since half of the ions in one of the sublattices exhibits different valence state and thus also different magnitude of the magnetic moment than the rest of the iron atoms, the system is in total ferrimagnetic. This magnetic ordering is reflected directly in the MXSW signal, which can thus be regarded as a footprint of the magnetic structure of the crystal. For the reflections with appropriate periodicity, the standing wave existing in the reflection domain increases the contribution of one sublattice to the overall XMCD signal, at the same time lowering the impact of the other one. Due to the movement of the nodes of the standing wave, for one angular side of the reflection domain one sublattice dominates the XMCD signal, whereas on the other side, the other one dominates. Obtained variations in the XMCD signal, that is the MXSW signal, are characteristic of a given distribution of the magnetic ions in the lattice. This means, that for an unknown structure, the MXSW signal can be used to obtain information about the relative magnitudes and orientations of the magnetic moments directly. This is tightly bound to the fact, that the MXSW signal is proportional to the magnetic standing wave structure factor, both its modulus and phase. It was shown in the text for some hypothetical arrangements of the magnetic moments in the magnetite structure, that any changes of the natural magnetic ordering would be reflected in the MXSW signal. This proves, that the new method can be used to track the changes in the magnetic ordering during phase transitions or changes imposed by other external perturbations like magnetic fields. Apart from magnetite, the simulation results were also presented for yttrium-iron-garnet and hematite. The latter exhibits an antiferromagnetic ordering. Even though no XMCD signal in the standard experimental geometry (one wave) can be observed for the antiferromagnetic system due to the zero net magnetisation, with the use of the standing wave the destructive influence of one of the sublattices can be switched off at the same time observing the magnetic effect coming from the other one. This makes observation of an XMCD effect from antiferromagnets possible, what is a new perspective.

Like all experimental methods, also the MXSW technique can be used only for a certain set of physical systems. A crystal lattice is needed to generate a standing wave, so only crystalline systems, or thin films deposited on a crystalline substrates, can be investigated. The mosaic spread of the crystal leads to smearing of the scattering effects in the reflection domain, including the standing wave, so the crystals used should be of good quality. Since the standing wave is generated by the atomic lattice, its periodicity is linked to the periodicity of the atomic structure. Therefore, no useful information can be obtained from the MXSW method for the magnetic structures exhibiting a higher period than the dimensions of the atomic lattice cell. As mentioned in the paragraph before, the MXSW method is ideal for studying ferri- and antiferromagnetic systems, as then the position sensitivity granted by the standing wave can be fully exploited. The fact that the energy of incoming x-rays for the MXSW has to be tuned to the absorption edge of the magnetic atoms in the sample, imposes a further limitation on the set of potential samples. The XMCD spectroscopy is usually performed at the $L_{2,3}$ and $M_{4,5}$ absorption edges in 3d metals. At these energies it is impossible to excite any Bragg reflection, which

could generate the needed standing wave. Therefore, the MXSW experiments can be performed for systems containing 5d or 4f metals ($L_{2,3}$ absorption edges). The 3d metals can also be studied, but then the weak XMCD effect at the K absorption edge has to be investigated.

Regarding the practical aspect of the method, it is similar to the standard XSW technique. Instead of normally used linearly polarised radiation, one uses a circularly polarised wave. The sample has to exhibit some magnetic properties. The absorption cross-section, and thus also the XMCD signal, are evaluated based on measuring the fluorescence radiation emitted by the sample. The actual experiment consists of angular rocking scans around the position corresponding to the Bragg angle, during which at each point the reflected beam intensity and full fluorescence spectrum are recorded. The MXSW signal is evaluated based on the fluorescence yield for each helicity. Even though full quantitative analysis yielding the absolute values of magnetic moments is not possible based on the XMCD signal recorded at fixed energy (energy integrals are needed), it is assumed that the MXSW signal reflects the relative changes in the magnetic moments between the sublattices. In the standard XMCD method the sample is usually being magnetised in an external magnetic field, whose orientation is changed in addition to helicity flipping. This approach allows to discard the artefacts related to polarisation and magnetisation switching from the XMCD signal and was also used in the experiments reported here. On the other hand, the external magnetic field perturbs the spontaneous magnetic ordering in the investigated sample, which is of the greatest interest. Therefore, future MXSW experiments should be preferably performed without external magnetic field.

The MXSW experiments reported were performed at the P09 beamline, PETRA III synchrotron at DESY, Hamburg. The first experiment was performed on a Pt_3Co single crystal at the L_3 absorption edge of platinum. Only scans for the (111) reflection were performed and yielded a clear variation in the XMCD signal in the reflection domain, what is the most important result of this particular investigation. The shape of the signal is the same as the one obtained by Jaouen *et al.* [46] for a similar system. The second experiment was performed on a YIG single crystal, as this is a ferrimagnetic system exhibiting magnetic sublattices, thus being ideal for the investigations using the new MXSW method. The superior quality of the crystal yielded a significant variation in the XMCD signal in the scans around the (444) reflection, despite the weakness of the effect at the K absorption edge of iron. Since the experiment was performed with the sample kept in the external magnetic field, whose orientation was reversed after each full angular scan, the spontaneous ferrimagnetic ordering in YIG did not persist. Instead, all the magnetic moments were aligned along the magnetic field lines, what is confirmed by the comparison between the experimental data and simulation result calculated based on this assumption. Already this result allows to conclude, that the MXSW theory developed within the scope of this work reproduces the experimental results.

Summarising, firm foundations of the new direct, atomically resolved method for magnetic structure investigations were developed. The theory allowed predictions of two new interesting phenomena — the possibility of the observation of the XMCD signal from the antiferromagnets and induction of circular dichroism by the π -polarised incoming wave under the x-ray standing wave regime. Via the simulations and experimental work it was shown, that the technique can be used for determination of magnetic moment arrange-

ments in crystals and thin films.

Further work on the theory of MXSW is planned. The ultimate aim is the development of a theory, in which scattering and absorption phenomena would be treated together. This would ensure a rigorous description of the influence of the XMCD effect on the scattering process. One can mention two existing approaches to the subject of dynamical scattering described using non-relativistic quantum mechanics [57–59] and quantum field theory [183]. They can be potentially used for further work on the MXSW theory.

Regarding further experimental development of the method, a second experiment on the YIG crystal is planned to fully explain the observed experimental artefacts. Also the MXSW scans at several energies in the vicinity of the absorption edge should be performed to check the assumption about the proportionality of the magnetic moment to the XMCD signal measured at fixed energy. Further on, an experiment without an external magnetic field should allow to obtain data showing the ferrimagnetic ordering of a crystal. As a next step, an experiment on an antiferromagnetic system (hematite) is also foreseen. This will be the very first observation of the magnetic dichroism effect in an antiferromagnet, made possible due to the utilisation of the standing wave.

Apart from the experiments on bulk crystals, an investigation of a thin film of double perovskite (DP) Sr_2CrWO_6 grown on SrTiO_3 is planned. Since the properties of the thin films are often different compared to their bulk counterparts, the magnetic structure may also vary. Sr_2CrWO_6 was reported to show the highest magnetoresistance from the whole DP family, higher by two orders of magnitude at low temperatures than other DPs [184]. Another interesting property of the thin film is, that it shows a significantly increased Curie temperature (above 500 K) compared to bulk [185]. Both the ferrimagnetic and half-metallic properties exhibited well above room temperature open up a possibility for application in spintronics. The magnetic structure of thin crystals is not easily accessible using neutron diffraction, which is traditionally utilised to study spatial arrangement of the magnetic moments. This is due to the weak interaction of the neutrons with matter, and the small beam fluxes compared to x-ray sources. In the case of Sr_2CrWO_6 it was stressed that the knowledge of the magnetic moment induced on the non-magnetic site (W in this case), is crucial for understanding the nature of magnetic exchange in DP compounds [186]. Even though the moment was already determined for powder samples [186], no investigation of thin films was reported so far.

In further perspective, the MXSW method can be applied to other thin films, including the ones grown from materials exhibiting magnetic sublattices, like magnetite. The orientation of the magnetic moments in magnetite thin film was reported to be different as in the bulk crystal [138]. Such fact would be reflected in the MXSW signal. Since now a rapid development of science at x-ray free electron lasers takes place (what includes also the XSW technique [187]), it is foreseen, that in the future it will be possible to perform also time-resolved MXSW experiments, where for example the magnetisation and demagnetisation dynamics could be observed directly. Nowadays a rapid progress in the field of magnetism can be observed, what includes materials for spintronics [188], topological materials [189] and magnetic semiconductors [190], all with high potential for technical applications. I believe, that the new MXSW technique can provide a new insight into the properties of these materials, providing the information about the magnetic structure directly and readily, also for thin films.

Appendix A

Detailed derivations

A.1 Dynamical theory of diffraction

A.1.1 Tiepoint coordinates

In this appendix a relation between the tiepoint coordinates X_0 , $X_{\mathbf{h}}$ and the geometrical parameters γ_0 , $\gamma_{\mathbf{h}}$, Θ_B , $\Delta\Theta$ is derived. This is done using the definition of the tiepoint coordinates 1.19 and the wavevector boundary condition $\mathbf{k}_0 = \mathbf{k}_0^a - k\kappa\mathbf{n}$.

For the coordinate X_0 it suffices to consider the length of the \mathbf{k}_0 in conjunction with the boundary conditions

$$k_0^2 = \mathbf{k}_0 \cdot \mathbf{k}_0 = (\mathbf{k}_0^a - k\kappa\mathbf{n}) \cdot (\mathbf{k}_0^a - k\kappa\mathbf{n}) = k^2 - 2k\kappa\mathbf{k}_0^a \cdot \mathbf{n} + k^2\kappa^2 \cong k^2 (1 - 2\kappa\gamma_0) \quad (\text{A.1})$$

In the last step one used the fact that $\mathbf{k}_0^a \cdot \mathbf{n} = k \cos \psi_0 = k\gamma_0$ and $\kappa^2 \approx 0$, because κ is small. Using the Taylor expansion for $\sqrt{1-x} = 1 - \frac{1}{2}x + \dots$, one can write that $k_0 = k(1 - \kappa\gamma_0)$. From the definition of the tiepoint coordinate it follows that

$$X_0 = \frac{k_0^2 - k^2(1 + \chi_0)}{2k} = -k(\kappa\gamma_0 + \frac{1}{2}\chi_0) \quad (\text{A.2})$$

what is the sought relation 1.22.

Similarly, for establishing equation for $X_{\mathbf{h}}$ one has to consider the length of the wavevector $\mathbf{k}_{\mathbf{h}}$. One starts with the diffraction condition $\mathbf{k}_{\mathbf{h}} = \mathbf{k}_0 + \mathbf{h}$ and gets

$$\begin{aligned} k_{\mathbf{h}}^2 &= (\mathbf{k}_0 + \mathbf{h})^2 = k_0^2 + 2\mathbf{k}_0 \cdot \mathbf{h} + h^2 = \\ &= k_0^2 + 2(\mathbf{k}_0^a - k\kappa\mathbf{n}) \cdot \mathbf{h} + h^2 \end{aligned} \quad (\text{A.3})$$

k_0^2 is already known and the length of the reciprocal lattice vector in diffraction experiment is $h^2 = (4\pi \sin \Theta_B / \lambda)^2 = 4k^2 \sin^2 \Theta_B$. One has to find the expression for $\mathbf{k}_0^a \cdot \mathbf{h}$. Following figure A.1 one has

$$\begin{aligned} \mathbf{k}_0^a \cdot \mathbf{h} &= kh \cos(\Theta_B + \Delta\Theta + \frac{\pi}{2}) = 2k^2 \sin \Theta_B \cos(\Theta_B + \Delta\Theta + \frac{\pi}{2}) = \\ &= -2k^2 \sin \Theta_B \sin(\Theta_B + \Delta\Theta) \end{aligned} \quad (\text{A.4})$$

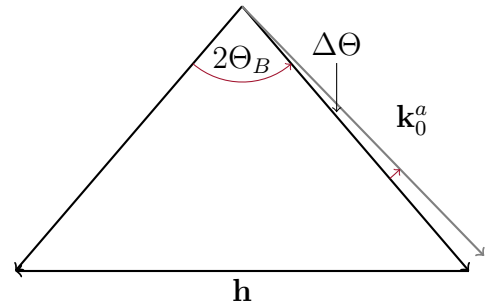


Figure A.1: Angular relation between the vectors \mathbf{k}_0^a , \mathbf{h} and $\mathbf{k}_{\mathbf{h}}$. $\Delta\Theta$ is the angular difference between the incidence defined by the Bragg's law (or diffraction condition) and the actual incidence direction given by the vector \mathbf{k}_0^a .

Now one uses the identity $\sin(\Theta_B + \Delta\Theta) = \sin\Theta_B \cos\Delta\Theta + \sin\Delta\Theta \cos\Theta_B$, keeping in mind that the departure angle $\Delta\Theta$ is very small, so $\sin(\Theta_B + \Delta\Theta) \cong \sin\Theta_B + \cos\Theta_B \Delta\Theta$. Continuing

$$\begin{aligned} \mathbf{k}_0^a \cdot \mathbf{h} &= -2k^2 \sin\Theta_B \sin(\Theta_B + \Delta\Theta) = -2k^2 \sin^2\Theta_B - 2k^2 \sin\Theta_B \cos\Theta_B \Delta\Theta = \\ &= -2k^2 \sin^2\Theta_B - k^2 \sin 2\Theta_B \Delta\Theta \end{aligned} \quad (\text{A.5})$$

Having that, the squared length of the wavevector reads

$$\begin{aligned} k_{\mathbf{h}}^2 &= k^2 (1 - 2\kappa\gamma_0) - 4k^2 \sin^2\Theta_B - 2k^2 \sin 2\Theta_B \Delta\Theta - 2k\kappa \mathbf{n} \cdot \mathbf{h} + 4k^2 \sin^2\Theta_B = \\ &= k^2 (1 - 2\sin 2\Theta_B \Delta\Theta) - 2k\kappa (\mathbf{k}_0 \cdot \mathbf{n} + \mathbf{h} \cdot \mathbf{n}) \\ &= k^2 (1 - 2\sin 2\Theta_B \Delta\Theta) - 2k\kappa \mathbf{k}_{\mathbf{h}} \cdot \mathbf{n} = k^2 (1 - 2\sin 2\Theta_B \Delta\Theta - 2\kappa\gamma_{\mathbf{h}}) \end{aligned} \quad (\text{A.6})$$

The second sought coordinate reads, from the definition

$$X_{\mathbf{h}} = \frac{k_{\mathbf{h}}^2 - k^2 (1 + \chi_0)}{2k} = -k \left(\frac{1}{2}\chi_0 + \sin 2\Theta_B \Delta\Theta + \kappa\gamma_{\mathbf{h}} \right) \quad (\text{A.7})$$

The tiepoint coordinates are related to each other. One can transform equation for $X_{\mathbf{h}}$ and get

$$\begin{aligned} X_{\mathbf{h}} &= \frac{\gamma_{\mathbf{h}}}{\gamma_0} X_0 + \frac{1}{2}k\chi_0\gamma - k \sin 2\Theta_B \Delta\Theta - \frac{1}{2}k\chi_0 \\ &= \gamma X_0 - k \left[\frac{1}{2}\chi_0 (1 - \gamma) + \sin 2\Theta_B \Delta\Theta \right] \end{aligned} \quad (\text{A.8})$$

A.1.2 General solution for X and ξ

The coordinates of the tiepoint X_0 and $X_{\mathbf{h}}$ fully define the general solution of the dynamical theory. To obtain the solution for X_0 , one inserts equation 1.24 (or equivalently A.8) into the dispersion surface equation 1.20. This eliminates the other unknown — $X_{\mathbf{h}}$. For convenience, one can introduce an abbreviation

$$\tilde{\eta} = \frac{1}{2}\chi_0 (1 - \gamma) + \sin 2\Theta_B \Delta\Theta \quad (\text{A.9})$$

From the dispersion surface equation and A.8

$$X_0 (\gamma X_0 - k\tilde{\eta}) = \frac{1}{4}k^2 \chi_{\mathbf{h}} \chi_{\bar{\mathbf{h}}} \mathfrak{P}^2 \quad (\text{A.10})$$

This quadratic equation is solved for the unknown X_0

$$\begin{aligned} |\gamma| \operatorname{sgn}(\gamma) X_0^2 - k\tilde{\eta} X_0 - \frac{1}{4}k^2 \chi_{\mathbf{h}} \chi_{\bar{\mathbf{h}}} \mathfrak{P}^2 &= 0 \\ |\gamma| X_0^2 - k\tilde{\eta} \operatorname{sgn}(\gamma) X_0 - \frac{1}{4}k^2 \chi_{\mathbf{h}} \chi_{\bar{\mathbf{h}}} \mathfrak{P}^2 \operatorname{sgn}(\gamma) &= 0 \\ \left(\sqrt{|\gamma|} X_0 - \frac{k\tilde{\eta} \operatorname{sgn}(\gamma)}{2\sqrt{|\gamma|}} \right)^2 - \frac{k^2 \tilde{\eta}^2}{4|\gamma|} - \frac{1}{4}k^2 \chi_{\mathbf{h}} \chi_{\bar{\mathbf{h}}} \mathfrak{P}^2 \operatorname{sgn}(\gamma) &= 0 \\ \left[\operatorname{sgn}(\gamma) \left(\operatorname{sgn}(\gamma) \sqrt{|\gamma|} X_0 - \frac{k\tilde{\eta}}{2\sqrt{|\gamma|}} \right) \right]^2 - \frac{1}{4}k^2 \chi_{\mathbf{h}} \chi_{\bar{\mathbf{h}}} \mathfrak{P}^2 \left(\frac{\tilde{\eta}^2}{|\gamma| \chi_{\mathbf{h}} \chi_{\bar{\mathbf{h}}} \mathfrak{P}^2} + \operatorname{sgn}(\gamma) \right) &= 0 \end{aligned}$$

$$\begin{aligned}
\left| \operatorname{sgn}(\gamma) \sqrt{|\gamma|} X_0 - \frac{k\tilde{\eta}}{2\sqrt{|\gamma|}} \right| &= \frac{1}{2} k \sqrt{\chi_{\mathbf{h}} \chi_{\bar{\mathbf{h}}}} |\mathfrak{P}| \sqrt{\frac{\tilde{\eta}^2}{|\gamma| \chi_{\mathbf{h}} \chi_{\bar{\mathbf{h}}} \mathfrak{P}^2} + \operatorname{sgn}(\gamma)} \\
\operatorname{sgn}(\gamma) \sqrt{|\gamma|} X_0 &= \frac{k\tilde{\eta}}{2\sqrt{|\gamma|}} \pm \frac{1}{2} k \sqrt{\chi_{\mathbf{h}} \chi_{\bar{\mathbf{h}}}} |\mathfrak{P}| \sqrt{\frac{\tilde{\eta}^2}{|\gamma| \chi_{\mathbf{h}} \chi_{\bar{\mathbf{h}}} \mathfrak{P}^2} + \operatorname{sgn}(\gamma)} \\
\operatorname{sgn}(\gamma) \sqrt{|\gamma|} X_0 &= \frac{1}{2} k \sqrt{\chi_{\mathbf{h}} \chi_{\bar{\mathbf{h}}}} |\mathfrak{P}| \left(\frac{\tilde{\eta}}{\sqrt{|\gamma|} \sqrt{\chi_{\mathbf{h}} \chi_{\bar{\mathbf{h}}}} |\mathfrak{P}|} \pm \sqrt{\frac{\tilde{\eta}^2}{|\gamma| \chi_{\mathbf{h}} \chi_{\bar{\mathbf{h}}} \mathfrak{P}^2} + \operatorname{sgn}(\gamma)} \right) \quad (\text{A.11})
\end{aligned}$$

Introducing the parameter η (equation 1.26) yields the sought solution for the coordinate of the tiepoint (equation 1.25)

$$X_0 = \frac{k \sqrt{\chi_{\mathbf{h}} \chi_{\bar{\mathbf{h}}}} |\mathfrak{P}|}{2 \sqrt{|\gamma|} \operatorname{sgn}(\gamma)} \left[\eta \pm \sqrt{\eta^2 + \operatorname{sgn}(\gamma)} \right] \quad (\text{A.12})$$

The second coordinate can be obtained from equation A.8. It reads

$$X_{\mathbf{h}} = \frac{1}{2} k \sqrt{\chi_{\mathbf{h}} \chi_{\bar{\mathbf{h}}}} |\mathfrak{P}| \sqrt{|\gamma|} \left[-\eta \pm \sqrt{\eta^2 + \operatorname{sgn}(\gamma)} \right] \quad (\text{A.13})$$

Now, having the solutions for X , the amplitude ratio can be obtained from its relation to tiepoint coordinate 1.21

$$\xi = \frac{2X_0}{k \chi_{\bar{\mathbf{h}}} \mathfrak{P}} = \frac{\operatorname{sgn}(\mathfrak{P}) \operatorname{sgn}(\gamma) \sqrt{\chi_{\mathbf{h}} \chi_{\bar{\mathbf{h}}}}}{\sqrt{|\gamma|} \chi_{\bar{\mathbf{h}}}} \left[\eta \pm \sqrt{\eta^2 + \operatorname{sgn}(\gamma)} \right] \quad (\text{A.14})$$

A.2 Time-dependent perturbation theory

A.2.1 Matrix elements in electric dipole approximation

In this appendix a transformation of the matrix element $\langle f | \mathbf{W}_0^\dagger | \phi_i \rangle = -\frac{e}{m_e} A_0^* \langle f | \mathbf{p} \cdot \hat{\boldsymbol{\varepsilon}}^* | \phi_i \rangle$ is presented. One uses the commutator relation 2.30, $p_j = -\frac{im_e}{\hbar} [r_j, \mathbf{H}_0]$.

$$\begin{aligned}
\langle f | \mathbf{W}_0^\dagger | \phi_i \rangle &= \frac{e}{m_e} \frac{im_e}{\hbar} A_0^* \{ \langle f | [x, \mathbf{H}_0] \varepsilon_x^* | \phi_i \rangle + \langle f | [y, \mathbf{H}_0] \varepsilon_y^* | \phi_i \rangle + \langle f | [z, \mathbf{H}_0] \varepsilon_z^* | \phi_i \rangle \} = \\
&= \frac{ie}{\hbar} A_0^* \{ \varepsilon_x^* \langle f | x \mathbf{H}_0 - \mathbf{H}_0 x | \phi_i \rangle + \varepsilon_y^* \langle f | y \mathbf{H}_0 - \mathbf{H}_0 y | \phi_i \rangle + \varepsilon_z^* \langle f | z \mathbf{H}_0 - \mathbf{H}_0 z | \phi_i \rangle \} = \\
&= \frac{ie}{\hbar} A_0^* \{ \varepsilon_x^* (\mathfrak{E}_i - \mathfrak{E}_f) \langle f | x | \phi_i \rangle + \varepsilon_y^* (\mathfrak{E}_i - \mathfrak{E}_f) \langle f | y | \phi_i \rangle + \varepsilon_z^* (\mathfrak{E}_i - \mathfrak{E}_f) \langle f | z | \phi_i \rangle \} = \\
&= ie A_0^* \omega_{if} \{ \varepsilon_x^* \langle f | x | \phi_i \rangle + \varepsilon_y^* \langle f | y | \phi_i \rangle + \varepsilon_z^* \langle f | z | \phi_i \rangle \} = \\
&= ie A_0^* \omega_{if} \langle f | \hat{\boldsymbol{\varepsilon}}^* \cdot \mathbf{r} | \phi_i \rangle \quad (\text{A.15})
\end{aligned}$$

In the transition from the second to the third line the Schrödinger equation $\mathbf{H}_0 | \phi_k \rangle = \mathfrak{E}_k | \phi_k \rangle$ was used.

A.2.2 Incident flux

Electric field is taken here in the regular form, without the complex conjugate (used definition of Poynting vector is valid for such a form)

$$\boldsymbol{\mathcal{E}} = -i\omega A_0 \boldsymbol{\varepsilon} e^{i\omega t - i\mathbf{k}\cdot\mathbf{r}} \quad (\text{A.16})$$

Magnetic field is related to the vector potential via $\boldsymbol{\mathcal{B}} = \text{rot}\boldsymbol{\mathcal{A}}$. Its component reads

$$\begin{aligned} \mathcal{B}_i &= \varepsilon_{ijk} \partial_j A_k = \varepsilon_{ijk} \partial_j A_0 \varepsilon_k e^{i\omega t - i\mathbf{k}\cdot\mathbf{r}} = \\ &= A_0 \varepsilon_{ijk} \varepsilon_k (-i) k_j e^{i\omega t - i\mathbf{k}\cdot\mathbf{r}} = -i A_0 \varepsilon_{ijk} k_j \varepsilon_k e^{i\omega t - i\mathbf{k}\cdot\mathbf{r}} \end{aligned} \quad (\text{A.17})$$

where ε_{ijk} is Levi-Civita symbol and Einstein's summation convention was used. The cross product component is equal

$$\begin{aligned} (\boldsymbol{\mathcal{E}} \times \boldsymbol{\mathcal{B}}^*)_i &= \varepsilon_{ijk} \mathcal{E}_j \mathcal{B}_k^* = \varepsilon_{ijk} (-i\omega A_0) \varepsilon_j e^{i\omega t - i\mathbf{k}\cdot\mathbf{r}} i A_0^* \varepsilon_{kmn} k_m \varepsilon_n^* e^{-i\omega t + i\mathbf{k}\cdot\mathbf{r}} = \\ &= \varepsilon_{kij} \varepsilon_{kmn} |A_0|^2 \omega \varepsilon_j \varepsilon_n k_m = \\ &= (\delta_{im} \delta_{jn} - \delta_{in} \delta_{jm}) |A_0|^2 \omega \varepsilon_j \varepsilon_n^* k_m = |A_0|^2 \omega (\varepsilon_j \varepsilon_j^* k_i - \varepsilon_j \varepsilon_i^* k_j) \end{aligned} \quad (\text{A.18})$$

The Poynting vector is thus

$$\mathbf{S} = \frac{\varepsilon_0 c^2}{2} |A_0|^2 \omega \left(\underbrace{(\boldsymbol{\varepsilon} \cdot \boldsymbol{\varepsilon}^*)}_{=1} \mathbf{k} - \underbrace{(\boldsymbol{\varepsilon} \cdot \mathbf{k})}_{=0} \boldsymbol{\varepsilon}^* \right) = \frac{\varepsilon_0 c^2}{2} |A_0|^2 \omega \mathbf{k}, \quad (\text{A.19})$$

and its length

$$S = \frac{1}{2} \varepsilon_0 c^2 |A_0|^2 k \omega \quad (\text{A.20})$$

The incident flux, given as $S/\hbar\omega$, is then

$$\Phi_0 = \frac{\varepsilon_0 c^2}{2\hbar} |A_0|^2 k \quad (\text{A.21})$$

A.3 MXSW theory

A.3.1 Polarisation-related quantities \mathfrak{A} , \mathfrak{B} and \mathfrak{C}

The absorption cross-section is determined by the \mathbf{a} , \mathbf{b} and \mathbf{c} transition rates and the quantities \mathfrak{A} , \mathfrak{B} and \mathfrak{C} related to the wavefield inducing the transition, in particular its polarisation state. The latter are given in general by the relations (4.10). The terms appearing in these general equations are for the case of the situation considered for MXSW experiment given by the relations 4.11 and 4.12. The explicit form of the quantities \mathfrak{A} , \mathfrak{B} and \mathfrak{C} is given below for completeness.

$$\begin{aligned} |\mathfrak{A}|^2 &= \varepsilon_\sigma^2 \left| 1 + \xi_\sigma e^{-i\mathbf{h}\cdot\mathbf{R}} \right|^2 \left(\sin^2 \varphi \cos^2 \vartheta_m + \cos^2 \varphi_m \right) + \\ &+ |\varepsilon_\pi|^2 \left| 1 - \xi_\pi e^{-i\mathbf{h}\cdot\mathbf{R}} \right|^2 \left(\cos^2 \varphi_m \cos^2 \vartheta_m + \sin^2 \varphi_m \right) \sin^2 \Theta_B + \\ &+ |\varepsilon_\pi|^2 \left| 1 + \xi_\pi e^{-i\mathbf{h}\cdot\mathbf{R}} \right|^2 \sin^2 \vartheta_m \cos^2 \Theta_B + \end{aligned}$$

$$\begin{aligned}
& - 2|\varepsilon_\pi|^2 \Re \left[(1 - \xi_\pi e^{-i\mathbf{h}\cdot\mathbf{R}}) (1 + \xi_\pi^* e^{i\mathbf{h}\cdot\mathbf{R}}) \right] \cos \varphi_m \sin \vartheta_m \cos \vartheta_m \sin \Theta_B \cos \Theta_B + \\
& - 2\varepsilon_\sigma \Re \left[\varepsilon_\pi^* (1 + \xi_\sigma e^{-i\mathbf{h}\cdot\mathbf{R}}) (1 - \xi_\pi^* e^{i\mathbf{h}\cdot\mathbf{R}}) \right] \sin \varphi_m \cos \varphi_m \sin^2 \vartheta_m \sin \Theta_B + \\
& - 2\varepsilon_\sigma \Re \left[\varepsilon_\pi^* (1 + \xi_\sigma e^{-i\mathbf{h}\cdot\mathbf{R}}) (1 + \xi_\pi^* e^{i\mathbf{h}\cdot\mathbf{R}}) \right] \sin \varphi_m \sin \vartheta_m \cos \vartheta_m \cos \Theta_B + \\
& + 2\Re \left\{ i \left[|\varepsilon_\pi|^2 (1 + \xi_\pi e^{-i\mathbf{h}\cdot\mathbf{R}}) (1 - \xi_\pi^* e^{i\mathbf{h}\cdot\mathbf{R}}) \sin \varphi_m \sin \vartheta_m \sin \Theta_B \cos \Theta_B + \right. \right. \\
& \quad \left. \left. + \varepsilon_\sigma \varepsilon_\pi^* (1 + \xi_\sigma e^{-i\mathbf{h}\cdot\mathbf{R}}) (1 + \xi_\pi^* e^{i\mathbf{h}\cdot\mathbf{R}}) \cos \varphi_m \sin \vartheta_m \cos \Theta_B + \right. \right. \\
& \quad \left. \left. - \varepsilon_\sigma \varepsilon_\pi^* (1 + \xi_\sigma e^{-i\mathbf{h}\cdot\mathbf{R}}) (1 - \xi_\pi^* e^{i\mathbf{h}\cdot\mathbf{R}}) \cos \vartheta_m \sin \Theta_B \right] \right\} \quad (\text{A.22a})
\end{aligned}$$

$$\begin{aligned}
|\mathfrak{B}|^2 &= \varepsilon_\sigma^2 \left| 1 + \xi_\sigma e^{-i\mathbf{h}\cdot\mathbf{R}} \right|^2 (\sin^2 \varphi_m \cos^2 \vartheta_m + \cos^2 \varphi_m) + \\
& + |\varepsilon_\pi|^2 \left| 1 - \xi_\pi e^{-i\mathbf{h}\cdot\mathbf{R}} \right|^2 (\cos^2 \varphi_m \cos^2 \vartheta_m + \sin^2 \varphi_m) \sin^2 \Theta_B + \\
& + |\varepsilon_\pi|^2 \left| 1 + \xi_\pi e^{-i\mathbf{h}\cdot\mathbf{R}} \right|^2 \sin^2 \vartheta_m \cos^2 \Theta_B + \\
& - 2|\varepsilon_\pi|^2 \Re \left[(1 - \xi_\pi e^{-i\mathbf{h}\cdot\mathbf{R}}) (1 + \xi_\pi^* e^{i\mathbf{h}\cdot\mathbf{R}}) \right] \cos \varphi_m \sin \vartheta_m \cos \vartheta_m \sin \Theta_B \cos \Theta_B + \\
& - 2\varepsilon_\sigma \Re \left[\varepsilon_\pi^* (1 + \xi_\sigma e^{-i\mathbf{h}\cdot\mathbf{R}}) (1 - \xi_\pi^* e^{i\mathbf{h}\cdot\mathbf{R}}) \right] \sin \varphi_m \cos \varphi_m \sin^2 \vartheta_m \sin \Theta_B + \\
& - 2\varepsilon_\sigma \Re \left[\varepsilon_\pi^* (1 + \xi_\sigma e^{-i\mathbf{h}\cdot\mathbf{R}}) (1 + \xi_\pi^* e^{i\mathbf{h}\cdot\mathbf{R}}) \right] \sin \varphi_m \sin \vartheta_m \cos \vartheta_m \cos \Theta_B + \\
& - 2\Re \left\{ i \left[|\varepsilon_\pi|^2 (1 + \xi_\pi e^{-i\mathbf{h}\cdot\mathbf{R}}) (1 - \xi_\pi^* e^{i\mathbf{h}\cdot\mathbf{R}}) \sin \varphi_m \sin \vartheta_m \sin \Theta_B \cos \Theta_B + \right. \right. \\
& \quad \left. \left. + \varepsilon_\sigma \varepsilon_\pi^* (1 + \xi_\sigma e^{-i\mathbf{h}\cdot\mathbf{R}}) (1 + \xi_\pi^* e^{i\mathbf{h}\cdot\mathbf{R}}) \cos \varphi_m \sin \vartheta_m \cos \Theta_B + \right. \right. \\
& \quad \left. \left. - \varepsilon_\sigma \varepsilon_\pi^* (1 + \xi_\sigma e^{-i\mathbf{h}\cdot\mathbf{R}}) (1 - \xi_\pi^* e^{i\mathbf{h}\cdot\mathbf{R}}) \cos \vartheta_m \sin \Theta_B \right] \right\} \quad (\text{A.22b})
\end{aligned}$$

$$|\mathfrak{C}|^2 = |\varepsilon_z|^2 \quad (\text{A.22c})$$

As stated in section 4.4, the quantities \mathfrak{A} , \mathfrak{B} and \mathfrak{C} can be split into the part which changes under the helicity reversal (denoted by double prime) and the part which remains unchanged (denoted by prime). Formally, $|\mathfrak{A}_\pm|^2 = \mathfrak{A}' \pm \mathfrak{A}''$, $|\mathfrak{B}_\pm|^2 = \mathfrak{B}' \pm \mathfrak{B}''$, $|\mathfrak{C}_\pm|^2 = \mathfrak{C}' \pm \mathfrak{C}''$, where "+" corresponds to the initial helicity, and "-" after the reversal. The explicit formulae for the prime and double prime quantities read

$$\begin{aligned}
\mathfrak{A}' &= \varepsilon_\sigma^2 \left| 1 + \xi_\sigma e^{-i\mathbf{h}\cdot\mathbf{R}} \right|^2 (\sin^2 \varphi_m \cos^2 \vartheta_m + \cos^2 \varphi_m) + \\
& + |\varepsilon_\pi|^2 \left| 1 - \xi_\pi e^{-i\mathbf{h}\cdot\mathbf{R}} \right|^2 (\cos^2 \varphi_m \cos^2 \vartheta_m + \sin^2 \varphi_m) \sin^2 \Theta_B + \\
& + |\varepsilon_\pi|^2 \left| 1 + \xi_\pi e^{-i\mathbf{h}\cdot\mathbf{R}} \right|^2 \sin^2 \vartheta_m \cos^2 \Theta_B + \\
& - 2|\varepsilon_\pi|^2 \Re \left[(1 - \xi_\pi e^{-i\mathbf{h}\cdot\mathbf{R}}) (1 + \xi_\pi^* e^{i\mathbf{h}\cdot\mathbf{R}}) \right] \cos \varphi_m \sin \vartheta_m \cos \vartheta_m \sin \Theta_B \cos \Theta_B + \\
& - 2\varepsilon_\sigma (\Re \varepsilon_\pi) \Re \left[(1 + \xi_\sigma e^{-i\mathbf{h}\cdot\mathbf{R}}) (1 - \xi_\pi^* e^{i\mathbf{h}\cdot\mathbf{R}}) \right] \sin \varphi_m \cos \varphi_m \sin^2 \vartheta_m \sin \Theta_B + \\
& - 2\varepsilon_\sigma (\Re \varepsilon_\pi) \Re \left[(1 + \xi_\sigma e^{-i\mathbf{h}\cdot\mathbf{R}}) (1 + \xi_\pi^* e^{i\mathbf{h}\cdot\mathbf{R}}) \right] \sin \varphi_m \sin \vartheta_m \cos \vartheta_m \cos \Theta_B + \\
& + 2\Re \left\{ i \left[|\varepsilon_\pi|^2 (1 + \xi_\pi e^{-i\mathbf{h}\cdot\mathbf{R}}) (1 - \xi_\pi^* e^{i\mathbf{h}\cdot\mathbf{R}}) \sin \varphi_m \sin \vartheta_m \sin \Theta_B \cos \Theta_B + \right. \right. \\
& \quad \left. \left. + \varepsilon_\sigma (\Re \varepsilon_\pi) (1 + \xi_\sigma e^{-i\mathbf{h}\cdot\mathbf{R}}) (1 + \xi_\pi^* e^{i\mathbf{h}\cdot\mathbf{R}}) \cos \varphi_m \sin \vartheta_m \cos \Theta_B + \right. \right. \\
& \quad \left. \left. - \varepsilon_\sigma (\Re \varepsilon_\pi) (1 + \xi_\sigma e^{-i\mathbf{h}\cdot\mathbf{R}}) (1 - \xi_\pi^* e^{i\mathbf{h}\cdot\mathbf{R}}) \cos \vartheta_m \sin \Theta_B \right] \right\} \quad (\text{A.23a})
\end{aligned}$$

$$\begin{aligned}
\mathfrak{A}'' &= 2\varepsilon_\sigma (\Im \varepsilon_\pi) \Re \left[i (1 + \xi_\sigma e^{-i\mathbf{h}\cdot\mathbf{R}}) (1 - \xi_\pi^* e^{i\mathbf{h}\cdot\mathbf{R}}) \sin \varphi_m \cos \varphi_m \sin^2 \vartheta_m \sin \Theta_B + \right. \\
& \quad \left. + i (1 + \xi_\sigma e^{-i\mathbf{h}\cdot\mathbf{R}}) (1 + \xi_\pi^* e^{i\mathbf{h}\cdot\mathbf{R}}) \sin \varphi_m \sin \vartheta_m \cos \vartheta_m \cos \Theta_B + \right. \\
& \quad \left. + (1 + \xi_\sigma e^{-i\mathbf{h}\cdot\mathbf{R}}) (1 + \xi_\pi^* e^{i\mathbf{h}\cdot\mathbf{R}}) \cos \varphi_m \sin \vartheta_m \cos \Theta_B + \right. \\
& \quad \left. - (1 + \xi_\sigma e^{-i\mathbf{h}\cdot\mathbf{R}}) (1 - \xi_\pi^* e^{i\mathbf{h}\cdot\mathbf{R}}) \cos \vartheta_m \sin \Theta_B \right] \quad (\text{A.23b})
\end{aligned}$$

$$\begin{aligned}
\mathfrak{B}' = & \varepsilon_\sigma^2 |1 + \xi_\sigma e^{-i\mathbf{h}\cdot\mathbf{R}}|^2 (\sin^2 \varphi_m \cos^2 \vartheta_m + \cos^2 \varphi_m) + \\
& + |\varepsilon_\pi|^2 |1 - \xi_\pi e^{-i\mathbf{h}\cdot\mathbf{R}}|^2 (\cos^2 \varphi_m \cos^2 \vartheta_m + \sin^2 \varphi_m) \sin^2 \Theta_B + \\
& + |\varepsilon_\pi|^2 |1 + \xi_\pi e^{-i\mathbf{h}\cdot\mathbf{R}}|^2 \sin^2 \vartheta_m \cos^2 \Theta_B + \\
& - 2|\varepsilon_\pi|^2 \Re [(1 - \xi_\pi e^{-i\mathbf{h}\cdot\mathbf{R}}) (1 + \xi_\pi^* e^{i\mathbf{h}\cdot\mathbf{R}})] \cos \varphi_m \sin \vartheta_m \cos \vartheta_m \sin \Theta_B \cos \Theta_B + \\
& - 2\varepsilon_\sigma (\Re \varepsilon_\pi) \Re [(1 + \xi_\sigma e^{-i\mathbf{h}\cdot\mathbf{R}}) (1 - \xi_\pi^* e^{i\mathbf{h}\cdot\mathbf{R}})] \sin \varphi_m \cos \varphi_m \sin^2 \vartheta_m \sin \Theta_B + \\
& - 2\varepsilon_\sigma (\Re \varepsilon_\pi) \Re [(1 + \xi_\sigma e^{-i\mathbf{h}\cdot\mathbf{R}}) (1 + \xi_\pi^* e^{i\mathbf{h}\cdot\mathbf{R}})] \sin \varphi_m \sin \vartheta_m \cos \vartheta_m \cos \Theta_B + \\
& - 2\Re \{ i [|\varepsilon_\pi|^2 (1 + \xi_\pi e^{-i\mathbf{h}\cdot\mathbf{R}}) (1 - \xi_\pi^* e^{i\mathbf{h}\cdot\mathbf{R}}) \sin \varphi_m \sin \vartheta_m \sin \Theta_B \cos \Theta_B + \\
& + \varepsilon_\sigma (\Re \varepsilon_\pi) (1 + \xi_\sigma e^{-i\mathbf{h}\cdot\mathbf{R}}) (1 + \xi_\pi^* e^{i\mathbf{h}\cdot\mathbf{R}}) \cos \varphi_m \sin \vartheta_m \cos \Theta_B + \\
& - \varepsilon_\sigma (\Re \varepsilon_\pi) (1 + \xi_\sigma e^{-i\mathbf{h}\cdot\mathbf{R}}) (1 - \xi_\pi^* e^{i\mathbf{h}\cdot\mathbf{R}}) \cos \vartheta_m \sin \Theta_B] \} \tag{A.24a}
\end{aligned}$$

$$\begin{aligned}
\mathfrak{B}'' = & 2\varepsilon_\sigma (\Im \varepsilon_\pi) \Re [i (1 + \xi_\sigma e^{-i\mathbf{h}\cdot\mathbf{R}}) (1 - \xi_\pi^* e^{i\mathbf{h}\cdot\mathbf{R}}) \sin \varphi_m \cos \varphi_m \sin^2 \vartheta_m \sin \Theta_B + \\
& + i (1 + \xi_\sigma e^{-i\mathbf{h}\cdot\mathbf{R}}) (1 + \xi_\pi^* e^{i\mathbf{h}\cdot\mathbf{R}}) \sin \varphi_m \sin \vartheta_m \cos \vartheta_m \cos \Theta_B + \\
& - (1 + \xi_\sigma e^{-i\mathbf{h}\cdot\mathbf{R}}) (1 + \xi_\pi^* e^{i\mathbf{h}\cdot\mathbf{R}}) \cos \varphi_m \sin \vartheta_m \cos \Theta_B + \\
& + (1 + \xi_\sigma e^{-i\mathbf{h}\cdot\mathbf{R}}) (1 - \xi_\pi^* e^{i\mathbf{h}\cdot\mathbf{R}}) \cos \vartheta_m \sin \Theta_B] \tag{A.24b}
\end{aligned}$$

$$\begin{aligned}
\mathfrak{C}' = & \varepsilon_\sigma^2 |1 + \xi_\sigma e^{-i\mathbf{h}\cdot\mathbf{R}}|^2 \sin^2 \varphi_m \sin^2 \vartheta_m + |\varepsilon_\pi|^2 |1 - \xi_\pi e^{-i\mathbf{h}\cdot\mathbf{R}}|^2 \cos^2 \varphi_m \sin^2 \vartheta_m \sin^2 \Theta_B + \\
& + |\varepsilon_\pi|^2 |1 + \xi_\pi e^{-i\mathbf{h}\cdot\mathbf{R}}|^2 \cos^2 \vartheta_m \cos^2 \Theta_B + \\
& + 2|\varepsilon_\pi|^2 \Re [(1 - \xi_\pi e^{-i\mathbf{h}\cdot\mathbf{R}}) (1 + \xi_\pi^* e^{i\mathbf{h}\cdot\mathbf{R}})] \cos \varphi_m \sin \vartheta_m \cos \vartheta_m \sin \Theta_B \cos \Theta_B + \\
& + 2\varepsilon_\sigma (\Re \varepsilon_\pi) \Re [(1 + \xi_\sigma e^{-i\mathbf{h}\cdot\mathbf{R}}) (1 - \xi_\pi^* e^{i\mathbf{h}\cdot\mathbf{R}}) \sin \varphi_m \cos \varphi_m \sin^2 \vartheta_m \sin \Theta_B + \\
& + (1 + \xi_\sigma e^{-i\mathbf{h}\cdot\mathbf{R}}) (1 + \xi_\pi^* e^{i\mathbf{h}\cdot\mathbf{R}}) \sin \varphi_m \sin \vartheta_m \cos \vartheta_m \cos \Theta_B] \tag{A.25a}
\end{aligned}$$

$$\begin{aligned}
\mathfrak{C}'' = & -2\varepsilon_\sigma (\Im \varepsilon_\pi) \Re \{ i [(1 + \xi_\sigma e^{-i\mathbf{h}\cdot\mathbf{R}}) (1 - \xi_\pi^* e^{i\mathbf{h}\cdot\mathbf{R}}) \sin \varphi_m \cos \varphi_m \sin^2 \vartheta_m \sin \Theta_B + \\
& + (1 + \xi_\sigma e^{-i\mathbf{h}\cdot\mathbf{R}}) (1 + \xi_\pi^* e^{i\mathbf{h}\cdot\mathbf{R}}) \sin \varphi_m \sin \vartheta_m \cos \vartheta_m \cos \Theta_B] \} \tag{A.25b}
\end{aligned}$$

A.4 Integral in the absorption correction

The integral appearing in the complete expression for the MXSW signal, where also the imaginary part of the wavevector is taken into account, reads

$$\mathcal{I}_2 = \int_0^\infty \exp \left\{ [k \Im \chi_0 + i ((X_0^\pi)^* - X_0^\sigma)] \frac{z}{\gamma_0} - \frac{\mu_{\text{lin}} z}{\sin \alpha} \right\} dz \tag{A.26}$$

It is evaluated in this appendix. At first the imaginary and real parts in the argument of the exponent are separated.

$$\begin{aligned} & \int_0^{\infty} \exp \left[\underbrace{k\Im\chi_0 \frac{z}{\gamma_0} + (\Im X_0^\sigma + \Im X_0^\pi) \frac{z}{\gamma_0} - \mu_{lin} \frac{z}{\sin \alpha}}_{\mu_1 z} \right] \exp \left[\underbrace{-i(\Re X_0^\sigma - \Re X_0^\pi) \frac{z}{\gamma_0}}_{-i\mu_2 z} \right] dz = \\ & = \int_0^{\infty} \exp(\mu_1 z) [\cos(\mu_2 z) - i \sin(\mu_2 z)] dz \end{aligned} \quad (\text{A.27})$$

where the symbols μ_1 and μ_2 have the meaning

$$\mu_1 = \left[\frac{k\Im\chi_0}{\gamma_0} + \frac{1}{\gamma_0} (\Im X_0^\sigma + \Im X_0^\pi) - \frac{\mu_{lin}}{\sin \alpha} \right] \quad (\text{A.28a})$$

$$\mu_2 = \frac{1}{\gamma_0} (\Re X_0^\sigma - \Re X_0^\pi) \quad (\text{A.28b})$$

The two integrals from equation (A.27) can be evaluated by parts. Due to the rule for differentiation of the product of two functions, one has the integral identity $\int f'g = fg - \int fg'$. Applying this twice yields

$$\begin{aligned} \int \exp(\mu_1 z) \cos(\mu_2 z) dz &= \frac{1}{\mu_1} \exp(\mu_1 z) \cos(\mu_2 z) + \frac{\mu_2}{\mu_1} \int \exp(\mu_1 z) \sin(\mu_2 z) dz = \\ &= \frac{1}{\mu_1} \exp(\mu_1 z) \cos(\mu_2 z) + \\ &+ \frac{\mu_2}{\mu_1} \left[\frac{1}{\mu_1} \exp(\mu_1 z) \sin(\mu_2 z) - \frac{\mu_2}{\mu_1} \int \exp(\mu_1 z) \cos(\mu_2 z) dz \right] \end{aligned} \quad (\text{A.29})$$

The desired integral appears again in the last line, so it can be added to both sides and one gets

$$\begin{aligned} & \int_0^{\infty} \exp(\mu_1 z) \cos(\mu_2 z) dz = \\ &= \frac{1}{1 + \frac{\mu_2^2}{\mu_1^2}} \left(\frac{1}{\mu_1} \exp(\mu_1 z) \cos(\mu_2 z) + \frac{\mu_2}{\mu_1^2} \exp(\mu_1 z) \sin(\mu_2 z) \right) \Bigg|_0^{\infty} = \\ &= \frac{1}{\mu_1^2 + \mu_2^2} (\mu_1 \exp(\mu_1 z) \cos(\mu_2 z) + \mu_2 \exp(\mu_1 z) \sin(\mu_2 z)) \Bigg|_0^{\infty} = \\ &= \lim_{z \rightarrow \infty} \left[\frac{1}{\mu_1^2 + \mu_2^2} (\mu_1 \exp(\mu_1 z) \cos(\mu_2 z) + \mu_2 \exp(\mu_1 z) \sin(\mu_2 z)) \right] - \frac{\mu_1}{\mu_1^2 + \mu_2^2} = \\ &= -\frac{\mu_1}{\mu_1^2 + \mu_2^2} \end{aligned} \quad (\text{A.30})$$

since $\exp(\mu_1 z)$ is a decreasing function approaching zero in the limit. μ_1 is negative as it is generally proportional to some effective absorption coefficient times minus one. This absorption coefficient cannot cause an amplification of the wave and thus it is positive.

The second integral can be calculated based on the first line of equation (A.29). It reads

$$\int \exp(\mu_1 z) \sin(\mu_2 z) dz = \frac{\mu_1}{\mu_2} \left[\int \exp(\mu_1 z) \cos(\mu_2 z) dz + \frac{1}{\mu_1} \exp(\mu_1 z) \cos(\mu_2 z) \right] \quad (\text{A.31})$$

With the limits

$$\begin{aligned} \int_0^{\infty} \exp(\mu_1 z) \sin(\mu_2 z) dz &= \frac{\mu_1}{\mu_2} \left\{ -\frac{\mu_1}{\mu_1^2 + \mu_2^2} - \frac{1}{\mu_1} \lim_{z \rightarrow \infty} [\exp(\mu_1 z) \cos(\mu_2 z)] + \frac{1}{\mu_1} \right\} = \\ &= \frac{\mu_1}{\mu_2} \left[-\frac{\mu_1}{\mu_1^2 + \mu_2^2} + \frac{1}{\mu_1} \right] = \frac{\mu_2}{\mu_1^2 + \mu_2^2} \end{aligned} \quad (\text{A.32})$$

The total integral reads

$$\int_0^{\infty} \exp \left\{ [k\Im\chi_0 + i((X_0^\pi)^* - X_0^\sigma)] \frac{z}{\gamma_0} - \frac{\mu \operatorname{Im} z}{\sin \alpha} \right\} dz = -\frac{\mu_1 + i\mu_2}{\mu_1^2 + \mu_2^2} \quad (\text{A.33})$$

Appendix B

2p \rightarrow 3d transitions

A diagram presenting the allowed transitions involving the operator Y_1^{-1} (i.e. fulfilling the condition $\Delta m_\ell = -1$) and their probabilities is shown in the main text (3.2). The remaining ones for the operators Y_1^1 ($\Delta m_\ell = 1$) and Y_1^0 ($\Delta m_\ell = 0$) are presented hereafter.

B.1 Transitions fulfilling $\Delta m_\ell = 1$

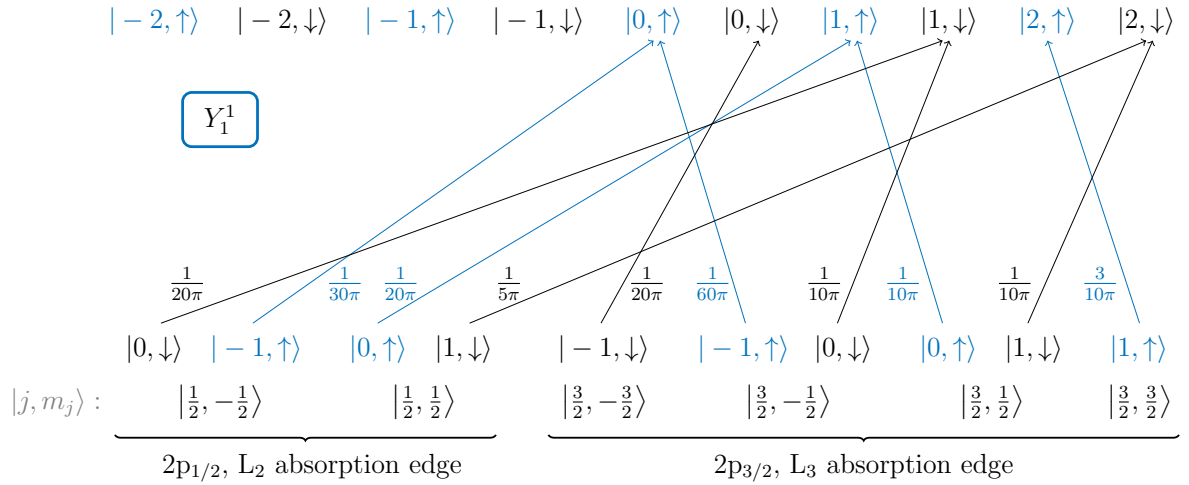


Figure B.1: Transitions from the 2p to the 3d states fulfilling the selection rule $\Delta m_\ell = 1$, for which the matrix elements of Y_1^1 operator are non-zero. The transitions with positive m_s are marked in blue colour for clarity. The transition strengths are written next to the arrows. The states in total angular momentum base are depicted at the bottom, for the others the abbreviation $| m_\ell, m_s = \uparrow \downarrow \rangle \equiv | \ell, m_\ell, s, m_s = \uparrow \downarrow \rangle$, where $\uparrow \equiv +\frac{1}{2}$, $\downarrow \equiv -\frac{1}{2}$, was used.

B.2 Transitions fulfilling $\Delta m_\ell = 0$

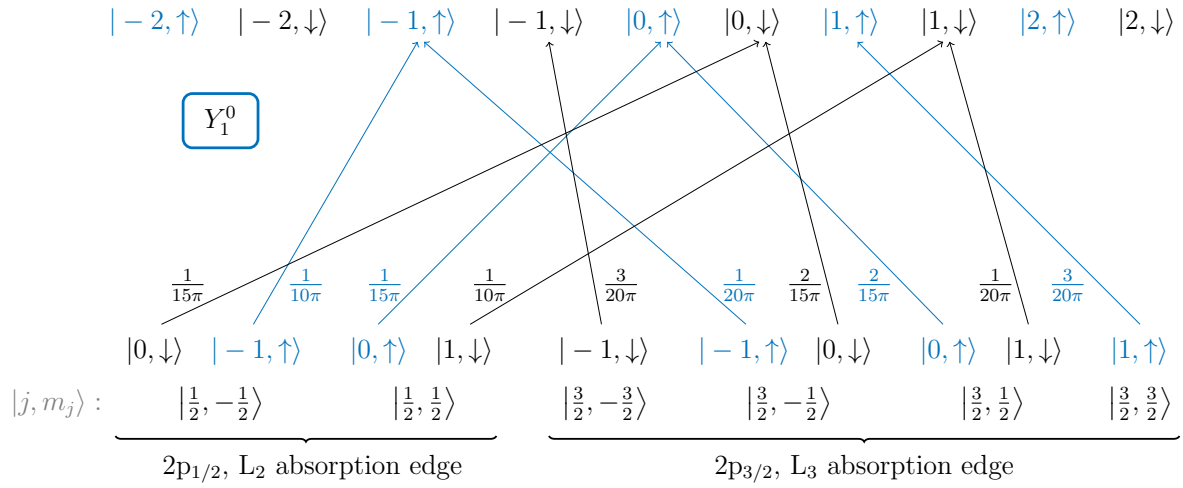


Figure B.2: Transitions from the 2p to the 3d states fulfilling the selection rule $\Delta m_\ell = 0$, for which the matrix elements of Y_1^0 operator are non-zero. The conventions used are the same as in fig. B.1.

Appendix C

Absorption correction related to XMCD

C.1 Influence on the phase of reflectivity

The absorption correction for the dynamical theory of diffraction and related to the XMCD effect is introduced in chapter 6. The change in the reflectivity curves caused by this correction is presented in figure 6.2 for two orientations of the magnetic moments (perpendicular and parallel to the reflecting lattice planes). In figure C.1 the changes in the phase of σ -component amplitude ratio ξ_σ after the correction are shown. One can see, that in the reflection domain, the difference almost vanishes.

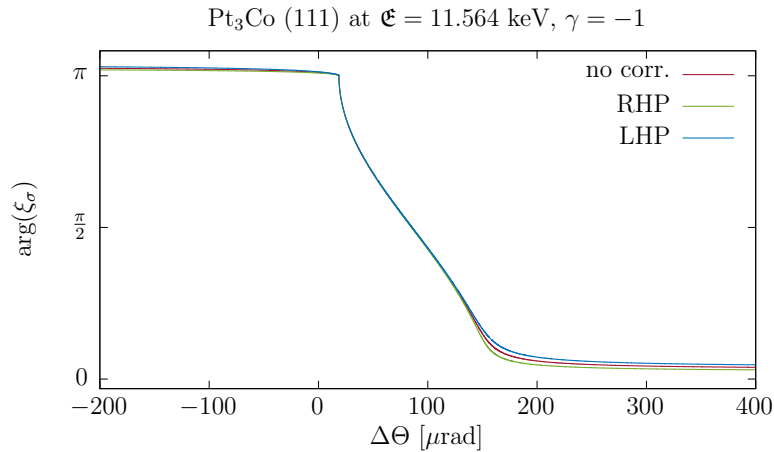


Figure C.1: The change of the phase of amplitude ratio ξ_σ for the σ -polarisation component after the introduction of the absorption correction related to the XMCD effect. The data for the alignment of the magnetic moments in the reflecting lattice planes is only shown, as for the natural magnetic structure (moments along [111] direction), the effect of the correction is even smaller. The data was simulated for the Pt₃Co crystal, (111) reflection.

Appendix D

Permanent magnet system

In section 7.1.2 it was mentioned that often in XMCD experiments, the investigated samples are magnetised using an external magnetic field. Thus, also in the case of the MXSW method being an extension of the standard XMCD spectroscopy, apart from flipping the helicity of the incoming beam, also the sample's magnetisation direction can be reversed. Even though the P09 experimental station, where the MXSW experiments reported in this work were performed, is equipped with an electromagnet system (see 7.3.3), there are certain reasons to develop a dedicated permanent magnet system for MXSW experiments.

First of all, the equipment based on the permanent magnets is very robust, as it does not require a complicated power supply system, as well as active cooling. Also, compared to an electromagnet, it is possible to achieve higher values of the magnetic field, keeping the system relatively compact. The latter is important, as in order to perform the MXSW scans, the sample has to be placed on the diffractometer, and so has to be also the magnet system.

There are important prerequisites for the magnet system for the MXSW experiment. The magnetic field has to be strong enough to magnetise the sample and there has to be a possibility to reverse the direction of the magnetic field. Apart from this, the sample has to be mounted somehow on the system, and the system on the diffractometer.

In this appendix two permanent magnet systems are presented. They were designed by Heiko Schulz-Ritter especially for the use in the future MXSW experiments. They can be easily mounted on the diffractometers using the standard IUCr mount. With respect to the electromagnet system from P09 beamline, where the sample is placed on a dedicated aluminium holder, which does not allow any pre-alignment of the sample, in the permanent magnet systems described here a goniometer head is used as a sample holder. This solution is a desired one for any experiments with magnetic field, where diffraction is involved and thus a precise orientation of the sample required. The first version of the permanent magnet system, where simply two magnets were used as the source of the magnetic field, provides around 150 mT. The second one, with the help of yokes provides 250 mT, what is almost double with respect to the 4-coil electromagnet at the P09 beamline.

D.1 First version

The 3D technical drawing of the first version of the permanent magnet system for the MXSW experiments is presented in figure D.1. Figure D.2 is a photo of the working realisation of the drawing.

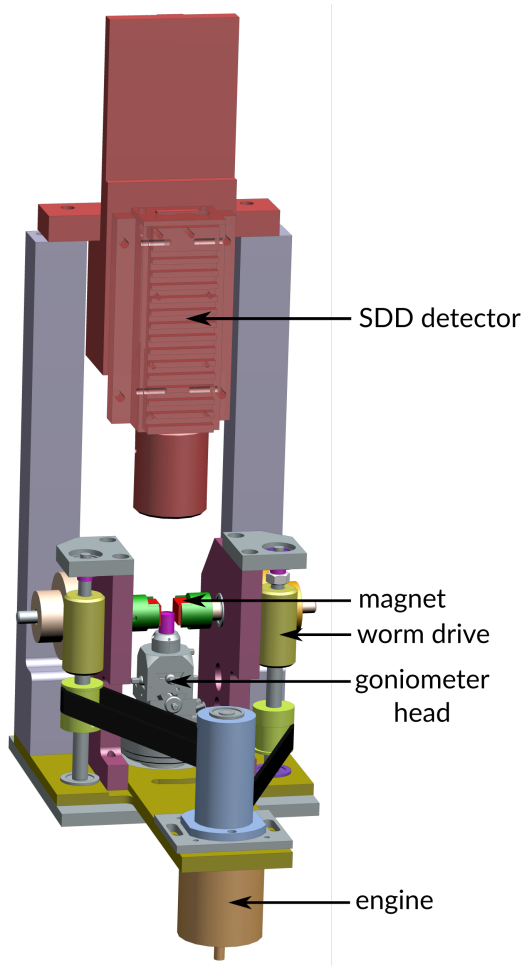


Figure D.1: The technical drawing in 3D of the first version of the permanent magnet system. The most important parts are marked in the figure.



Figure D.2: The photo of the first version of the the permanent magnet system.

The system consists of five crucial assemblies of parts: the engine and the transmission system, the permanent magnets glued in the holders, the sample holder (goniometer head), the connection for placing the system on the diffractometer and the holder for the fluorescence (SDD) detector.

The engine makes the change of the direction of the magnetic field possible, via the rotation of the permanent magnets. The movement of the engine is translated to the magnet holders via two rubber belts (black in the drawing D.1) and worm drives. The magnets (red) are glued in the holders (green) and connected to the transmission system, which enables rotation. The magnets can rotate 2π rad round the axis perpendicular to

the direction of the incoming beam (when the system is on the diffractometer in the zero position) and to the biggest face of the magnets. Among other possibilities, this allows to have the magnetic field parallel (and antiparallel) to the incoming beam, reflected beam, and reflecting lattice planes (for lattice planes parallel to the physical surface). The magnets used are small neodymium permanent ones, in the shape of cuboid.

The sample is placed on the goniometer head (Huber GmbH, model 1005), which is in turn mounted on the IUCr mount integrated in the bottom of the system. Below the base plane of the set-up, there is a connector enabling mounting of the system on the diffractometer.

Additionally a holder for the SDD detector used in the MXSW experiments for measuring the fluorescence spectra is integrated with the permanent magnet system. The detector is mounted on the dedicated plastic holder, which protects it from the influence of electronic noise possibly coming from the engine and additionally allows the adjustment of the sample-detector distance. The position of the SDD is restricted in the current design to the normal exit angle ($\alpha = \frac{\pi}{2}$). In case of experiments where the detection of fluorescence is not needed, the holder for the detector can be easily dismantled.

As measured with the Hall probe, the system provides around 150 mT of magnetic field at the position on the sample surface. The magnetic field can have an arbitrary orientation in the plane parallel to the biggest face of the permanent magnets (perpendicular to the magnets rotation axis).

D.2 Second version

Since the strength of the field of 150 mT might be too small for many of the interesting magnetic systems, an upgrade of the permanent magnet system was designed. The 3D technical drawing is presented in figure D.3, and the practical realisation in figure D.4.

With respect to the first version (section D.1), the main modification comprises here the part with permanent magnets. In the second version bigger magnets (gray in figure D.3) are used, and the field is guided from them towards the sample by two yokes (red and green). This idea allows to concentrate the magnetic field flux into the smaller volume, what results in a higher value of \mathbf{B} on the sample surface. Apart from this part of the system, the remaining ones are, at least conceptually, unchanged.

As measured with the Hall probe, the second version of the magnet system provides a superb value of around 250 mT of the magnetic field on the sample surface.

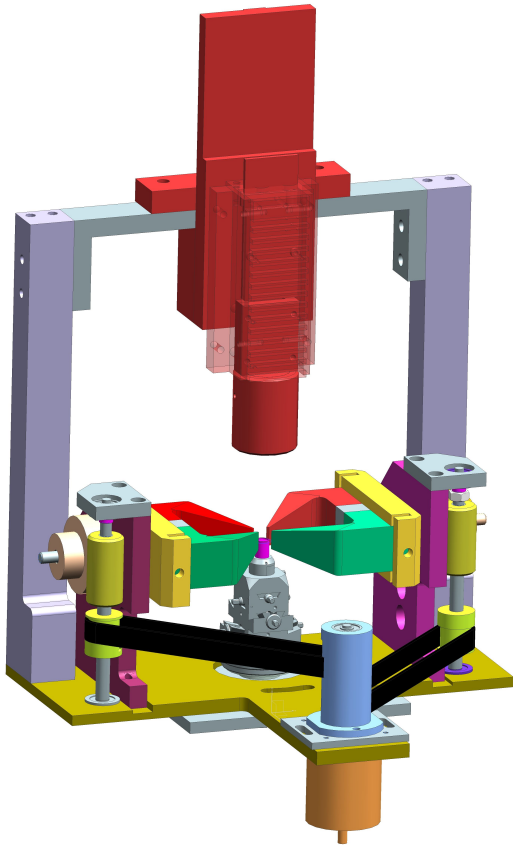


Figure D.3: The technical drawing in 3D of the second version of the permanent magnet system. Most of the parts are the same as for the first version. The major difference is the usage of bigger magnets (gray) and yokes (green and red part).

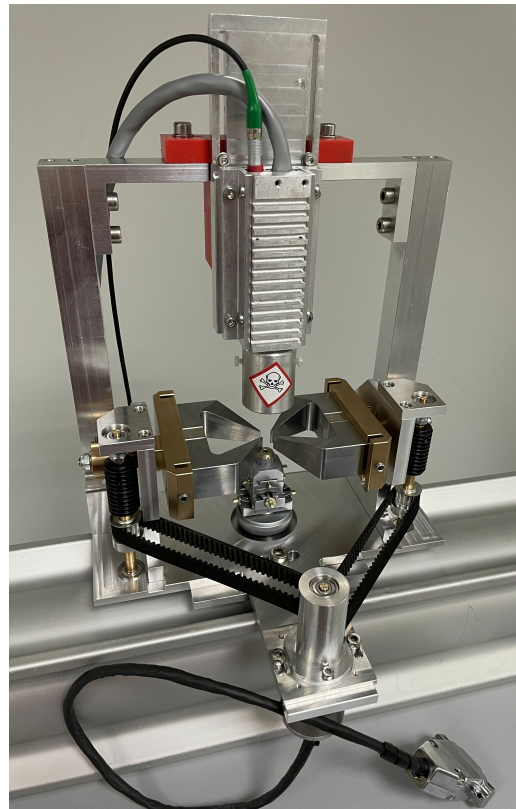


Figure D.4: The photo of the second version of the the permanent magnet system.

Appendix E

Experimental details

E.1 Pt₃Co hysteresis curve

The hysteresis curve was measured at the DESY Nanolab laboratory using the PPMS. The obtained data is shown in figure E.1. It shows, that the magnetic field of 150 mT is enough to magnetise the sample and reach the level of saturation magnetisation. The magnetic field during the measurement was aligned parallel to the sample surface, like in the MXSW experiment.

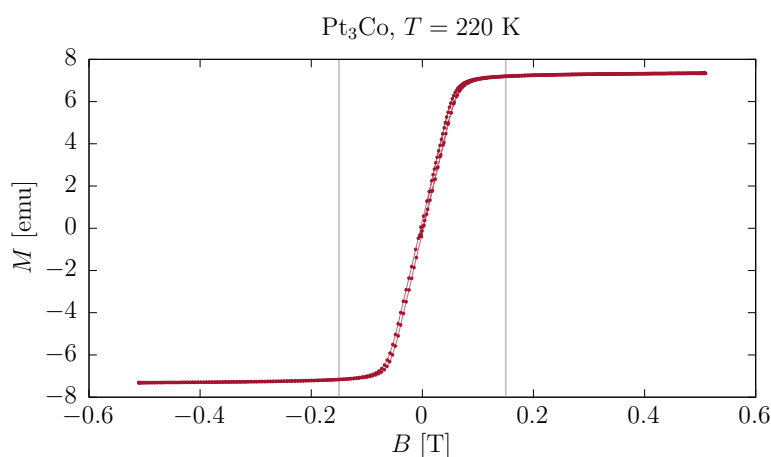


Figure E.1: Hysteresis curve for the single crystal sample of Pt₃Co. The data was obtained using the PPMS device at 220 K. Gray vertical lines mark the amplitudes of the magnetic field provided by the electromagnet used in the MXSW experiment.

E.2 Energy spectrum for YIG

In order to determine the energy for the MXSW experiment, an energy spectrum around the iron K absorption edge was measured. The σ -polarised radiation was used, and the sample oriented away from any Bragg reflections. The obtained energy spectrum is shown in figure E.2.

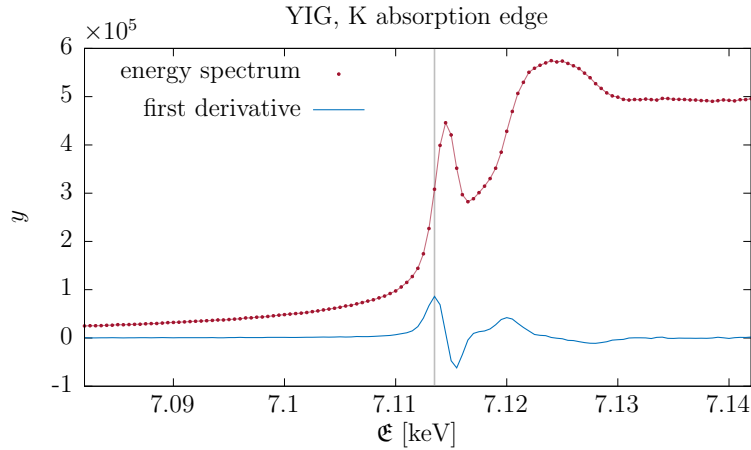


Figure E.2: Energy spectrum for a YIG crystal measured in the vicinity of the Fe K absorption edge. Linearly σ -polarised radiation was used. The measure of the absorption cross-section was obtained by integrating the iron K_{α} fluorescence line. The maximum of the first derivative of the energy spectrum corresponding to the energy of 71135 eV (marked by gray vertical line) was used to determine the energy value for the MXSW experiment.

E.3 Argon fluorescence yield

The comparison between the iron and argon fluorescence yields supports the hypothesis that during the (444) reflection scans another reflection was also excited. It is seen in the argon fluorescence yield as another increase in intensity, on the low angular side of the reflection domain. It coincides with the decrease (caused by the extinction effect) in the Fe fluorescence yield, what can be seen in figure E.3.

E.4 In- and out-of-field reflectivity

Even though the scans recorded without magnetic field cannot be used to calculate the XMCD signal, due to the observed artefact, an interesting feature was observed between the reflectivity recorded for the sample in an external magnetic field and without the field. The data is plotted in figure E.4. An observed shift might be related to the magnetostriction effect. The shift in the position of the curve maximum is $22.68 \mu\text{rad}$, what using Bragg's law translates to the difference of interplanar spacing $\Delta d_{(444)} = -9.20 \pm 1.95 \text{ fm}$, or equivalently $\Delta d_{(444)}/d_{(444)} = (-4.64 \pm 2.46) \cdot 10^{-5}$. The shift in the peak position is not caused by the mechanical movement of the sample, since then the shift between the $+\mathbf{B}$ and $-\mathbf{B}$ settings would be observed.

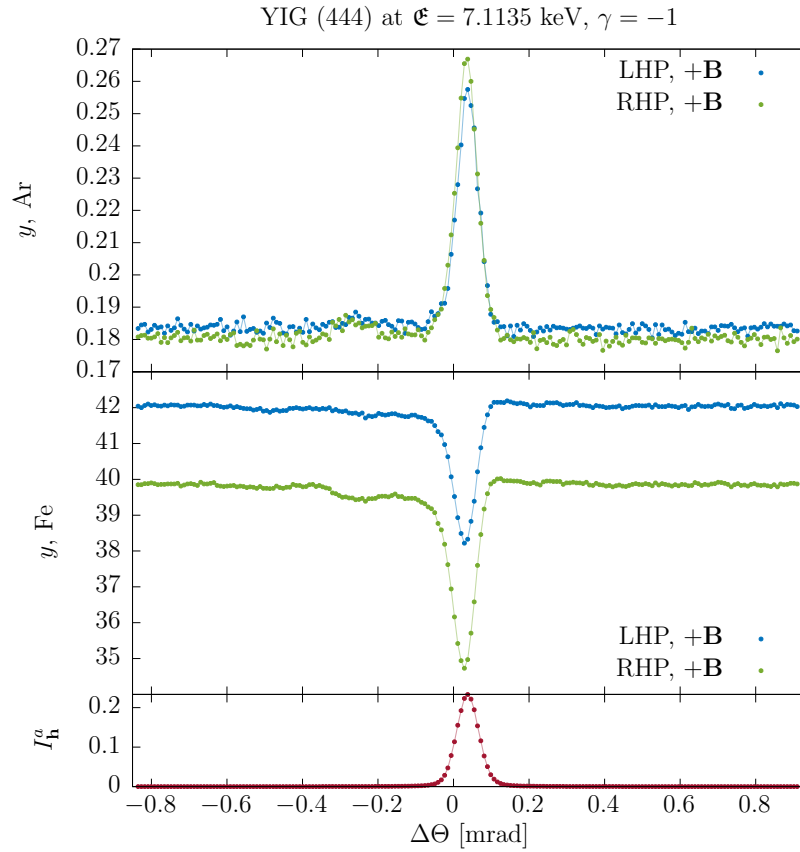


Figure E.3: Fluorescence yield of argon compared with the fluorescence yield of iron. An increase of the argon fluorescence in the reflection domain is caused by the absorption of the (444) reflected beam in the air. A small increase seen in the low angular side of the reflection domain can be a manifestation of another reflected wave, which due to the different propagation direction does not reach the APD detector. Note, that for one helicity (RHP) a greater increase is observed (and a greater decrease caused by the extinction in the Fe fluorescence).

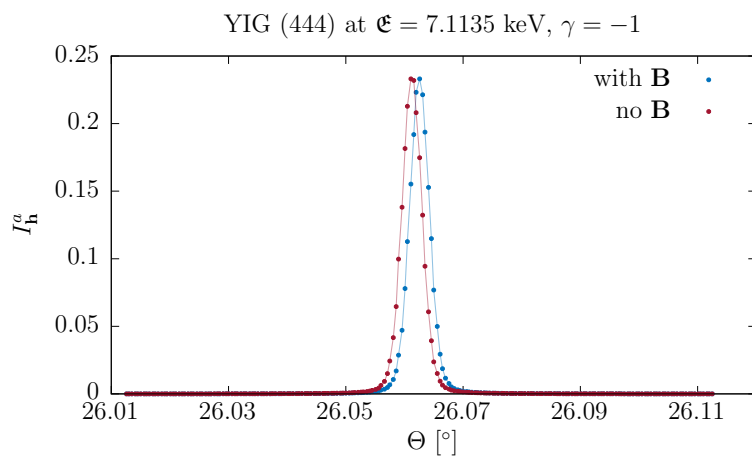


Figure E.4: Reflected beam intensity for a YIG crystal, (444) reflection. Comparison between the data measured with and without the external magnetic field. The data was normalised to the maximum of the theoretical curve (calculated from dynamical theory for YIG, convolved with monochromator reflectivity). The shift of the maximum of reflectivity might be related to the magnetostriction.

List of Symbols

\mathcal{A}	— vector potential
A	— amplitude of the vector potential
\mathfrak{A}	— a quantity from the expression for the absorption cross-section (equation (3.8)) describing the component of the EM field inducing transitions with $\Delta m_\ell = -1$
\mathfrak{A}'	— the part of \mathfrak{A} , which does not change under the helicity reversal
\mathfrak{A}''	— the part of \mathfrak{A} , which changes under the helicity reversal
a_0	— spatial extent of the electron wavefunction
\mathfrak{a}	— a quantity from the expression for the absorption cross-section defined by equation (3.1.3) and being a spin-dependent transition rate of transitions with $\Delta m_\ell = -1$
\mathcal{B}	— magnetic induction
B	— amplitude of the magnetic induction
\mathfrak{B}	— a quantity from the expression for the absorption cross-section (equation (3.8)) describing the component of the EM field inducing transitions with $\Delta m_\ell = 1$
\mathfrak{B}'	— the part of \mathfrak{B} , which does not change under the helicity reversal
\mathfrak{B}''	— the part of \mathfrak{B} , which changes under the helicity reversal
b_n	— n -th coefficient from equation (2.6)
\mathfrak{b}	— a quantity from the expression for the absorption cross-section defined by equation (3.1.3) and being a spin-dependent transition rate of transitions with $\Delta m_\ell = 1$
\mathcal{C}	— constants from the expression for the absorption cross-section, $\mathcal{C} = (4\pi)^2 \alpha_f \hbar \omega$
C_G	— multiplicative scaling factor in Gaussian function

\mathfrak{C}	— a quantity from the expression for the absorption cross-section (equation (3.8)) describing the component of the EM field inducing transitions with $\Delta m_\ell = 0$
\mathfrak{C}'	— the part of \mathfrak{C} , which does not change under the helicity reversal
\mathfrak{C}''	— the part of \mathfrak{C} , which changes under the helicity reversal
c	— speed of light
c_n	— n -th coefficient in the expansion of the state vector in the basis of eigenvectors
\mathfrak{c}	— a quantity from the expression for the absorption cross-section defined by equation (3.1.3) and being a spin-dependent transition rate of transitions with $\Delta m_\ell = 0$
\mathcal{D}	— dielectric vector
d	— crystal's thickness
$d_{\mathbf{h}}$	— interplanar spacing of the lattice planes associated with \mathbf{h}
\mathcal{E}	— electric field
\mathbf{E}	— amplitude of the electric field
\mathfrak{E}	— energy
e	— elementary charge
$F_{\mathbf{h}}$	— structure factor
$F_{sw}^{\mathbf{h}}$	— standing wave structure factor
$F_{msw}^{\mathbf{h}}$	— magnetic standing wave structure factor
f	— atomic scattering factor
f^0	— non-resonant part of the atomic scattering factor
f', f''	— dispersion corrections to the scattering factor
f_c	— coherent fraction
G	— atomic distribution function
\mathcal{H}	— magnetic field
\mathbf{H}	— Hamilton operator
\mathbf{h}	— reciprocal lattice vector (with 2π prefactor)
h_P	— Planck constant
\hbar	— reduced Planck constant
\mathcal{I}	— integral

I	— intensity of the EM wave
I_{sw}	— normalised intensity of the standing wave
i	— imaginary unit, $i^2 = -1$
\mathbf{J}	— total angular momentum operator
j	— total angular momentum quantum number
\mathbf{k}	— wavevector
k	— length of the wavevector in vacuum
\mathbf{k}_m	— magnetic structure propagation vector
\mathbf{L}	— orbital angular momentum operator
ℓ	— azimuthal quantum number
\mathbf{M}	— magnetisation
\mathbf{m}	— magnetic moment
m_e	— electron mass
m_ℓ	— magnetic quantum number
m_s	— spin magnetic quantum number
\mathcal{N}	— an integer number ($\mathcal{N} \in \mathbb{Z}$)
N	— number of atoms in the unit cell
N_h	— number of electron-holes
\mathbf{n}	— unit vector normal to the physical surface of the crystal
n	— number of atoms of a given kind in the unit cell
n	— principal quantum number
\mathbf{n}	— refractive index
\mathbf{P}	— polarisation vector
P_{fi}	— probability of transition from the state $ i\rangle$ to $ f\rangle$
\mathfrak{P}	— polarisation factor
\mathbf{p}	— momentum
p_c	— coherent position
\mathcal{R}	— radial integral
\mathbf{R}	— rotation matrix
\mathbf{R}	— position of the atom (its nucleus)

R_{Th}	— Thomson scattering length
$R_{n\ell}$	— radial part of the wavefunction
R_ξ	— residual parameter
\mathbf{r}	— position
$\tilde{\mathbf{r}}$	— position of the electron with respect to nucleus
\mathbf{S}	— spin operator
\mathbf{S}	— Poynting vector
S	— footprint of the beam on the crystal surface
$S_0, S_{\mathbf{h}}$	— cross-sections of the beams
s	— spin quantum number
T	— temperature
t	— time
U	— potential energy
\mathbf{V}	— external perturbation operator such that $\mathbf{W} = v\mathbf{V}$
V_{nk}	— matrix element of the operator \mathbf{V} , $V_{nk} = \langle \phi_n \mathbf{V} \phi_k \rangle$
V_{cell}	— volume of the unit cell
\mathbf{W}	— external perturbation operator
W_{nk}	— matrix element of the operator \mathbf{W} , $W_{nk} = \langle \phi_n \mathbf{W} \phi_k \rangle$
w_{fi}	— probability rate, $w_{fi} = P_{fi}/t$
X	— tiepoint coordinate
$Y_\ell^{m\ell}$	— spherical harmonic
y	— secondary emission yield (electron or fluorescence)
$z_{\mathbf{h}}$	— fractional coordinate in the direction of \mathbf{h} , $z_{\mathbf{h}} \in [0; 1]$
z_{eff}	— effective thickness
α	— angle between the crystal surface and the direction towards the secondary emission detector (figure 1.7)
α_f	— fine structure constant, $\alpha_f = e^2/4\pi\epsilon_0\hbar c$
β	— parameter in the polarisation vector (equation (1.49)) related to the amplitudes of polarisation components
γ	— asymmetry ratio, $\gamma = \gamma_{\mathbf{h}}/\gamma_0$

γ_0	— cosine of the angle between the refracted wave wavevector and surface normal $\gamma_0 = \cos \psi_0$
$\gamma_{\mathbf{h}}$	— cosine of the angle between the reflected wave wavevector and surface normal, $\gamma_{\mathbf{h}} = \cos \psi_{\mathbf{h}}$
Δ	— real number, $\Delta \in [0; d_{\mathbf{h}}]$
δ	— parameter of the polarisation vector (equation (1.49)) related to the phase difference between the polarisation components
δ_{jk}	— Kronecker delta
$\delta(x)$	— Dirac delta functional
$\boldsymbol{\varepsilon}$	— polarisation vector
$\hat{\boldsymbol{\varepsilon}}$	— polarisation unit vector
$\hat{\boldsymbol{\varepsilon}}_{\sigma}$	— σ -polarisation unit vector
$\hat{\boldsymbol{\varepsilon}}_{0\pi}, \hat{\boldsymbol{\varepsilon}}_{\mathbf{h}\pi}$	— π -polarisation unit vectors
ε_{σ}	— component of the polarisation vector in the direction of $\hat{\boldsymbol{\varepsilon}}_{\sigma}$, $\varepsilon_{\sigma} \in \mathbb{R}$
ε_{π}	— component of the polarisation vector in the direction of $\hat{\boldsymbol{\varepsilon}}_{0\pi}$, $\varepsilon_{\pi} \in \mathbb{C}$
ε_0	— vacuum permittivity
ε_{ijk}	— Levi-Civita symbol
ζ	— spin-dependent transition rate
η	— deviation parameter from the dynamical theory of diffraction, defined by eq. (1.26)
Θ	— incidence angle between the incoming beam and lattice planes
Θ_B	— Bragg angle
$\Delta\Theta$	— departure from the incidence corresponding to the Bragg angle, $\Delta\Theta = \Theta - \Theta_B$
ϑ	— azimuthal angle in spherical coordinate system
ϑ_x	— an angle between the magnetic moment and propagation direction of the wave in the XMCD experiment (see figure 3.1)
ϑ_m	— an angle between the magnetic moment and the reciprocal lattice vector \mathbf{h} of the reflection (see figure 4.2)
κ	— small complex number, such that $\mathbf{k}_0 = \mathbf{k}_0^a - k\kappa\mathbf{n}$
Λ	— parameter labelling the states forming a continuum
λ	— wavelength
μ	— effective absorption coefficient

μ_{lin}	— linear absorption coefficient
μ_1	— total absorption coefficient for the MXSW signal (equation (4.52a))
μ_2	— a quantity related to Pendellösung period, from the absorption correction for the complex wavevector for the MXSW signal (equation (4.52b))
μ_B	— Bohr magneton, $\mu_B = e\hbar/2m_e$
μ_0	— vacuum permeability
Ξ	— XMCD signal from one atom calculated as a difference between the cross-sections for opposite helicities
$\Xi_{\mathbf{m}}$	— XMCD signal from one atom calculated as a difference between the cross-sections for opposite magnetic moment orientations
Ξ_1	— the part of the quantities \mathfrak{A} , \mathfrak{B} and \mathfrak{C} from the expression for the XMCD signal under the XSW regime, proportional to $\Im\varepsilon_\pi$ and defined by equation (4.13a)
Ξ_2	— the part of the expression for the XMCD signal under the XSW regime proportional to $\Im\varepsilon_\pi$ and defined by equation (4.13b)
Ξ_3	— the part of the expression for the XMCD signal under the XSW regime proportional to $\Re\varepsilon_\pi$ and $ \varepsilon_\pi $, defined by equation (4.15)
Ξ_4	— the part of the quantities \mathfrak{A} , \mathfrak{B} from the expression for the XMCD signal under the XSW regime, defined by equation (4.16)
ξ	— amplitude ratio, $\xi = E_{\mathbf{h}}/E_0$
Π_{circ}	— circular polarisation rate in a given direction
Π_γ	— circular polarisation rate in the propagation direction
Π_e^s	— spin-polarisation of the photoelectron
Π_e^ℓ	— orbital-polarisation of the photoelectron
$\boldsymbol{\sigma}$	— Pauli matrices
σ	— absorption cross-section
σ_G	— width of the Gaussian function
ϱ	— density of states
$\Delta\varrho_f^s$	— imbalance in the density of spin-polarised empty final states, $\Delta\varrho_f^s = \varrho_f^\uparrow - \varrho_f^\downarrow$
$\Delta\varrho_f^\ell$	— orbital-polarised density of empty final states
ρ	— electron density
τ	— angle between the lattice planes and crystal's surface
Υ	— MXSW signal from many atoms

Υ_2	— the part of the expression for the MXSW signal, defined by equation (4.32) and being a normalised sum of the Ξ_2 terms over the atoms in the unit cell
Υ_3	— the part of the expression for the MXSW signal, defined by equation (4.33) and being a normalised sum of the Ξ_3 terms over the atoms in the unit cell
v	— parameter in the perturbation theory, $\mathbf{W} = v\mathbf{V}$
Φ	— photon flux
φ	— polar angle in spherical coordinate system
φ_x	— a polar angle used to parametrise the propagation direction of the wave in the XMCD experiment (see figure 3.1)
φ_m	— an angle between the scattering plane and the magnetic moment (see figure 4.2)
$\phi_{\mathbf{n},\ell,m_\ell}$	— atomic wavefunction
$ \phi\rangle$	— stationary quantum state of the system
χ	— susceptibility
ψ_0	— angle between the surface normal and the refracted beam, $\psi_0 = \angle(\mathbf{n}, \mathbf{k}_0)$
$\psi_{\mathbf{h}}$	— angle between the surface normal and the reflected beam, $\psi_{\mathbf{h}} = \angle(\mathbf{n}, \mathbf{k}_{\mathbf{h}})$
$ \psi\rangle$	— quantum state of the system
Ω	— parameter labelling the states forming a continuum, together with energy
ω	— angular frequency
ω_{nk}	— Bohr angular frequency, $\hbar\omega_{nk} = \mathcal{E}_n - \mathcal{E}_k$

List of Abbreviations

ADC	—	analog-to-digital converter
APD	—	avalanche photodiode
DESY	—	Deutsches Elektronen-Synchrotron
DP	—	double perovskite
EH	—	experimental hutch
EM	—	electromagnetic
FEL	—	free electron laser
FPGA	—	field programmable gate array
LHP	—	left-handed polarisation
MXSW	—	magnetic x-ray standing waves
PIPS	—	passivated implanted planar silicon
PPMS	—	physical properties measurement system
RHP	—	right-handed polarisation
SAXS	—	small angle x-ray scattering
SDD	—	silicon drift diode
YIG	—	yttrium-iron-garnet
XMCD	—	x-ray magnetic circular dichroism
XMLD	—	x-ray magnetic linear dichroism
XRMR	—	x-ray resonant magnetic reflectivity
XSW	—	x-ray standing waves

References

- [1] J. Wilkins, B. J. Schoville, R. Pickering, L. Gliganic, B. Collins, K. S. Brown, J. von der Meden, W. Khumalo, M. C. Meyer, S. Maape, A. F. Blackwood, and A. Hatton, *Innovative Homo sapiens behaviours 105,000 years ago in a wetter Kalahari*, Nature **592**, 248 (2021).
- [2] A. Authier, *Early Days of X-ray Crystallography*, Oxford University Press, Oxford, 2013.
- [3] W. H. Bragg, *X-rays and Crystals*, Nature **90**, 219 (1912).
- [4] R. R. Fu, J. L. Kirschvink, N. Carter, O. C. Mazariegos, G. Chigna, G. Gupta, and M. Grapponne, *Knowledge of magnetism in ancient Mesoamerica: Precision measurements of the potbelly sculptures from Monte Alto, Guatemala*, J. Archaeol. Sci. **106**, 29 (2019).
- [5] H. C. Ørsted, *Experimenta Circa Effectum Conflictus Electrici In Acum Magneticam*, (1820).
- [6] E. Ising, *Beitrag zur Theorie des Ferromagnetismus*, Z. Phys. **31**, 253 (1925).
- [7] W. Heisenberg, *Zur Theorie des Ferromagnetismus*, Z. Phys. **49**, 619 (1928).
- [8] J. Rodríguez-Carvajal and J. Villain, *Magnetic structures*, C. R. Phys. **20**, 770 (2019).
- [9] D. Sayre, *X-Ray Crystallography: The Past and Present of the Phase Problem*, Struct. Chem. **13**, 81 (2002).
- [10] C. Giacovazzo, *Direct Phasing in Crystallography. Fundamentals and Applications*, Oxford University Press, Oxford, 1998.
- [11] E. Weckert and K. Hümmel, *Multiple-Beam X-ray Diffraction for Physical Determination of Reflection Phases and its Applications*, Acta Crystallogr. A **53**, 108 (1997).
- [12] J. Zegenhagen, *Surface structure determination with X-ray standing waves*, Surf. Sci. Rep. **18**, 199 (1993).
- [13] M. J. Bedzyk and G. Materlik, *Two-beam dynamical diffraction solution of the phase problem: A determination with x-ray standing-wave fields*, Phys. Rev. B **32**, 6456 (1985).
- [14] K. Tomiyasu, R. Oishi-Tomiyasu, M. Matsuda, and K. Matsuhira, *A new mathematical approach to finding global solutions of the magnetic structure determination problem*, Sci. Rep. **8**, 16228 (2018).
- [15] C. G. Darwin, *The theory of X-ray reflection*, Phil. Mag. **27**, 315 (1914).
- [16] C. G. Darwin, *The theory of X-ray reflection. Part II*, Phil. Mag. **27**, 675 (1914).
- [17] M. Renninger, *Messungen zur Röntgenstrahl-Optik des Idealkristalls. I. Bestätigung der Darwin-Ewald-Prins-Kohler-Kurve*, Acta Crystallogr. **8**, 597 (1955).
- [18] R. Bubáková, J. Drahoukoupil, and A. Fingerland, *Single crystal diffraction pattern of germanium*, Czech. J. Phys. B **11**, 199 (1961).

-
- [19] W. Kossel, V. Loeck, and H. Voges, *Die Richtungsverteilung der in einem Kristall entstandenen charakteristischen Röntgenstrahlung*, Z. Phys. **94**, 139 (1935).
- [20] M. von Laue, *Röntgenstrahl-Interferenzen*, Akademische Verlagsgesellschaft, Frankfurt am Main, 1960.
- [21] G. Borrmann, *Über Extinktionsdiagramme von Quarz*, Phys. Z. **42**, 157 (1941).
- [22] G. Borrmann, *Die Absorption von Röntgenstrahlen im Fall der Interferenz*, Z. Phys. **127**, 297 (1950).
- [23] J. W. Knowles, *Anomalous Absorption of Slow Neutrons and X-rays in Nearly Perfect Single Crystals*, Acta Crystallogr. **9**, 61 (1956).
- [24] B. W. Batterman, *Effect of Dynamical Diffraction in X-Ray Fluorescence Scattering*, Phys. Rev. **133**, 759 (1964).
- [25] A. Rodriguez-Fernandez, A. Diaz, A. H. S. Iyer, M. Vezzhak, K. Wakonig, M. H. Colliander, and D. Carbone, *Imaging Ultrafast Dynamical Diffraction Wave Fronts in Strained Si with Coherent X Rays*, Phys. Rev. Lett. **127**, 157402 (2021).
- [26] V. B. Novikov and T. V. Murzina, *Borrmann effect in Laue diffraction in one-dimensional photonic crystals under a topological phase transition*, Phys. Rev. B **99**, 245403 (2019).
- [27] J.-P. Guigay and M. S. del Rio, *X-ray focusing by bent crystals: focal positions as predicted by the crystal lens equation and the dynamical diffraction theory*, J. Synchrotron Rad. **29**, 148 (2022).
- [28] X. Huang, X. Shi, and L. Assoufid, *X-ray beam monitoring and wavelength calibration using four-beam diffraction*, J. Synchrotron Rad. **29**, 159 (2022).
- [29] J. Zegenhagen and A. Kazimirov, *X-Ray Standing Waves in a Nutshell*, in *The X-ray standing wave technique. Principles and Applications*, edited by J. Zegenhagen and A. Kazimirov, World Scientific, Singapore, 2013.
- [30] C. C. Silva, D. Dombrowski, N. Atodiressei, W. Jolie, F. F. zum Hagen, J. Cai, P. T. P. Ryan, P. K. Thakur, V. Caciuc, S. Blügel, D. A. Duncan, T. Michely, T.-L. Lee, and C. Busse, *Spatial variation of geometry, binding, and electronic properties in the moiré superstructure of MoS₂ on Au(111)*, 2D Mater. **9**, 025003 (2022).
- [31] A. V. Rogachev, N. N. Novikova, M. V. Kovalchuk, Y. N. Malakhova, O. V. Konovalov, N. D. Stepina, E. A. Shlyapnikova, I. L. Kanev, Y. M. Shlyapnikov, and S. N. Yakunin, *Permeation of Nanoparticles into Pulmonary Surfactant Monolayer: In Situ X-ray Standing Wave Studies*, Langmuir **38**, 3630 (2022).
- [32] P. T. P. Ryan, D. J. Payne, T.-L. Lee, and D. A. Duncan, *Quantitative structure determination of adsorbed formate and surface hydroxyls on Fe₃O₄ (001)*, Phys. Chem. Chem. Phys. **24**, 488 (2022).
- [33] P. Ryan, P. J. Blowey, B. S. Sohail, L. A. Rochford, D. A. Duncan, T.-L. Lee, P. Starrs, G. Costantini, R. J. Maurer, and D. P. Woodruff, *Thermodynamic Driving Forces for Substrate Atom Extraction by Adsorption of Strong Electron Acceptor Molecules*, J. Phys. Chem. C **126**, 6082 (2022).
- [34] L. Hörmann, A. Jeindl, and O. T. Hofmann, *From a bistable adsorbate to a switchable interface: tetrachloropyrazine on Pt(111)*, Nanoscale **14**, 5154 (2022).
- [35] D. P. Woodruff and D. A. Duncan, *X-ray standing wave studies of molecular adsorption: why coherent fractions matter*, New J. Phys. **22**, 113012 (2020).

- [36] B. W. Batterman, *Detection of foreign atoms by their x-ray fluorescence scattering*, Phys. Rev. Lett. **22**, 703 (1969).
- [37] M. Sugiyama, S. Maeyama, S. Heun, and M. Oshima, *Chemical-state-resolved x-ray standing-wave analysis using chemical shift in photoelectron spectra*, Phys. Rev. B **51**, 14778(R) (1995).
- [38] M. J. Bedzyk, *X-ray standing wave at the total reflection condition*, in *The X-ray standing wave technique. Principles and Applications*, edited by J. Zegenhagen and A. Kazimirov, World Scientific, Singapore, 2013.
- [39] M. J. Bedzyk and J. A. Libera, *X-ray standing wave in multilayers*, in *The X-ray standing wave technique. Principles and Applications*, edited by J. Zegenhagen and A. Kazimirov, World Scientific, Singapore, 2013.
- [40] S.-K. Kim and J. B. Kortright, *Modified Magnetism at a Buried Co/Pd Interface Resolved with X-Ray Standing Waves*, Phys. Rev. Lett. **86**, 1347 (2001).
- [41] S.-H. Yang, B. S. Mun, N. Mannella, S.-K. Kim, J. B. Kortright, J. Underwood, F. Salmassi, E. Arenholz, A. Young, Z. Hussain, M. A. V. Hove, and C. S. Fadley, *Probing buried interfaces with soft x-ray standing wave spectroscopy: application to the Fe/Cr interface*, J. Phys.: Condens. Matter **14**, L407 (2002).
- [42] K. Sato, M. Sugawara, T. Jinno, M. Toyoda, T. Hatano, A. Arai, and M. Yanagihara, *X-ray magnetic circular dichroism studies for Fe/Si interfaces using standing waves*, J. Phys.: Conf. Ser. **83**, 012012 (2007).
- [43] M. A. Andreeva and E. E. Odintsova, *X-Ray Circular Dichroism under Reflection from Antiferromagnetically Coupled Multilayers*, Moscow Univ. Phys. **67**, 196 (2012).
- [44] P. Jonnard, M. Wu, J.-M. André, K. L. Guen, F. Schäfers, A. Sokolov, E. Filatova, A. Verna, Z. Wang, and Q. Huang, *Dichroism of x-ray fluorescence under standing waves regime in magnetic periodic multilayers*, <hal-01783440> (2018).
- [45] A. X. Gray, F. Kronast, C. Papp, S.-H. Yang, S. Cramm, I. P. Krug, F. Salmassi, E. M. Gullikson, D. L. Hilken, E. H. Anderson, P. Fischer, H. A. Dürr, C. M. Schneider, and C. S. Fadley, *Standing-wave excited soft x-ray photoemission microscopy: Application to Co microdot magnetic arrays*, Appl. Phys. Lett. **97**, 062503 (2010).
- [46] N. Jaouen, F. Wilhelm, A. Rogalev, and J. Goulon, *Magnetism of Impurities Probed with X-ray Standing Waves*, AIP Conf. Proc. **879**, 1707 (2007).
- [47] H. Kawata, T. Iwazumi, N. Shiotani, and F. Itoh, *First measurement of site-specific normal and magnetic XANES by using a standing wave field*, in *Resonant Anomalous X-Ray Scattering. Theory and Applications*, edited by G. Materlik, C. J. Sparks, and K. Fischer, Elsevier Science B.V., Amsterdam, 1994.
- [48] S. Macke, J. E. Hamann-Borrero, R. J. Green, B. Keimer, G. A. Sawatzky, and M. W. Haverkort, *Dynamical Effects in Resonant X-Ray Diffraction*, Phys. Rev. Lett. **117**, 115501 (2016).
- [49] J. M. Cowley, *Diffraction Physics*, Elsevier, Amsterdam, 1995.
- [50] J. Als-Nielsen and D. McMorrow, *Elements of Modern X-ray Physics*, John Wiley & Sons, Ltd, Chichester, 2001.
- [51] B. E. Warren, *X-ray diffraction*, Dover Publications, New York, 1990.
- [52] A. Authier, *Dynamical Theory of X-Ray Diffraction*, Oxford University Press, Oxford, 2001.

- [53] B. W. Batterman and H. Cole, *Dynamical Diffraction of X Rays by Perfect Crystals*, Rev. Mod. Phys. **36**, 681 (1964).
- [54] Z. G. Pinsker, *Dynamical Scattering of X-Rays in Crystals*, Springer-Verlag, Berlin Heidelberg, 1978.
- [55] J. D. Jackson, *Classical Electrodynamics*, Wiley, New York, 1962.
- [56] F. de Bergevin and M. Brunel, *Diffraction of X-rays by Magnetic Materials. I. General Formulae and Measurements on Ferro- and Ferrimagnetic Compounds*, Acta Crystallogr. **A37**, 314 (1981).
- [57] G. Molière, *Quantenmechanische Theorie der Röntgenstrahlinterferenzen in Kristallen. I. Ableitung und allgemeine Diskussion der dynamischen Grundgleichungen*, Ann. Phys. **35**, 272 (1939).
- [58] G. Molière, *Quantenmechanische Theorie der Röntgenstrahlinterferenzen in Kristallen. II. Dynamische Theorie der Brechung, Reflexion und Absorption von Röntgenstrahlen*, Ann. Phys. **35**, 297 (1939).
- [59] G. Molière, *Ausbau der quantenmechanischen Dispersionstheorie im Sinne eines von M. von Laue stammenden Verfahrens*, Ann. Phys. **36**, 265 (1939).
- [60] V. E. Dmitrienko, *Forbidden Reflections due to Anisotropic X-ray Susceptibility of Crystals*, Acta Crystallogr. **A39**, 29 (1983).
- [61] V. E. Dmitrienko, *Polarization anisotropy of X-ray atomic factors and ‘forbidden’ resonant reflections*, Acta Crystallogr. **A61**, 481 (2005).
- [62] V. E. Dmitrienko, *Anisotropy of X-ray Susceptibility and Bragg Reflections in Cubic Crystals*, Acta Crystallogr. **A40**, 89 (1984).
- [63] S. Ji, C. Song, J. Koo, K.-B. Lee, Y. J. Park, J. Y. Kim, J.-H. Park, H. J. Shin, J. S. Rhyee, B. H. Oh, and B. K. Cho, *Interference of Magnetic and Anisotropic Tensor Susceptibility Reflections in Resonant X-Ray Scattering of GdB₄*, Phys. Rev. Lett. **91**, 257205 (2003).
- [64] G. Thorkildsen, H. B. Larsen, E. Weckert, F. Mo, and R. H. Mathiesen, *Three-beam resonant X-ray diffraction in germanium – Laue transmission cases*, Acta Crystallogr. **A61**, 460 (2005).
- [65] P. J. Brown, A. G. Fox, E. N. Maslen, M. A. O’Keefeand, and B. T. M. Willis, *6.1. Intensity of diffracted intensities*, International Tables for Crystallography **C**, 554 (2006).
- [66] C. T. Chantler, K. Olsen, R. A. Dragoset, J. Chang, A. R. Kishore, S. A. Kotochigova, and D. S. Zucker, *Detailed Tabulation of Atomic Form Factors, Photoelectric Absorption and Scattering Cross Section, and Mass Attenuation Coefficients for Z = 1-92 from E = 1-10 eV to E = 0.4-1.0 MeV*, <https://www.nist.gov/pml/x-ray-form-factor-attenuation-and-scattering-tables>.
- [67] P. P. Ewald, *Zur Begründung der Kristalloptik. Teil III: Die Kristalloptik der Röntgenstrahlen*, Ann. Phys. **54**, 557 (1917).
- [68] J. Zegenhagen and A. Kazimirov, editors, *The X-ray standing wave technique. Principles and Applications*, World Scientific, Singapore, 2013.
- [69] J. A. Golovchenko, J. R. Patel, D. R. Kaplan, P. L. Cowan, and M. J. Bedzyk, *Solution to the Surface Registration Problem Using X-Ray Standing Waves*, Phys. Rev. Lett. **49**, 560 (1982).
- [70] Z. Zhang, P. Fenter, L. Cheng, N. C. Sturchio, M. J. Bedzyk, M. L. Machesky, and D. J. Wesolowski, *Model-independent X-ray imaging of adsorbed cations at the crystal–water interface*, Surf. Sci. Lett. **554**, 95 (2004).

-
- [71] C. Cohen-Tannoudji, B. Diu, and F. Laloë, *Quantum mechanics*, Hermann, Paris, 1977.
- [72] P. A. M. Dirac, *On the Theory of Quantum Mechanics*, Proc. Roy. Soc. A **112**, 661 (1926).
- [73] F. W. Byron and R. W. Fuller, *Mathematics of classical and quantum physics*, Addison-Wesley Publishing Company, Reading, 1969.
- [74] P. A. M. Dirac, *The Quantum Theory of the Emission and Absorption of Radiation*, Proc. Roy. Soc. A **114**, 243 (1927).
- [75] J. Orear and E. Fermi, *Nuclear Physics: A Course Given by Enrico Fermi at the University of Chicago*, University of Chicago Press, Chicago, 1950.
- [76] W. Pauli, *Zur Quantenmechanik des magnetischen Elektrons*, Z. Phys. **43**, 601 (1927).
- [77] F. Baudelet, *X-ray magnetic circular dichroism*, in *Neutron and X-ray Spectroscopy*, edited by F. Hippert, E. Geissler, J. L. Hodeau, E. Lelièvre-Berna, and J. R. Regnard, Springer, Dordrecht, 2006.
- [78] A. Fontaine, *Interaction of x-rays with matter: x-ray absorption spectroscopy*, in *Neutron and synchrotron radiation for condensed matter studies. Volume I. Theory, instruments and methods*, edited by J. Baruchel, J. L. Hodeau, M. S. Lehmann, J. R. Regnard, and C. Schlenker, EDP Sciences - Springer-Verlag, Berlin, 1993.
- [79] I. A. Vartanyants and J. Zegenhagen, *Theory of photoelectron emission from an x-ray interference field*, in *The x-ray standing wave technique. Principles and applications*, edited by J. Zegenhagen and A. Kazimirov, World Scientific, Singapore, 2013.
- [80] J. Stöhr and H. C. Siegmann, *Magnetism. From Fundamentals to Nanoscale Dynamics*, Springer-Verlag, Berlin Heidelberg, 2006.
- [81] D. Sébilleau, *X-ray and Electron Spectroscopies: An Introduction*, in *Magnetism: A Synchrotron Radiation Approach*, edited by E. Beaurepaire, H. Bulou, F. Scheurer, and J.-P. Kappler, Springer-Verlag, Berlin Heidelberg, 2006.
- [82] G. Schütz, W. Wagner, W. Wilhelm, P. Kienle, R. Zeller, R. Frahm, and G. Materlik, *Absorption of Circularly Polarized X Rays in Iron*, Phys. Rev. Lett. **58**, 737 (1987).
- [83] E. C. Stoner, *Collective electron ferromagnetism*, Proc. Roy. Soc. A **165**, 372 (1938).
- [84] J. Stöhr, *Exploring the microscopic origin of magnetic anisotropies with X-ray magnetic circular dichroism (XMCD) spectroscopy*, J. Magn. Magn. Mater. **200**, 470 (1999).
- [85] L. Baumgarten, *X-ray Absorption Spectroscopy*, in *Scattering Methods for Condensed Matter Research: Towards Novel Applications at Future Sources*, edited by M. Angst, T. Brückel, D. Richter, and R. Zorn, Forschungszentrum Jülich GmbH, Jülich, 2012.
- [86] J. Stöhr and Y. Wu, *X-Ray Magnetic Circular Dichroism: Basic Concepts and Theory for 3d Transition Metal Atoms*, in *New Directions in Research with Third-Generation Soft X-Ray Synchrotron Radiation Sources*, edited by A. S. Schlachter and F. J. Wuilleumier, Kluwer Academic Publishers, Dordrecht, 1994.
- [87] J. Stöhr, *X-ray magnetic circular dichroism spectroscopy of transition metal thin films*, J. Electron Spectrosc. Relat. Phenom. **75**, 253 (1995).
- [88] A. Rogalev, F. Wilhelm, N. Jaouen, J. Goulon, and J.-P. Kappler, *X-ray Magnetic Circular Dichroism: Historical Perspective and Recent Highlights*, in *Magnetism: A Synchrotron Radiation Approach*, edited by E. Beaurepaire, H. Bulou, F. Scheurer, and J.-P. Kappler, Springer-Verlag, Berlin Heidelberg, 2006.

- [89] S. W. Lovesey and S. P. Collins, *X-Ray Scattering and Absorption by Magnetic Materials*, Clarendon Press, Oxford, 1996.
- [90] M. Tanabashi et al., *Review of Particle Physics*, Phys. Rev. D **98**, 030001 (2018).
- [91] R. Wienke, G. Schütz, and H. Ebert, *Determination of local magnetic moments of 5d impurities via spin-dependent absorption*, J. Appl. Phys. **69**, 6147 (1991).
- [92] H. Ebert and R. Zeller, *Theoretical study of the magnetic x-ray dichroism of Os, Ir, Pt, and Au impurities in Fe*, Phys. Rev. B **42**, 2744 (1990).
- [93] J. Bartolomé, A. I. Figueroa, F. Bartolomé, L. M. García, F. Wilhelm, and A. Rogalev, *d-band magnetism of Ag, Au, Pd and Pt studied with XMCD*, Solid State Phenom. **194**, 92 (2012).
- [94] G. Y. Guo, *What does the K-edge x-ray magnetic circular dichroism spectrum tell us?*, J. Phys.: Condens. Matter **8**, L747 (1996).
- [95] G. Schütz, M. Knülle, R. Wienke, W. Wilhelm, W. Wagner, P. Kienle, and R. Frahm, *Spin-dependent photoabsorption at the L-edges of ferromagnetic Gd and Tb metal*, Z. Phys. B **73**, 67 (1988).
- [96] H. Ebert, G. Schütz, and W. M. Temmerman, *Theoretical study of the magnetic x-ray dichroism of hcp-Gd*, Solid State Commun. **76**, 475 (1990).
- [97] B. T. Thole, P. Carra, F. Sette, and G. van der Laan, *X-Ray Circular Dichroism as a Probe of Orbital Magnetization*, Phys. Rev. Lett. **68**, 1943 (1992).
- [98] P. Carra, B. T. Thole, M. Altarelli, and X. Wang, *X-Ray Circular Dichroism and Local Magnetic Fields*, Phys. Rev. Lett. **70**, 694 (1993).
- [99] C. F. Hague, J.-M. Mariot, P. Strange, P. J. Durham, and B. L. Gyorffy, *Observation of magnetic circular dichroism in Fe $L_{2,3}$ x-ray-fluorescence spectra*, Phys. Rev. B **48**, 3560 (1993).
- [100] S. Eisebitt, J. Lüning, W. F. Schlotter, M. Lörger, O. Hellwig, W. Eberhardt, and J. Stöhr, *Lensless imaging of magnetic nanostructures by X-ray spectro-holography*, Nature **432**, 885 (2004).
- [101] C. Tieg, R. Frömter, D. Stickler, S. Hankemeier, A. Kobs, S. Streit-Nierobisch, C. Gutt, G. Grübel, and H. P. Oepen, *Imaging the in-plane magnetization in a Co microstructure by Fourier transform holography*, Opt. Express **18**, 27251 (2010).
- [102] P. Fischer, R. Zeller, G. Schütz, G. Goerigk, and H.-G. Haubold, *Magnetic Small Angle X-Ray Scattering*, J. Phys. IV Proc. **7**, 753 (1997).
- [103] P. Strange, P. J. Durham, and B. L. Gyorffy, *Dichroic X-Ray Fluorescence*, Phys. Rev. Lett. **67**, 3590 (1991).
- [104] A. Juhin, P. Sainctavit, K. Ollefs, M. Sikora, A. Filipponi, P. Glatzel, F. Wilhelm, and A. Rogalev, *X-ray magnetic circular dichroism measured at the Fe K-edge with a reduced intrinsic broadening: x-ray absorption spectroscopy versus resonant inelastic x-ray scattering measurements*, J. Phys.: Condens. Matter **28**, 505202 (2016).
- [105] R. M. Galéra, J. P. Rueff, A. Rogalev, C. Giorgetti, and E. Dartyge, *XMCD at the Co K-edge in RCo₂ intermetallics: influence of the rare earths*, J. Synchrotron Rad. **6**, 676 (1999).
- [106] H. Wang, C. Bryant, D. W. Randall, L. B. LaCroix, E. I. Solomon, M. LeGros, and S. P. Cramer, *X-ray Magnetic Circular Dichroism Sum Rule Analysis of the Blue Copper Site in Plastocyanin. A Probe of Orbital and Spin Angular Momentum*, J. Phys. Chem. B **102**, 8347 (1998).

- [107] H. Wang, C. Bryant, M. LeGros, X. Wang, and S. P. Cramer, *Fluorescence-Detected X-ray Magnetic Circular Dichroism of Well-Defined Mn^{II} and Ni^{II} Doped in MgO Crystals: Credential Evaluation for Measurements on Biological Samples*, J. Phys. Chem. A **116**, 10082 (2012).
- [108] F. M. F. de Groot, M. A. Arrio, P. Saintavit, C. Carrier, and C. T. Chen, *Fluorescence yield detection: why it does not measure the x-ray absorption cross section*, Solid State Commun. **92**, 991 (1994).
- [109] C. Piamonteze, P. Miedema, and F. M. F. de Groot, *Accuracy of the spin sum rule in XMCD for the transition-metal L edges from manganese to copper*, Phys. Rev. B **80**, 184410 (2009).
- [110] B. Liu, C. Piamonteze, M. U. Delgado-Jaime, R.-P. Wang, J. Heidler, J. Dreiser, R. Chopdekar, F. Nolting, and F. M. F. de Groot, *Sum rule distortions in fluorescence-yield x-ray magnetic circular dichroism*, Phys. Rev. B **96**, 054446 (2017).
- [111] The Mathworks, Inc., Natick, Massachusetts, *MATLAB version 9.5.0.944444 (R2018b)*, 2018.
- [112] A. H. Geisler and D. L. Martin, *A New Superlattice in Co-Pt Alloys*, J. Appl. Phys. **23**, 375 (1952).
- [113] M. Menzinger and A. Paoletti, *Magnetic Moments and Unpaired-Electron Densities in CoPt₃*, Phys. Rev. **143**, 365 (1966).
- [114] H. Berg and J. B. Cohen, *Long-Range Order and Ordering Kinetics in CoPt₃*, Metall. Trans. **3**, 1797 (1972).
- [115] A. S. Darling, *Cobalt-Platinum Alloys. A Critical Review of Their Constitution and Properties*, Platinum Metals Rev. **7**, 96 (1963).
- [116] K. Momma and F. Izumi, *VESTA 3 for three-dimensional visualization of crystal, volumetric and morphology data*, J. Appl. Crystallog. **44**, 1271 (2011).
- [117] H. J. Albert and L. R. Rubin, *Magnetic Properties of the Platinum Metals and Their Alloys*, in *Platinum Group Metals and Compounds*, edited by U. V. Rao, American Chemical Society, Washington, DC, 1971.
- [118] M. Menzinger and A. Paoletti, *Finite-temperature anisotropy of PtCo magnets*, IEEE Trans. Magn. **39**, 2917 (2003).
- [119] S. Suga and S. Imada, *Magnetic dichroism in core absorption and photoemission*, J. Electron Spectrosc. Relat. Phenom. **92**, 1 (1998).
- [120] A. Kootte, C. Haast, and R. A. de Groot, *The electronic structure of ordered binary Co-Pt compounds*, J. Phys.: Condens. Matter **3**, 1133 (1991).
- [121] A. C. Thompson, D. T. Attwood, E. M. Gullikson, M. R. Howells, J. B. Kortright, A. L. Robinson, J. H. Underwood, K.-J. Kim, J. Kirz, I. Lindau, P. Pianetta, H. Winick, G. P. Williams, and J. H. Scofield, *X-ray data booklet*, Lawrence Berkeley National Laboratory, Berkeley, 2001.
- [122] A. A. Mills, *The Lodestone: History, Physics, and Formation*, Ann. For. Sci. **61**, 273 (2004).
- [123] P. Wasilewski and G. Kletetschka, *Lodestone: Natures only permanent magnet-What it is and how it gets charged*, Geophys. Res. Lett. **26**, 2275 (1999).
- [124] M. E. Fleet, *Structure of Magnetite*, Acta Crystallogr. **B37**, 917 (1981).
- [125] E. J. W. Verwey, *Electronic Conduction of Magnetite (Fe₃O₄) and its Transition Point at Low Temperatures*, Nature **144**, 327 (1939).

- [126] F. Walz, *The Verwey transition — a topical review*, J. Phys.: Condens. Matter **14**, R285 (2002).
- [127] Z. Tarnawski, A. Wiecheć, M. Madej, D. Nowak, D. Owoc, G. Król, Z. Kąkol, L. Kolwicz-Chodak, A. Kozłowski, and T. Dawid, *Studies of the Verwey Transition in Magnetite*, Acta Phys. Pol. A **106**, 771 (2004).
- [128] J. P. Wright, J. P. Attfield, and P. G. Radaelli, *Long Range Charge Ordering in Magnetite Below the Verwey Transition*, Phys. Rev. Lett. **87**, 266401 (2001).
- [129] S. Klotz, G. Rousse, T. Strässle, C. L. Bull, and M. Guthrie, *Nuclear and magnetic structure of magnetite under pressure to 5.3 GPa and at low temperatures to 130 K by neutron scattering*, Phys. Rev. B **74**, 012410 (2006).
- [130] L. Néel, *Propriétés magnétiques de l'état métallique et énergie d'interaction entre atomes magnétiques*, Ann. Phys. **11**, 232 (1936).
- [131] P. Weiss and R. Forrer, *La saturation absolue des ferromagnétiques et les lois d'approche en fonction du champ et de la température*, Ann. Phys. **10**, 279 (1929).
- [132] K. P. Belov, *Electronic processes in magnetite (or, "Enigmas of magnetite")*, Usp. Fiz. Nauk **163**, 53 (1993).
- [133] S. Ruiz-Gómez, L. Pérez, A. Mascaraque, A. Quesada, P. Prieto, I. Palacio, L. Martín-García, M. Foerster, L. Aballe, and J. de la Figuera, *Geometrically defined spin structures in ultrathin Fe_3O_4 with bulk like magnetic properties*, Nanoscale **10**, 5566 (2018).
- [134] E. Goering, *Large hidden orbital moments in magnetite*, Phys. Status Solidi B **248**, 2345 (2011).
- [135] C. G. Shull, E. O. Wollan, and W. A. Strauser, *Magnetic Structure of Magnetite and Its Use in Studying the Neutron Magnetic Interaction*, Phys. Rev. **81**, 483 (1951).
- [136] E. Lima Jr., A. L. Brandl, A. D. Arelaro, and G. F. Goya, *Spin disorder and magnetic anisotropy in Fe_3O_4 nanoparticles*, J. Appl. Phys. **99**, 083908 (2006).
- [137] R. Aragón, *Cubic magnetic anisotropy of nonstoichiometric magnetite*, Phys. Rev. B **46**, 5334 (1992).
- [138] P. Morrall, F. Schedin, S. Langridge, J. Bland, M. F. Thomas, and G. Thornton, *Magnetic moment in an ultrathin magnetite film*, J. Appl. Phys. **93**, 7960 (2003).
- [139] V. Cherepanov, I. Kolokolov, and V. L'vov, *The saga of YIG: spectra, thermodynamics, interaction and relaxation of magnons in a complex magnet*, Phys. Rep. **229**, 81 (1992).
- [140] S. Geller and M. Gilleo, *Crystal structure and ferrimagnetism of yttrium-iron garnet, $Y_3Fe_2(FeO_4)_3$* , J. Phys. Chem. Solids **3**, 30 (1957).
- [141] M. Bonnet, A. Delapalme, H. Fuess, and M. Thomas, *Refinement of the Structure of Yttrium Iron Garnet (YIG). A Case of Severe Extinction and Absorption*, Acta Crystallogr. **B31**, 2233 (1975).
- [142] A. Bouguerra, G. Fillion, E. K. Hlil, and P. Wolfers, *$Y_3Fe_5O_{12}$ yttrium iron garnet and lost magnetic moment (computing of spin density)*, J. Alloys Comp. **442**, 231 (2007).
- [143] D. Rodic, M. Mitric, R. Tellgren, H. Rundlof, and A. Kremenovic, *True magnetic structure of the ferrimagnetic garnet $Y_3Fe_5O_{12}$ and magnetic moments of iron ions*, J. Magn. Magn. Mater. **191**, 137 (1999).
- [144] S. Shamoto, T. U. Ito, H. Onishi, H. Yamauchi, Y. Inamura, M. Matsuura, M. Akatsu, K. Kodama, A. Nakao, T. Moyoshi, K. Munakata, T. Ohhara, M. Nakamura, S. Ohira-Kawamura, Y. Nemoto, and K. Shibata, *Neutron scattering study of yttrium iron garnet*, Phys. Rev. B **97**, 054429 (2018).

- [145] R. L. Blake, R. E. Hessevick, T. Zoltai, and L. W. Finger, *Refinement of the hematite structure*, Am. Mineral. **51**, 123 (1966).
- [146] C. G. Shull, W. A. Strauber, and E. O. Wollan, *Neutron Diffraction by Paramagnetic and Antiferromagnetic Substances*, Phys. Rev. **83**, 333 (1951).
- [147] F. J. Morin, *Magnetic Susceptibility of $\alpha\text{Fe}_2\text{O}_3$ and $\alpha\text{Fe}_2\text{O}_3$ with Added Titanium*, Phys. Rev. **78**, 819 (1950).
- [148] R. Nathans, S. J. Pickart, H. A. Alperin, and P. J. Brown, *Polarized-Neutron Study of Hematite*, Phys. Rev. **136**, A1641 (1964).
- [149] A. H. Hill, F. Jiao, P. G. Bruce, A. Harrison, W. Kockelmann, and C. Ritter, *Neutron Diffraction Study of Mesoporous and Bulk Hematite, $\alpha\text{Fe}_2\text{O}_3$* , Chem. Mater. **20**, 4891 (2008).
- [150] I. Dzyaloshinsky, *A thermodynamic theory of "weak" ferromagnetism of antiferromagnetics*, J. Phys. Chem. Solids **4**, 241 (1958).
- [151] T. Moriya, *Anisotropic Superexchange Interaction and Weak Ferromagnetism*, Phys. Rev. **120**, 91 (1960).
- [152] T. G. Worlton and D. L. Decker, *Neutron Diffraction Study of the Magnetic Structure of Hematite to 41 kbar*, Phys. Rev. **171**, 596 (1968).
- [153] C. Malgrange, C. Carvalho, L. Braicovich, and J. Goulon, *Transfer of circular polarization in Bragg crystal X-ray monochromators*, Nucl. Instrum. Meth. in Phys. Res. A **308**, 390 (1991).
- [154] Q. Shen, *Effects of a General X-ray Polarization in Multiple-Beam Bragg Diffraction*, Acta Crystallogr. **A49**, 605 (1993).
- [155] A. Smekhova, D. Schmitz, N. V. Izarova, M. Stuckart, S. F. Shams, K. Siemensmeyer, F. M. F. de Groot, P. Kögerler, and C. Schmitz-Antoniak, *Intramolecular crossover from unconventional diamagnetism to paramagnetism of palladium ions probed by soft X-ray magnetic circular dichroism*, Commun. Chem. **3**, 96 (2020).
- [156] W. T. Fuhrman, J. C. Leiner, J. W. Freeland, M. van Veenendaal, S. M. Koohpayeh, W. A. Phelan, T. M. McQueen, and C. Broholm, *Magnetic dichroism in the Kondo insulator SmB_6* , Phys. Rev. B **99**, 020401(R) (2019).
- [157] P. J. Duke, *Synchrotron Radiation. Production and Properties*, Oxford University Press, Oxford, 2000.
- [158] E. Weckert, *The potential of future light sources to explore the structure and function of matter*, IUCrJ **2**, 230 (2015).
- [159] T. Gog and S. M. Durbin, *UHV rotary manipulator with arcsecond resolution for x-ray standing-wave experiments*, Rev. Sci. Instrum **60**, 3030 (1989).
- [160] M. K. Tiwari, G. Das, and M. J. Bedzyk, *X-ray standing wave analysis of nanostructures using partially coherent radiation*, Appl. Phys. Lett. **107**, 103104 (2015).
- [161] J. A. Golovchenko, B. M. Kincaid, R. A. Levesque, A. E. Meixner, and D. R. Kaplan, *Polarization Pendellösung and the Generation of Circularly Polarized X Rays with a Quarter-Wave Plate*, Phys. Rev. Lett. **57**, 202 (1986).
- [162] S. Petitgirard, I. Daniel, Y. Dabin, H. Cardon, R. Tucoulou, and J. Susini, *A diamond anvil cell for x-ray fluorescence measurements of trace elements in fluids at high pressure and high temperature*, Rev. Sci. Instrum. **80**, 033906 (2009).

- [163] W. Kabsch, *XDS*, Acta Crystallogr. **D66**, 125 (2010).
- [164] J. Stempfer, S. Francoual, D. Reuther, D. K. Shukla, A. Skaugen, H. Schulte-Schrepping, T. Kracht, and H. Franz, *Resonant scattering and diffraction beamline P09 at PETRA III*, J. Synchrotron Rad. **20**, 541 (2013).
- [165] K. Balewski, W. Brefeld, W. Decking, H. Franz, R. Röhlberger, and E. Weckert, editors, *PETRA III: A Low Emittance Synchrotron Radiation Source. Technical Design Report*, DESY, Hamburg, 2004.
- [166] S. Francoual, J. Stempfer, D. Reuther, D. K. Shukla, and A. Skaugen, *Double phase-retarder set-up at beamline P09 at PETRA III*, J. Phys.: Conf. Ser. **425**, 132010 (2013).
- [167] J. Stempfer, J. R. L. Mardegan, S. Francoual, L. S. I. Veiga, L. Bouchenoire, T. Spitzbart, and H. Zink, *Fast helicity switching of X-ray circular polarization at beamline P09 at PETRA III*, AIP Conf. Proc. **1741**, 030017 (2016).
- [168] T. Kuschel, C. Klewe, J.-M. Schmalhorst, F. Bertram, O. Kuschel, T. Schemme, J. Wollschläger, S. Francoual, J. Stempfer, A. Gupta, M. Meinert, G. Götz, D. Meier, and G. Reiss, *Static Magnetic Proximity Effect in Pt/NiFe₂O₄ and Pt/Fe Bilayers Investigated by X-Ray Resonant Magnetic Reflectivity*, Phys. Rev. Lett. **115**, 097401 (2015).
- [169] M. R. Squillante, R. Farrell, J. C. Lund, F. Sinclair, G. Entine, and K. R. Keller, *Avalanche diode low energy x-ray and nuclear particle detector*, IEEE Trans. Nucl. Sci. **33**, 336 (1986).
- [170] S. Kishimoto, *Avalanche Photodiodes as Fast X-ray Detectors*, J. Synchrotron Rad. **5**, 275 (1998).
- [171] A. Ochi, Y. Nishi, and T. Tanimori, *Study of a large area avalanche photodiode as a fast photon and a soft X-ray detector*, Nucl. Instrum. Meth. in Phys. Res. A **378**, 267 (1986).
- [172] T. Eggert, O. Boslau, P. Goldstrass, and J. Kemmer, *Silicon drift detectors with enlarged sensitive areas*, X-Ray Spectrom. **33**, 246 (2004).
- [173] G. Lutz, *Silicon drift and pixel devices for X-ray imaging and spectroscopy*, J. Synchrotron Rad. **13**, 99 (2006).
- [174] J. C. Lagarias, J. A. Reeds, M. H. Wright, and P. E. Wright, *Convergence Properties of the Nelder-Mead Simplex Method in Low Dimensions*, SIAM J. Optim. **9**, 112 (1998).
- [175] G. A. F. Seber and C. J. Wild, *Nonlinear Regression*, NJ: Wiley-Interscience, Hoboken, 2003.
- [176] <https://uk.mathworks.com/help/stats/nlinfit.html>.
- [177] S. Brandt, *Data Analysis. Statistical and Computational Methods for Scientists and Engineers*, Springer, Heidelberg, 2014.
- [178] J. R. L. Mardegan, private communication.
- [179] D. Weller, H. Brändle, G. Gorman, C.-J. Lin, and H. Notarys, *Magnetic and magneto-optical properties of cobalt-platinum alloys with perpendicular magnetic anisotropy*, Appl. Phys. Lett. **61**, 2726 (1998).
- [180] <https://www.mtixtl.com/YIG-c-05D05C1.aspx>.
- [181] E. J. J. Mallmann, A. S. B. Sombra, J. C. Goes, and P. B. A. Fechine, *Yttrium Iron Garnet: Properties and Applications Review*, Solid State Phenom. **202**, 65 (2013).

-
- [182] B. B. Krichevtsov, S. V. Gastev, S. M. Suturin, V. V. Fedorov, A. M. Korovin, V. E. Bursian, A. G. Banshchikov, M. P. Volkov, M. Tabuchi, and N. S. Sokolov, *Magnetization reversal in YIG/GGG(111) nanoheterostructures grown by laser molecular beam epitaxy*, Sci. Technol. Adv. Mater. **18**, 351 (2017).
- [183] M. Ashkin and M. Kuriyama, *Quantum Theory of X-Ray Diffraction by a Crystal*, J. Phys. Soc. Jpn. **21**, 1549 (1966).
- [184] J. Zhang, W.-J. Ji, J. Xu, X.-Y. Geng, J. Zhou, Z.-B. Gu, S.-H. Yao, and S.-T. Zhang, *Giant positive magnetoresistance in half-metallic double-perovskite Sr_2CrWO_6 thin films*, Sci. Adv. **3**, e1701473 (2017).
- [185] A. Venimadhav, F. Sher, J. P. Attfield, and M. G. Blamire, *High Curie temperature in B-site ordered Sr_2CrWO_6 epitaxial thin films*, Solid State Commun. **138**, 314 (2006).
- [186] P. Majewski, S. Geprägs, A. Boger, M. Opel, A. Erb, R. Gross, G. Vaitheeswaran, V. Kanchana, A. Delin, F. Wilhelm, A. Rogalev, and L. Alff, *Magnetic moments of W 5d in Ca_2CrWO_6 and Sr_2CrWO_6 double perovskites*, Phys. Rev. B **72**, 132402 (2005).
- [187] G. Mercurio, I. A. Makhotkin, I. Milov, Y. Y. Kim, I. A. Zaluzhnyy, S. Dziarzhyski, L. Wenthaus, I. A. Vartanyants, and W. Wurth, *Surface structure determination by x-ray standing waves at a free-electron laser*, New J. Phys. **21**, 033031 (2019).
- [188] H. Zhong, A. Finco, J. Fischer, A. Haykal, K. Bouzehouane, C. Carr 'etéro, F. Godel, P. Maletinsky, M. Munsch, S. Fusil, V. Jacques, and V. Garcia, *Quantitative Imaging of Exotic Antiferromagnetic Spin Cycloids in $BiFeO_3$ Thin Films*, Phys. Rev. Appl. **17**, 044051 (2022).
- [189] R. Sharma and S. K. Mishra, *Interfacial skyrmion in magnetic thin films and its applications*, J. Magn. Magn. Mater. **551**, 169107 (2022).
- [190] T. Dietl, *A ten-year perspective on dilute magnetic semiconductors and oxides*, Nat. Mater. **9**, 965 (2010).

Acknowledgements

A successful accomplishment of this project would not be possible without the help of many people. This included discussions, assistance during experimental work and simply building up a friendly atmosphere in the work place. I would like to thank:

- **Martin Tolkiehn** for sparking my interest in dynamical theory of diffraction via the inspiring lecture during the DESY Summer Programme, and for proposing this interesting topic of the project. I am thankful for numerous discussions about science and life, introducing me into the research at the large scale facility and helping me to understand the experimental and technical aspects of the diffraction methods.
- **Edgar Weckert** for being the advisor for this thesis. I highly appreciate an opportunity for scientific conversations and proofreading of the dissertation's text.
- **Andreas Stierle** for being the advisor for this thesis and inviting me to a number of Nanolab seminars, where I could present the progress in my work.
- **Nina Rohringer** and **Caren Hagner** for showing an interest in my work and being the members of the commission for my defence.
- **Heiko Schulz-Ritter** for the great help with any technical aspects of my work, especially the design of the permanent magnet systems. I thank You for making my time in Hamburg more pleasurable due to your sense of humour, numerous discussions and encouraging me to start to use German in our conversations.
- **Leila Noohinejad** for a number of common synchrotron shifts, during which we learnt about our research fields. I thank You for being a wonderful office-mate, numerous conversations and showing me some aspects of Iranian culture.
- **Sebastian Thieß** for plenty of conversations about science, life and politics, during which we drank hektoliters of tea and ate dozens of *Schokokuss*, and which broadened my horizons at the same time making being at DESY really enjoyable.
- the group of the **P09 beamline**. In particular **Sonia Francoual**, **Jose Renato Linares Mardegan** and **Julian Bergtholdt** for all the help before and during the experiments. I thank Jose for fruitful discussion regarding the analysis of the XMCD data.
- **Wiebke Ohm** for letting me work under your supervision during the DESY Summer Programme and introducing to the research at PETRA III. This wonderful experience encouraged me for further scientific work in general and at DESY in particular.
- **Carsten Paulmann** for his patience when explaining me the principles of the operation of kappa diffractometer and basics of single crystal data analysis.
- **Jan Karl Horst Timm** for being my mentor during my PhD work and being open for discussion about any difficulties.

- **Sarmad Adeel** for showing interest in my work and for a number of discussions about your work and politics.
- **Agnieszka Huć** for proofreading the fragments of the text of the dissertation.
- **Maximilian Morgenbesser** and **Alexander Viernstein** for discussions about the x-ray standing waves and for providing the Sr_2CrWO_6 thin film samples.
- **Rebeca Ibarra** for providing the samples of $\text{Mn}_{1.5}\text{PtSn}$ thin films.
- **Cornelius Strohm**, **Tatiana Gurieva** and **Kai Schlage** for the magnetic measurements of the samples.
- **Giuseppe Mercurio** for showing a great interest in my work and for fruitful discussions, which guided me towards further development of the MXSW method.
- **Steffen Tober** for interesting and useful discussions about your work and magnetite.
- **Matthias Riepp** for showing interest in my project and for the discussion, which helped me to understand some aspects of the magnetic holography.
- **Markus Tischer** for help with designing a permanent magnet system, particularly for the idea of using yokes.
- the **community of PETRA III Ada Jonath hall** for making coming to work not a duty, but a pleasure.

Special thanks to my family and friends!